

# Rapid Prototyping of Microfluidic Devices: Realization of Magnetic Micropumps, Fuel Cells and Protein Preconcentrators

THÈSE N° 4915 (2010)

PRÉSENTÉE LE 17 DÉCEMBRE 2010

À LA FACULTÉ SCIENCES ET TECHNIQUES DE L'INGÉNIEUR

LABORATOIRE DE MICROSYSTÈMES 2

PROGRAMME DOCTORAL EN MICROSYSTÈMES ET MICROÉLECTRONIQUE

ÉCOLE POLYTECHNIQUE FÉDÉRALE DE LAUSANNE

POUR L'OBTENTION DU GRADE DE DOCTEUR ÈS SCIENCES

PAR

Meng SHEN

acceptée sur proposition du jury:

Prof. M. A. Ionescu, président du jury

Prof. M. Gijs, directeur de thèse

Dr L. Dovat, rapporteur

Prof. P. Murali, rapporteur

Prof. P. Woias, rapporteur



ÉCOLE POLYTECHNIQUE  
FÉDÉRALE DE LAUSANNE

Suisse  
2010



# Abstract

With the growing importance of miniaturized energy applications and the development of micro Total Analysis Systems ( $\mu$ TAS), we have realized microfluidic devices, namely, magnetic micropumps, microfluidic fuel cells and membrane-based protein preconcentrators, all having high application potential in future. The choice of rapid prototyping microfabrication technologies and the selection of affordable materials are important aspects, when thinking of commercialization. Thus, we have employed powder blasting, polymer molding and assembly technologies during devices fabrication throughout the thesis.

The first type of microfluidic device that we present is a poly(methyl methacrylate) (PMMA) ball-valve micropump with two different designs of the electromagnetic actuator, as optimized by the finite element method. The integration of a permanent magnet in a flexible polydimethylsiloxane (PDMS) membrane, which is clamped into PMMA structure, is proposed for providing a large stroke of the pumping membrane, making the micropump bubble-tolerant and self-priming. Focusing on low power consumption for  $\mu$ TAS integration, another type of magnetic micropump with active valves is realized. It consists of a microfluidic chamber structure in glass that is assembled with a PDMS sheet, which comprises two valving membranes and a central actuation membrane, having each an integrated permanent magnet that is peristaltically actuated by a rotating arc-shaped permanent magnets assembly. A lumped circuit model is developed to predict and describe the frequency-dependent flow rate behavior for this type of pump. Powder blasting and PDMS molding rapid prototyping technologies are employed for realization of these two types of micropumps.

Fuel cells with fluid delivery and removal options, having chemical reaction sites and electrode structures that can be realized in a microfluidic format, have high potential for applications. Therefore, microfluidic direct methanol fuel cells with embedded ion-permselective medium are studied and such type of fuel cell is realized by integrating a narrow Nafion strip in a molded elastomeric structure. A mechanical clamping assembly technology enables leakage-free operation and stable performance. The characterization reveals its output power density, using  $\text{H}_2\text{O}_2$ -based oxidant, is among the high-performance direct methanol fuel cells in microscale.

Re-using the technology of the fuel cell chip, with its particular ion-permselective Nafion membrane and assembly method, we also have developed a protein preconcentrator with high purification performance. Our device can preconcentrate negatively charged biomolecules located at the anodic compartment side of the Nafion strip within only a few minutes with a high

## Abstract

preconcentration factor. Moreover, a complex microfluidic finite element model is proposed to study and understand the physics of the preconcentration effect.

Finally, we conclude the thesis with an outlook on future developments based on our work of the project and on the assembly technologies for microfluidic device integration.

**Key words:** rapid prototyping, micropump, direct methanol fuel cell, protein preconcentrator, Lab-On-a-Chip, Nafion



# Résumé

Avec l'importance croissante des applications d'énergie miniaturisées et le développement de laboratoire sur puce ou micro-Total Analysis-Systems ( $\mu$ TAS), nous avons réalisé dispositifs microfluidiques ayant de large applications dans le futur : des micropompes magnétiques, des piles à combustible direct et des pré-concentrateurs membranaires de protéines. De point de vue de commercialisation, la réalisation de dispositifs de prototypage par des technologies de microfabrication rapides et par utilisation de matériaux peu coûteux sont des aspects importants. Dans ce travail de thèse, ces dispositifs microfluidiques ont été fabriqués en utilisant différentes techniques : usinage par sablage, moulage de polymère et assemblage.

Le premier type de dispositif microfluidique que nous présentons est une micropompe magnétique en polyméthacrylate de méthyle (PMMA) et utilise des billes comme valves. Deux conceptions différentes de l'actionneur électromagnétique ont été étudiées et optimisées par la méthode des éléments finis. Pour les deux cas, une membrane flexible en polydiméthylsiloxane (PDMS), collée au PMMA, contenant un aimant permanent est utilisée pour obtenir un large déplacement de la membrane pendant l'opération de pompage ce qui permet d'améliorer les tolérances de la micropompe face aux bulles et à l'auto-amorçage. Visant une faible consommation de puissance, un autre type de micropompe magnétique avec des valves actives est proposée. Elle se compose d'un réservoir microfluidique en verre et d'une membrane flexible en PDMS. La couche en PDMS est conçue pour réaliser trois zones membranaires ayant chacune un aimant permanent. Un système tournant contenant un ensemble d'aimants en forme d'arc permet d'actionner ces valves de manière indépendante selon mouvement péristaltique. Un modèle de circuit pour prévoir et décrire le comportement du flux d'écoulement en fonction de la fréquence du signal d'actuation a été développé. Pour la fabrication de ces micropompes, nous avons utilisé la technique d'usinage par sablage et le moulage de PDMS.

Les piles à combustible avec des sites de réactions chimiques et des électrodes structurées pouvant être réalisées au format microfluidique possèdent un large potentiel d'applications. Par conséquent, nous proposons des piles microfluidiques au méthanol direct incorporant une membrane échangeuse d'ions en Nafion. Ce type de pile à combustible est réalisé en assemblant une fine couche en Nafion dans une structure moulée en élastomère. Leur assemblage par serrage mécanique permet de garantir leur fonctionnement sans fuites et une meilleure stabilité de leur performance. En utilisant un oxydant à base de  $H_2O_2$ , la caractérisation de ces piles présente une densité de puissance de sortie parmi les plus performants des piles au méthanol miniaturisées.

La technologie de fabrication du dispositif à pile à combustible avec sa membrane échangeuse d'ions en Nafion et la méthode d'assemblage ont été réutilisés pour fabriquer un pré-concentrateur de protéines avec des performances d'épuration élevées. Notre dispositif permet une pré-concentration des biomolécules chargés négativement dans le compartiment anodique du côté de la membrane en Nafion en seulement quelques minutes avec un facteur de pré-concentration très élevé. En plus, un modèle complexe par éléments finis de la structure microfluidique est proposé afin d'étudier et de comprendre la physique de l'effet de pré-concentration.

Enfin, nous concluons la thèse avec une vue d'ensemble sur les développements futurs se basant sur ce travail de thèse et sur les technologies pour l'intégration de ces dispositifs microfluidiques.

**Mots Clés:** prototypage rapide, micropompe, pile à combustible direct au méthanol, pré concentrateur de protéines, laboratoire sur puce, Nafion

# Table of Contents

<b>ABSTRACT .....</b>	<b>I</b>
<b>RÉSUMÉ .....</b>	<b>III</b>
<b>TABLE OF CONTENTS .....</b>	<b>V</b>
<b>ABBREVIATIONS .....</b>	<b>XI</b>
<b>1 GENERAL INTRODUCTION.....</b>	<b>1</b>
<b>1.1 INTRODUCTION.....</b>	<b>1</b>
<b>1.2 MICROFLUIDICS AND LAB-ON-A-CHIP .....</b>	<b>2</b>
<b>1.3 THESIS SCOPE AND OUTLINE .....</b>	<b>3</b>
<b>REFERENCES .....</b>	<b>4</b>
<b>2 BACKGROUND AND THEORETICAL ASPECTS .....</b>	<b>7</b>
<b>2.1 THEORETICAL MICROFLUIDICS .....</b>	<b>8</b>
2.1.1 <i>Fluid parameters and definitions.....</i>	8
2.1.2 <i>Fluid laws.....</i>	10
2.1.3 <i>Pressure driven flow.....</i>	12
2.1.4 <i>Fluid-structure interaction (FSI).....</i>	13
2.1.5 <i>RLC equivalent model.....</i>	15
2.1.6 <i>Electrodynamics in microfluidic systems.....</i>	17
<b>2.2 BASICS OF MAGNETIC ACTUATION.....</b>	<b>21</b>
2.2.1 <i>Basic concepts of magnetism .....</i>	21
2.2.2 <i>Magnetic materials .....</i>	22
2.2.3 <i>Principle of electromagnetic actuation.....</i>	24
2.2.4 <i>Principle of rotating magnetic actuation .....</i>	25
<b>2.3 ION CONDUCTANCE IN MICROFLUIDIC SYSTEMS.....</b>	<b>26</b>
2.3.1 <i>General equations for ionic liquid solutions.....</i>	26
2.3.2 <i>Ion-permselective medium.....</i>	27
2.3.3 <i>Transport in ion-permselective membrane .....</i>	28
2.3.4 <i>Concentration polarization near a membrane mediated by electrical field .....</i>	29
<b>2.4 CONCLUSION .....</b>	<b>32</b>
<b>REFERENCES .....</b>	<b>33</b>
<b>3 STATE-OF-THE-ART .....</b>	<b>35</b>
<b>3.1 STATE-OF-THE-ART ON MAGNETICALLY ACTUATED MICROPUMPS.....</b>	<b>36</b>
3.1.1 <i>Actuators .....</i>	36
3.1.2 <i>Valving principles.....</i>	40

3.1.3 Micropumps.....	43
3.1.4 Conclusion.....	47
<b>3.2 STATE-OF-THE-ART ON MICRO-DIRECT METHANOL FUEL CELLS.....</b>	<b>47</b>
3.2.1 Basic parameters of a micro-direct methanol fuel cell.....	48
3.2.2 Scaling law for a micro fuel cell.....	51
3.2.3 Challenges in micro scale direct methanol fuel cells.....	51
3.2.4 Literature review on structure design of micro-direct methanol fuel cell.....	52
3.2.5 Literature review on PEM integration in micro fuel cell.....	54
3.2.6 Conclusion.....	56
<b>3.3 STATE-OF-THE-ART ON MICROFLUIDIC BIOMOLECULE PRECONCENTRATORS.....</b>	<b>56</b>
3.3.1 Basic operation parameters and principle.....	56
3.3.2 Classification of nanojunction-based preconcentrators.....	57
3.3.3 Literature review on modeling of preconcentrator devices.....	60
3.3.4 Applications of preconcentrator devices.....	62
3.3.5 Conclusion.....	63
<b>3.4 RAPID PROTOTYPING TECHNOLOGIES FOR MICROFLUIDIC DEVICES.....</b>	<b>63</b>
3.4.1 Rapid prototyping of plastics.....	63
3.4.2 Elastomeric material molding.....	65
3.4.3 Rapid microstructuring of glass.....	67
3.4.4 Simplified cutting technology.....	69
3.4.5 Bonding technology.....	71
3.4.6 Conclusion.....	73
<b>REFERENCES.....</b>	<b>74</b>
<b>4 MICROFABRICATION TECHNOLOGIES FOR RAPID PROTOTYPING.....</b>	<b>81</b>
<b>4.1 RAPID PROTOTYPING I: POWDER BLASTING MICRO-EROSION PROCESS.....</b>	<b>82</b>
4.1.1 Experimental setup.....	82
4.1.2 Mechanism of powder blasting.....	83
4.1.3 PMMA microchip fabricated by powder blasting.....	84
4.1.4 Glass microchip fabricated by powder blasting.....	85
<b>4.2 RAPID PROTOTYPING II: PDMS MOLDING TECHNOLOGY.....</b>	<b>89</b>
4.2.1 Molding of the magnetic PDMS membrane for PMMA micropumps.....	89
4.2.2 Molding of the magnetic PDMS sheet for active-valve micropumps.....	90
4.2.3 PDMS microchannels replicated from a SU8 mold.....	92
<b>4.3 RAPID PROTOTYPING III: CUTTING AND INTEGRATION OF THE NAFION STRIP.....</b>	<b>94</b>
4.3.1 Preparing the Nafion strip.....	94
4.3.2 Integration of the Nafion strip.....	95

<b>4.4 CONCLUSION</b> .....	<b>96</b>
<b>REFERENCES</b> .....	<b>96</b>
<b>5 BALL-VALVE MICROPUMPS ACTUATED BY PLANAR ELECTROMAGNETIC ACTUATORS</b> ....	<b>99</b>
<b>5.1 INTRODUCTION</b> .....	<b>100</b>
5.1.1 Advantages of planar compact electromagnets .....	100
5.1.2 Design and working principle .....	100
<b>5.2 ELECTROMAGNETIC ACTUATOR REALIZATION</b> .....	<b>103</b>
5.2.1 Realization of a first type of compact electromagnetic actuator .....	103
5.2.2 Realization of a second type of planar cylindrical electromagnetic actuator .....	109
5.2.3 Comparison with commercial electromagnets .....	112
<b>5.3 MICROPUMPS FABRICATION</b> .....	<b>112</b>
5.3.1 Magnetic membrane fabrication .....	112
5.3.2 Microfluidic layers design and fabrication .....	112
<b>5.4 MICROPUMPS CHARACTERIZATION</b> .....	<b>114</b>
5.4.1 Experimental setup .....	114
5.4.2 Ball-valve design and characterization .....	115
5.4.3 Frequency-dependent flow rate and backpressure for the pumping of water .....	115
<b>5.5 SIMPLIFIED LUMPED CIRCUIT MODEL</b> .....	<b>117</b>
<b>5.6 PERFORMANCE COMPARED WITH OTHER MICROPUMPS</b> .....	<b>118</b>
<b>5.7 CONCLUSION</b> .....	<b>120</b>
<b>REFERENCES</b> .....	<b>121</b>
<b>6 ACTIVE-VALVE MICROPUMP ACTUATED BY A ROTATING MAGNETIC ASSEMBLY</b> .....	<b>125</b>
<b>6.1 INTRODUCTION</b> .....	<b>126</b>
6.1.1 Necessity for low power micropump .....	126
6.1.2 Design and working principle .....	126
<b>6.2 ROTATING MAGNETIC ASSEMBLY AS ACTUATOR</b> .....	<b>128</b>
6.2.1 Actuation sequence analysis .....	128
6.2.2 Magnetic force measurement .....	130
<b>6.3 MICROPUMP FABRICATION</b> .....	<b>130</b>
<b>6.4 MICROPUMP CHARACTERIZATION</b> .....	<b>131</b>
6.4.1 Micropump characterization .....	131
6.4.2 Backflow effect study .....	133
<b>6.5 LUMPED CIRCUIT MODEL</b> .....	<b>134</b>
6.5.1 RLC equivalent circuit .....	134
6.5.2 Comparison with experimental results .....	137
<b>6.6 COMPARISON WITH THE STATE-OF-THE-ART</b> .....	<b>138</b>

<b>6.7 CONCLUSION .....</b>	<b>139</b>
<b>REFERENCES .....</b>	<b>140</b>
<b>7 MONOLITHIC MICRO-DIRECT METHANOL FUEL CELL WITH MICROFLUIDIC CHANNEL-INTEGRATED NAFION STRIP .....</b>	<b>143</b>
<b>7.1 INTRODUCTION.....</b>	<b>144</b>
7.1.1 <i>Advantages of planar microfluidic fuel cells .....</i>	144
7.1.2 <i>Design and working principle .....</i>	144
<b>7.2 EXPERIMENTAL.....</b>	<b>145</b>
7.2.1 <i>Microfabrication process.....</i>	145
7.2.2 <i>Chemicals and reactions.....</i>	146
7.2.3 <i>Backend process and measurement setup .....</i>	147
<b>7.3 MICRO-DMFC CHARACTERIZATION.....</b>	<b>148</b>
7.3.1 <i>Current density dependent cell potential and power density.....</i>	148
7.3.2 <i>Durability study .....</i>	150
7.3.3 <i>The effect of oxidant composition .....</i>	151
7.3.4 <i>Study of external pumping .....</i>	152
7.3.5 <i>Comparison with the state-of-the-art .....</i>	153
<b>7.4 CONCLUSION .....</b>	<b>154</b>
<b>REFERENCES .....</b>	<b>154</b>
<b>8 MICROFLUIDIC PROTEIN PRECONCENTRATORS USING MICROCHANNEL-INTEGRATED NAFION STRIP: EXPERIMENT AND MODELING.....</b>	<b>157</b>
<b>8.1 INTRODUCTION.....</b>	<b>158</b>
8.1.1 <i>Necessity of using preconcentrators for biomolecule analysis .....</i>	158
8.1.2 <i>Design and working principles.....</i>	159
<b>8.2 EXPERIMENTAL.....</b>	<b>160</b>
8.2.1 <i>Materials and chemicals .....</i>	160
8.2.2 <i>Microfluidic device fabrication.....</i>	160
8.2.3 <i>Protocols and measurement setup .....</i>	161
<b>8.3 CHARACTERIZATIONS .....</b>	<b>161</b>
8.3.1 <i>Time dependent preconcentration .....</i>	161
8.3.2 <i>Study the effect of voltage difference across anodic microchannel .....</i>	163
<b>8.4 SIMULATIONS AND DISCUSSIONS .....</b>	<b>164</b>
8.4.1 <i>Model based on coupled equations.....</i>	164
8.4.2 <i>Results and discussions.....</i>	168
<b>8.5 COMPARISON WITH THE STATE-OF-THE-ART.....</b>	<b>170</b>
<b>8.6 CONCLUSION .....</b>	<b>171</b>

<b>REFERENCES</b> .....	<b>172</b>
<b>9 CONCLUSION AND OUTLOOK</b> .....	<b>177</b>
<b>9.1 CONCLUSION</b> .....	<b>177</b>
<b>9.2 OUTLOOK</b> .....	<b>178</b>
<b>ACKNOWLEDGEMENT</b> .....	<b>181</b>
<b>PUBLICATIONS</b> .....	<b>183</b>
<b>CURRICULUM VITAE</b> .....	<b>185</b>

## Contents



# Abbreviations

2D	2-dimensional
3D	3-dimensional
AC	Alternating current
BSA	Bovine serum albumin
CCD	Charge-coupled device
CP	Concentration polarization
DBL	Diffusion boundary layer
DC	Direct current
EDL	Electrical double layer
ELISA	Enzyme-linked immunosorbent assay
EOF	Electro-osmotic flow
FEM	Finite element method
FITC	Fluorescein isothiocyanate
FSI	Fluid-structure interaction
ICEO	Induced-charge electro-osmosis
LOC	Lab-on-a-chip
DMFC	Direct methanol fuel cell
MEA	Membrane electrode assembly
MEMS	Microelectromechanical Systems
$\mu$ TAS	Micro-Total Analysis Systems
OCP	Open circuit potential
PBS	Phosphate buffered saline
PCR	Polymerase chain reaction
PDMS	Polydimethylsiloxane
PEM	Proton exchange membrane
PET	Polyethylene terephthalate
PMMA	Poly(methyl methacrylate)
RLC	Resistance-Inductance-Capacitance
SCR	Space charge region
SEM	Scanning electron microscopy

## Abbreviations

# Chapter 1

## General introduction

### 1.1 Introduction

An important milestone of modern and commercial microtechnology is definitely 1971. This year, the first commercial microprocessor in silicon (Si) was produced by Intel Corporation (*4004 Microprocessor*, Intel Corporation). Inspired by the success in the industry of microelectronics, numerous activities in this field have been focused on silicon integrated circuit manufacturing, leading to the high number of actual available products, like processors, memories, cell phone components and many others. With time, these technologies provided the basis for microscale systems and devices in silicon as well as in other types of materials, like glass, plastics, polymers etc. Since the 1990's, representative mass market Microelectromechanical Systems (MEMS) products have emerged, such as digital optical devices<sup>1</sup> (Fig. 1-1a), physical parameters sensing like acceleration<sup>2</sup> (shown in Fig. 1-1b), pressure sensors, inkjet printer nozzles and microactuators.

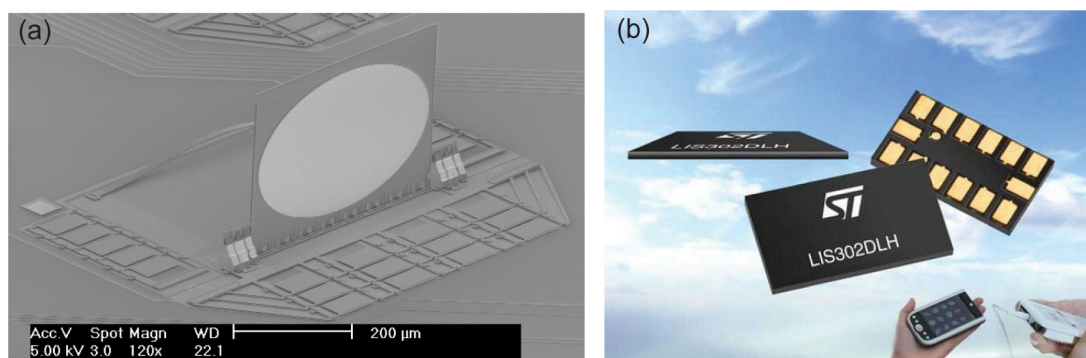


Figure 1-1: (a) Scanning electron microscopy (SEM) image of a free-rotating switch mirror<sup>1</sup> and (b) world's thinnest MEMS accelerometer from STMicroelectronics<sup>2</sup>.

Subsequently, these market breakthroughs have induced the development of chemical, biosensing, diagnosis and biomedical microsystems, resulting in the end fully integrated, automated, miniaturized platforms equipped with user-friendly interface. As these applications always call for small quantities of liquid sample and reagents for analytical detection, microfluidic technology is highly predicted<sup>3</sup>. Nowadays, as microfluidics is becoming much more

widespread, many inter-disciplinary research groups from various domains of science and engineering are working on the implementation of an analytical laboratory in the microfluidic-chip format. As such, this field has made its own mark and is widely known as that of “Lab-on-a-chip (LOC)” or “Micro Total Analysis Systems ( $\mu$ TAS)”.

## 1.2 Microfluidics and Lab-On-a-Chip

Many laboratory techniques in the area of biology and chemistry require fluid handling which involves time-consuming and repetitive manipulation tasks. A LOC is not simply a network of microfluidic channels but it is an integrated microfluidic platform to incorporate different phases of sample preparation, processing, preconcentration, separation and detection. It also includes other functions depending on the application, such as pumps, valves, sensors, electronics, optical modules, miniaturized power sources, etc. Therefore, a LOC can be considered as a complex microsystem with mechanical, electronic, fluid functions, etc. Fig. 1-2a is the block diagram of a series of functions that are to be realized in an integrated microfluidic system for biological analysis. Schematic illustration of an integrated microsystem used for bio-chemical analysis and detection of DNA is shown in Fig. 1-2b<sup>4</sup>.

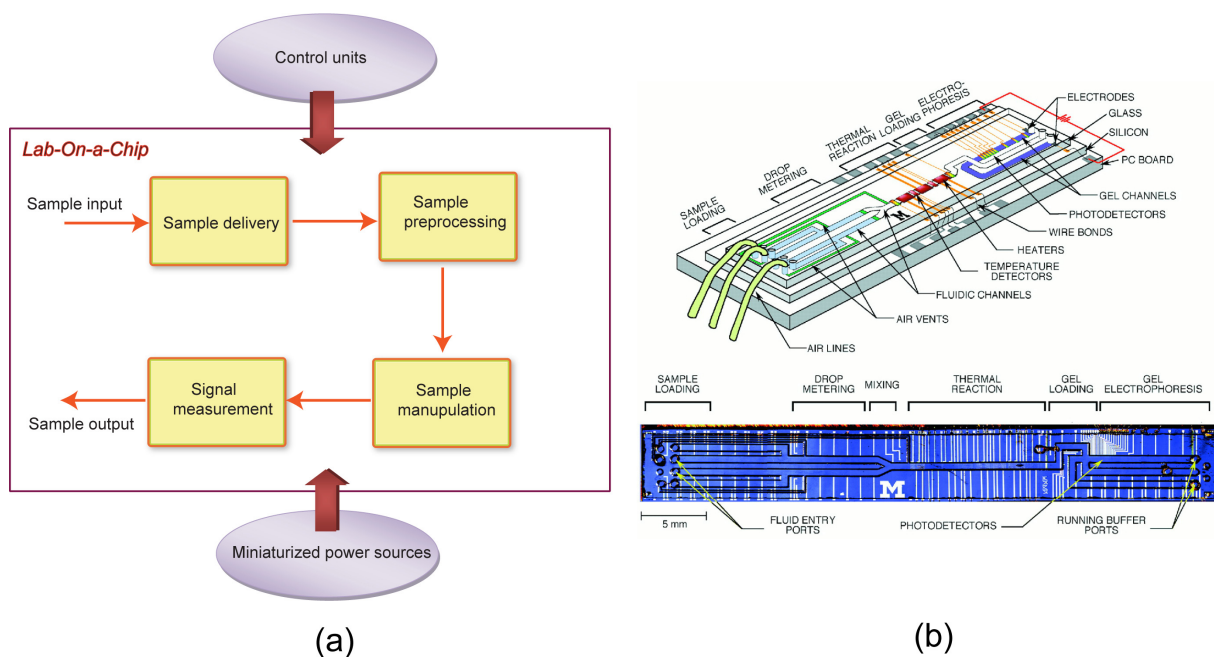


Figure 1-2: Schematic illustration of (a) lab-on-a-chip concept and (b) an integrated system for DNA detection<sup>4</sup>.

Certain types of LOC systems have been commercially realized: for example, on-chip electrophoresis on cell analysis devices. A good example is the Agilent’s 2100 Bioanalyzer together with its cell assays extension (see Fig. 1-3a)<sup>5</sup>. STMicroelectronics (a manufacture

specialized in traditional Si chips for IC) and Mobidiag<sup>®</sup> developed a new LOC application for DNA-based detection of sepsis-causing bacteria (see Fig. 1-3b)<sup>6</sup>. Providing faster and more reliable results than obtainable in conventional laboratory systems, a miniaturized compact analysis enables high-sensitivity disease detection, resulting in potentially lower overall costs of the healthcare system.

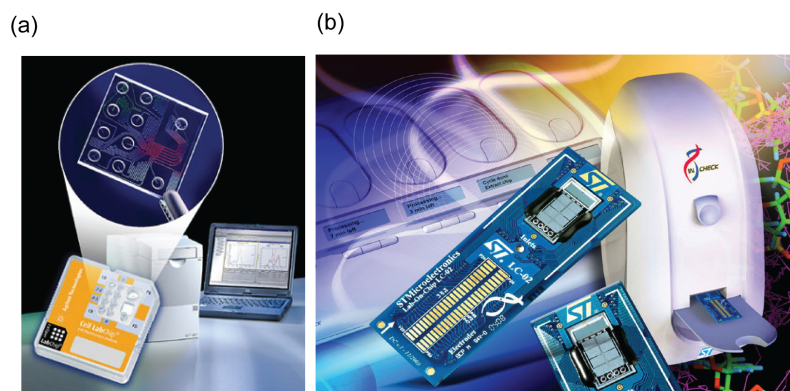


Figure 1-3: (a) Agilent's lab-on-a-chip for cell analysis<sup>5</sup>. (b) STMicroelectronics and Mobidiag Unveil Lab-on-a-chip for Rapid Bacterial Diagnosis<sup>6</sup>.

LOCs provide advantages that can considerably vary depending on their applications. Typical advantages are:

- Low fluid volumes consumption
- Higher analysis and control speed of the chip and better efficiency
- Massive parallelization due to compactness, allowing high-throughput analysis
- Cost-effective disposable chips, fabricated in mass production
- Safer platform for chemical, radioactive or biological studies
- Portable and low operation power

The recent developments in  $\mu$ TAS domain have been summarized in a series of review articles by A. Manz *et al.*<sup>7-9</sup>.

### 1.3 Thesis scope and outline

Due to the significance of fluid transport in integrated microfluidic devices, pumping concepts and components are widely studied, always aiming compact volume implantation, low power consumption, precise dispensing, as well as high efficiency. Thus, integration of efficient micropumps is extremely crucial for further developments in the  $\mu$ TAS field<sup>9,10</sup>. However, since power consumption and operation voltage have always been issues, extensive attention should be focused on the power systems. Miniaturized fuel cells for portable electronic equipment are

considered rather close-to-market for a number of reasons: they can be realized in a small format, and microstructured fuel cells enable higher overall energy density than batteries. Small fuel cells with fluid delivery and removal, reaction sites and electrode structures all confined to microfluidic format appears to be easily integratable into a  $\mu$ TAS<sup>11</sup>. In the field of protein analysis, improvement in speed of analysis, and reduction in sample loss, can be achieved when many sample preparation steps can be integrated with the analysis at the chip level<sup>12</sup>. Preconcentration before analysis is a crucial step in the development of multifunctional integrated microfluidic devices, for the forthcoming reasons: first, detection of trace or lowabundance species is enabled; second, because the micrometer dimensions of the fluidic channels lead to less sensitive optical detection than that obtainable in microscopic scale fluidic devices, preconcentration not only improves detection sensitivity but also enhances the signal-to-noise ratio. With the growing demand for  $\mu$ TAS, the use of rapid prototyping microfabrication technologies and the selection of affordable materials (plastics, polymers etc.) are the key factors for definition of LOC products<sup>13</sup>.

Briefly, the objectives of this thesis are two-fold: first, the development of high-efficiency  $\mu$ TAS components, like magnetic micropumps, microfluidic fuel cells and membrane-based protein preconcentrators which are important devices for the reasons described above; second, the promotion of rapid prototyping technologies in  $\mu$ TAS, having in mind that low-cost and disposable devices are the trend of the LOC market.

In [Chapter 2](#), the theoretical background of microfluidics, magnetism as well as ion transport in microscale devices, on which the thesis is based, are presented. Following, in [Chapter 3](#), the state-of-the-art in the area of magnetic micropumps, microfluidic fuel cells, membrane-based protein preconcentrators and techniques of rapid prototyping are reviewed. Rapid prototyping technologies used in this thesis work are explained in detail in [Chapter 4](#), in which, powder blasting, polymer molding and assembly technology will be discussed. In [Chapter 5](#), plastic ball-valve micropumps with two differently shaped magnetic actuators are described, while another type of magnetic micropump with active valves actuated by a rotating magnetic assembly is presented in [Chapter 6](#). Next, as a miniaturized power source, a microfluidic direct methanol fuel cell with embedded Nafion strip is studied in [Chapter 7](#). In [Chapter 8](#), based on the same ion-selective Nafion material and integration method, a protein preconcentrator with efficient performance is demonstrated; also, in this chapter, a complex numerical model is proposed to study the physics of preconcentration. I conclude the thesis with an outlook on the future developments of my current work and show its potential for further microfluidic device integration ([Chapter 9](#)).

## References

1. Lin, L. Y.; Goldstein, E. L. In Micro-electro-mechanical systems (MEMS) for WDM optical-crossconnect

- networks, *Military Communications Conference Proceedings* 1999, 2, pp 954-957
2. <http://www.st.com/stonline/stappl/cms/press/news/year2009/p2388.htm>
  3. Abgrall, P.; Gué, A.-M., Lab-on-chip technologies: making a microfluidic network and coupling it into a complete microsystem- a review. *Journal of Micromechanics and Microengineering* 2007, 17, R15-R49.
  4. Burns, M. A.; Johnson, B. N.; Brahmasandra, S. N.; Handique, K.; Webster, J. R.; Krishnan, M.; Sammarco, T. S.; Man, P. M.; Jones, D.; Heldsinger, D.; Mastrangelo, C. H.; Burke, D. T., An Integrated Nanoliter DNA Analysis Device. *Science* 1998, 282, 484-487.
  5. <http://www.chem.agilent.com/en-US/Products/Instruments/lab-on-a-chip/2100bioanalyzer/cellsolutions/Pages/default.aspx>
  6. <http://www.st.com/stonline/press/news/year2005/t1695f.htm>
  7. Vilkner, T.; Janasek, D.; Manz, A., Micro Total Analysis Systems. Recent Developments. *Analytical Chemistry* 2004, 76, 3373-3386.
  8. Dittrich, P. S.; Tachikawa, K.; Manz, A., Micro Total Analysis Systems. Latest Advancements and Trends. *Analytical Chemistry* 2006, 78, 3887-3908.
  9. West, J.; Becker, M.; Tombrink, S.; Manz, A., Micro Total Analysis Systems: Latest Achievements. *Analytical Chemistry* 2008, 80, 4403-4419.
  10. Laser, D. J.; Santiago, J. G., A review of micropumps. *Journal of Micromechanics and Microengineering* 2004, 14, R35-R64.
  11. Kjeang, E.; Djilali, N.; Sinton, D., Microfluidic fuel cells: A review. *Journal of Power Sources* 2009, 186, 353-369.
  12. Song, S.; Singh, A., On-chip sample preconcentration for integrated microfluidic analysis. *Analytical and Bioanalytical Chemistry* 2006, 384, 41-43.
  13. Qin, D.; Xia, Y.; Rogers, J.; Jackman, R.; Zhao, X.-M.; Whitesides, G., Microfabrication, Microstructures and Microsystems. In *Microsystem Technology in Chemistry and Life Science, Topics in Current Chemistry*, 1998, 194, pp 1-20.





# *Chapter 2*

## **Background and Theoretical Aspects**

**Abstract:** In this chapter, we provide the theoretical background for our work on magnetic micropumps, direct methanol fuel cells in the microfluidic format and protein preconcentrators. First, a number of concepts that are of reference for our microfluidic devices are introduced. Second, electrostatics in microfluidic phenomena including electroosmosis and electrophoresis, which are involved in our preconcentration chip, are presented. Third, the aspects of magnetism as well as the design criteria of magnetic actuation are described, forming the basis for the compact and miniaturized magnetic actuators of our magnetic micropumps. Finally, we present the theoretical background related to the nanoporous membrane, which is behaving as ion conductor for protons in our fuel cell application and as ion-permselective medium for electrolyte ions in our protein preconcentration application, respectively. The latter is very important for the concentration polarization effect during protein preconcentration process.

## 2.1 Theoretical microfluidics

Theoretical microfluidics deals with the flow of fluids and of suspensions in submillimeter-sized systems mediated by external forces. Though hydrodynamics is an old discipline that has been well studied, microfluidic technology benefits from a better theoretical insight of the fluidic phenomena occurring in LOC systems. Physics of microfluidics is quite complex, involving elements of classical physics and chemistry, fluid mechanics, electrostatics, thermodynamics, statistical mechanics, elasticity, polymer physics, etc.<sup>1,2</sup>. Notably, the microscale dimensions induce different and intriguing physical phenomena, which are prominent on the macroscale. This section is mainly based on and adapted from the references<sup>1-4</sup>.

### 2.1.1 Fluid parameters and definitions

#### Scaling law

When analyzing the physical properties of microsystems, it is instructive to introduce the concept of *scaling law* at the first beginning. A scaling law expresses the variation of physical quantities with the size  $l$  of the given system, while keeping other parameters such as time, pressure, temperature, *etc.* as constant. For instance, considering volume forces, such as gravity and inertia, and surface forces, such as surface tension and viscosity, the basic scaling law for the ratio of these two classes of forces can generally be written as:

$$\frac{\text{Surface force}}{\text{Volume force}} \propto \frac{l^2}{l^3} = l^{-1} \xrightarrow{l \rightarrow 0} \infty \quad (2-1)$$

This scaling law implies that when scaling down the microsystem's dimension to the microscale in LOC systems, the volume forces become less dominant than the surface forces.

#### Steady flow

*Steady flow* refers to the condition where the fluid properties at a point in the system do not change over time. Otherwise, flow is called unsteady. It indicates that there is no time dependent parameter in steady flow equations ( $\partial/\partial t = 0$ ).

#### Reynolds number

The *Reynolds number* is a dimensionless parameter obtained from dimensional analysis and it interprets the ratio of inertial force to viscous force, expressed as:

$$R_e = \frac{\text{inertial force}}{\text{viscous force}} = \frac{\rho U D}{\mu} \quad (2-2)$$

with  $U$  the mean velocity of the fluid (m/s),  $\rho$  the density of fluid (kg/m<sup>3</sup>),  $D$  the characteristic

channel dimension (for example, the hydraulic diameter of a pipe) and  $\mu$  the dynamic viscosity ( $\text{N}\cdot\text{s}/\text{m}^2$ ) of the fluid. Estimating the Reynolds number provides us with information on the flow type, either turbulent or laminar, which can simplify the resolution of the microfluidic governing equations. Due to the small dimensions of microchannels,  $Re$  is usually much less than 100, often smaller than 1.0. In this Reynolds number regime, flow is completely laminar and no turbulence occurs. Typically, the transition from laminar flow to turbulence generally occurs in the range of Reynolds numbers of 2000.

### Hydraulic diameter

The *hydraulic diameter*, which is a commonly used term when handling flow in noncircular tubes and channels, is defined as follows:

$$D_H = 4 \cdot \frac{\text{cross sectional area}}{\text{wetted perimeter}} = 4 \cdot \frac{A}{P} \quad (2-3)$$

For a rectangular duct (used in the following *RLC* model for micropump, see [Chapter 5](#) and [Chapter 6](#)), which is fully filled with fluid, the hydraulic diameter is equal to  $D_H = 2 \cdot \frac{w \cdot h}{w + h}$ , where  $w$  and  $h$  the width and height of the rectangle, respectively.

### Incompressible flow

An *incompressible flow* is a fluid flow, in which the divergence of velocity is zero  $\nabla \cdot \mathbf{u} = 0$ . A common criterion to distinguish whether a fluid is incompressible or not is to calculate the Mach number  $M$ , which is the ratio of the flow velocity to the speed of sound:

$$M = \frac{u}{c} = \frac{\text{flow velocity}}{\text{sound speed}} \quad (2-4)$$

The upper value  $M < 0.3$  is often used as the limit of validity of the incompressible fluid assumption in microfluidic devices.

### Hydrostatic pressure

The *hydrostatic pressure* of water ( $\text{H}_2\text{O}$ ) refers to the pressure exerted at the base of a column of water at ambient pressure and at room temperature. For a given column height  $H$ , the hydrostatic pressure  $\Delta p$  is written as follows:

$$\Delta p = \rho_{\text{H}_2\text{O}} \cdot g \cdot H \quad (2-5)$$

with  $\rho_{\text{H}_2\text{O}} \approx 10^3 \text{ kg}/\text{m}^3$  the density of water and  $g$  the earth gravitational acceleration ( $\text{m}/\text{s}^2$ ).

For instance, a 1 meter water column generates the hydrostatic pressure of 100 mbar or 10 kPa, a unit commonly used for pump's backpressure evaluation.

### *Electrical double layer*

The aqueous solutions are conductive due to the ubiquitous presence of dissolved ions (e.g., from dissolved salts, ionic groups on surfaces, or dissociated water molecules), thus the solid-liquid interfaces tend to develop surface charge, and the latter attracts oppositely charged counterions in the liquid but repels co-ions which are similarly charged. The resulting ionic *electrical double layer* (EDL) screens the surface charge over a characteristic *Debye length*  $\lambda_D$ . With the exception of these charged double layers, the fluid keeps a neutral state.

### *Vortex*

A *vortex* (*plural*: vortices) shows a spinning or even turbulent pattern of the fluid flow. The types of vortex are often limited to free (irrotational) vortices and forced (rotational) vortices as distinction. For instance, considering a free vortex, the fluid near the center of the vortex circulates faster than the fluid far from the center. At the same time, the inner streamlines have a shorter distance to travel to complete a ring. The tangential velocity is expressed as follows:

$$v_\theta = \frac{\Gamma}{2\pi r} \quad (2-6)$$

where  $\Gamma$  ( $\text{m}^2/\text{s}$ ) is the circulation (defined as line integral around a closed curve of the fluid velocity) and  $r$  is the radial distance from the center of the vortex.

## 2.1.2 Fluid laws

### *Conservation laws*

#### ➤ Conservation of mass

The conservation of mass in a fluid flow indicates that the mass in a closed system will be kept as constant. In other words, the incoming mass equals the outgoing mass. The equation can be described in terms of the fluid velocity  $\mathbf{u}$  in vector format:

$$\frac{\partial \rho}{\partial t} + \nabla \cdot (\rho \mathbf{u}) = 0 \quad (2-7)$$

If the fluid density  $\rho$  is constant, the equation will be rewritten as:

$$\nabla \cdot \mathbf{u} = 0 \quad (2-8)$$

This is also called the continuity equation for incompressible fluids, because in many cases, especially in microfluidics, the flow velocity is much smaller than the speed of sound.

#### ➤ Conservation of momentum

The total momentum of the fluid within a fixed volume  $V$  will increase because of a net influx of momentum across the bounding surface  $S$  by bulk flow and because of the external forces acting on the fluid. For the incompressible fluid, the equation can be written as:

$$\rho \left[ \frac{\partial \mathbf{u}}{\partial t} + (\mathbf{u} \cdot \nabla) \mathbf{u} \right] = -\nabla p + \nabla \cdot \vec{\tau} + \vec{f} \quad (2-9)$$

where  $p$  the pressure exerting on the volume,  $\vec{\tau}$  the viscous stress tensor, and  $\vec{f}$  the external body force on the volume.

➤ Conservation of energy

The third governing equation to be established is the heat-transfer equation of the fluid relating the rate of change of the energy density to the energy density flux. The equation is expressed as:

$$Q - W = \Delta E \quad (2-10)$$

where  $Q$  the heat added to the fluidic system,  $W$  the work done by the system and  $\Delta E$  the energy change. Distinction should be applied on the parameter  $E$ , which, for example, can be written as:

$$E = U + E_k + E_p + E_{ext} \quad (2-11)$$

with  $U$  the internal energy,  $E_k$  the kinetic energy,  $E_p$  the energy due to the potential of the system and  $E_{ext}$  the energy from the external field, like an applied electrical field or magnetic field from an external electromagnet.

### Hagen-Poiseuille law

*Hagen-Poiseuille* equation is a law that gives the pressure drop over a fluid column flowing through a long cylindrical pipe. This also describes the friction losses in the pipe. The assumptions of the equation are that the flow is constantly viscous, incompressible and through a pipe with hydraulic diameter  $D_H$  which is significantly smaller than its length. The volumetric flow rate through a pipe or duct of length  $\Delta x$  is expressed as follows:

$$Q = \frac{dVolume}{dt} = \frac{\pi D_H^4 (-\Delta p)}{128 \mu \Delta x} \quad (2-12)$$

Thus, the variation of pressure through the pipe is written as:

$$\Delta p = - \frac{128 \mu \Delta x Q}{\pi D_H^4} \quad (2-13)$$

In the following [Section 2.1.5](#), the fluidic resistance will be derived from this formula.

**Navier-Stokes equation**

The *Navier-Stokes (N-S) equation* is derived from the conservation equations for a fluid and it can evidently be used when describing the incompressible fluid flow ( $\nabla \cdot \mathbf{u} = 0$ ) through an arbitrary control volume. The vector form of the equation is written as follows:

$$\rho \left[ \frac{\partial \mathbf{u}}{\partial t} + (\mathbf{u} \cdot \nabla) \mathbf{u} \right] = -\nabla p + \mu \nabla^2 \mathbf{u} + \vec{f}$$

↓  
Unsteady  
acceleration

↓  
Convective  
acceleration

↓  
Pressure  
gradient

↓  
Viscous  
force

↓  
Other  
external forces

(2-14)

The physical meanings are indicated just below the equation.

**Flow in porous media**

The Navier-Stokes equation is restricted to describing the flow in a free medium and not applicable to a porous system, like a nanoporous ion-selective membrane. Here, in order to explore the fluid behavior in the membrane of both fuel cells ([Chapter 7](#)) and preconcentrators ([Chapter 8](#)), we introduce the Navier-Stokes-Brinkman system interrelating the velocity  $\mathbf{u}$ , pressure gradient  $\nabla p$ , external body force  $f$ , as well as parameters involved in the porous medium. The Brinkman equation is written as <sup>5, 6</sup>:

$$\frac{\rho}{\varepsilon_p} \frac{\partial \mathbf{u}}{\partial t} + \frac{\mu}{\kappa} \mathbf{u} = -\nabla p + \frac{\mu}{\varepsilon_p} \nabla^2 \mathbf{u} + \vec{f}$$

$$\nabla \cdot \mathbf{u} = 0$$
(2-15)

with  $\kappa$  the permeability ( $\text{m}^2$ ) of porous media and  $\varepsilon_p$  the porosity. When  $\varepsilon_p = 1$  and  $\kappa \rightarrow \infty$ , the equation will be back to Navier-Stokes equation.

**2.1.3 Pressure driven flow**

Pressure-driven flow is widely used for transport of liquids or reactants inside microfluidic channels or chambers<sup>7</sup>. It can be either realized by utilizing laboratory pumps or external driving forces. Here, we assume a steady, non-slip flow confined between fixed parallel plates in absence of the external forces (see [Fig. 2-1](#)).

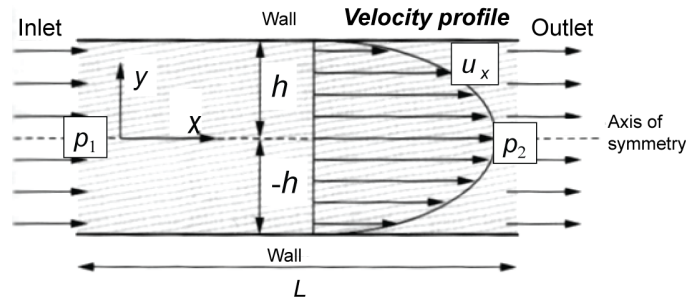


Figure 2-1: Velocity profile of a flow restricted between parallel plates when driven by a pressure difference  $p_1-p_2$ <sup>7</sup>.

Therefore, the Navier-Stokes equation (Eq. 2-14) is rewritten as:

$$0 = -\frac{\partial p}{\partial x} + \mu \frac{\partial^2 u}{\partial y^2} \quad (2-16)$$

Suppose the pressure gradient for flow driving is constant  $k$ , thus,  $p = p_0 - kx$ . Then, the equation will be simplified as follows:

$$\mu \frac{\partial^2 u}{\partial y^2} = -k \rightarrow u = -\frac{ky^2}{2\mu} + Cy + D \quad (2-17)$$

By applying the boundary condition ( $u=0$  at  $y=h, -h$ ), the unknown factor of  $C, D$  becomes 0 and  $\frac{kh^2}{2\mu}$ , respectively. Hence the velocity profile can be expressed as:

$$u = \frac{k(h^2 - y^2)}{2\mu} \quad (2-18)$$

The velocity profile of such fully developed pressure-driven flow is parabolic, as indicated in Fig. 2-1.

#### 2.1.4 Fluid-structure interaction (FSI)

The type of the driven flow discussed in this section is induced by physical force from mechanically deformed walls made of soft materials. This strategy is really practical when the walls of microfluidic channels or chambers are sufficiently compliant, so that significant deformation can be achieved with moderate force. Since soft polymeric materials having an elastic modulus several orders less than traditional hard materials like silicon or glass, they are widely used for applications like pumping, valving, etc.

The governing principle of such fluid-structure interaction comprises the following elements: driving actuation, deformable membrane and the coupling hydrodynamics<sup>8</sup>.

For an incompressible fluid, the Navier-Stokes equation is utilized here to describe the fluid

motion under a certain external pressure originating from a deformable membrane<sup>9, 10</sup>:

$$\rho \left[ \frac{\partial \mathbf{u}}{\partial t} + (\mathbf{u} \cdot \nabla) \mathbf{u} \right] = -\nabla p + \mu \nabla^2 \mathbf{u} + \rho \mathbf{g} \quad (2-19)$$

Under the action of excitation pressure  $p_e$  (in this thesis, it is the magnetic force acting on a membrane-embedded magnet), the vertical displacement of the membrane  $w_m$  obeys the normal strain-stress equation:

$$D_m \nabla^4 w_m + \rho_m h \frac{\partial^2 w_m}{\partial t^2} = p_e - p \quad (2-20)$$

where  $D_m$  the rigidity of the membrane,  $\rho_m$  the membrane mass density,  $h$  the thickness of membrane and  $p$  the pressure due to the fluid. A point worth noting here is that the pressure used here denotes the actual absolute pressure minus the environmental pressure (see the schematics in Fig. 2-2a).

By solving the set of equations (Eqs. 2-19 and 2-20), the membrane displacement and fluid velocity or flow rate can be obtained. For membrane displacement, as revealed in Fig. 2-2b, the comparison between the states with and without taking into account the influence of the fluid emphasizes the importance of considering FSI in microfluidic devices<sup>10</sup>.

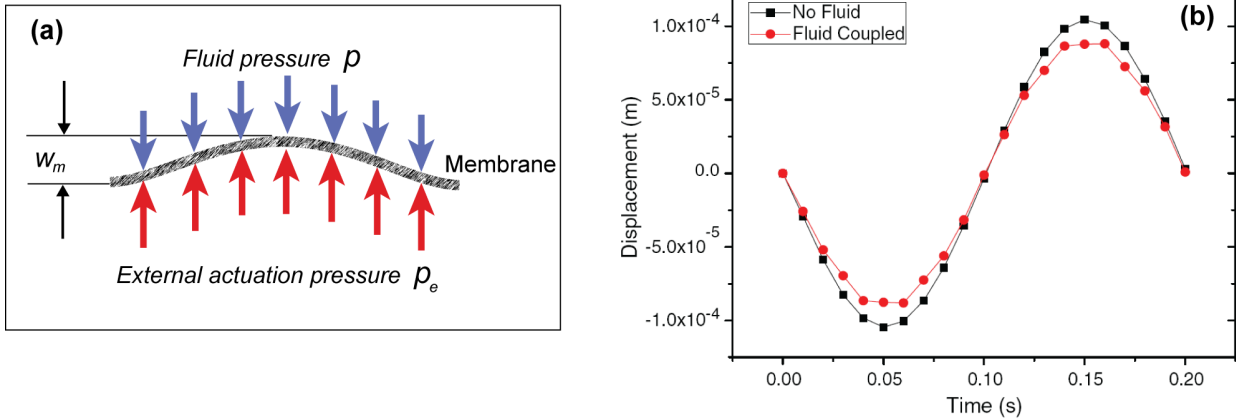


Figure 2-2: (a) The schematic of membrane deflection when subjected to the exerted pressures. (b) Membrane displacement versus time with or without fluid damping effect<sup>10</sup>.

Compliance causes soft membranes or walls to deform and store extra fluid under influence of pressure. Therefore, it is reasonable to make an analogy of this effect with the behavior of capacitors in electronic circuits. These systems intrinsically demonstrate the characteristics of capacitance ( $C$ ) and resistance ( $R$ ), a resulting  $RC$  time and low-pass filter properties. This method opens intriguing possibilities to eliminate cumbersome steps in analytical equations or numerical simulations. The details will be introduced in the Section 2.1.5, where ball-valve micropumps and



active-valve micropumps are analyzed by analogous electronic circuits.

### 2.1.5 RLC equivalent model

#### *Definitions of RLC hydraulic elements*

A viscous fluid passing through a channel gives rise to a pressure drop at certain channel. By assuming that all the fluid in the channel is incompressible and newtonian, the Hagen-Poiseuille law (Eq. 2-13) will govern the relation between the pressure drop and fluid flow. Thus, a fluidic resistance for a channel (length  $l$ , hydraulic diameter  $D_H$ ) is defined as:

$$R = \frac{128\mu l}{\pi D_H^4} \quad (2-21)$$

The fluid inertial effect can be modeled simply by fluidic inductance, by taking into account the acceleration of the fluid in a channel or a pipe. An inductance has the following relationship between the pressure drop  $p(t)$  (voltage) and flow acceleration  $\dot{Q}(t)$  (current):

$$L = \frac{p(t)}{\dot{Q}(t)} \quad (2-22)$$

Using Newton's second law, the force  $F$  exerted on a fluid mass  $m$  (density  $\rho$ ) confined in a duct with cross-section  $S$  and length  $l$ , will generate an acceleration  $\frac{du}{dt}$ , thus, the relation obeys:

$$p(t) = \frac{F}{S} = \rho l \frac{du}{dt} \quad (2-23)$$

Combining Eq. 2-22 and Eq. 2-23, the fluidic inductance is written as:

$$L = \frac{\rho l}{S} \quad (2-24)$$

Generally, the pipe or a channel can be modeled as the combination of fluidic resistance and inductance. The fluidic capacitance is defined by estimating the variation of volume  $\Delta V$  when applying a pressure difference  $\Delta p$ :

$$C = \frac{\Delta V}{\Delta p} \quad (2-25)$$

Table 2-1 summarizes the equivalent hydraulic elements with their corresponding electrical analogues. It forms the basis of our following lumped circuit model for the micropumps.

Table 2-1: Equivalent between hydraulic and electrical models.

Fluidic element	Electrical equivalence
Pressure $p$	Voltage $U$
Flow rate $Q$	Current $I$
Fluidic resistance (friction losses) $R = \frac{128 \mu l}{\pi D_H^4}$	Resistance $R$
Fluidic inductance (inertia) $L = \frac{\rho l}{S}$	Inductance $L$
Fluidic capacitance (energy store) $C = \frac{\Delta V}{\Delta p}$	Capacitance $C$
Valve	Diode $D$

**RLC equivalent model of reciprocating pump with ideal valves**

The hydraulic system of a reciprocating pump with ideal valves (see the schematic in Fig. 5-1 in Chapter 5) can be modeled as a RLC equivalent circuit (see Fig. 2-3)<sup>11, 12</sup>. The current  $I$  and voltage  $U$  represent the flow rate  $Q$  and backpressure  $P$ , respectively. The liquid in the channel induces both a resistive ( $R$ ) and an inertial ( $L$ ) effect. The membrane plays the role of a capacitance ( $C$ ), and its inertial effect can be neglected in comparison with the fluid inertia. For simplification of the model, we are assuming that the valves are ideal diodes. Using the defined equivalent elements, we are able to construct the corresponding electrical circuit which can be either solved analytically or simulated in the software.

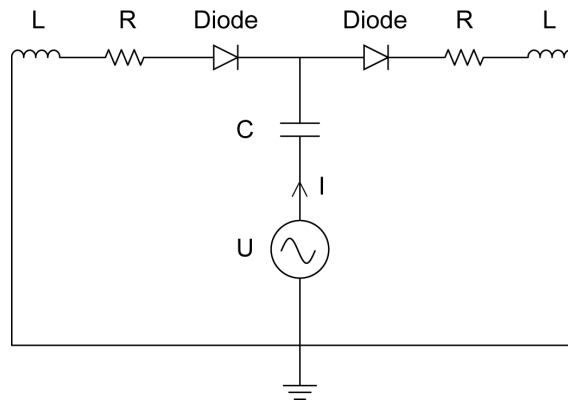


Figure 2-3: RLC equivalent model of a reciprocating pump having two ideal valves<sup>2, 11, 12</sup>.

When disregarding the mass of the flexible membrane, the deflection of membrane can be described with spring theory and its relation with the external pressure is written as follows:

$$F = \Delta p A_m = \frac{\Delta V}{C} A_m = \frac{A_m x}{C} A_m = Kx \tag{2-26}$$

Thus, the capacitance is deduced as  $C = \frac{A_m^2}{K}$ , where  $A_m$  the area of membrane/chamber interface, and  $K$  the membrane stiffness.

Though we did not consider the losses due to the membrane deflection, this simple model is already good enough to predict the pump performance. When operating in pumping mode ( $U > 0$ ), there is only a flow in the right part of the circuit. Thus, the impedance of the circuit is:

$$Z = R + j(L\omega - \frac{1}{C\omega}) \quad (2-27)$$

and the corresponding resonance frequency is:

$$f_{o,th} = \frac{1}{2\pi} \sqrt{\frac{1}{LC}} \quad (2-28)$$

In this thesis, a sinusoidal wave ( $\omega = 2\pi f$ )  $P(t) = P_s \sin \omega t$  is always used as actuation signal. For simplicity, we used the flow rate  $Q_0$  at the resonant frequency obtained from experimental results, and we can deduce the average frequency-dependent flow rate:

$$Q(t) = Q_0 \sqrt{\frac{\omega^2}{\omega^2 + \left(\frac{L}{R}\omega^2 - \frac{1}{RC}\right)^2}} \quad (2-29)$$

This equation will be applied for modeling the ball-valve micropump in [Chapter 5](#).

It is obvious that utilizing an equivalent electrical circuit model considerably reduces the complexity; nevertheless, if the converted circuit become more complex (for example, the valve is no longer ideal), electrical circuit designing tools like MATLAB® Simulink are required to build and solve the modeled circuits. In [Chapter 6](#), based on this method, the active-valve micropump is very well analyzed.

### 2.1.6 Electrodynamics in microfluidic systems

In electrokinetic platforms, microfluidic unit operations are controlled by electrical fields acting on electric charges, or electrical field gradients acting on electrical dipoles. Depending on buffers and/or sample, several electrokinetic effects such as electroosmosis, electrophoresis and polarization superimpose on each other<sup>3</sup>.

One obvious way to couple electromagnetism to hydrodynamics is incorporating the electrical body force  $\rho_{el}\mathbf{E}$  in the Navier–Stokes equation, with  $\rho_{el}$  the charge density (C/m<sup>3</sup>):

$$\rho \left[ \frac{\partial \mathbf{u}}{\partial t} + (\mathbf{u} \cdot \nabla) \mathbf{u} \right] = -\nabla p + \mu \nabla^2 \mathbf{u} + \rho_{el} \mathbf{E} \quad (2-30)$$

The fundamental set of equations for describing the electrical field  $\mathbf{E}$  as function of charge

density in the system is:

$$\begin{aligned} \mathbf{E} &= -\nabla\phi \\ \nabla^2\phi &= -\frac{\rho_{el}}{\varepsilon_0\varepsilon_r} \end{aligned} \quad (2-31)$$

with  $\phi$  the electrical potential,  $\varepsilon_0$  vacuum permittivity,  $\varepsilon_r$  the relative dielectric constant.

### **Electrophoresis**

The movement of a charged object (of say dissolved or suspended material) relative to a stationary liquid is induced by an applied electrical field  $\mathbf{E}$  (see Fig. 2-4).

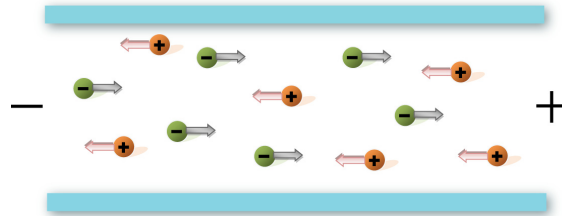


Figure 2-4: Migration of ions in electrophoresis.

The velocity of the ions  $v_{ei}$  depends on the strength of the electrical field and the mobilities of the ions, which can be obtained by assuming the electrophoretic force be balanced by frictional drag force. If the molecule structure is treated as a simple sphere with radius  $r$  and charge  $Q$  immersed in electrolyte having viscosity  $\mu$ , the mobility is:

$$\mu_{ei} = \frac{v_{ei}}{|E|} = \frac{Q}{6\pi\mu r} \quad (2-32)$$

For example,  $\text{Na}^+$  has the electrophoretic mobility of  $5 \times 10^{-8} \text{ m}^2 / (\text{Vs})$  and in an electrical field of  $1600 \text{ V/m}$ , the electrophoretic velocity equals to  $0.08 \text{ mm/s}$ .

### **Electroosmosis**

Electro-osmosis flow (EOF) is a non-equilibrium effect<sup>3</sup>, where a liquid is brought to move relative to a charged surface by an applied external potential gradient  $\nabla\phi$ . Generally speaking, electroosmosis phenomena are divided into two categories: (i) the traditional one with fixed charge density along the fluidic channel walls (see Fig. 2-5); (ii) induced-charge electroosmosis (ICEO), in which fluid flow is driven by electrical field acting on space charges induced near a polarized surface.

First, the Debye length  $\lambda_D$  is expressed as<sup>3</sup>:

$$\lambda_D \equiv \kappa^{-1} = \left( \frac{\varepsilon_0 \varepsilon_r RT}{\sum_i z_i^2 F^2 c_i} \right)^{1/2} \quad (2-33)$$

where  $F$  Faraday constant,  $R$  gas constant,  $T$  the temperature,  $z_i$  the valance of the  $i^{\text{th}}$  ion,  $c_i$  the electrolyte molar concentration of the  $i^{\text{th}}$  ion. The zeta potential  $\zeta$  caused by the charged Debye layer is written as:

$$\zeta \equiv \frac{q}{\varepsilon_0 \varepsilon_r \kappa} \quad (2-34)$$

where  $q$  is the surface charge density.

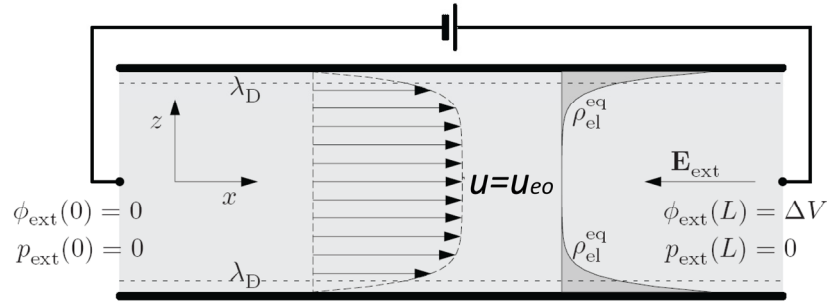


Figure 2-5: The velocity profile  $\mathbf{u}$  and the negative Debye-layer charge density profile in an ideal EOF inside a cylindrical channel with positively charged walls<sup>3</sup>.

The external electrical field is applied in the negative  $x$  direction:  $E = -\mathbf{E}e_x$ . In absence of an external pressure difference and gravity, one can rewrite the Eq. 2-30 and Eq. 2-31 into the following form, by assuming the steady-state condition:

$$0 = \mu \partial_z^2 u_{eo_x}(z) + [\varepsilon_0 \varepsilon_r \partial_z^2 \phi_{eq}(z)] E \quad (2-35)$$

where  $\phi_{eq}$  the electrical potential due to the Debye layer charged density  $\rho_{el}^{eq}$ .

Employing the boundary condition  $v_x(\pm \frac{h}{2}) = 0$ , one can easily obtain a fluid velocity:

$$u_{eo_x}(z) = \frac{\varepsilon_0 \varepsilon_r}{\mu} [\zeta - \phi_{eq}(z)] E \quad (2-36)$$

It represents a velocity that exponentially approaches Smoluchowski's constant slip,

$$u_{eo} = \frac{\varepsilon_0 \varepsilon_r \zeta}{\mu} E \quad (2-37)$$

This ideal EOF is valid in the limit of  $\lambda_D \ll a$ . When the Debye length  $\lambda_D$  is comparable with the scale length  $a$ , it will overlap inside of the channel which are of nanoscale size. With current nanotechnology, it is possible to make such nanochannels and materials with nanopores intentionally. As a result, the EOF will be dramatically suppressed as  $\lambda_D$  is increased beyond the value of  $a$  and the profile will be changed into the parabolic shape. Detailed explanations are given in the book by H. Bruus<sup>3</sup>.

In the final part of this section, we would like to discuss the inhomogeneous charges occurring due to the charged liquid, which are induced around conducting or polarized surfaces<sup>1,13</sup>. These give rise to the nonlinear phenomena in recent studies. Here we illustrate perhaps the simplest example of induced-charge electroosmosis, as proposed by T.M. Squires *et al*<sup>13</sup> (see Fig. 2-6). In steady state, the induced zeta potential  $\zeta$  equals to  $ER$ , where  $E$  the electrical field and  $R$  the radius of sphere. Thus, an induced-charge electroosmotic slip velocity is established as function of external electrical field:

$$u_{eo} \approx \frac{\epsilon_0 \epsilon_r R}{\mu} E^2 \quad (2-38)$$

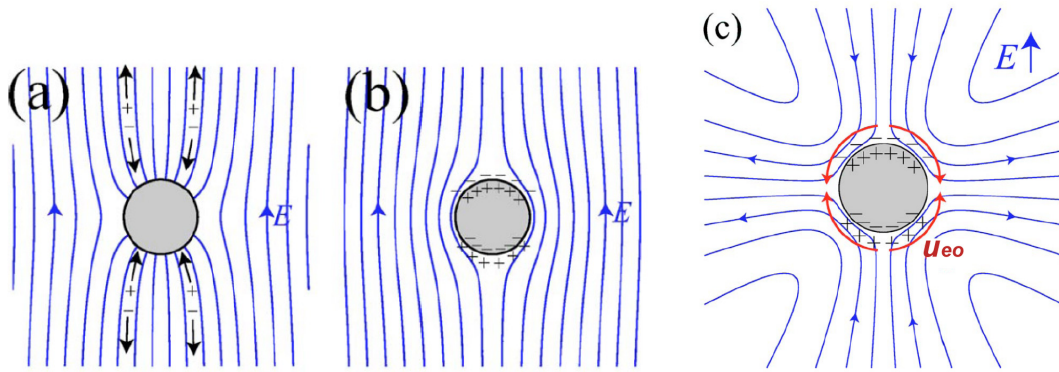


Figure 2-6: (a) A suddenly applied electrical field intersects a conducting cylinder. The mobile ions accumulate in an induced charge double layer adjacent to the conducting surface. (b) Steady state is achieved when the induced double layer has developed sufficiently that no field lines penetrate the double layer. (c) The steady-state ICEO flow established around a conducting cylinder<sup>13</sup>.

Finally, by comparing and deriving these two types of EOF analytically, it is clear that the induced-charge electroosmosis, which is proportional to the square of the applied electrical field, will definitely enhance the electrokinetic effects in microfluidics. It has been proven by our modeling for the protein preconcentration device (Chapter 8), where the two types of EOF are taken into account.

## 2.2 Basics of magnetic actuation

We provide both magnetic concepts and the theoretical basis (as adapted mainly from the reference<sup>2</sup>) for the realization of electromagnetic actuators and a rotating magnetic assembly which are used for our ball-valve micropump and active-valve micropump, respectively.

### 2.2.1 Basic concepts of magnetism

#### *Origin of magnetism*

Magnetic properties are resulting from the arrangement of local magnetic moments. At the atomic level, the magnetic moments originate from either the orbital motion of the electrons around the nucleus or the spin moment of the electron around its own axis. Various sorts of magnetism originate from different spin arrangement in which the lowest magnetic energy that is reached, as shown in Fig. 2-7.

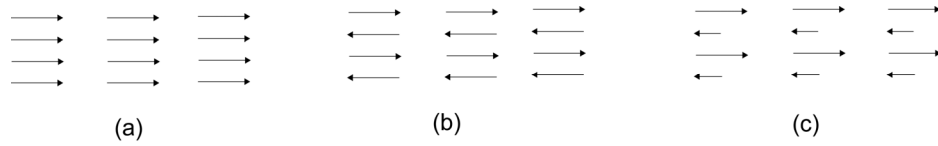


Figure 2-7: Spin arrangement of a (a) ferromagnetic, (b) antiferromagnetic and (c) ferrimagnetic material.

In a ferromagnetic material (Fig. 2-7a), the spins are aligned not only parallel but also in the identical direction. The orientations of the spins in Fig. 2-7b are opposite, though they are parallel aligned, and this results in the antiferromagnetic properties of the material. In Fig. 2-7c, the spins are parallel aligned, with opposite orientations, but the intensities of the two are different, corresponding to the a ferrimagnetic material.

#### *Magnetic quantities*

The magnetic field  $\vec{H}$ , magnetic induction  $\vec{B}$  and magnetization  $\vec{M}$  are related by:

$$\vec{B} = \mu_0(\vec{H} + \vec{M}) \quad (2-39)$$

where  $\mu_0$  is the permeability of vacuum.  $\vec{M}$  is expressed in terms of the density of net magnetic dipole moments  $\vec{m}$  in the material. A relation between  $\vec{M}$  and  $\vec{H}$  is:

$$\vec{M} = \chi\vec{H} \quad (2-40)$$

Therefore, we can rewrite Eq. 2-39 into the following:

$$\vec{B} = \mu_0(1 + \chi)\vec{H} = \mu_0\mu_r\vec{H} \quad (2-41)$$

the dimensionless parameters  $\chi$  and  $\mu_r$  are the magnetic susceptibility and relative permeability, respectively.

### 2.2.2 Magnetic materials

#### Classification of ferromagnetic materials

Ferromagnetic materials may be classified according to their basic magnetic properties: remanence ( $B_r$ ), coercive field ( $H_c$ ) and Curie temperature ( $T_c$ ). Based on these features, these materials can be divided into soft or hard magnetic materials (see Fig. 2-8a)<sup>14</sup>. The comparison of the magnetic properties of most commonly used magnetic materials is given in Fig. 2-8b<sup>2</sup>.

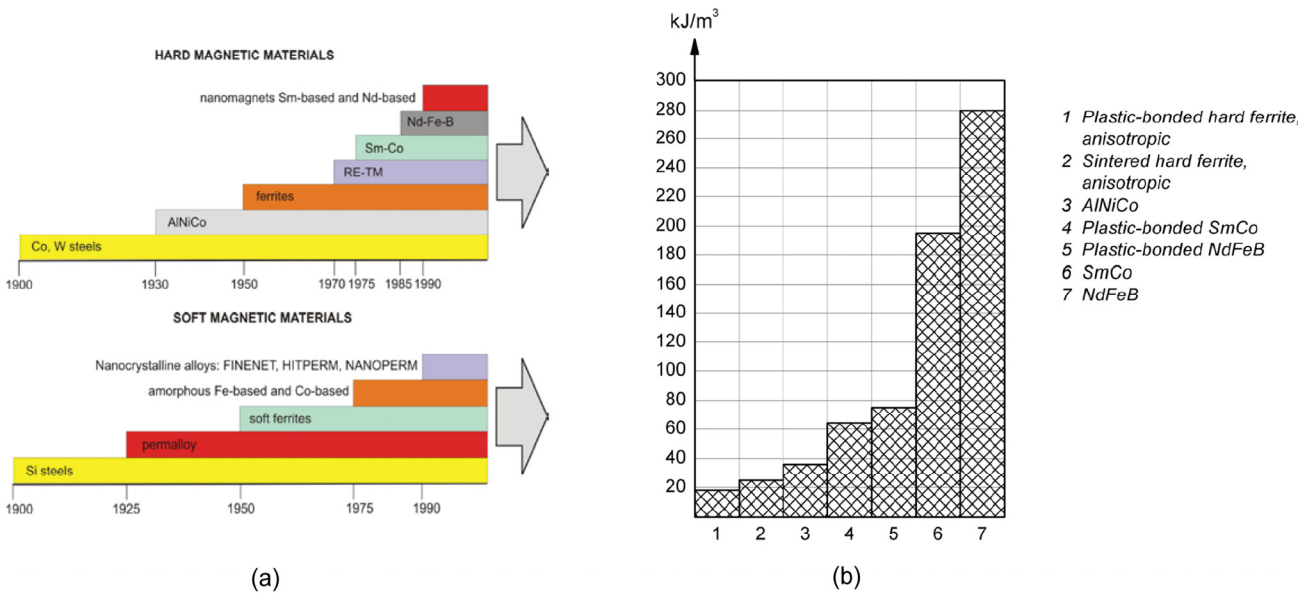


Figure 2-8: (a) Classification and development of ferromagnetic materials<sup>14</sup>. (b) Comparison of maximum energy ( $B \cdot H$  maximum value) of some magnetic materials (typical values)<sup>2</sup>.

For soft magnetic materials, the value of coercive force is very low (for an ideal material, the coercive field is equal zero), which means that the material, when previously strongly magnetized by an external magnetic field undergoes complete demagnetization when the magnetic field is removed. On the other hand, in hard magnetic materials, after removal of magnetic field, they stay strongly magnetized and are in fact permanent magnets. The typical response of a soft magnetic material in a magnetic field is shown in Fig. 2-9a. The hard magnetic material that exhibits the magnetization curve of the type is depicted in Fig. 2-9b.



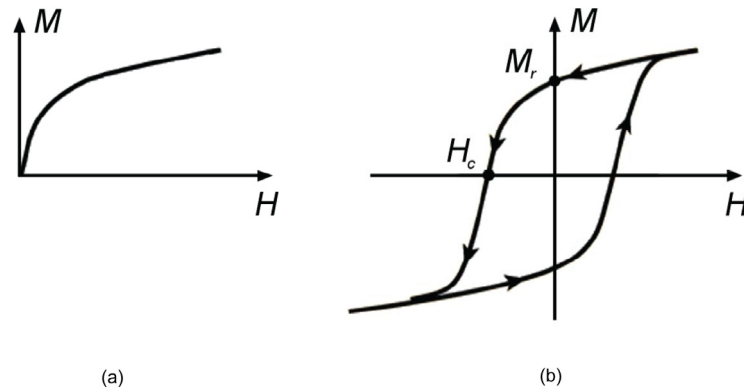


Figure 2-9: Typical magnetization curves for (a) soft and (b) hard magnetic materials<sup>2</sup>.

### Permanent magnets

Generally, permanent magnets should typically produce a high magnetic field, having low physical mass and be resistant to external demagnetization effects.

As illustrated in Fig. 2-8b, Neodymium-Iron-Boron (NdFeB) is a composite material with high energy density ( $\vec{B} \cdot \vec{H}$ ). Utilizing such magnets, we can achieve high-performance electromagnetic actuators and magnetic motors. However, despite their excellent magnetic properties, NdFeB magnets are unstable at moderate to high temperatures and are highly susceptible to corrosion in environments of high humidity. Protection to chemical corrosion can be achieved by using these NdFeB magnets in a plastic-bonded form, however, NdFeB magnets in this form exhibit weaker magnetism than their sintered counterparts. In our work, NdFeB magnets embedded in a polymer thin membrane offer a good trade-off solution.

Evaluating the magnetic properties of permanent magnets enables understanding the technological basis for designing the electromagnetic actuation. For example, the magnetization  $M$  (in the  $z$  direction, perpendicular to magnet's flat surface) for a cylindrical magnet (length  $L$ , radius  $a$ ) can be obtained by measuring the magnetic flux density at the height  $z$  above the central point of magnet surface. The expression we used is<sup>15</sup>:

$$\vec{B}_z = \frac{\mu_0 M}{2} \left[ \frac{z+L}{\sqrt{(z+L)^2 + a^2}} - \frac{z}{\sqrt{z^2 + a^2}} \right] \quad (2-42)$$

Generally, the ratio between  $\mu_0 M$  and  $B_{z,0}$  (the magnetic flux density at the flat surface) for the cylindrical magnet (length/diameter  $\approx 1$ ) is an approximated value of 0.5<sup>16</sup>. In our electromagnetic actuation design, the magnetization value of a permanent magnet used in the a finite element method (FEM) simulation is calculated in this way from the measurement of  $B_{z,0}$  (see Chapter 5).

### Soft iron

Soft iron, due to its high magnetic permeability among the soft magnetic materials, has been widely used for magnetic field amplification and flux confinement in plenty of applications like electromagnets, motors, transformers and inductors. In this thesis, soft iron, as a magnetic core, plays a significant role in concentrating the magnetic field generated by coil.

The permeability  $\mu(H)$  of soft iron is not a constant when subjected to different external magnetic fields. The flux density increases in proportion to the field strength until it reaches its limit and cannot increase any more, becoming almost constant as the field strength continues to increase. This is because there is a limit to the amount of flux density that can be generated by the core. As reported from literature, it saturated at the magnetic flux density of 2.2 T<sup>17</sup>.

### 2.2.3 Principle of electromagnetic actuation

Electromagnetic actuation is based on the force created between an electrical coil and a magnet (see Fig. 2-10)<sup>18</sup>. Considering its application in a micropump system, the electromagnetic actuator should provide the oscillating force on a membrane-embedded magnet which gives rise to the periodical volume change of the pump.

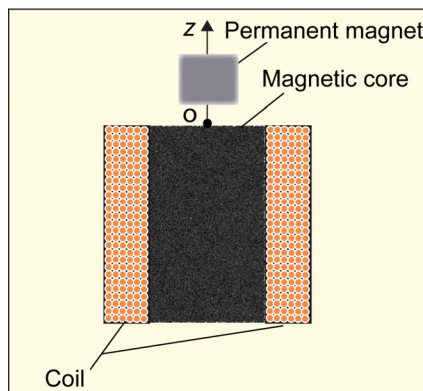


Figure 2-10: Schematic cross-section of a simple electromagnetic actuator (not scaled).

There are certain design criteria that should be addressed:

- *Coil*: high filling factor, planar design for MEMS requirement
- *Magnetic core*: soft magnetic material with high permeability for focusing the magnetic flux
- *Permanent magnet*: high density magnetization  $M$
- *Heating*: as low as possible
- *Structure design*: prevent leakage of the magnetic flux produced by the coil

The most popular and simplest way to predict the electromagnetic actuator's performance is using the following equation, by assuming a permanent magnet (magnetization  $M_z$  and volume  $V$ )

that is subjected to an external magnetic field<sup>2</sup>:

$$F_z = M_z \int_V \frac{d}{dz} B_z dV \quad (2-43)$$

If one knows the gradient of the magnetic flux density  $\frac{dB_z}{dz}$  at a specific distance, one can roughly estimate the force  $F_z$  to optimize the design of the actuator. For example, as reported from our paper, for an air gap of 1.5 mm,  $\frac{dB_z}{dz}$  is around 40 T/m (results can be either obtained from FEM simulation or from the analytical method). Thus, the force on the permanent magnet (diameter 3 mm, height 3 mm, magnetization 506 kA/m) is about 400 mN, which is in excellent agreement with our measured force<sup>11</sup>.

However, this equation fails to distinguish the unsymmetrical repulsive and attractive forces in our electromagnetic actuation system, because it is a non-trivial task to incorporate a soft iron structure into Eq. 2-43. Therefore, precise measurements of magnetic forces are required and details on this can be found in Chapter 5. Apart from the rough estimation based on the equation above, there are some other methods that can accelerate the design and optimization: (1) equivalent magnetic circuit<sup>19</sup>, (2) FEM simulation<sup>11, 12, 20</sup>. The latter will be demonstrated in Chapter 5.

#### 2.2.4 Principle of rotating magnetic actuation

A rotating magnetic field is a magnetic field which changes direction at (ideally) a constant angular rate. A coil with alternating current, as a component normally integrated in an electromagnetic actuator, can impose a rotating-like magnetic field on the permanent magnet. But it is also pretty interesting to exploit novel ways to generate the rotating magnetic field to actuate the magnet. As inspired by some commercial synchronous motors in the market, utilizing rotating arc-shaped permanent magnets could be an effective strategy to substantially reduce the power consumption and avoid the heating problems.

Let us first consider a pair of parallel magnetized arc magnets, which can be self-assembled (angle:  $0^\circ < \theta < 360^\circ$ , in Fig. 2-11), and the magnetization normal to the surface is expressed as<sup>21</sup>:

$$M_{normal} = \frac{B_r \cdot \sin \theta}{\mu_0} \quad (2-44)$$

with  $B_r$  the remanence.

When the assembly rotates, a magnetic field with sine wave character is therefore produced, and is proportional to  $\sin \omega t$  ( $\omega$  is the angular speed for rotation). The application of this type of actuation will be demonstrated in our active-valve micropump system<sup>22</sup>(Chapter 6).

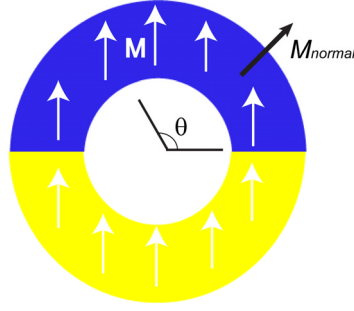


Figure 2-11: Schematic of a pair of parallel magnetized arc magnets in self-assembly mode.

## 2.3 Ion conductance in microfluidic systems

In this section, we illustrate the origin and dependence on various system parameters of the ionic conductance within a microfluidic fuel cell<sup>23</sup> as well as in nanoporous preconcentration<sup>24</sup>. The origin of ion-permselectivity of a nanoporous membrane is analyzed, and, furthermore, we examine the role of ion conductance in a microfluidic fuel cell. A particularly complex concentration polarization develops in a preconcentration unit, as external electrical fields are superimposed on internal chemical and electrical potential gradients.

### 2.3.1 General equations for ionic liquid solutions

When ions are in solution, there are three mechanisms for ionic motion: Brownian motion (thermal), ordered drift due to a potential (voltage) field, and diffusion, ordered drift down a concentration gradient. The flux of ions in the fluid is described using Nernst-Planck equation for different dissolved ionic species, which describes their combined motion by migration, diffusion and convection<sup>3</sup>:

$$\frac{\partial c_i(t)}{\partial t} = -\nabla \cdot \mathbf{N}_i = \nabla(D_i \nabla c_i(t) + z_i c_i(t) D_i \frac{F}{RT} \nabla \phi(t)) - (\nabla c_i(t) \cdot \mathbf{u}(t) + c_i(t) \nabla \cdot \mathbf{u}(t)) \quad (2-45)$$

where  $\phi$  the local electrical potential,  $\mathbf{N}$  the ion flux.  $c_i$ ,  $D_i$  and  $z_i$  the molar concentration of ionic species  $i$ , diffusion coefficient of ionic species  $i$  and its corresponding valence, respectively.  $\mathbf{u}$  is the fluid velocity. The local electrical potential  $\phi$  within the liquid arises from the distribution of ions in microfluidic system and is described as:

$$\nabla^2 \phi = -\frac{F \sum_i z_i c_i}{\epsilon_0 \epsilon_r} \quad (2-46)$$

The Navier-stokes equation for a fluid including the electrical body force that can migrate the ions in the solution is written as:

$$\rho \left[ \frac{\partial \mathbf{u}}{\partial t} + (\mathbf{u} \cdot \nabla) \mathbf{u} \right] = -\nabla p + \mu \nabla^2 \mathbf{u} + F \sum_i z_i c_i \mathbf{E} \quad (2-47)$$

The set of equations (Eqs. 2-45, 2-46 and 2-47) is able to model a microfluidic system containing ions.

### 2.3.2 Ion-permselective medium

An ion-permselective medium is a nanoporous membrane or a series of nanochannels, which may be used to separate ions by allowing the preferential transport of either cations (in the case of a cation-exchange membrane) or anions (in the case of an anion exchange membrane). The ion selectivity is attributed to the surface charge existing on the nanopores or the nanochannels, which induce an exclusion-enrichment effect; i.e., co-ions of the surface charges are excluded, while counterions are enriched.

In this thesis, only cation-selective membranes are discussed. To achieve high-efficiency of ion permselectivity, the membrane must possess the following desirable properties: 1. high cation conductivity; 2. adequate mechanical strength and stability; 3. stable chemical and electrochemical properties under operating conditions; 4. very low leakage between two electrolytes on both sides of the membrane; 5. low costs.

The permselective membrane used currently in portable fuel cell and biomolecule preconcentration applications have perfluorinated groups with attached sulfonic acid which bear high surface charge density. Nafion, a perfluorinated polymer produced by DuPont, is extensively used, since it has high cation conductivity, good chemical stability and mechanical strength. Its structure is shown in Fig. 2-12.

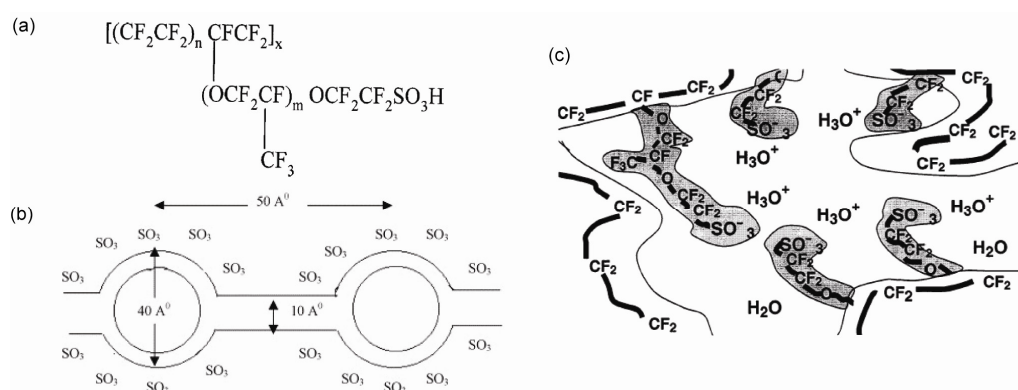


Figure 2-12: (a) General chemical formula of Nafion 117 from Dupont<sup>25</sup>. (b) The Phenomenological sketch of the nano structure in Nafion solid polymer electrolytes<sup>23</sup>. (c) Transport phenomena of species in Nafion membranes<sup>26</sup>.

The mechanical strength of Nafion membranes arises from the interaction of the perfluorinated backbone chains. For its use as a positive ion conductor, the porous membrane

contains about 20 wt% water forming hydration shells around the fixed covalently bonded anionic sulfonic acid groups. For proton transport, as seen from Fig. 2-12c, the conductivity is assigned to hydrated protons ( $\text{H}_3\text{O}^+$ ) as positive charge carriers. For the charge passage through the membrane, a percolated sponge-like microstructure supplies the transport channels<sup>26</sup>.

In moderate ionic strength buffer (<10 mM), since the pore size of Nafion membrane is only several nanometers, the electrical double layer, as calculated from Eq. 2-33, which is of the same order as pore size, can overlap.

### 2.3.3 Transport in ion-permselective membrane

#### *Electrostatic potential*

The surface potential  $\phi$  along a charged pore (length  $l$ , radius  $r_0$ ) of the membrane is an important quantity to describe the ionic transport behavior, and can be written as<sup>27</sup>:

$$\phi = -\frac{RT}{F} \ln \left[ 16 \frac{B}{(1-B)^2} \left( \frac{L_D}{r_0} \right)^2 \right] \quad (2-48)$$

where  $B = 1 - \frac{4\varepsilon_0\varepsilon_r RT}{r_0 F \sigma_{eff}}$  and  $L_D = \sqrt{\frac{4\varepsilon_0\varepsilon_r RT}{2F^2 c_b}}$ ,  $\sigma_{eff}$  the effective surface charge density,  $c_b$  the background proton concentration in the case of fuel cell.

#### *Hydrodynamics*

By assuming the gravity, convective and inertial effects are neglected for the electrolytic solution in the membrane, the Brinkman equation, Eq. 2-15 describing the flow in porous media can be extended to Schlögl's equation<sup>27, 28</sup>:

$$\mathbf{u}(t) = -\frac{\kappa_\phi}{\mu} \sum_i z_i c_i F \nabla \phi - \frac{\kappa}{\mu} \nabla p \quad (2-49)$$

The electroneutrality expression is:

$$z_f c_f + \sum_i z_i c_i = 0 \quad (2-50)$$

where  $\phi$  the external electrical potential,  $\kappa_\phi$  the electrokinetic permeability ( $\text{m}^2$ ),  $\kappa$  the hydraulic permeability of the membrane ( $\text{m}^2$ ),  $c_f$  the concentration of fixed charge (with valance  $z_f$ ) at membrane.  $z_i$  and  $c_i$  are the valance of the one type of ion in the liquid and it's corresponding ionic concentration, respectively. For a membrane used in a fuel cell, the only mobile ions in the pore fluid are  $\text{H}^+$ , thus, Eq. 2-50 can be written as  $z_f c_f = c_{\text{H}^+}$ .

**Current density**

Combining Eq. 2-45 and the current density expression  $\tilde{i} = F \sum_i z_i \mathbf{N}_i$ , and meanwhile, assuming the continuity for an incompressible flow, we can obtain the relation between current density  $\tilde{i}$  and electrical potential  $\phi$  over the membrane <sup>28</sup>:

$$\nabla \phi = \frac{-\tilde{i}}{K} - \frac{F}{K} \sum_i z_i D_i \nabla c_i + \frac{F}{K} \sum_i z_i c_i \mathbf{u}(t) \quad (2-51)$$

where  $K = (F^2/RT) \sum_i z_i^2 D_i c_i$ .

Therefore, these equations (Eqs. 2-48, 2-49, 2-50, 2-51) provide consistent description of transport in ion-permselective membrane.

**2.3.4 Concentration polarization near a membrane mediated by electrical field**

The mechanism for biomolecule preconcentrators in Chapter 8 is ion concentration polarization (CP). It is one of the fundamental electrochemical transport phenomena that have been observed at nanoporous membranes when exposed to an external electrical field <sup>29,30</sup>. The following subsections are based and adapted from the references<sup>29,30</sup>.

**Concentration polarization**

When an external electrical field is applied through a nanochannel/nanoporous membrane, electrokinetic transport is superimposed on the diffusion<sup>29</sup>. This ionic current transport can induce considerable forces on electrolytes in the nanometer-sized apertures, as a result of which convection has to be considered. CP, a complex set of effects related to the formation of ionic concentration gradients in the electrolyte solution adjacent to an ion-selective interface, does occur under these conditions (as seen from Fig. 2-13).

At the anodic side of a cation-selective nanochannel/nanoporous membrane, the anions move away and cannot be compensated by the few anions that remain in the nanochannel/nanopores. Due to the electroneutrality, cations and anions are reduced by the same amount in front of the nanochannel/nanopores on the anodic side. As a consequence, a concentration gradient is established. Meanwhile, at the cathodic side, an accumulation of cations occurs, because the number of cations transferred through the nanochannel is more than that can be carried away by the electrical current. The transferred number of anions in the nanochannel is almost zero and therefore they get accumulated at the cathodic side of the nano-sized structure. Electroneutrality also has to be fulfilled in this ionic enrichment zone.

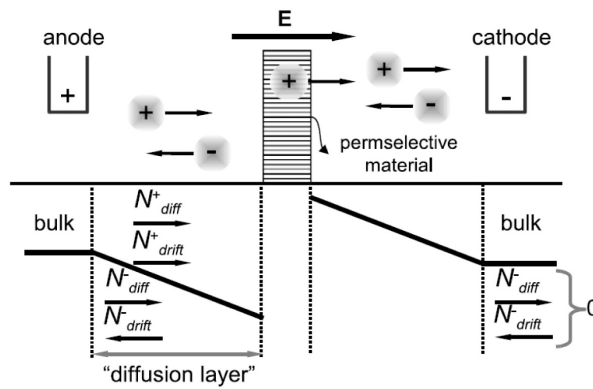


Figure 2-13: Schematic diagram of the ion concentration distribution near of a cation-permselective material<sup>29</sup>.

**Concentration polarization in a strong electrical field**

With increasing electrical field strength the concentration of ions in the depleted zone is dramatically decreased towards zero and diffusion transport through the diffusion boundary layer (DBL) is limited. Upon further increase of the applied potential, the intensive induced space charge develops. This phenomena is represented in the form of three layers (see Fig. 2-14)<sup>30</sup>.

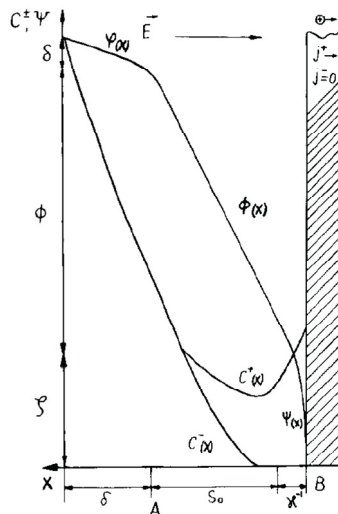


Figure 2-14: Schematic representation of the distributions of co-ions  $C^-(x)$ , counter-ions  $C^+(x)$  and electric potential  $\psi$  in the concentration polarization zone (A).  $\bar{E}$  is the external electrical field,  $j^+$  is the counterion flow inside the membrane (B), the co-ion flows inside the membrane is zero.  $\delta$ ,  $S_0$  and  $\kappa^{-1}$  are the thicknesses of the approximately electroneutral diffusion layer, the bulk charge layer and the diffuse part of the double layer, respectively;  $\varphi$ ,  $\Phi$  and  $\zeta$  are the electrical potential in the diffusion layer, in the bulk charge layer and in the diffuse layer, respectively<sup>30</sup>.

Nearest to the surface there is the diffuse part of the EDL  $\kappa^{-1}$ , although its structure deviates



somewhat from that of the equilibrium due to the influence of the passing electrical current. Near the external boundary of the concentration polarization zone, a diffusion layer  $\delta$  exists in which the electrolyte concentration decreases with decreasing distance from the surface, but keeps the electroneutrality. A structure-induced space charge appears between the diffuse part of the double layer and the diffusion layer. This induced space charge layer  $S_0$  grows with increasing current density and can substantially exceed the diffusion layer thickness.

Induced space charge appears at that membrane side where counterions enter it from the bulk electrolyte, while the co-ions move in the opposite direction. This causes co-ion depletion at this side of the membrane. In turn, it leads to a diffusion flow from the electrolyte to the membrane surface. Since there is no co-ion flow inside the membrane, this implies that in every point of the diffuse and diffusion layer electromigration and diffusion of co-ions are exactly balanced, as described below:

$$-D^- \frac{\partial C^-}{\partial x} + D^- C^- \frac{e}{kT} \frac{\partial \psi}{\partial x} = 0 \quad (2-52)$$

Integrating the equation above, one can obtain a Boltzmann-like distribution for the co-ions  $C^-$ :

$$C^-(x) = C_0 \exp\left[\frac{e(\psi(x) - \psi(x^*))}{kT}\right] \quad (2-53)$$

where  $D^-$  is diffusion coefficient of the co-ion,  $e$  the elementary charge,  $T$  the temperature,  $k$  Boltzmann's constant,  $C_0$  the bulk concentration of co-ions (molecules per volume),  $\psi$  the electrical potential, and  $x$  the distance from the membrane surface,  $x^*$  the outer boundary of the concentration polarization zone, i.e.,  $C^-(x^*) = C_0$ .

Under the influence of the increasing applied electrical field, the reduction of the co-ion concentration results in a concomitant decrease of the counterion concentration. However, it is not necessary to assume that this decrease is an exact replica of the co-ion concentration reduction at every position. If one compares [Eq. 2-52](#), the corresponding equation for counterion ( $C^+$ ) is expressed as:

$$-D^+ \frac{\partial C^+}{\partial x} - D^+ C^+ \frac{e}{kT} \frac{\partial \psi}{\partial x} = j^+ \quad (2-54)$$

After integrating this equation, it becomes:

$$C^+(x) = C_0 \exp\left[-\frac{e\psi(x)}{kT}\right] - e^{-\frac{e\psi(x)}{kT}} j^+ \int_0^x e^{\frac{e\psi(x)}{kT}} dx \quad (2-55)$$

It is concluded that a bulk charge is generated, the density of which is given by:

$$\rho(x) = e[C^+ - C^-] \quad (2-56)$$

**Electro-osmotic slip of the second kind**

If an external electrical field near the cation-permselective membrane has not only the normal component  $E_n$  but also a tangential component  $E_t$ , the normal component of the electrical field  $E_n$  generates the induced space charge, while the tangential component leads to a driving force  $dF_t$  for each volume element  $dV$ <sup>30</sup>:

$$dF_t = \rho(x)E_t(x)dV \quad (2-57)$$

The liquid containing the induced space charge will be moved along the cation-permselective membrane surface by such force. It is quite obvious that the appearance of liquid slip of this kind is identical to that for electroosmotic slip. Thus, this nonlinear phenomenon is named as electroosmotic slip of the second kind or induced-charge electroosmosis, as schematically described in Fig. 2-15.

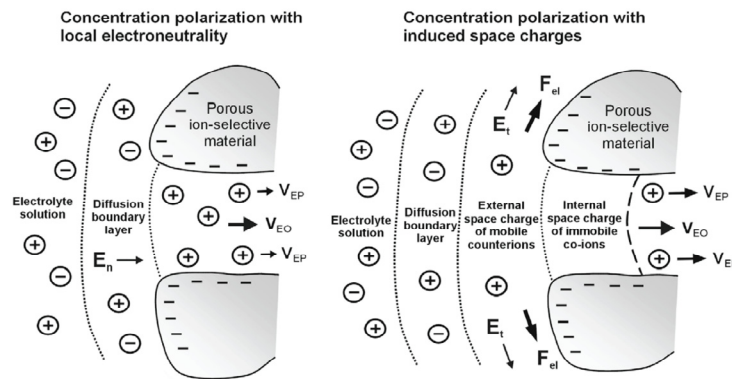


Figure 2-15: Different stages of CP induced by the normal component of the applied field ( $E_n$ ).  $F_{el}$  denotes body force interaction between the SCR (fluid-side space charge region of the secondary EDL) and the tangential component of the applied field ( $E_t$ ), leading to electroosmosis of the second kind outside the ion-permselective domain<sup>31</sup>.

**2.4 Conclusion**

In this chapter, we have systematically introduced some related theoretical aspects that provide the basic knowledge for the microfluidic devices in the thesis. First, we have introduced basic concepts occurring in microfluidic devices in general by emphasizing their particular physics properties on microscale. Microfluidic phenomena mediated by an external electrical field include electroosmosis and electrophoresis. Subsequently, following the basics of magnetism, we have summarized the design criteria of electromagnetic actuation, providing some theoretical basis for compact and miniaturized electromagnetic/magnetic actuation for our micropumps. Finally, we have described the theory of nanoporous membranes in microfluidic systems: first, it can be used

to describe ion transport for proton in fuel cell application; second, it allows describing the behavior of an ion-permselective medium for electrolyte ions under an external electrical field, which is at the basis of the concentration polarization effect in a protein preconcentrator.

## References

1. Squires, T. M.; Quake, S. R., Microfluidics: Fluid physics at the nanoliter scale. *Reviews of Modern Physics* 2005, 77, 977-1026.
2. Yamahata, C., Magnetically actuated micropump, *PhD Thesis, Ecole Polytechnique Fédérale de Lausanne*. 2005.
3. Bruus, H., *Theoretical microfluidics*. Oxford Univ. Press: Oxford, 2008.
4. Gravesen, P.; Branebjerg, J.; Jensen, O., Microfluidics-a review. *Journal of Micromechanics and Microengineering* 1993, 3, 168-182.
5. Laptev, V. Numerical solution of coupled flow in plain and porous media. *PhD thesis, Universit sbibliothek*, 2003.
6. Hill, A.; Carr, M., Nonlinear stability of the one-domain approach to modelling convection in superposed fluid and porous layers. *Proceedings of the Royal Society A: Mathematical, Physical and Engineering Science* 466, 2695-2705.
7. [http://www.chemeng.queensu.ca/courses/CHEE223/lectures/documents/Ch15\\_differential\\_momentum\\_balance.ppt](http://www.chemeng.queensu.ca/courses/CHEE223/lectures/documents/Ch15_differential_momentum_balance.ppt)
8. Heil, M., An efficient solver for the fully coupled solution of large-displacement fluid-structure interaction problems. *Computer Methods in Applied Mechanics and Engineering* 2004, 193, 1-23.
9. Pan, L. S.; Ng, T. Y.; Wu, X. H.; Lee, H. P., Analysis of valveless micropumps with inertial effects. *Journal of Micromechanics and Microengineering* 2003, 13, 390-399.
10. Zhou, Y.; Amirouche, F., Study of fluid damping effects on resonant frequency of an electromagnetically actuated valveless micropump. *The International Journal of Advanced Manufacturing Technology* 2009, 45, 1187-1196.
11. Shen, M.; Yamahata, C.; Gijs, M., A high-performance compact electromagnetic actuator for a PMMA ball-valve micropump. *Journal of Micromechanics and Microengineering* 2008, 18, 025031 (9pp).
12. Shen, M.; Yamahata, C.; Gijs, M., Miniaturized PMMA ball-valve micropump with cylindrical electromagnetic actuator. *Microelectronic Engineering* 2008, 85, 1104-1107.
13. Squires, T. M.; Bazant, M. Z., Induced-charge electro-osmosis. *Journal of Fluid Mechanics* 2004, 509, 217-252.
14. Dobrzański, L. A.; Drak, M.; Ziębowicz, B., Materials with specific magnetic properties. *Journal of Achievements in Materials and Manufacturing Engineering* 2006, 17, 37-40.
15. Lee, J. K., Measurement of magnetic fields in axial field motors. *Magnetics, IEEE Transactions on* 1992, 28, 3021-3023.
16. [www.femm.info/Archives/misc/BarMagnet.pdf](http://www.femm.info/Archives/misc/BarMagnet.pdf)
17. Iwashita, Y.; Kumada, M., Permanent Magnet Quadrupole Lens with Variable Strength. in *ICFA Nanobeam*

2002Workshop, CERN-Proceedings-2003-001, IPHE Document 2003-007, AB Division, pp. 153–155..

18. Klein, J.; Guckel, H., High winding density micro coils for magnetic actuators. *Microsystem Technologies* 1998, 4, 172-175.
19. Ko, C. H.; Yang, J. J.; Chiou, J. C., Efficient magnetic microactuator with an enclosed magnetic core. *Journal of Microlithography, Microfabrication, and Microsystems* 2002, 1, 144-149.
20. Pan, C. T.; Yang, H.; Chou, M. C.; Shen, S. C., Integrated electromagnetic microactuators with a large driving force. *Microsystem Technologies* 2005, 12, 173-179.
21. Zhu, Z. Q., Improved analytical model for predicting the magnetic field distribution in brushless permanent-magnet machines. *IEEE transactions on magnetics* 2002, 38, 229-238.
22. Shen, M.; Dovat, L.; Gijss, M. A. M., Magnetic active-valve micropump actuated by a rotating magnetic assembly. *Sensors and Actuators B: Chemical* 2009, in press.
23. Smitha, B.; Sridhar, S.; Khan, A. A., Solid polymer electrolyte membranes for fuel cell applications--a review. *Journal of Membrane Science* 2005, 259, 10-26.
24. Hötzel, A.; Tallarek, U., Ionic conductance of nanopores in microscale analysis systems: Where microfluidics meets nanofluidics. *Journal of Separation Science* 2007, 30, 1398-1419.
25. Slade, S.; Campbell, S. A.; Ralph, T. R.; Walsh, F. C., Ionic Conductivity of an Extruded Nafion 1100 EW Series of Membranes. *Journal of The Electrochemical Society* 2002, 149, A1556-A1564.
26. Haubold, H. G.; Vad, T.; Jungbluth, H.; Hiller, P., Nano structure of Nafion: a SAXS study. *Electrochimica Acta* 2001, 46, 1559-1563.
27. Colinart, T.; Didierjean, S.; Lottin, O.; Maranzana, G.; Moyne, C., Transport in PFSA Membranes. *Journal of The Electrochemical Society* 2008, 155, B244-B257.
28. Biylkoglul, A., Review of proton exchange membrane fuel cell models. *International Journal of Hydrogen Energy* 2005, 30, 1181-1212.
29. Kim, S.; Wang, Y.; Lee, J.; Jang, H.; Han, J., Concentration polarization and nonlinear electrokinetic flow near a nanofluidic channel. *Physical review letters* 2007, 99, 44501 (4pp).
30. Dukhin, S. S., Electrokinetic phenomena of the second kind and their applications. *Advances in Colloid and Interface Science* 1991, 35, 173-196.
31. Leinweber, F. C.; Tallarek, U., Nonequilibrium Electrokinetic Effects in Beds of Ion-Permeable Particles. *Langmuir* 2004, 20, 11637-11648.

# *Chapter 3*

## **State-Of-The-Art**

**Abstract:** This chapter mainly focuses on recent development in the field of micropumps, micro-direct methanol fuel cells, biomolecule preconcentrators, as well as of the microfabrication techniques aiming rapid prototyping. In the first part, we describe and summarize the most commonly used actuation methods, with emphasis on magnetic actuators, valving principles in microsystems and we present an overview of several types of reciprocating micropumps encountered in the literature. Next, after elaborating some basic concepts on micro-direct methanol fuel cells, we present a literature review on microfluidic flow plates design as well as on the aspect of proton exchange membrane modification and integration, which are at the basis of our work. In the third part, to further understand the complex dynamic processes involved in biomolecule preconcentrators, we review several advanced preconcentration devices, either made of nanochannels or porous membrane, with focus on the physical mechanisms. Finally, the classification of rapid prototyping technologies in microfluidic devices fabrication is presented of particular interest for this thesis, and rapid microstructuring of PMMA, PDMS, and glass are described in detail. Also, bonding techniques commonly used in literature as a key step for realizing microfluidic devices are presented.

### 3.1 State-of-the-art on magnetically actuated micropumps

Microfluidics has emerged from MEMS-technology as an important research field with numerous applications. Micropump is one of the most significant components for fluid handling, transport and dispensing and can be based on a large variety of operating principles<sup>1,2</sup>. The purpose of this section is to outline systematically the working and design principles of micropump systems, including actuation methods and valving types (see Fig. 3-1). Special attention will be focused on a literature review of magnetic actuation and displacement micropumps, which are at basis of two micropump systems developed in this thesis.

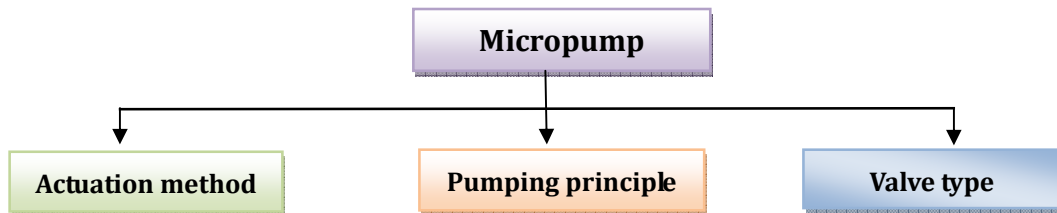


Figure 3-1: The main aspects of micropump system components.

#### 3.1.1 Actuators

The actuator is a functional system which enables the energy transformation from electrical or thermal form into the work output (i.e. mechanical). The ideal actuator can provide a large displacement or stroke with reasonable force under low operation power consumption. The actuators used for a microscale system should meet an additional criterion: they should have a small volume for easy integration.

##### *Classification of microactuators*

Generally, microactuators inspired by MEMS technology or standard micromachining are divided into the following categories by a survey paper of Roger G. Gilbertson<sup>3</sup>.

- *Electromagnetic*---motion of electrical current
- *Electrostatic*---a build-up or deficit of free electrons
- *Pneumatic*---physical expansion due to the external sources, *i.e.* thermal
- *Piezoelectric*---dimensional change when subjected to an electrical field
- *Shape memory*---material properties change when cycled above or below  $T_c$
- *Magnetostrictive*---material exhibit shape change under magnetic field
- *Electrorheological*---certain fluid viscosity change due to electrical field
- *Electrohydrodynamic*---motion of particle in polar fluid due to electrical field

In particular, we focus on several types of the following type of actuators:

- Electromagnetic

Electromagnetic actuation has been described earlier in [Chapter 2](#). The magnetic force as

deduced from the Lorentz force is expressed as:

$$\vec{F}_{mag} = I \int_l d\vec{l} \times \vec{B} \quad (3-1)$$

indicating the interaction between a wire carrying current (current  $I$ , length  $l$ ) and a permanent magnet with magnetic induction  $\vec{B}$ .

Typical examples of electromagnetic devices include electrical motors, solenoids, relays, speaker coils, and cathode ray tubes. Since electromagnetic fields can exist over a wide range of temperatures, performance is primarily limited by the properties of the materials used in constructing the actuator. Electromagnetic fields arise and disappear rapidly, thus permitting devices with very fast operation speeds. The major advantage of electromagnetic actuation over the other types is its deflection capacity and easy manufacturability. However, in order to achieve a large magnetic force from the actuation, current requirements always result in heating issues, which will greatly reduce the actuation efficiency. On the other hand, from the scaling point of the magnetic force, the more the coil turns or the longer the wire length, the larger the force. Therefore, miniaturization of electromagnetic actuator is always a challenge. Utilizing the magnet-magnet interaction could be an alternative to eliminating the heating effects but still keeping a high actuation force, the principle of which was described earlier in [Chapter 2](#).

#### ➤ Electrostatic

Electrostatic actuation is based on the Coulomb attraction forces between charged surfaces. The electrostatic force  $F_{es}$  arising from the two plates (area  $A$ , gap  $d$ ) due to a voltage difference  $V$  is written as:

$$F_{es} = \frac{1}{2} \epsilon_0 A \left( \frac{V}{d} \right)^2 \quad (3-2)$$

where  $\epsilon_0$  is the permittivity of free space. In order to obtain large electrostatic force, the gap between two electrodes should be as small as possible. Thus, the stroke will be limited, typically only tens or hundreds of micrometer. But one should notice that it is characterized by a fast response time and that the required power is really limited compared to the electromagnetic actuation. It shows the electrostatic actuation is an excellent candidate for integrated in miniaturized system when small stroke is not the issue.

#### ➤ Pneumatic

Pneumatic actuation is realized using external sources. On-chip pressure sources like compressed air or use of a thermopneumatic method makes it suitable for portable applications.

For example, in thermopneumatic actuation, volume expansion of fluid dependent on the heating is used. The fluid inside a control chamber can be converted to a gas upon heating or can simply be an expanding gas.

➤ **Piezoelectric**

Piezoelectric actuation is realized by means of the strain induced in a piezoelectric material (e.g. lead zirconate titanate or PZT, zinc oxide or ZnO) when subjected in an applied electrical field. It is characterized by a fast response time and a high energy density. However, the fabrication of integrated piezoelectric microactuators in Si-based microsystems requires the deposition of the thin film of piezoelectric material onto the silicon in clean room. It is the reason why most of the Si-based micropumps generally have a piezoelectric disc glued on the actuation membrane of the micropump.

*Comparison of microactuators*

In order to select the suitable type of actuation for our micropump systems, it is useful to investigate the different types of actuator on aspects of their advantages and disadvantages.

*Table 3-1: Comparison of different actuators.*

<b>Actuator</b>	<b>Displacement</b>	<b>Response time</b>	<b>Efficiency</b>	<b>Power density</b>
Electromagnetic	Large	Fast	High	High
Electrostatic	Very small	Very fast	Very high	Low
Pneumatic	Medium	Medium	Very high	High
Piezoelectric	Very small	Fast	Very high	High
Shape memory	Large	Slow	Low	High

Table 3-1 shows the comparison of displacement range, response time, efficiency and power density for different actuator types. Among them, an electromagnetic actuator exhibits the most advantages in cases where large displacement and efficiency are required and when miniaturization is the secondary consideration. Therefore, using external electromagnetic or magnetic actuation enables simple, low-cost and rapid prototypable micropump systems.

*Some examples of electromagnetic/magnetic actuators*

➤ *Membrane-embedded magnet with planar micro-coil*

In the work of Y-C. Lee *et al.*<sup>4</sup>, the actuator was designed to have a permanent magnet mounted on a flexible PDMS diaphragm and a planar copper micro-coil patterned on a bottom glass substrate by using an electron-beam evaporation process in the clean room (see Figs. 3-2a and



3-2b). The results revealed that, in the device, the target diaphragm deflection of  $110\ \mu\text{m}$  can be obtained using a compression force of  $220\ \mu\text{N}$  generated by a micro-coil, at an input current of  $0.6\ \text{A}$  when consuming  $2.2\ \text{W}$ .

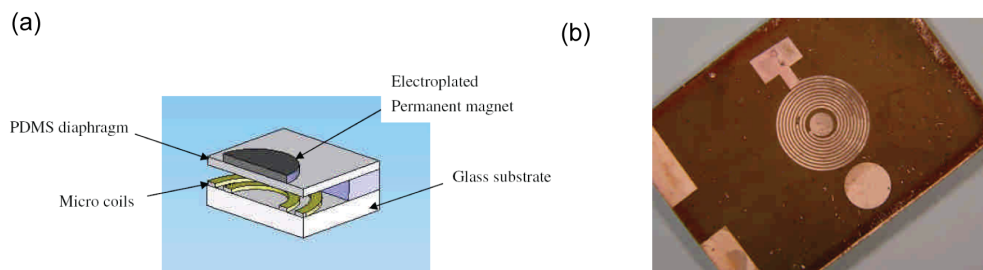


Figure 3-2: (a) Schematic illustration of an electromagnetic actuator and (b) photograph of the fabricated coil<sup>4</sup>.

➤ *Coil-embedded membrane with iron core surrounded magnet*

As seen from Fig. 3-3, K-H Kim *et al.* demonstrated an actuator having a flat parylene diaphragm, spiral copper wire and permanent magnet<sup>5</sup>. A core substrate of iron was fabricated to increase the magnetic flux density in the radial direction of the coil plane, which was proved by a FEM calculation. The static deflection of the flat diaphragm was  $15\ \mu\text{m}$  when using the pneumatic pressure of  $500\ \text{Pa}$ , and the dynamic deflection (peak-to-peak) was  $20\ \mu\text{m}$ , at the input current of  $100\ \text{mA}$  at  $1\ \text{Hz}$  and  $50\%$  duty ratio.

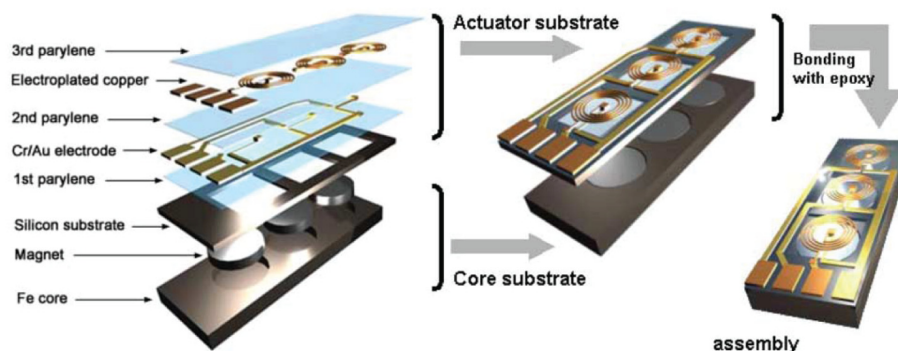


Figure 3-3: The structure of the actuator with parylene embedded coil, permanent magnet and iron core<sup>5</sup>.

➤ *Magnetic trapping with a rotating permanent magnet*

Q. Ramadan *et al.* proposed the rotation of periodically arranged permanent magnets close to a fluidic channel carrying a suspension of magnetic particles for trapping and releasing of the particles along the fluidic channel in a periodic manner<sup>6</sup>. As shown in Fig. 3-4, the magnetic force changes during the magnet rotation from a maximum to a minimum then back to a maximum. This approach represents a step forward toward the application of a magnetic field with

easy-handling at low cost, and has potential to be used as magnetic actuator for a magnetic membrane.

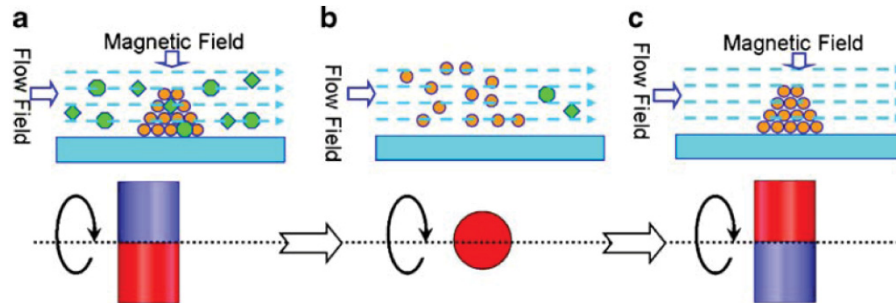


Figure 3-4: The alternate trapping and releasing of a magnetic particle suspension by rotation of magnet. Magnetic particles are trapped when the magnetic force is a maximum and are released when the magnetic force becomes a minimum (as indicated in a, b and c)<sup>6</sup>.

### 3.1.2 Valving principles

Microvalves, as one of the most essential components for microfluidic devices, are widely studied, especially for microflow regulation. In this section, a classification of microvalves will be given. Some detailed examples of microvalves including both passive and active valves which are quite related to the valving principles used in the thesis are described.

#### *Classification of microvalves*

Microvalves can be roughly categorized as shown in Fig. 3-5. Most of them generally fall into one of two major categories: (i) *active* microvalves, using *mechanical* and *non-mechanical* moving parts, as well as *external systems*; (ii) *passive* microvalves, using *mechanical* and *non-mechanical* moving parts. More details can be found in the review article of W.O. Kwang *et al.*<sup>7</sup>.

- *Active valves*: The opening and closure of the valves are controlled actively by means of external forces like electromagnetic<sup>8</sup>, magnetic, electrostatic<sup>9</sup> forces and the fluid environment (pH values etc.)<sup>10</sup>.
- *Passive valves*: There are no external actuation sources for passive valves and its valving effect is obtained from the pressure difference across the valve.

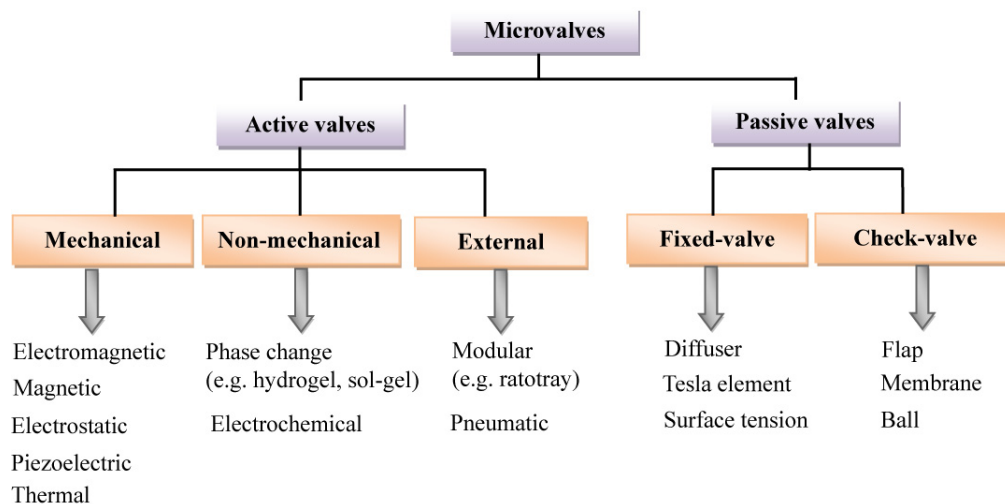


Figure 3-5: Classification of microvalves.

As reported from literature, the passive valves, due to their easy-integration properties, are most widely adopted in reciprocating micropumps. On the other hand, as benefiting from less complex designs, active-valves using external actuation are able to rectify flow more efficiently. Thus, a ball valve, representing a fluidic diode, is incorporated in our electromagnetically actuated micropump, and a magnetically controlled membrane valve is investigated in our active-valve micropump.

#### Some examples of valving principles

##### ➤ Active valve: electromagnetically controlled valve

To realize a pressure regulating valve for a glaucoma implant, as shown in Fig. 3-6, B. Bae *et al.*<sup>8</sup> proposed an optimized electromagnetically driven valve that comprised a permanent magnet, a soft membrane and a coil. The actual valve size was  $9.2 \times 9.2 \times 3.1 \text{ mm}^3$ . The experimental results showed that precise pressure control was possible, and hence there was a high probability that the desired intraocular pressure can be obtained with good control performance, when the pressure-regulating valve was implanted.

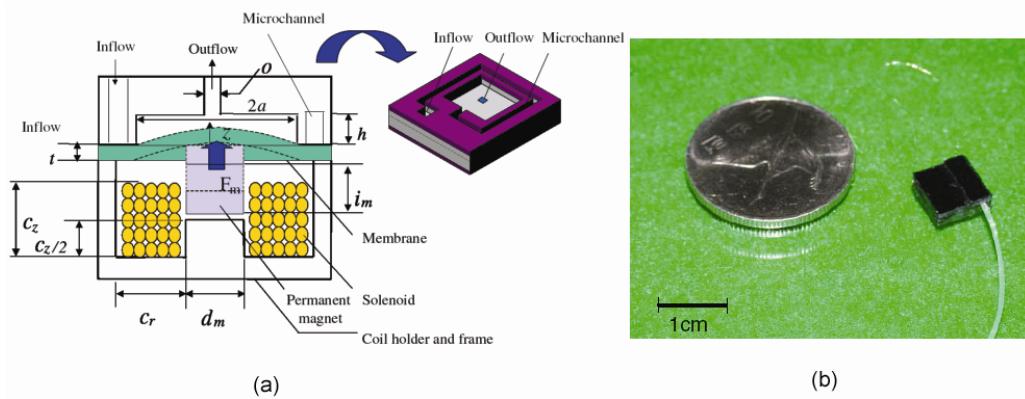


Figure 3-6: (a) Configuration of an electromagnetically controlled valve and (b) its realization<sup>8</sup>.

➤ *Passive valve: diaphragm valve*

A Silicon-on-Insulator (SOI)-based micro check valve has been designed, fabricated and tested by H. Min *et al.*<sup>11</sup>. Fabricated on a single SOI wafer (see from Fig. 3-7), the micro check valve has been characterized by a high frequency response, low leakage rate and simple fabrication process. It had negligible leakage rate observed in the reverse flow direction at a pressure of up to 600 kPa.

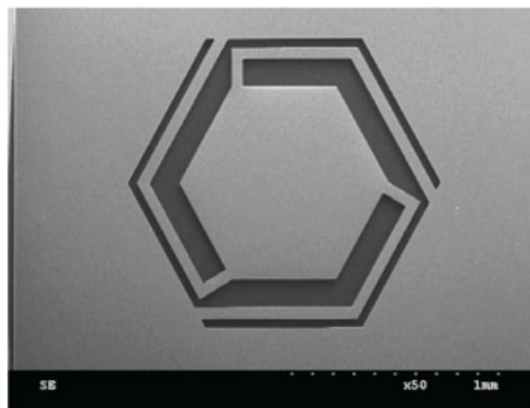


Figure 3-7: Front view of the micro diaphragm check valve<sup>11</sup>.

➤ *Passive valve: ball valve*

A one-way ball valve integrated in a micropump has been designed and fabricated by T. Pan *et al.*<sup>12</sup>, using simple and reproducible PDMS molding technology structured by microtube connections, as shown in Fig. 3-8. Leakage measurements for the ball check valves indicated the valves perfect sealing at pressures lower than 5 kPa. A leakage of less than 1 μL/min was measured between 5 kPa and 30 kPa.

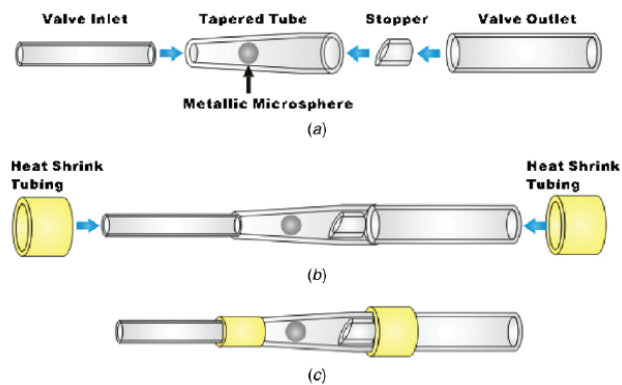


Figure 3-8: Illustration of (a) basic components, (b) assembling process and (c) final packaging of the micro-ball valve (not to scale)<sup>12</sup>.

### 3.1.3 Micropumps

In this section, we categorize micropumps according to the manner and means by which they produce fluid flow and pressure. The working principle and basic parameters of a reciprocating micropump will be described before giving the detailed examples from literature of the micropumps.

#### Classification of micropumps

The classification of micropumps adopted from a review article of D.J. Laser *et al.*<sup>2</sup>, illustrated in Fig. 3-9, is applicable to pumps in general and is essentially an extension of the system set forth by W.C. Krutzch *et al.*<sup>13</sup> for traditional pumps.

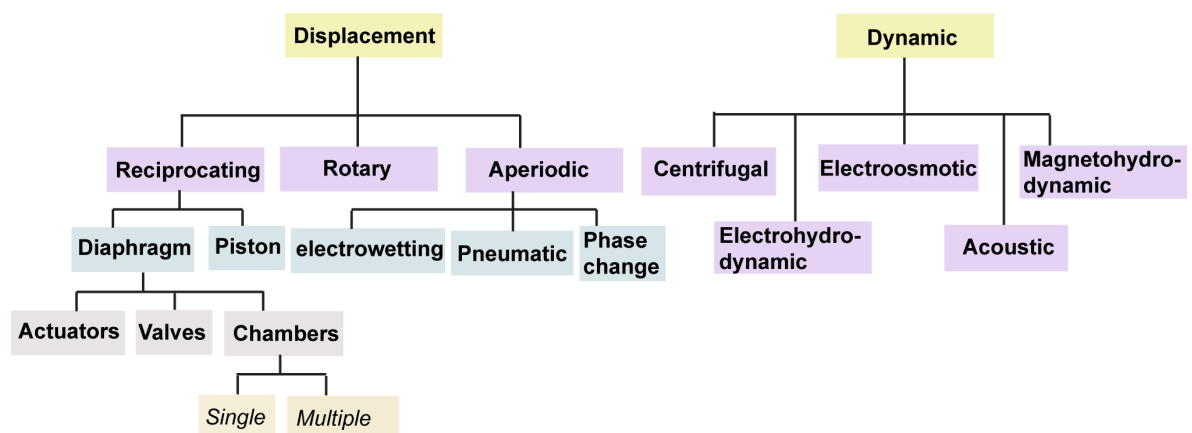


Figure 3-9: Classification of micropumps (adapted version from D.J. Laser *et al.*<sup>2</sup>).

The micropumps are distinguished into two main categories and we will focus particularly on a reciprocating micropump, in which energy is periodically added to the system by means of the force applied on the boundaries of a fluid-containing volume. Generally, a pulsating flow will be

produced for reciprocating-type micropumps, while the flow pattern for a dynamic micropump is continuous and much more stable. However, in most applications, the latter becomes invalid for transporting high-viscous fluid.

### *Parameters for reciprocating micropump design*

#### ➤ *Compression ratio*

A significant parameter for designing the reciprocating micropump with self-priming capacities is

the *compression ratio*  $\varepsilon = \frac{\Delta V}{V_0}$ , where  $\Delta V$  is the volume stroke of actuation membrane and  $V_0$

the total dead volume of the pump. Inspired by the work done by M. Richter *et al.*<sup>14</sup>, we carry out the simplified calculations for the minimum compression ratio for the micropumps developed in the thesis (see [Chapter 5](#) and [Chapter 6](#)). We believe this also provide us the criterion for choosing the actuation method.

#### ➤ *Power of pump*

The power delivered by the fluid can be expressed as<sup>2</sup>:

$$P_{pump} = \frac{\Delta P_{max} \cdot Q_{max}}{4} \quad (3-3)$$

where  $\Delta P_{max}$  the maximum backpressure when the flow rate of pump falls to zero, and  $Q_{max}$  the maximum flow rate obtained in absence of backpressure.

#### ➤ *Efficiency of pump*

The efficiency of pump  $\eta_{pump}$  is written as:

$$\eta_{pump} = \frac{P_{pump}}{P_{actuator}} \quad (3-4)$$

with  $P_{actuator}$  the power consumed by the external actuator. The pump efficiency is affected by multiple factors, such as friction losses, fluid leakage (refer to valving efficiency), etc.<sup>2</sup>.

### *Some examples of displacement micropumps*

A survey through the literature reveals that one of the very first documents about a miniaturized pump is a patent of L. J. Thomas and S. P. Bessman dating from 1975<sup>15</sup>. The device designed for implantation into the human body, consisted of a solenoid valve connected to a variable pumping chamber which was actuated by two opposed piezoelectric disc benders. Smits *et al.* abandoned the fully immersed actuator and realized a peristaltic micropump with active valves, as was published in 1990<sup>16</sup>. The first diaphragm micropump with passive check-valves

was presented by H. T. G. van Lintel *et al.* in 1988<sup>17</sup>. The work of Smits and Van Lintel marks the beginning of a multitude of micro diaphragm pump developments that lasts until today. Most of the devices realized are based on the diaphragm type or the peristaltic type described above, but with varying valve geometries, actuation mechanisms and fabrication technologies<sup>18</sup>. Microfluidic systems with integrated micropumps have since then triggered interest for a wide range of applications. These devices are encountered in LOC devices for biological applications<sup>19</sup>, as well as in microelectronics for the cooling of chips<sup>20</sup>.

Literature review shows that the displacement pumps are the most frequently used pumps for microfluidic devices<sup>1, 2</sup>. The following illustrative examples will be mainly focused on diaphragm micropumps with both single and multiple chambers (peristaltic), since they form the technical basis for the realization of our micropumps.

#### ➤ *Diaphragm micropump-single chamber*

A diaphragm micropump actuated by an external electromagnetic actuator was proposed by P. Dario *et al.*<sup>21</sup>, and has been extensively studied since then, because of its easy adaption in a modular way and because it has the benefit of a separate optimization of micropump and actuation unit<sup>22,23</sup>. C. Yamahata *et al.*<sup>24</sup> designed and experimentally realized nozzle/ diffuser structures for application in a PMMA micropump (see [Fig. 3-10](#)).

The combination of the nozzle/diffuser elements with an electromagnetically actuated PDMS membrane, characterized by a large deflection amplitude, resulted in a self-priming micropump with which they successfully pumped water and air with flow rate of 0.4 mL/min and 7 mL/min, respectively.

Meanwhile, some research groups developed miniaturized planar coils for electromagnetic actuation to greatly eliminate the size of the actuator, for example, C.Y. Lee *et al.* realized a valveless impedance micropump with four major components: a copper micro coil, a microchannel, an upper glass cover plate and a PDMS diaphragm with a magnet mounted on its upper surface<sup>4</sup>. The flow rate of 7.2 mL/min could be achieved at an actuation frequency of 200 Hz with a current of 0.6 A. However, this requires complex clean room fabrication for the copper coil and the integration of magnetic flux concentrator-magnetic core becomes very difficult. Nevertheless, the field of displacement micropumps is not limited to the micropump with integrated magnetic membranes which give rise to the large pumping stroke. Some other displacement micropumps using thermopneumatic actuation<sup>25</sup>, shape-memory alloy<sup>26</sup>, electrostatic actuation<sup>27</sup> and electrowetting<sup>28</sup> are also extensively studied, aiming the various applications, such as precise dispensing.



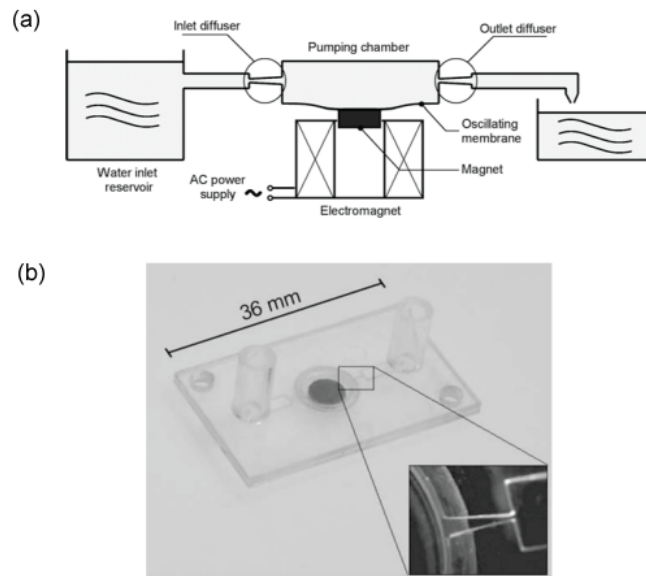


Figure 3-10: (a) Schematic diagram of a diffuser-nozzle micropump with external electromagnetic actuation. (b) Photograph of a diffuser-nozzle micropump with magnetic membrane<sup>24</sup>.

### ➤ Peristaltic micropumps

Numerous ways are existing to peristaltically pump the liquid. For example, as a milestone, M.A. Unger *et al.* used soft lithography to realize multiple layer microfluidic systems containing pneumatically driven active valves and a peristaltic micropump made of silicone elastomer<sup>29</sup>. It had a typical flow rate of 2.5 nL/s when actuated at 75 Hz with an applied pneumatic pressure of 50 kPa.

Compared to the thermopneumatic actuation used in the peristaltic micropump<sup>30</sup>, electrostatic<sup>31</sup> and piezoelectric actuation<sup>32, 33</sup> benefiting from low power consumption and easy programmable actuation sequence are commonly utilized. Using multilayer parylene technology, J. Xie *et al.* proposed an entire surface-micromachined peristaltic micropump by electrostatic actuation<sup>31</sup>. With 3-phase actuation, a maximum flow rate of 1.7 nL/min and backpressure of 1.6 kPa were achieved at 20 Hz actuation frequency.

Magnetic actuation was also demonstrated to provide an effective and easy method to actuate the peristaltic micropump. T. Pan *et al.* developed a robust low-cost PDMS peristaltic micropump with magnetic drive<sup>34</sup>. As illustrated in Fig. 3-11, a base layer incorporated the microchannel while a middle layer contained the actuation membrane. The top layer encapsulated three small permanent magnetic rods in three small chambers. A small DC motor (6 mm in diameter and 15 mm in length) with three permanent magnets stagger-mounted on its shaft was used to actuate the membrane-mounted magnets to generate a peristaltic waveform. A maximum pumping rate of about 24  $\mu$ L/min at the speed of 1700 rpm with power consumption of 11 mW was demonstrated.



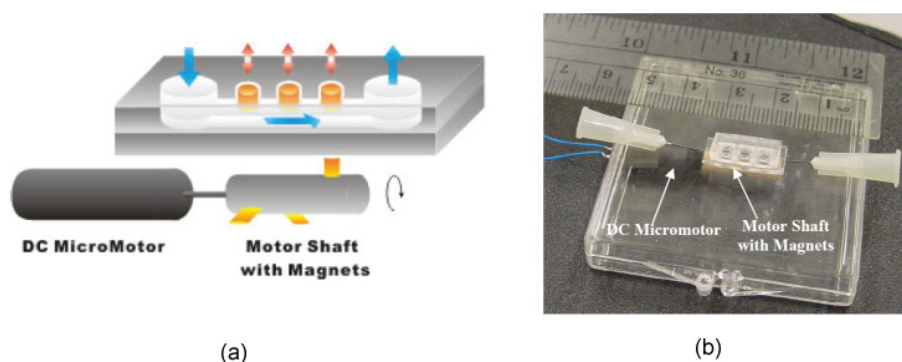


Figure 3-11: (a) A perspective view of PDMS micropump and (b) Peristaltic micropump with its magnetic actuation ready for measurement <sup>34</sup>.

A disposable peristaltic magnetically actuated micropump has been realized by L. Yobas *et al.*<sup>35</sup>. A unique feature of this pump is the use of readily-available stainless-steel ball coupled with rotating rare-earth magnets as reconfigurable actuating elements on softstate microfluidic devices.

### 3.1.4 Conclusion

In this section, we have presented the most commonly used magnetic actuation methods and valving principles in microsystems, and we have also given an overview of the different types of displacement micropumps encountered in the literature.

For the envisaged applications in the thesis, reciprocating micropumps become particularly interesting due to their relative easiness of implementation compared to other mechanical pumping principles. Furthermore, pressure-driven flow is capable of transporting both conducting and non conducting liquids. Electromagnetic/magnetic actuation retained our attention mainly for its large stroke capabilities, enabling an external and contactless actuation.

## 3.2 State-of-the-art on micro-direct methanol fuel cells

Energy needs for portable electronics have been rising rapidly in the past few years due to the increasing functionalities of portable devices. Fuel cells that convert chemical energy into electrical energy, when inspired by microtechnologies, are being considered as the dominant power provider instead of current battery for higher energy densities and smaller package volume (see Fig. 3-12a)<sup>36</sup>. A schematic of a fuel cell is shown in Fig. 3-12b.

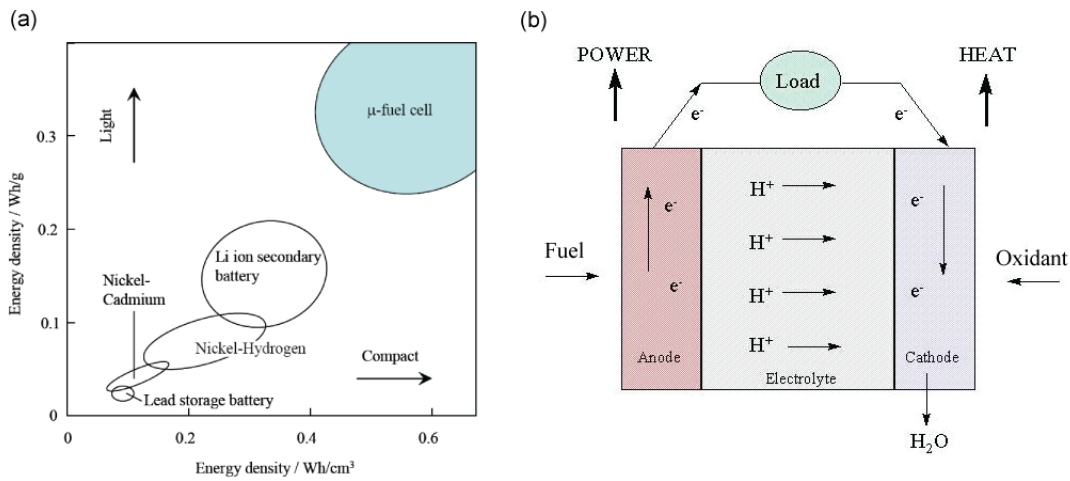


Figure 3-12: (a) Comparison of energy density and (b) schematic of the fuel cell working principle<sup>37</sup>.

In this section, basic parameters involved in fuel cells will be first outlined. Afterwards, it is imperative to analyze some challenges in developing a micro-direct methanol fuel cell (micro-DMFC). Furthermore, we will present a literature review on micro-DMFCs, detailing in particular aspects of both structure design and membrane integration.

### 3.2.1 Basic parameters of a micro-direct methanol fuel cell

Depending on the type of fuel and electrolytes used, fuel cells are categorized as alkali fuel cells, phosphoric acid fuel cells, solid oxide fuel cells and solid polymer fuel cells. Because the electrolyte of solid polymer fuel cells is made of polymer, it can work at relatively low temperature, which presents a substantial advantage for portable applications. The micro-direct methanol fuel cell, as one of the common type of solid polymer fuel cells, will be discussed in detail.

#### *Basic components of a typical micro fuel cell*

As shown in Fig. 3-13, the central part of a micro fuel cell is a porous proton exchange membrane (PEM) (one type of cation-permselective membranes), which is in contact with an anode and a cathode on each side. The anode and cathode each consists of different layers such as carrier substrate, current collector, diffusion layer and catalyst layer. The fuel is supplied continuously to the anode and an oxidant such as oxygen from air is fed continuously to the cathode. The electrochemical reactions are activated at the catalytic electrodes<sup>38</sup>.

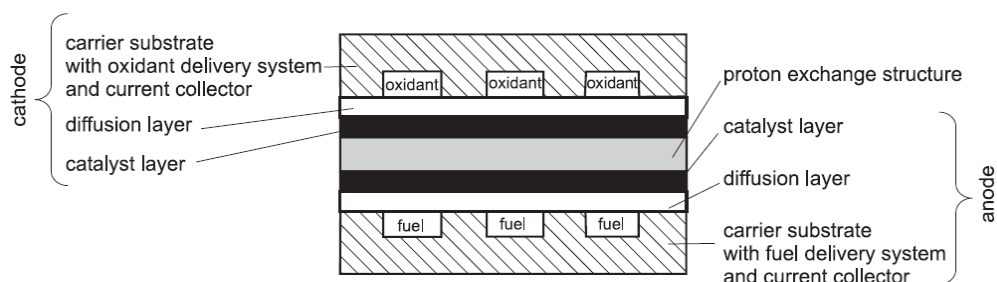
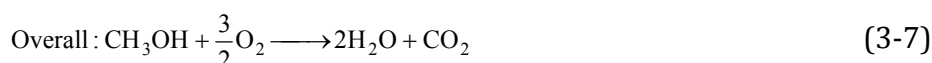
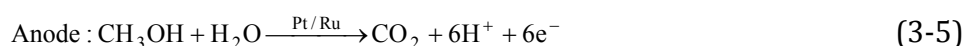


Figure 3-13: Basic components of a typical micro fuel cell <sup>38</sup>.

Protons generated at the anode pass through the PEM, while the electrons produce a current through the external load. In the case of using methanol as the fuel, the reactions at the anode and cathode are:



Compared to hydrogen, methanol is much cheaper to be produced and easy to be stored. Due to its high energy content, methanol appears to be the better candidate for portable applications.

### Polarization curve

In an ideal (reversible) fuel cell, the cell voltage is independent on the current drawn. Practically, the reversible cell voltage is not realized even under open-circuit (zero current) conditions due to the certain irreversibilities that arise during fuel cell operation.

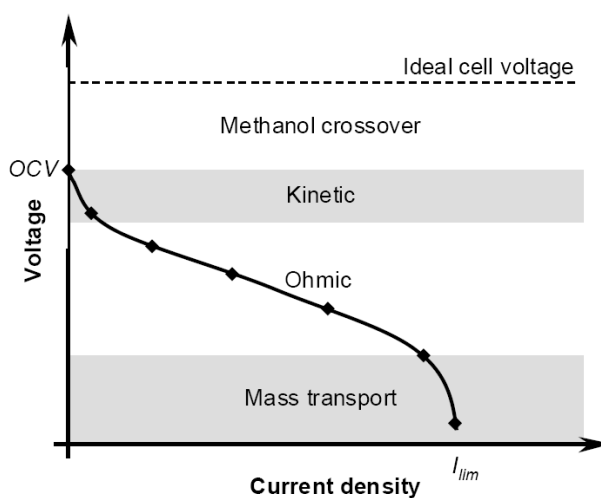


Figure 3-14: Typical polarization curve for direct methanol fuel cell.

The difference between actual cell voltage at a given current density (current per unit active electrode area) and the reversible cell voltage for the reaction is defined as overvoltage. The typical polarization curve is shown in Fig. 3-14.

Prominent sources of overvoltage in a fuel cell are<sup>39,40</sup>:

➤ *Mixed potential at electrodes*

It is caused by the unavoidable parasitic reactions that tend to lower the equilibrium electrode potential. The particularly important reason for the mixed potential is the crossover of fuel through the electrolyte from anode to cathode or vice versa. This is the dominant source of losses at open circuit, especially in DMFCs where fuel crossover can be high.

➤ *Activation losses*

It arises predominantly due to the kinetics at the electrodes. Examples include sluggish oxygen reduction kinetics at the cathodes and methanol oxidation at the anode of a direct methanol fuel cell.

➤ *Ohmic losses*

It is due to the resistive losses in the electrolyte and in the electrodes.

➤ *Mass transport losses*

Non-reacting diffusion in the gas-diffusion layer and reacting diffusion in the electrode layers are the main reasons for this type of losses.

The combined contributions of these sources of overvoltage cause the cell voltage output to decrease with increasing current density. A plot of cell voltage vs. current density is known as a polarization curve. The analytic expression that best describes the behavior above in the entire current density range is given by the equation<sup>40</sup>:

$$E = E_0 - b \log(i) - Ri - me^{ni} \quad (3-8)$$

where,

$$E_0 = E_r + b \log(i_0) \quad (3-9)$$

$E_r$  is the reversible potential (calculated from Gibbs's free energy and temperature,  $E_r=1.21$  V for DMFC),  $b$  is the Tafel slope, and  $i_0$  is the exchange current density for the oxygen reduction reaction. The parameter  $R$  is the predominant ohmic resistance in the cell with a small contribution from the charge transfer resistance of the anodic reaction and the electronic resistance in the electrodes and cell fixtures.  $m$  and  $n$  are parameters governing the semi-exponential decrease of cell potential with high current density due to mass transport overpotential.

The power density of the fuel cell is expressed by the relation:

$$P = E \cdot i \quad (3-10)$$

The slope of  $P$  versus  $i$  or  $P$  versus  $E$  plot is a parabola if  $E$  versus  $i$  relation is linear. The parabola is

distorted for low temperature fuel cells because of the semi logarithmic relation between cell potential and current density at low value of  $i$ .

### 3.2.2 Scaling law for a micro fuel cell

The miniaturization of a fuel cell should take into consideration a scaling law<sup>38</sup>. Assuming a scaling factor of  $S$ , the ratio of surface area to volume is  $S^{-1}$ . It reveals that the surface effect will become dominant in micro fuel cell. The Peclet number  $Pe$  (the ratio of the thermal energy convected to the fluid to the thermal energy conducted within the fluid) and Reynolds number  $Re$  are scaled as  $S$ . The pressure drop scales as  $S^3$ .

Based on these scaling analyses, we are able to deduce both advantages and drawbacks of micro-scaled fuel cell:

- The dominant surface effects favor the reaction conditions and thus enhance the cell performance.
- The high pressure drop helps to improve diffusion of the fuel and the oxidant to the membrane through diffusion layer.
- The relationship between the Peclet number and the Reynolds number is  $Pe \approx 1000 Re$  for liquids. The relatively large Peclet number in a micro-DMFC implies a dominant convection transport, which may effectively prevent fuel from diffusing toward the PEM.

### 3.2.3 Challenges in micro scale direct methanol fuel cells

Miniaturization is not a simple scaling down of a larger system. Rather, each component of the fuel cell must be redesigned with an eye towards optimization in miniaturized format. The power density generated by a fuel cell must also be given high priority and this is proportional to the stack size and active cell area. As pointed out in some review articles, we explain several technological challenges that are quite related to our work before literature review of the micro-DMFC. More detailed explanations can be found in the review of S.K. Kamarudin *et al.*<sup>36</sup>.

#### ➤ *Methanol crossover*

Methanol crossover (methanol molecules diffuse through the membrane and are directly oxidized by oxygen at the catalytic surface on the cathode) in a micro-DMFC is still the most important fundamental problem to solve in order to stimulate the development of high-efficiency systems. Methanol crossover causes two detrimental consequences: self-discharge of methanol and a drastic reduction of the cathode voltage. Thus, a moderate concentration of methanol should be selected<sup>41</sup>.

#### ➤ *Management of heat*

For a micro-DMFC, less than around 30% of the total energy will be connected to generate

electricity, while the rest becomes heat. The heat produced in the system need to be dissipated; otherwise the accumulated heat might cause appreciable drawbacks for portable systems.

➤ *Low energy*

When a smaller system is considered, the energy decreases drastically. This has limited the application of DMFC systems for micro-size portable devices.

➤ *Management of water*

Control systems associated with water and methanol management add considerably to the complexity of micro-DMFC systems, particularly those being developed for portable applications. Thus, it is highly demanded to recycle the water produced at cathode to anode for fuel dilution.

➤ *Lifetime and duration*

The aging mechanism of micro-DMFC system is still a topic to be investigated, even though it is generally known that the operational conditions, such as fuel/oxidant flow rate and operating temperature, can affect fuel cell lifetime and durability.

➤ *Membrane electrode assembly (MEA)*

In order to realize the commercial micro-DMFCs, the requirement of a more effective and suitable MEA part that enables electricity generation from chemical energy for micro-DMFC application is inevitable. MEAs that are widely used in conventional DMFCs can be conveniently integrated in a sandwich-type micro-DMFC, while planar micro-DMFC, is unable to utilize it directly. Therefore, in planar micro-DMFCs, apart from the use of commercial or self-patterned ion-exchange membrane, some extra steps are necessary to realize catalytic electrodes via microtechnologies.

**3.2.4 Literature review on structure design of micro-direct methanol fuel cell**

A micro-fuel cell system must be miniaturized and compact for portable applications. Researchers are developing systems that can achieve the optimum balance of cost, efficiency, reliability and durability. Two approaches are currently investigated: scaling down of fuel cell systems using conventional assembling methods, or to redesign every component using MEMS technology. Here, we present literature aspects corresponding only to the latter approach with both bipolar and planar constructions (see Fig. 3-15).

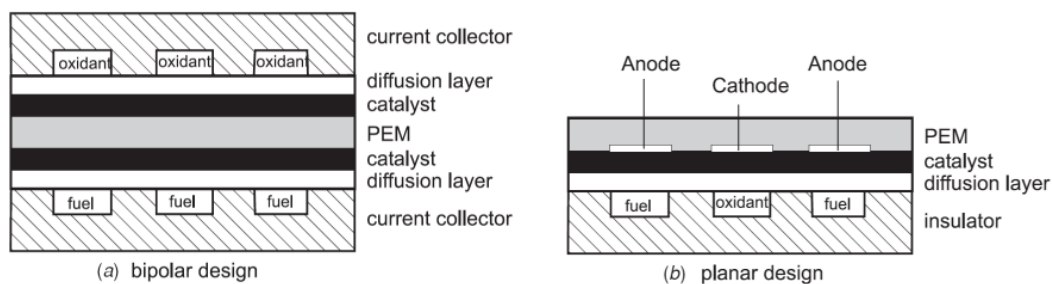


Figure 3-15: Two basic designs of micro fuel cells: (a) bipolar, (b) planar (not to scale)<sup>38</sup>.

### *Some examples of bipolar micro-direct methanol fuel cells*

Apart from the drastically decreased size, the application of MEMS technology in a direct methanol fuel cell usually results in the change of cell materials, which can, for example, be based on silicon. In fact, the major advantage of MEMS technology is in making the bipolar plate smaller with higher precision, leading to the high potential of mass production<sup>36,38</sup>.

There are various types of attractive substrate materials that can be used for bipolar plates in order to make the DMFC smaller<sup>42</sup>. These are silicon<sup>43</sup>, printed-circuit boards (PCB)<sup>44</sup> and photopolymers<sup>45</sup> and flexible polymer substrates<sup>46</sup>.

Based on the different concepts of fuel delivery and fuel handling, micro fuel cells can be configured with various flow channel patterns. The parallel channels reduce the supplying pressure and decrease the mean fuel velocity at a constant flow rate. The lower velocity leads to a longer residence time and better fuel diffusion. This design was implemented by S.W. Cha *et al.*<sup>47</sup> in SU-8, and by R. Hahn *et al.*<sup>48</sup> in polymer/steel composite. The serpentine/parallel design increases the channel length and thus the pressure drop, leading to better fuel permeability. This design reduces the pressure drop by using numerous parallel channels. T.J. Yen *et al.*<sup>49,50</sup> used a DRIE system to etch three parallel/serpentine microchannels of  $750\ \mu\text{m} \times 400\ \mu\text{m}$  in silicon. S. Hsieh *et al.*<sup>51</sup> used an excimer laser to machine four parallel/serpentine microchannels in PMMA.

### *Some examples of planar micro-direct methanol fuel cells*

The approach shown in Fig. 3-15b has several advantages and differs in many ways from bipolar designs<sup>36</sup>:

- It integrates of the anode and cathode onto a single substrate.
- The isolation of fuel and oxidant prevents the over-crossing the fuel and oxidants streams.
- The efficiency of the current collectors is high, because the catalyst layers are directly supported on the metal.
- The characteristic length of the system, a distance that the protons travel from anode to cathode, can be simply adjusted by MEMS technology.

S. Motokawa *et al.* realized a micro-DMFC using a series of fabrication steps adapted to a silicon wafer, including photolithography, DRIE, and electron beam deposition as shown in Fig. 3-16<sup>52</sup>. The anodic and cathodic microchannels were fabricated using a monolithic Si wafer and this enabled the system to be in a compact size (active area =  $0.018\ \text{cm}^2$ ) with less substrate material used. A conventional electrolyte membrane (DuPont's Nafion membrane) and catalysts (Pt/Ru for anode and Pt for cathode) were used. Current collectors, namely Ti/Au, were deposited by electron beam and the lift-off method. Preliminary tests showed that this microsystem generated  $0.78\ \text{mW}/\text{cm}^2$  at  $3.6\ \text{mA}/\text{cm}^2$ .

Later on, Z. Y. Xiao *et al.*<sup>53</sup> presented a serially connected monolithic fuel cell array based on

planar configuration. High surface area catalysts were integrated on the chip by selective electrodeposition. The peak power density of the twin-cell array was  $0.85 \text{ mW/cm}^2$  fueled by 1 M methanol at room temperature.

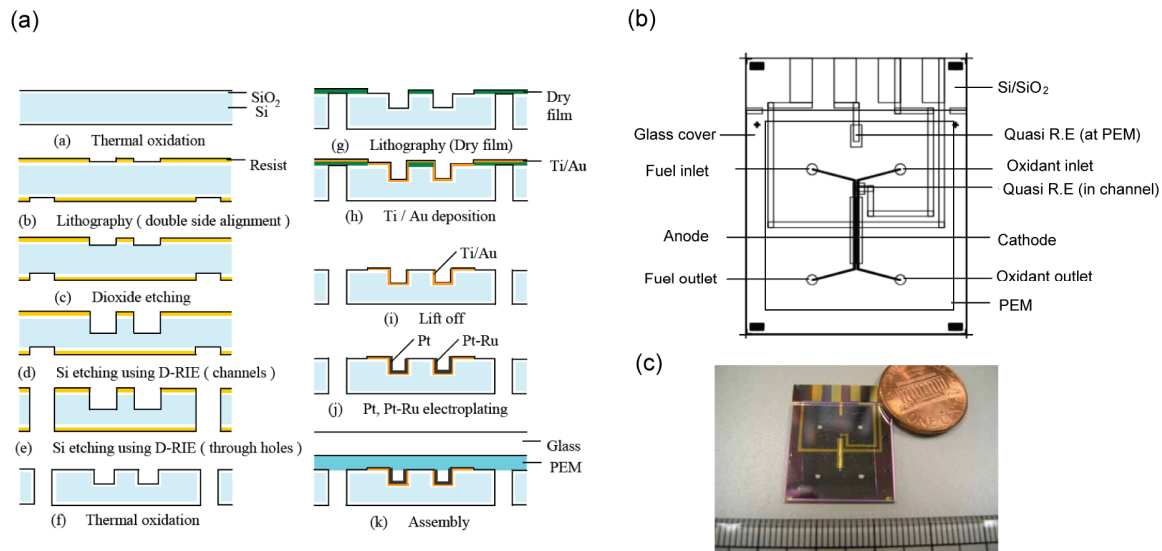


Figure 3-16: (a) Schematic of fabrication flow of a planar micro-DMFC, (b) schematic diagram of in-plane micro-DMFC and (c) Photograph of a fabricated micro-DMFC<sup>52</sup>.

### 3.2.5 Literature review on PEM integration in micro fuel cell

Besides the flow channel design in a micro-DMFC, PEM integration in the micro fuel cell is always a non-trivial task. Appropriate surface modification and novel patterning methods of PEM using MEMS technology are critical to drastically enhance the micro fuel cell's performance. Literature described in this section will not be restricted only to micro-DMFC, and extensive knowledge regarding the PEM integration demonstrated in various micro fuel cell types are gathered here.

#### *Some examples of commercial PEM modification*

The modification of the PEM using MEMS technology is critical for improving the overall performance of a micro-DMFC. Using nanoimprint PEM, Y. Zhang *et al.*<sup>54</sup> obtained better performance of a MEMS-based DMFC, since it facilitated the formation of the three-phase reaction interface of fuel, electrolyte and catalyst.  $\gamma$ -ray radiation and electroless palladium deposition on a Nafion117 membrane invented by X.W. Liu *et al.*<sup>55</sup> enabled the micro-DMFC producing reasonable power density, which was as high as  $4.9 \text{ mW/cm}^2$  under 2 M methanol solution at room temperature.

To enhance the compatibility between electrode and membrane and also reduce methanol crossover from anode to cathode in direct methanol fuel cells, a Nafion membrane coated with a



Polyvinylidene Fluoride (PVDF) copolymer/Nafion blend has been put forward by K.Y. Cho *et al.*<sup>56</sup>. This coated Nafion showed reduced methanol crossover and an enhancement in cell performance due to its improved compatibility with the electrode compared to that of native Nafion.

### Some examples of PEM patterning

Though numerous successful examples have already demonstrated the effectiveness and technical feasibility of modification of a commercial PEM, triggered by the development of patterning technology in MEMS, some efforts have been directed towards patterning a PEM via MEMS-based techniques.

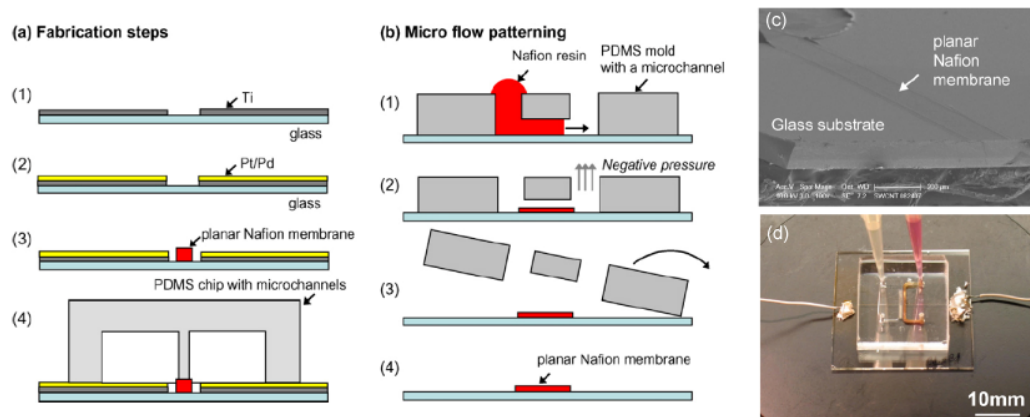


Figure 3-17: (a) Fabrication steps, (b) principle of microflow patterning technology, (c) SEM image of patterned Nafion membrane on a glass substrate and (d) photograph of a single PDMS fuel cell<sup>57</sup>.

Y. A. Song *et al.*<sup>57</sup> have adopted a planar fuel cell design by surface-patterning a submicron-thick Nafion membrane on a glass substrate instead of sandwiching a thin Nafion sheet (fabrication flow shown in Figs. 3-17a, 3-17b and 3-17c). A PDMS chip and a Nafion patterned glass substrate can be assembled using oxygen plasma bonding which allows simple and rapid in-plane integration of the Nafion membrane into a PEM-based microfluidic fuel cell without cumbersome clamping. They used 8.8 M HCOOH as the fuel and 10 mM KMnO<sub>4</sub> as the oxidant at ambient temperature. Their fabricated fuel cell (see Fig. 3-17d) produced a maximum current density up to 86.66 μA/cm<sup>2</sup> (the total current output was 5.82 μA) at a flow rate of 1 μL/min.

A high voltage DMFC can be achieved by the integration of a micro DMFC array on one substrate as proposed by T. Ito *et al.*<sup>46</sup>. They fabricated micro-DMFCs on a photosensitive glass substrate containing a micro-holes array with PEM patterned by pipeting a Nafion solution into the micro-holes.

### *Some examples of alternatives to using a commercial PEM*

Nafion (DuPont) membrane, as mentioned above, is a solid electrolyte that is commonly used in micro fuel cell. With adoption of MEMS technology, porous membranes made of silicon or other kinds of materials are also attractive.

Recently, S.M. Mitrovski *et al.*<sup>58</sup> introduced a novel proton exchange concept using a liquid electrolyte confined inside a microchannel network. This concept may potentially solve the problem of dehydration in PEM-based micro fuel cells. Porous silicon can be fabricated in an anodization process in a buffered HF solution. S. Liu *et al.*<sup>59</sup> recently fabricated nanochannels in a glass substrate. The channels were 1 mm long and 100  $\mu\text{m}$  wide but only a few hundred nanometres in depth. These channels also achieved conductivities in the order of 0.01–0.1 S/cm.

### **3.2.6 Conclusion**

In this section, we have presented some basic concepts of micro scaled fuel cells with particular focus on micro-DMFCs. The literature review on both micro-DMFC structure design and PEM integration provided a background and useful basis of our own work.

For the envisaged applications in our project, the planar design of a micro-DMFC is chosen because of the low-cost and rapid prototyping microfabrication strategy. In addition, the various methods of integrating PEM, as described above, will allow us to develop our own micro-DMFC by combining advantages of MEMS and microfluidics technology.

## **3.3 State-of-the-art on microfluidic biomolecule preconcentrators**

Recently, a novel type of electrokinetic concentration devices has been developed in a microfluidic format, enabling efficient trapping of biomolecules. These devices were widely studied, not only due to their potential application in biomolecule sensing, but also due to the physical phenomenon related to ion concentration polarization (CP) inherent in operating electrokinetic concentration devices.

In this section, the fundamentals of design rules will be introduced at first. Subsequently, two types of biomolecule preconcentrators are described with some illustrative examples. We also focus on modeling activities for these types of systems for disclosing the physics of concentration polarization and other electrokinetic nonlinear phenomena in such devices. Last, biomedical applications of these developed preconcentrators will be briefly stated.

### **3.3.1 Basic operation parameters and principle**

While there have been several types of nanofluidic preconcentrators developed during the past couple of years, the basic mechanisms employed in these systems are identical. Single-gated

devices with one nanojunction or nanoporous membrane are commonly used by researchers, as illustrated in Fig. 3-18<sup>60</sup>.

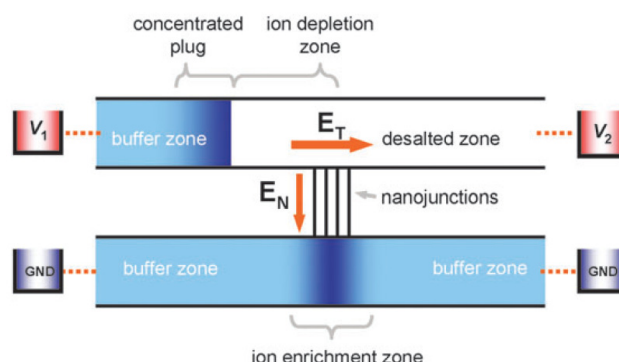


Figure 3-18: Schematic diagram of a single-gated electrokinetic preconcentrator in a typical micro/nanofluidic hybrid channel system with the electrical configurations under DC bias<sup>60</sup>.

The electrical field through the ion-permselective nanojunctions ( $E_N$ ) generates an ion depletion and enrichment region in the anodic and cathodic channel, respectively. This normal electric field is imposed by applying a voltage difference between anode and cathode. A voltage difference ( $V_1 > V_2$ ) at the anodic compartment is utilized generate a tangential electric field ( $E_T$ ) along the anodic side microchannel. This field cause electroosmotic flow through the microchannel that brings the target molecules into the region, where they will be trapped by the CP maintained by the permselective current through the junction.

$E_T$  and  $E_N$  should be carefully chosen by considering the microchannel dimensions, nanojunction properties and buffer concentration. Since the electrokinetic stability of the concentration process in the depletion region is mainly governed by  $E_N$ , a too high value of  $E_N$  would induce an ever-expanding depletion region, reducing the trapping efficiency. The accumulation speed increases with higher  $E_T$ , since the electroosmotic flow is enhanced accordingly. However, if  $E_T$  exceeds a critical value, the concentrated plug (see Fig. 3-18) cannot be maintained and begins to escape out of the ion depletion zone. Details can be found in the review article of S.J. Kim *et al.*<sup>60</sup>.

### 3.3.2 Classification of nanojunction-based preconcentrators

Realization of biomolecule preconcentration devices involves fabrication and integration of nanoscale fluidic features, which can be either nanoporous membrane or nanochannels.

#### *Some examples of nanochannel-based preconcentrators*

The first silicon preconcentrator device with planar silicon nanochannels as junctions was built using standard photolithography and reactive ion etching (RIE) on silicon wafers, followed by

wafer bonding to seal the microfluidic channels (see Figs. 3-19a and 3-19b)<sup>61</sup>. The electrokinetic trapping and collection could be maintained for several hours and concentration factors as high as  $10^6$ - $10^8$  have been demonstrated.

To increase the ion flux and device trapping efficiency, a fabrication strategy has recently been developed that enables building multiple high-aspect-ratio vertical nanochannels with a width of  $\sim 50$  nm at a depth of  $\sim 40$   $\mu\text{m}$ , shown in Figs. 3-19c and 3-19d. These can be realized by combination of deep reactive ion etching (DRIE) and subsequent thermal oxidation<sup>62</sup>.

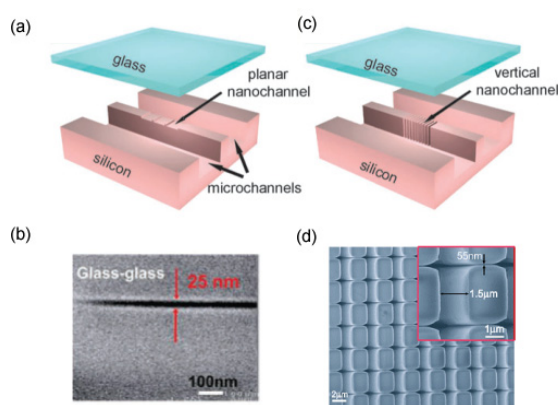


Figure 3-19: (a) Schematic design of preconcentrator with planar nanochannel<sup>60</sup>, (b) SEM photograph of etched planar nanochannel<sup>63</sup>, (c) schematic design of preconcentrator with vertical nanochannel<sup>60</sup> and (d) SEM photograph of vertical nanochannel<sup>62</sup>.

However, from the aspect of commercialization or affordability, nanochannel in Si is less suited for mass production. Hence, S. Chung *et al.*<sup>64</sup> were able to adopt the wrinkle formation method on PDMS by oxygen plasma treatment and pre-stress releasing. A sinusoidal wrinkle pattern exhibited nanometer-scale dimensions with surface changes between 50–600 nm and periods between 100–3500 nm. By applying a high voltage ( $>1000$  V) between two closely adjacent microchannels, nanogaps were formed between the microchannels via electrical breakdown, as has been demonstrated by J.H. Lee *et al.*<sup>65</sup>. By using such device, the concentration factor of 70 pL  $\beta$ -phycoerythrin proteins can be as high as  $10^4$  within 1 h. Such technology was also used by H. Yu *et al.* to form nanofissures, but on a different material, poly ethylene terephthalate (PET)<sup>66</sup>.

By reversibly bonding PDMS to a glass substrate, S.M. Kim *et al.* fabricated a really simple preconcentration device<sup>67</sup>. The nanojunction formed between PDMS and glass played a charge-selective role, enabling trapping charged biomolecules efficiently under an applied electric field with a concentration factor up to  $10^3$ - $10^6$ . The mechanism and one fluorescent image are shown in Figs. 3-20a and 3-20b, respectively.

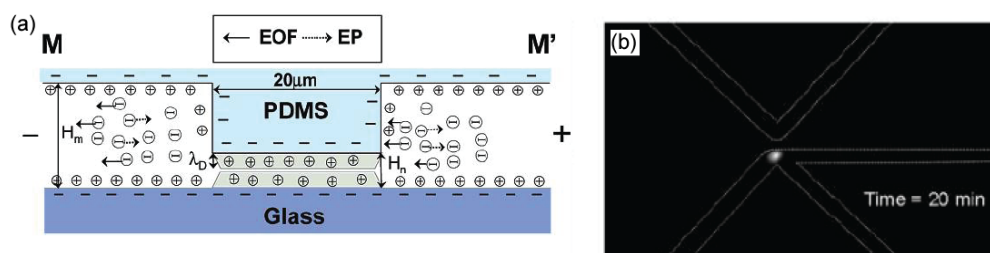


Figure 3-20: (a) Electrokinetic preconcentration mechanism based on a nanojunction formed by reversible bonding between PDMS and glass. (b) The fluorescence image of 10 nM pre-concentrated BSA after being subjected 20 min to 200 V within anodic channel, with the cathodic channel connected to ground<sup>67</sup>.

### Some examples of nanoporous membrane based preconcentrators

Instead of fabricating nanochannels in between two microchannels, one can use variety of microtechnologies to integrate a nanoporous membrane into the preconcentrator as ion-permselective medium.

Nafion, either as a membrane or a resin, allows achieving a good ion-selectivity and was successfully patterned on a glass substrate via microflow patterning or stamping (see Fig. 3-21a)<sup>68</sup>. A PDMS preconcentration device with an integrated ion-selective Nafion membrane is shown in Fig. 3-21b. Utilizing this concentrator chip, one could achieve a concentration volume of  $\beta$ -phycoerythrin of 200 pL with a concentration factor as high as  $\sim 10^5$  within 20 min. As suggested by Y.A. Song *et al.*<sup>57</sup>, one can also pattern the junction lithographically and fill it with microbeads and infiltrate Nafion resin into the solid bead matrix which allows realization of a robust perm-selective membrane.

S. Song *et al.*<sup>69</sup> used laser-patterning of nanoporous zwitterionic polymer membranes at the junction of a cross channel in a microchip to integrate protein concentration with an electrokinetic injection scheme. Local and spatially averaged concentration is increased by 4 and 2 orders of magnitude, respectively, upon injection with voltages (70-150 V) and concentration times of 100 s.

A negatively charged hydrogel microplug was incorporated into a microchannel by photopolymerization of an appropriate hydrogel precursor. It served as a nanoporous membrane, determining the electrokinetic behavior between the adjoining microchannel compartments and resulted in an efficient preconcentrator, as described in different research articles of R. Dhopeswarkar *et al.*<sup>70</sup> and A.V. Hatch *et al.*<sup>71</sup>. The recent progress made by P. Kim *et al.* proved again the feasibility of this method and of the heterogeneous nanojunctions<sup>72</sup>.

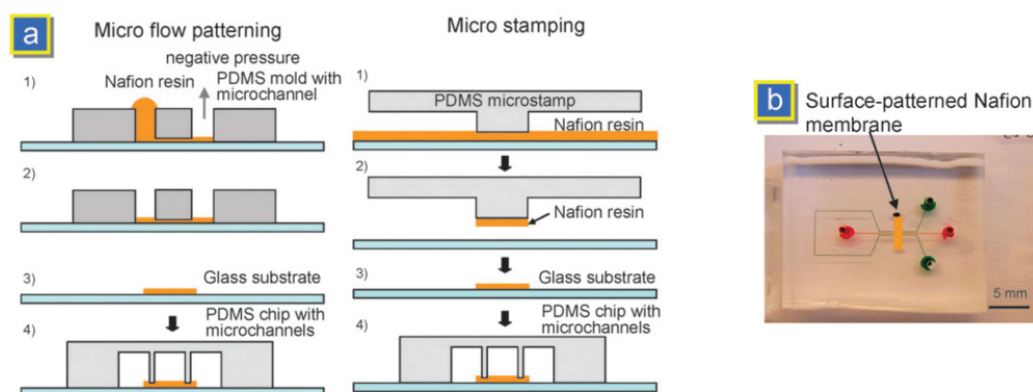


Figure 3-21: (a) Schematic of the micro-flow patterning and micro contact printing techniques used to pattern a planar Nafion membrane on a glass substrate. (b) PDMS preconcentrator with integrated surface-patterned ion-permeable membrane<sup>68</sup>.

Besides photopolymerization technology, K.W. Hoeman *et al.* developed an analyte preconcentration device using a porous titania membrane fabricated via sol-gel chemistry as nanojunction between two glass microchannels<sup>73</sup>.

### 3.3.3 Literature review on modeling of preconcentrator devices

#### *Some examples of CP modeling*

Detailed modeling of the CP effect in molecular concentration devices has not yet been achieved due to the numerous technical challenges. However, some achievements have been already made in the field of nonlinear kinetics near a permselective medium for providing insight into the preconcentrator behavior<sup>60</sup>.

I. Rubinstein *et al.* did quite pioneering work in this field, regarding convection induced by non-equilibrium electro-osmosis in front of an ion exchange membrane in the course of concentration polarization under the passage of electrical current through the membrane<sup>74, 75</sup>. X.Z. Jin *et al.* conducted a two-dimensional simulation based on the Poisson, Nernst-Planck and Navier-Stokes equations for a hybrid micro-nanofluidic device<sup>76</sup>. Not only the CP effect was computed at the two of micro-nanochannel junctions (as indicated in Fig. 3-22a), but also the nonlinear kinetic flow due to the net space charge in the depletion zone was disclosed numerically (see Fig. 3-22b). It forms excellent theoretical basis for using such device for biomolecule preconcentration.

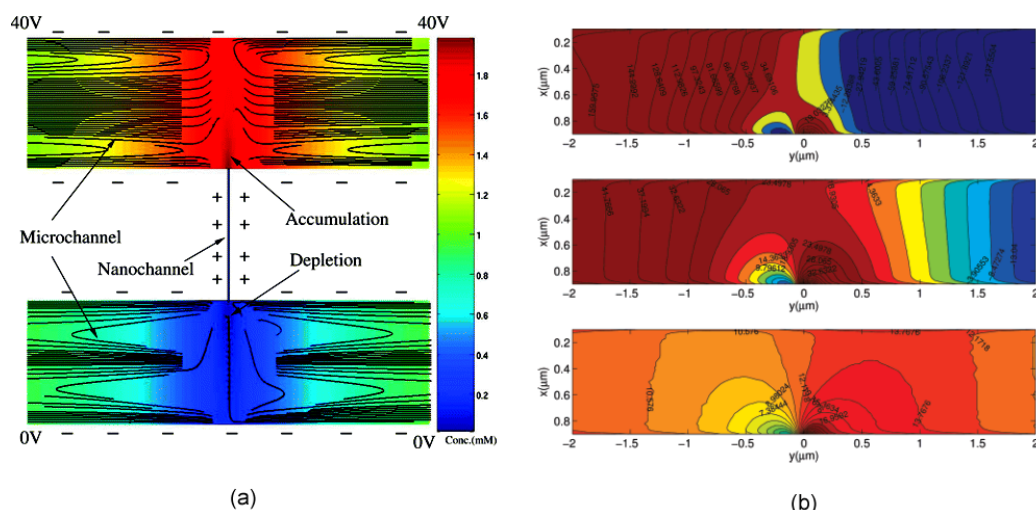


Figure 3-22: (a) Depletion and accumulation at nano-microchannel junctions under application of an external applied potential of 40 V at the anodic channel and ground potential at the cathodic channel. (b) The net space charge in the depletion region within the lower microchannel (Top: at  $t = 26$  ms; Middle: at  $t = 30$  ms; Bottom: at  $t = 45$  ms)<sup>76</sup>.

Similar simulation results were also achieved by K.D. Huang *et al.*, for microchannels connected by a cross-form microchip, in which the two side channels were attached to the main channel via a nanochannel bridge<sup>77</sup>.

#### Some examples of preconcentration modeling

Based on these exciting progresses made in understanding the CP effect at a nano-microchannel junction, some research groups took further steps towards full simulations of some preconcentrator devices.

A. Plecis *et al.* pointed out that the competition between electroosmotic dragging force and the highly nonlinear electrophoretic force induced by the CP effect was responsible for four preconcentration regimes that can arise at both anodic and cathodic side of the nanochannel<sup>78</sup>. Similar work on a single nanochannel preconcentration model has been conducted by Y. Wang *et al.*, who demonstrated the possibility of direct use of the Navier-Stokes equation without any approximation, like taking a limited-thin-EDL<sup>79</sup>.

Though single nanochannel model is sufficient to explain the preconcentration mechanism, it always fails to describe the real systems which are normally tens of micrometer in size. R. Dhopeswarkar *et al.*<sup>70</sup> reported a one-dimensional model for a preconcentration device using a set of coupled Poisson, Nernst-Planck and Navier-Stokes equations. In this model, the whole porous membrane was described as a medium with fixed volume charge concentration. By simplifying the EOF in the microchannels with Helmholtz-Smoluchowski velocity slip at the wall, they were able to numerically solve the non-trivial spatiotemporal behavior of ions and



biomolecules. However, this model was confined only to explain the concentration occurs at the cathodic porous membrane-microchannel interface, where EOF had only a side effect on preconcentration.

Further work from the same group has been published recently, and it built a model for electrical field gradient focusing in the anodic microchannel segment using an embedded bipolar electrode in the microchannel instead of a permselective membrane<sup>80</sup>.

### 3.3.4 Applications of preconcentrator devices

Traditional amplification methods improve the sensitivity of assays by increasing the signal generated after the initial binding reactions. The electrokinetic preconcentrator can provide an efficient tool to enhance the initial-binding simply by increasing the concentration of low-abundance analytes.

The first application of the nanofluidic preconcentrator as an enhancing tool for the immunoassay has been demonstrated with a bead-based assay<sup>81</sup>. First, the surface-functionalized microbeads were captured in front of the nanochannels. Afterwards, the sample molecules were concentrated on the antibody-immobilized beads, thus enhancing the immuno reaction. The steps of immunoassay are shown in Fig. 3-23a. With a 30 min preconcentration time, the authors were able to enhance the immunoassay sensitivity (with molecular background) more than 500 fold, decreasing the limit of detection from the higher 50 pM to the sub 100 fM range. As indicated in Fig. 3-23b, they could switch the range of the given bead-based assay (from 10–10 000 ng/ml to 0.01–10 000 ng/ml) to have a broader dynamic range of detection.

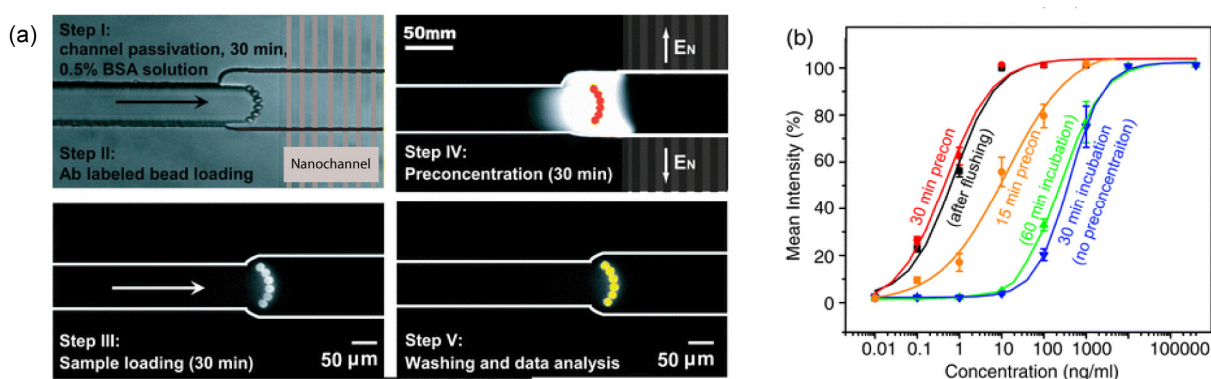


Figure 3-23: (a) Integration of a bead-based assay in a nanofluidic preconcentrator. Beads are trapped in front of the nanochannels. (b) Immunosensing without and with preconcentration in a nanofluidic bead-based assay<sup>81</sup>.

Other applications of preconcentration devices like enhancing enzyme-based assays<sup>82</sup> and sample prefractionation<sup>83</sup> were demonstrated in recent publications from Prof. J. Han's group, respectively. Detailed information can also be found in a review article by S.J. Kim *et al.*<sup>60</sup>. A more



astonishing recent advancement, realized by the same group, is a small scale seawater desalination system using the ion concentration polarization principle<sup>84</sup>.

### 3.3.5 Conclusion

The literature review of the preconcentration mechanism, the way the devices were fabricated as well as their modeling based on coupling mass-charge transfer equations, enabled us accumulating a wide knowledge of the preconcentration phenomena.

With respect to rapid-prototyping, in our own work, a Nafion strip shaped via cutting technology from commercial membrane instead of expensive fabrication of nanochannels or porous membranes will be selected as ion permselective medium for generating CP under an applied electrical field.

## 3.4 Rapid prototyping technologies for microfluidic devices

Despite the current enthusiasm for microfluidics, the generally arduous fabrication procedures required to fabricate these devices have limited the technology often to research groups with access to well-equipped clean-room facilities. In terms of microfabrication, the functional device should be characterized by the following desirable properties:

- Ease of manufacturing
- Appropriate microfabrication technology for various geometries
- Low substrate cost
- Short fabrication cycle

The aim of this section is to investigate the rapid prototyping microtechnologies used for realization of microfluidic components: embossing, injection molding, molding and cutting using different base materials (like PMMA, PDMS, glass, polymeric membrane).

### 3.4.1 Rapid prototyping of plastics

#### *Hot Embossing*

Hot embossing in combination with a polymer substrate, mainly PMMA and poly(carbonate) (PC), fulfills most of the criteria listed above for device fabrication and has been used in the manufacturing of the polymer micro-components described below<sup>85</sup>.

The process itself consists of the following steps<sup>85</sup>, as shown in Fig. 3-24: (a) The polymer substrate is placed and heated in vacuum to a temperature just above the glass transition temperature. (b) The master structure (normally either silicon or metal) is also heated to the same (or slightly higher) temperature. (c) The master structure is pressed into the polymer substrate with a force of typically 500 N/cm<sup>2</sup> in the case of PMMA. (d) Master and substrate are

isothermally cooled to a temperature just below  $T_g$  and then demolded.

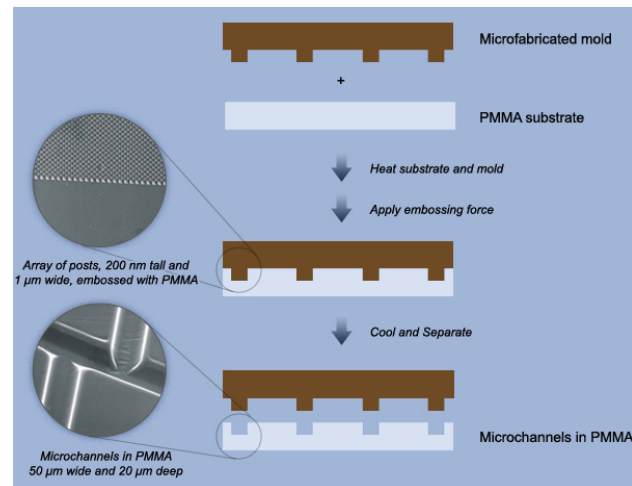


Figure 3-24: Schematic of a hot embossing process<sup>86</sup>.

Some microfluidic components have been embossed in PMMA substrates, for example, the technique was used to realize valveless micropumps, as demonstrated by A. Olsson *et al.*<sup>87</sup>. The technology has also been adopted to form the tapered microchannel in micro-DMFC to realize pumping function, as demonstrated by N. Paust *et al.*<sup>88</sup>. Based on silicon nanotechnology, some groups were able to pattern sub hundred nanometer deep channels onto a PMMA substrate via hot embossing which offered a quite simply way to realize nanochannels in batch<sup>89</sup>, and the technique also provides the possibility to integrate such nanochannels into PMMA-based preconcentration devices.

### **Injection molding**

Injection molding is one of the most commonly used processes in industry to form a variety of everyday objects. Briefly, prepolymerized pellets of thermoplastic are melted and injected under high pressure into a heated molding cavity (as illustrated in Fig. 3-25a)<sup>90</sup>. A full plastic commercially available micropump (*IMM thinXXS XXS2000*) invented by Thin XXS microtechnology AG appeared on the market, aiming microfluidic applications like precise dosing, etc<sup>91</sup>.

The disadvantages of this technique are the need for an often mechanically complicated molding tool which is capable withstanding high temperatures and forces while retaining the highest mechanical precision. Moreover, as the material undergoes a phase change in the process, internal stresses, shrinkage and birefringence are always big issues when molding microsystems with small feature size <sup>90</sup>.

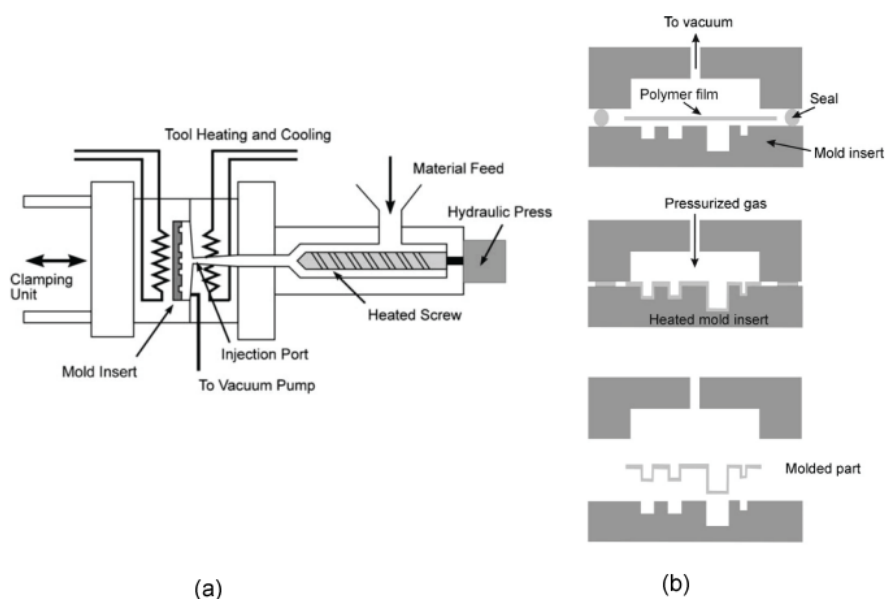


Figure 3-25: (a) Cross-sectional view of an injection molding machine<sup>90</sup>. (b) Diagram of the micro thermoforming process<sup>85</sup>.

### Micro thermoforming

Some recent developments on plastic microfabrication are related to micro thermoforming technology, inspired by industrial mass production techniques for thin-wall plastic devices like yoghurt cups<sup>85</sup>. As depicted in Fig. 3-25b, a thin polymer foil (typically  $\leq 50 \mu\text{m}$ ) is clamped in a mold tool. Subsequently, the foil is heated up to approximately  $10 \text{ }^\circ\text{C}$  above  $T_g$  and pressed into the microstructured master at 40–60 bar. The polymer then is cooled down to  $20 \text{ }^\circ\text{C}$  below  $T_g$  and the part is demolded. S. Giselbrecht *et al.*<sup>92</sup> put forward a tissue culture platform based on micro-thermoforming technology on Polyester or PC films. The feasibility of microfabrication of thin PMMA layers using this novel method was also proven.

### Other techniques

Some other methods of rapid prototyping of plastic microfluidic devices are: laser ablation, precise mechanical machining, and powder blasting. For the first two techniques, the examples have already been demonstrated and details can be found in a review article by H. Becker *et al.*<sup>85</sup>. Complete description and application of powder blasting will be presented in Chapter 4, since it is the technology we have chosen for constructing two types of micropumps.

### 3.4.2 Elastomeric material molding

So far, the most widely published technology for microstructuring elastomeric material for microfluidic devices is casting. Polydimethylsiloxane (PDMS) is a well-known elastomeric material used extensively for biochips due to its biocompatible and disposable properties. Once a master is

obtained via either clean room-based soft lithography or simply traditional precision machining, the typical process flow (see Fig. 3-26) results in elastomeric structures with high accuracy<sup>93</sup>.

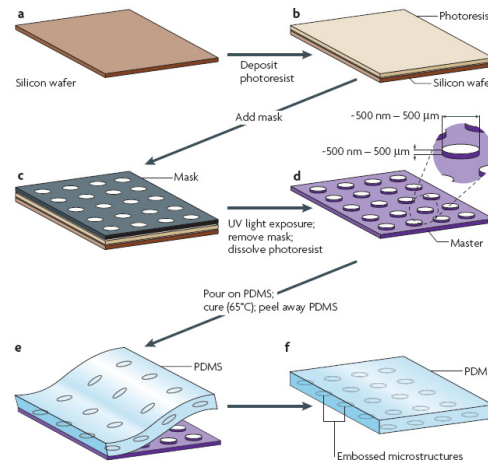


Figure 3-26: The process flow of forming PDMS microstructures<sup>93</sup>.

A mixture of prepolymer and its polymerizing curing agent is then poured over the master and cured at room temperature in about 48 hours or at elevated temperatures, e.g. 30 min at 115 °C. The curing temperature and ratio of the curing agent to the prepolymer concentration determine the stiffness of the elastomeric sheet, which can thus be easily adjusted depending on various applications. After curing, the elastomer sheet is simply peeled away from the master.

Some microfluidic components made from PDMS are of particular interests here. For example, to fulfill the self-priming capacities for our reciprocating micropump, PDMS with its low young's module is a good candidate for realizing the pumping membrane<sup>29, 94</sup>. Multilayer soft lithography was employed to fabricate valves and pumps on PDMS with large deformability<sup>29</sup>. The thickness of the membrane can be easily varied by the spincoating method or by varying of the mold.

Other efforts have been made to integrate some rigid components into a PDMS membrane instead of gluing or adhesive bonding. T. Pan *et al* proposed a full PDMS micropump by simply molding a magnet into a membrane and by placing the micro balls as check valves into microchannels, respectively<sup>12</sup>. Also a planar coil has been embedded into a membrane with a permanent magnet placed externally for forming the electromagnetic actuator system<sup>95</sup>.

Since PDMS exhibits good resistance to most chemicals<sup>96</sup>, some groups molded micro fuel cell channel plates from it, instead of doing complex clean room processing of silicon<sup>97</sup>.

Biocompatibility is one of the most attractive properties of PDMS, thanks to which, this casting technology plays a significant role in bio-microfluidic chip realization by considerably reducing the complexity and time cycle that is involved in fabrication. For example, as proposed by J.H. Lee *et al*, PDMS/glass hybrid preconcentrator devices gave rise to high-efficiency concentration for charged

biomolecules, thanks to the easily moldable PDMS that moreover can simply accommodate additional microfabrication steps like surface patterning of Nafion<sup>68</sup>.

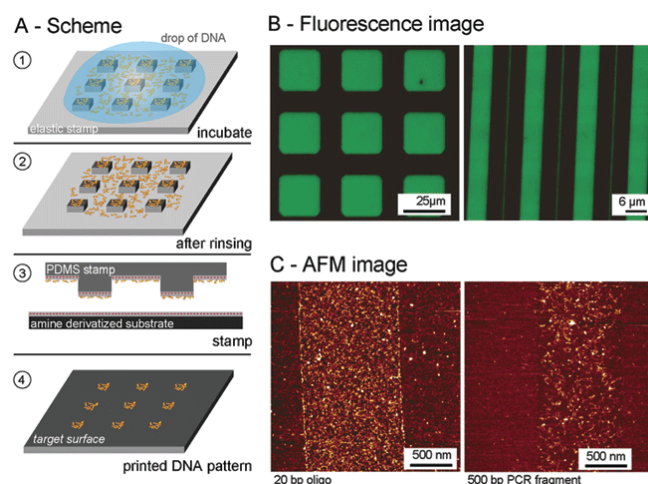


Figure 3-27: Microcontact printing of DNA molecules. (A) Scheme of DNA printing. (B) Fluorescence images of patterned fluorescein (FITC)-labeled oligonucleotides on a glass surface after printing. (C) AFM images revealing the printed DNA molecules deposited as patterns on mica substrates<sup>98</sup>.

When complete disposable bio-microarrays (DNA, cell, protein) are envisaged, PDMS is always chosen prior to the other kind of substrates<sup>99</sup>. In this case, after the normal fabrication process, as illustrated in Fig. 3-26, microstructures in PDMS formed elastomeric stamps to transfer layers of biomolecules onto the target substrate (see Fig. 3-27)<sup>98</sup>.

### 3.4.3 Rapid microstructuring of glass

Due to its beneficial optical properties, surface stability and solvent compatibility, glass has huge application for realization of microfluidic devices. However, since microfabrication techniques for glass are typically clean-room based like wet and dry etching, photolithography, electron beam lithography, etc, the high cost will likely limit the usage of glass for disposable devices.

Aiming for low-cost, rapid prototypable microfluidic devices made of glass, some developments have been achieved to simplify glass microfabrication towards the level of common laboratory techniques.

#### *Simplified masking*

By avoiding the use of thin metal layer as mask, S.I. Fujii *et al.*<sup>100</sup> developed a method for microstructuring on a glass plate via photolithography using a high-viscosity photoresist as an etching mask, followed by etching using 15% ammonium hydrogenfluoride solution at 30 °C.

A toner-mediated lithographic technology for rapid prototyping of glass microchannels has

been developed by the Laboratory of Microfabrication at Brazilian Synchrotron Light Laboratory (LNLS)<sup>101</sup>. The microfabrication technology can be divided into three sub-steps: i) preparation of toner masks by a direct-printing process on wax paper and thermal transfer onto the glass surface; ii) wet chemical etching using hydrofluoric acid solution; and iii) bonding the glass plates via a thermal process.

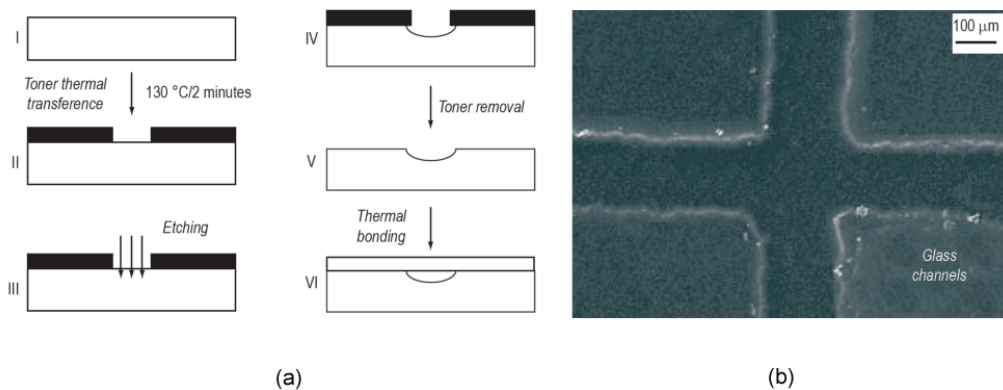


Figure 3-28: (a) Toner-mediated microfabrication process. (b) A micrograph of the cross intersection of the resulting device<sup>101</sup>.

Fig. 3-28a depicts the technology and the etched microchannels are shown in Fig. 3-28b. It shows that the channel wall did not present a perfect definition due to the low resolution of the laser printer and the thermal transfer step. This device was successfully used for electrophoretic separation.

### Rapid etching methods

When the requirement of less processing time for microstructuring a glass substrate dominates over the achievement of the micro-scale precision, laser ablation and powder blasting are advantageous with respect to traditional wet and dry etching.

*Laser ablation* involves the use of a pulsed laser to remove the material from a glass substrate. The shape of the etched channel is determined by whether or not a mask is utilized during processing and the roughness is dependent on the parameters (like pulse energy, pulse duration etc.) of the laser used. More detailed analysis can be found in the article by D.M. Karnakis *et al.*<sup>102</sup>.

*Powder blasting* is a powerful technology using micro-scaled abrasive powders which are accelerated by compressed air to a nozzle, enabling rapid prototyping of glass substrates with a precision of tens of microns in a short time. The masks used for this process can be metal, photosensitive polymer or PDMS, depending on the feature size required by different applications.



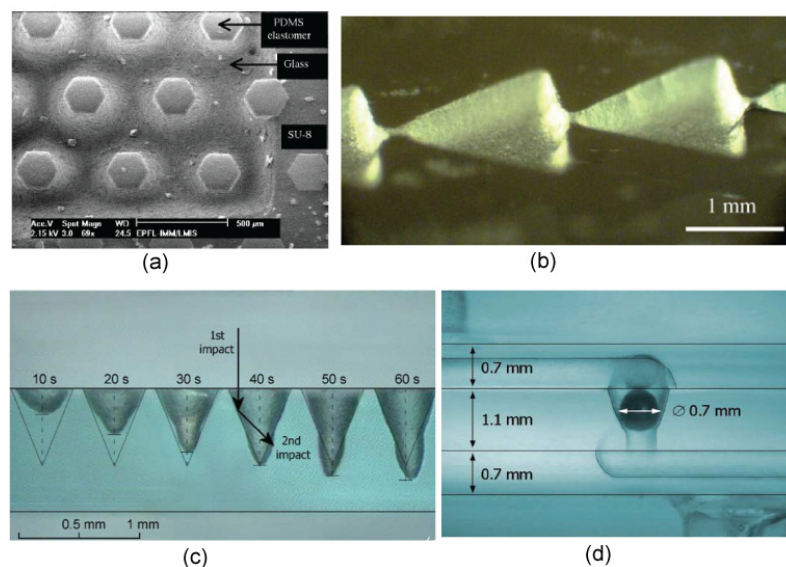


Figure 3-29: (a) SEM photograph of a glass wafer covered with PDMS masking structures after powder blasting<sup>103</sup>. (b) Photograph of a powder blasted 3 dimensional mixer<sup>104</sup>. (c) Evolution of the powder blasting erosion profile of a hole in glass materia <sup>105</sup>. (d) Photograph of an integrated ball valve<sup>105</sup>.

For example, as shown in Fig. 3-29a, the thickness and the resolution of a PDMS mask are those imposed by a primary SU-8 mould<sup>103</sup>. As SU-8 photolithography allows processing of thick and high-aspect ratio structures, complimentary PDMS masks with similar properties can be realized. Thanks to the brittleness of SU8, it can be quite easily removed by powder blasting and leaves the glass surface underneath ready to be etched. As mentioned before, this technology has been widely used in our laboratory to realize numerous microfluidic components like mixers<sup>104</sup> (Fig. 3-29b), micropumps<sup>105</sup> (Figs. 3-29c and 3-29d), ferrite cores, electrophoresis chip etc.

In chapter 4, we will systematically describe the setup and procedure of powder blasting as well as the erosion mechanism.

### 3.4.4 Simplified cutting technology

Low-cost and rapid prototyping strategy rely on certain flexible technologies, which can be easily realized by tools available in daily life. Simple cutting methods usually comprise the use of a direct single razor blade or a programmable plotter cutter.

#### Razor blade

Knife, an extremely common tool, after certain treatment, is able to be exploited in microfabrication processes. First, the simplest way is to cut directly using a paper cutter or razor blade without any automation. This technology was adjusted to PDMS and has been successfully adopted for realization of preconcentration devices by S.J. Kim *et al.* An ion-permselective membrane was formed by guiding a droplet of Nafion solution into the cut microchannel (as

illustrated in Fig. 3-30a)<sup>106</sup>.

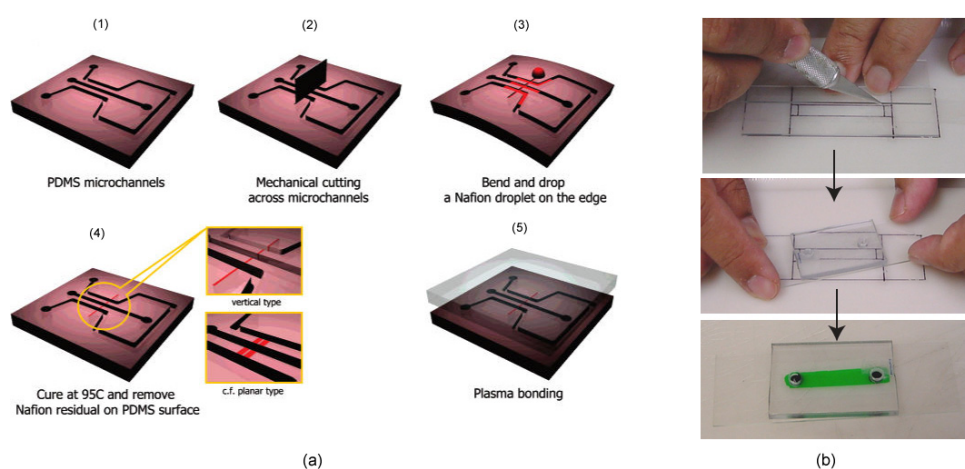


Figure 3-30: (a) The fabrication process of a preconcentration device by cutting a PDMS channel to accommodate a self-sealing Nafion membrane<sup>106</sup>. (b) Fabrication of a fluidic channel using double-side tape and sharp blade<sup>107</sup>.

R. Kumar *et al.* presented a modification of this method using 3M double-sided adhesive tape and heat-curing using an inexpensive heat press<sup>107</sup>. The resulting devices had a uniform height of  $\sim 80$  micrometers. Only a cut border and a sharp razor blade were required in this rapid process, as seen in Fig. 3-30b. Since this technology is cost-effective and can be done in any general laboratory, it becomes an interesting option for realization of disposable microfluidic devices if the feature size is hundreds of micrometers.

### Xurography

Xurography using double-sided adhesive tape is an effective and reliable prototyping alternative to traditional clean room processes<sup>108</sup>. By utilizing a cutting/knife plotter together with geometrical design offered by any CAD software, the unwanted portions of the polymers can be removed and the remaining polymer is placed on a substrate for use. Using polymers with adhesives on both sides allows for rapid bonding and sealing. Another appealing characteristic of xurography is its dimensional accuracy of  $10 \mu\text{m}$  with feature variability down to  $2 \mu\text{m}$ . It was first used for forming microstructures in 2005 by D.A. Bartholomeusz *et al.*, who gave detailed information about material and cutting plotter settings<sup>108</sup>.

In order to adapt this straightforward technology into a standard PDMS microfluidic device fabrication flow, PDMS/tape composites were created by spinning a thin layer of PDMS over double-sided adhesive tape<sup>109</sup>. Then the PDMS/tape composite was patterned to create channels using xurography, and bonded to a PDMS slab. After removing the backing paper from the tape, a complete microfluidic system could be created by placing the construct onto nearly any substrate,



including glass, plastic or metal-coated glass/silicon substrates. The process flow and microscopy graph of microfluidic channel are described in Figs. 3-31a and 3-31b, respectively.

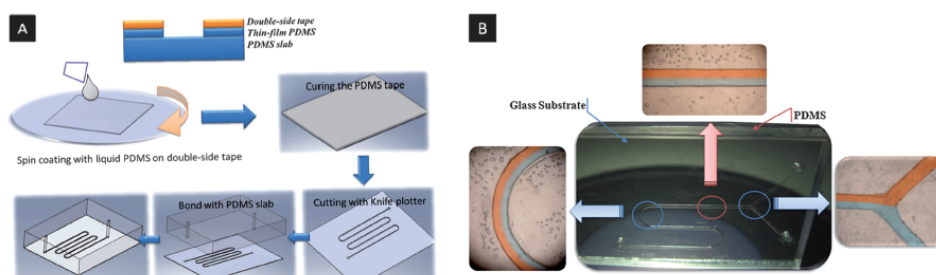


Figure 3-31: (a) Process steps for the rapid prototyping of microfluidic structures using a PDMS/polymer tape composite. (b) The microfluidic channel fabricated using the PDMS/polymer tape composite method was tested with blue and orange dye to show the functionality of the microfluidic device. (Channel width  $400\mu\text{m}$ .)<sup>109</sup>.

### 3.4.5 Bonding technology

A final but critical step in fabricating microfluidic devices is bonding, which not only determines the lifetime but also affects the devices performance and reproducibility. Microfluidic bonding techniques are categorized into indirect bonding and direct bonding. The former involves the use of an intermediate layer as adhesive to seal two substrates and this layer should be as thin as possible to ensure the minimum influence on the device's performance. In contrast, direct bonding mates two substrates without requiring an additional interface in between<sup>110</sup>. In order to facilitate disposable applications and overcome the difficulties when some substrates are less adapted to the bonding process, reversible bonding becomes popular in assembly of microfluidic devices. Here we explore a range of bonding techniques, which are relevant to this thesis.

#### Adhesive bonding

*PDMS thin layer as adhesive* is quite useful not only for PDMS-PDMS bonding, but also for glass-PDMS bonding. As illustrated in Fig. 3-32, bonding microfluidic channels of two representative soft materials (PDMS substrate on a PDMS plate) is simply realized using an adhesive PDMS layer<sup>111</sup>. The bond strength for the integrate unit can be as high as 400 kPa (with cross-sectional view of the bonded channel shown in the right-lower part of Fig. 3-32). Later on, using this novel PDMS interface, W.W.Y. Chow *et al.*<sup>112</sup> were able to irreversibly bond two PMMA plates without introducing any non-biocompatible material as adhesive.

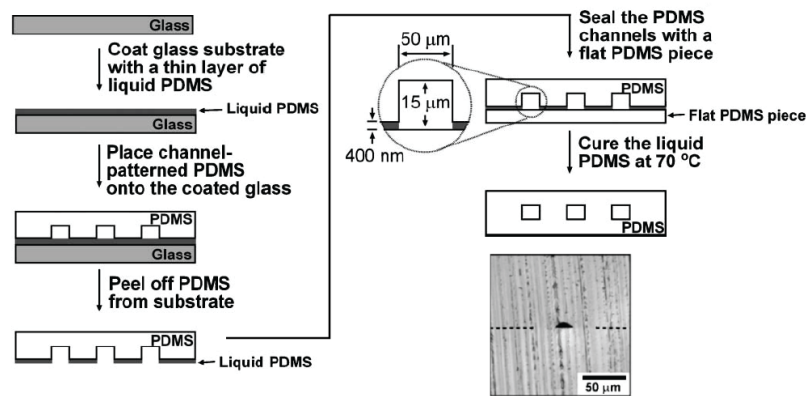


Figure 3-32: Schematic illustration of the bonding procedure with a thin gluing layer of PDMS prepolymer. The inset shows the bonded microfluidic channel<sup>111</sup>.

*Double side adhesive tape* offers a flexible method for realizing microfluidic chips without any bonding facilities, however, these adhesive layers should be already patterned before use. Xurography becomes a good option for transferring microstructures onto adhesives, a technology that was described in detail in the section before.

### **Fusion bonding**

During thermal bonding, substrates are heated to a temperature near or above the  $T_g$  of one or both of the substrate materials, while applying a pressure to increase mating contact forces. Since this fusion bonding technology is widely used for various substrates, including glass, silicon as well as thermoplastics and was also well developed in our lab by D. Solignac *et al.*<sup>113</sup>, it is a technology used in glass/glass bonding for constructing active-valve micropumps. Successful examples of applying this technology for micropump realization was demonstrated by C. Yamahata *et al.*<sup>105, 114</sup>.

### **Solvent bonding**

Some researchers proposed solvent bonding, since it provides relatively strong bonding, without introducing any additional adhesive material. When a thermoplastic surface is partially dissolved, polymer chains become mobile and can readily diffuse across the solvated layer, leading to extensive intertwining of chains between the surfaces and resulting in exceptionally strong bonds. However, care should be taken because the microchannels can also be destroyed by the solvent<sup>115</sup>.

### **Reversible bonding**

In some particular cases, when the microfluidic substrates are bio-functionalized, or consist of versatile materials with different surface properties, it becomes very challenging to apply traditional rapid irreversible bonding methods to assemble the chip. Here, reversible bonding

offers an appropriate solution, which usually requires an external mechanical clamping setup in order to prevent any leakage.

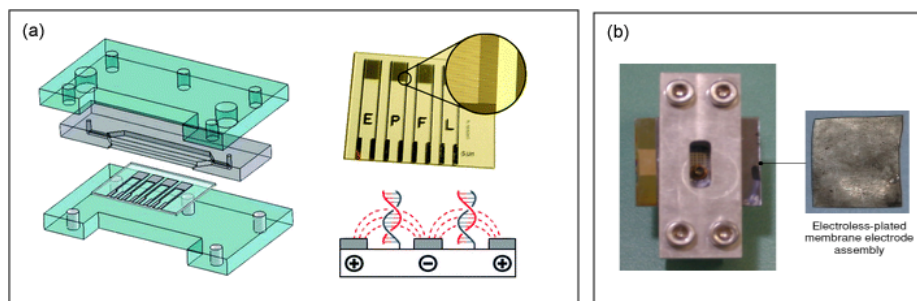


Figure 3-33: (a) Schematic diagram of a glass biochip mounted in its microfluidic package clamped by top and bottom PMMA slides (left), Biochip with 4 interdigitated micro-electrode sensors (upper right) and schematic of biochip working principle (lower right) <sup>116</sup>. (b) Prototyped single fuel cell with MEA that is mechanically assembled <sup>117</sup>.

D. Berdat *et al.*<sup>116</sup> investigated the analytical performance of an interdigitated electrode sensor for the label-free detection of DNA, by monitoring the complex impedance of 5  $\mu\text{m}$  wide interdigitated Pt microelectrodes on a glass substrate. They reported that the mechanical fixation for assembly of a PDMS microfluidic substrate and a functionalized glass substrate was preferred over oxygen plasma bonding that could destroy the biological DNA probe layer on the sensor surface (see Fig. 3-33a). Furthermore, B. Song *et al.*<sup>118</sup> demonstrated reversible clamping can effectively incorporate and seal a piece of tissue into a microfluidic device.

The concept is also extensively used for assembly of micro fuel cells, since MEA is an inert material and its thermal bonding to fragile silicon or glass substrates is less reliable, even at high pressure. Reversible bonding enables not only leakage-free properties but also easy replacement of degraded MEA after long time use, as indicated in Fig. 3-33b<sup>52, 117</sup>.

### 3.4.6 Conclusion

In this section, the systematic classification of rapid prototyping technologies in microfluidic devices fabrication has been presented. Of particular interest for this thesis, rapid microstructuring techniques of PMMA, PDMS, and glass have been elaborately described in combination with the-state-of-the-art. Taking up and modifying some rapid prototyping methods, we are able to pattern our PMMA and glass slides for micropump realization and to use a molded PDMS layer as actuation membrane (Details can be found in Chapter 5 and Chapter 6). As a popular and simple microfabrication method illustrated in literature, cutting plays a crucial role in forming the Nafion strip for our fuel cell (Chapter 7) and preconcentration (Chapter 8) devices. Finally, a variety of rapid bonding techniques have been listed, which are the key for the stability of whole microfluidic

device.

## References

1. Nguyen, N.-T.; Huang, X.; Chuan, T. K., MEMS-Micropumps: A Review. *Journal of Fluids Engineering* 2002, *124*, 384-392.
2. Laser, D. J.; Santiago, J. G., A review of micropumps. *Journal of Micromechanics and Microengineering* 2004, *14*, R35.
3. Gilbertson, R.G.; Busch, J.D., A survey of micro-actuators technologies for future spacecraft missions. *The Journal of the British Interplanetary Society* 1996, *49*, 129-138.
4. Lee C.-Y.; Chang, T.-H.; Wen, C.-Y., A MEMS-based valveless impedance pump utilizing electromagnetic actuation. *Journal of Micromechanics and Microengineering* 2008, *18*, 035044 (9pp).
5. Kim, K. H.; Yoon, H. J.; Jeong, O. C.; Yang, S. S., Fabrication and test of a micro electromagnetic actuator. *Sensors and Actuators A: Physical* 2005, *117*, 8-16.
6. Ramadan, Q.; Lau, T.; Ho, S., Magnetic-based purification system with simultaneous sample washing and concentration. *Analytical and Bioanalytical Chemistry* 396, 707-714.
7. Kwang, W. O.; Chong, H. A., A review of microvalves. *Journal of Micromechanics and Microengineering* 2006, *16*, R13-R39.
8. Bae, B.; et al., In vitro experiment of the pressure regulating valve for a glaucoma implant. *Journal of Micromechanics and Microengineering* 2003, *13*, 613-619.
9. Sato, K.; Shikida, M., An electrostatically actuated gas valve with an S-shaped film element. *Journal of Micromechanics and Microengineering* 1994, *4*, 205-209.
10. Beebe, D. J.; Moore, J. S.; Bauer, J. M.; Yu, Q.; Liu, R. H.; Devadoss, C.; Jo, B.-H., Functional hydrogel structures for autonomous flow control inside microfluidic channels. *Nature* 2000, *404*, 588-590.
11. Min, H.; Du, H.; Ling, S.F.; Fu, Y.; Chen, Q.; Chow, L.; Li, B., A silicon-on-insulator based micro check valve. *Journal of Micromechanics and Microengineering* 2004, *14*, 382-387.
12. Pan, T.; McDonald, S.; Kai, E.; Ziaie, B., A magnetically driven PDMS micropump with ball check-valves. *Journal of Micromechanics and Microengineering* 2005, *15*, 1021-1026.
13. Krutzch, W. C.; Cooper, P., Introduction: classification and selection of pumps. In *Pump Handbook*, ed. I. J. K. e., Ed. McGraw-Hill Inc.: New York, 2001.
14. Richter, M.; Linnemann, R.; Woias, P., Robust design of gas and liquid micropumps. *Sensors and Actuators A: Physical* 1998, *68*, 480-486.
15. Thomas Jr, Lyell J., (San Pedro, CA, 90731); Bessman, Samuel P., (Los Angeles, CA, 90033) Micro pump powered by piezoelectric disk benders. 1976.
16. Smits, J. G., Piezoelectric micropump with three valves working peristaltically. *Sensors and Actuators A: Physical* 1990, *21*, 203-206.
17. Van Lintel, H. T. G.; Van De Pol, F. C. M.; Bouwstra, S., A piezoelectric micropump based on micromachining of

silicon. *Sensors and Actuators* 1988, 15, 153-167.

18. Woias, P. In *Micropumps: summarizing the first two decades*, Microfluidics and BioMEMS, San Francisco, CA, USA, 2001; pp 39-52.
19. Mitchell, P., Microfluidics-downsizing large-scale biology. *Nature Biotechnology* 2001, 19, 717-721.
20. Jiang, L.; Mikkelsen, J.; Koo, J. M.; Huber, D.; Yao, S.; Zhang, L.; Zhou, P.; Maveety, J. G.; Prasher, R.; Santiago, J. G.; Kenny, T. W.; Goodson, K. E., Closed-loop electroosmotic microchannel cooling system for VLSI circuits. *IEEE Transactions on Components and Packaging Technologies* 2002, 25, 347-355.
21. Dario, P.; Croce, N.; Carrozza, M.C.; Varallo, G., A fluid handling system for a chemical microanalyzer. *Journal of Micromechanics and Microengineering* 1996, 6, 95-98.
22. Böhm, S.; Olthuis, W.; Bergveld, P., A plastic micropump constructed with conventional techniques and materials. *Sensors and Actuators A: Physical* 1999, 77, 223-228.
23. Santra, S.; Holloway, P.; Batich, C. D., Fabrication and testing of a magnetically actuated micropump. *Sensors and Actuators B: Chemical* 2002, 87, 358-364.
24. Yamahata, C.; Lotto, C.; Al-Assaf, E.; Gijs, M. A. M., A PMMA valveless micropump using electromagnetic actuation. *Microfluid. Nanofluid.* 2005, 1, 197-207.
25. Van de Pol, F.; Van Lintel, H.; Elwenspoek, M.; Fluitman, J., A thermopneumatic micropump based on micro-engineering techniques. *Sensors and Actuators A: Physical* 1990, 21, 198-202.
26. Benard, W. L.; Kahn, H.; Heuer, A. H.; Huff, M. A., Thin-film shape-memory alloy actuated micropumps. *Journal of Microelectromechanical Systems*, 1998, 7, 245-251.
27. Zengerle, R. K., S; Richter, M; Richter, A, A bidirectional silicon micropump. *17<sup>th</sup> IEEE International Conference on MEMS*, Amsterdam, Netherlands 1995, pp. 19-24.
28. Yun, K.; Cho, I.; Bu, J.; Kim, C.; Yoon, E., A surface-tension driven micropump for low-voltage and low-power operations. *Journal of Microelectromechanical Systems*, 2002, 11, 454-461.
29. Unger, M. A.; Chou, H.-P.; Thorsen, T.; Scherer, A.; Quake, S. R., Monolithic Microfabricated Valves and Pumps by Multilayer Soft Lithography. *Science* 2000, 288, 113-116.
30. Jeong, O.; Park, S.; Yang, S.; Pak, J., Fabrication of a peristaltic PDMS micropump. *Sensors and Actuators A: Physical* 2005, 123, 453-458.
31. Xie, J.; Shih, J.; Lin, Q.; Yang, B.; Tai, Y.-C., Surface micromachined electrostatically actuated micro peristaltic pump. *Lab on a Chip* 2004, 4, 495-501.
32. Goldschmidtböing, F.; Doll, A.; Heinrichs, M.; Woias, P.; Schrag, H.; Hopt, U., A generic analytical model for micro-diaphragm pumps with active valves. *Journal of Micromechanics and Microengineering* 2005, 15, 673-683.
33. Pham, M.; Nguyen, T.; Goo, N., Development of a peristaltic micropump for bio-medical applications based on mini LIPCA. *ICIUS 2007*, Bali, Indonesia 2008.
34. Pan, T.; Kai, E.; Stay, M.; Barocas, V.; Ziaie, B., A magnetically driven PDMS peristaltic micropump, *Proceedings of 26<sup>th</sup> Annual International Conference of the IEEE EMBS, San Francisco, USA*, 2004; pp 2639-2642.
35. Yobas, L.; Tang, K.-C.; Yong, S.-E.; Ong, E. K.-Z., A disposable planar peristaltic pump for lab-on-a-chip. *Lab on a Chip* 2008, 8, 660-662.

36. Kamarudin, S. K.; Daud, W. R. W.; Ho, S. L.; Hasran, U. A., Overview on the challenges and developments of micro-direct methanol fuel cells (DMFC). *Journal of Power Sources* 2007, *163*, 743-754.
37. [http://www.grc.nasa.gov/WWW/Electrochemistry/images/fuel\\_cell.jpg](http://www.grc.nasa.gov/WWW/Electrochemistry/images/fuel_cell.jpg)
38. Nam-Trung, N.; Siew Hwa, C., Micromachined polymer electrolyte membrane and direct methanol fuel cells--a review. *Journal of Micromechanics and Microengineering* 2006, *16*, R1-R12.
39. Ramani, V., Fuel cells. *Electrochemical Society Interface* 2006, 41-44.
40. Srinivasan, S., *Fuel cells: From fundamentals to applications*. Springer Verlag: 2006.
41. Cowey, K.; Green, K. J.; Mepsted, G. O.; Reeve, R., Portable and military fuel cells. *Current Opinion in Solid State and Materials Science* 2004, *8*, 367-371.
42. Kundu, A.; Jang, J. H.; Gil, J. H.; Jung, C. R.; Lee, H. R.; Kim, S. H.; Ku, B.; Oh, Y. S., Micro-fuel cells--Current development and applications. *Journal of Power Sources* 2007, *170*, 67-78.
43. Jiang, Y.; Wang, X.; Zhong, L.; Liu, L., Design, fabrication and testing of a silicon-based air-breathing micro direct methanol fuel cell. *Journal of Micromechanics and Microengineering* 2006, *16*, S233-S239.
44. O'Hayre, R.; Braithwaite, D.; Hermann, W.; Lee, S.-J.; Fabian, T.; Cha, S.-W.; Saito, Y.; Prinz, F. B., Development of portable fuel cell arrays with printed-circuit technology. *Journal of Power Sources* 2003, *124*, 459-472.
45. Cha, S. W.; O'Hayre, R.; Park, Y.-I.; Prinz, F. B., Electrochemical impedance investigation of flooding in micro-flow channels for proton exchange membrane fuel cells. *Journal of Power Sources* 2006, *161*, 138-142.
46. Ito, T.; Kimura, K.; Kunitatsu, M., Characteristics of micro DMFCs array fabricated on flexible polymeric substrate. *Electrochemistry Communications* 2006, *8*, 973-976.
47. Cha, S. W.; O'Hayre, R.; Prinz, F. B., The influence of size scale on the performance of fuel cells. *Solid State Ionics* 2004, *175*, 789-795.
48. Hahn, R.; Wagner, S.; Schmitz, A.; Reichl, H., Development of a planar micro fuel cell with thin film and micro patterning technologies. *Journal of Power Sources* 2004, *131*, 73-78.
49. Yen, T. J.; Fang, N.; Zhang, X.; Lu, G. Q.; Wang, C. Y., A micro methanol fuel cell operating at near room temperature. *Applied Physics Letters* 2003, *83*, 4056-4058.
50. Lu, G. Q.; Wang, C. Y.; Yen, T. J.; Zhang, X., Development and characterization of a silicon-based micro direct methanol fuel cell. *Electrochimica Acta* 2004, *49*, 821-828.
51. Hsieh, S. S.; Kuo, J. K.; Hwang, C. F.; Tsai, H. H., A novel design and microfabrication for a micro PEMFC. *Microsystem Technologies* 2004, *10*, 121-126.
52. Motokawa, S.; Mohamedi, M.; Momma, T.; Shoji, S.; Osaka, T., MEMS-based design and fabrication of a new concept micro direct methanol fuel cell ( $\mu$ -DMFC). *Electrochemistry Communications* 2004, *6*, 562-565.
53. Xiao, Z.; Feng, C.; Chan, P. C. H.; Hsing, I. M., Monolithically integrated planar microfuel cell arrays. *Sensors and Actuators B: Chemical* 2008, *132*, 576-586.
54. Zhang, Y.; Lu, J.; Shimano, S.; Zhou, H.; Maeda, R., Development of MEMS-based direct methanol fuel cell with high power density using nanoimprint technology. *Electrochemistry Communications* 2007, *9*, 1365-1368.
55. Liu, X.; Suo, C.; Zhang, Y.; Wang, X.; Sun, C.; Li, L.; Zhang, L., Novel modification of Nafion®117 for a MEMS-based micro direct methanol fuel cell ( DMFC). *Journal of Micromechanics and Microengineering* 2006, *16*,

S226-S232.

56. Cho, K.-Y.; Eom, J.-Y.; Jung, H.-Y.; Choi, N.-S.; Lee, Y. M.; Park, J.-K.; Choi, J.-H.; Park, K.-W.; Sung, Y.-E., Characteristics of PVdF copolymer/Nafion blend membrane for direct methanol fuel cell (DMFC). *Electrochimica Acta* 2004, *50*, 583-588.
57. Song, Y.-A.; Batista, C.; Sarpeshkar, R.; Han, J., Rapid fabrication of microfluidic polymer electrolyte membrane fuel cell in PDMS by surface patterning of perfluorinated ion-exchange resin. *Journal of Power Sources* 2008, *183*, 674-677.
58. Mitrovski, S. M.; Elliott, L. C. C.; Nuzzo, R. G., Microfluidic Devices for Energy Conversion: Planar Integration and Performance of a Passive, Fully Immersed H<sub>2</sub>-O<sub>2</sub> Fuel Cell. *Langmuir* 2004, *20*, 6974-6976.
59. Liu, S.; Pu, Q.; Gao, L.; Korzeniewski, C.; Matzke, C., From Nanochannel-Induced Proton Conduction Enhancement to a Nanochannel-Based Fuel Cell. *Nano Letters* 2005, *5*, 1389-1393.
60. Kim, S. J.; Song, Y.-A.; Han, J., Nanofluidic concentration devices for biomolecules utilizing ion concentration polarization: theory, fabrication, and applications. *Chemical Society Reviews* 39, 912-922.
61. Wang, Y.-C.; Stevens, A. L.; Han, J., Million-fold Preconcentration of Proteins and Peptides by Nanofluidic Filter. *Analytical Chemistry* 2005, *77*, 4293-4299.
62. Mao, P.; Han, J., Massively-parallel ultra-high-aspect-ratio nanochannels as mesoporous membranes. *Lab on a Chip* 2009, *9*, 586-591.
63. Mao, P.; Han, J., Fabrication and characterization of 20 nm planar nanofluidic channels by glass-glass and glass-silicon bonding. *Lab on a Chip* 2005, *5*, 837-844.
64. Chung, S.; Lee, J. H.; Moon, M.-W.; Han, J.; Kamm, R. D., Non-Lithographic Wrinkle Nanochannels for Protein Preconcentration. *Advanced Materials* 2008, *20*, 3011-3016.
65. Lee, J. H.; Chung, S.; Kim, S. J.; Han, J., Poly(dimethylsiloxane)-Based Protein Preconcentration Using a Nanogap Generated by Junction Gap Breakdown. *Analytical Chemistry* 2007, *79*, 6868-6873.
66. Yu, H.; Lu, Y.; Zhou, Y.-g.; Wang, F.-b.; He, F.-y.; Xia, X.-h., A simple, disposable microfluidic device for rapid protein concentration and purification via direct-printing. *Lab on a Chip* 2008, *8*, 1496-1501.
67. Kim, S. M.; Burns, M. A.; Hasselbrink, E. F., Electrokinetic Protein Preconcentration Using a Simple Glass/Poly(dimethylsiloxane) Microfluidic Chip. *Analytical Chemistry* 2006, *78*, 4779-4785.
68. Lee, J. H.; Song, Y.-A.; Han, J., Multiplexed proteomic sample preconcentration device using surface-patterned ion-selective membrane. *Lab on a Chip* 2008, *8*, 596-601.
69. Song, S.; Singh, A. K.; Kirby, B. J., Electrophoretic Concentration of Proteins at Laser-Patterned Nanoporous Membranes in Microchips. *Analytical Chemistry* 2004, *76*, 4589-4592.
70. Dhopeswarkar, R.; Crooks, R. M.; Hlushkou, D.; Tallarek, U., Transient Effects on Microchannel Electrokinetic Filtering with an Ion-Permeable Membrane. *Analytical Chemistry* 2008, *80*, 1039-1048.
71. Hatch, A. V.; Herr, A. E.; Throckmorton, D. J.; Brennan, J. S.; Singh, A. K., Integrated Preconcentration SDS-PAGE of Proteins in Microchips Using Photopatterned Cross-Linked Polyacrylamide Gels. *Analytical Chemistry* 2006, *78*, 4976-4984.
72. Kim, P.; Kim, S. J.; Han, J.; Suh, K. Y., Stabilization of Ion Concentration Polarization Using a Heterogeneous

Nanoporous Junction. *Nano Letters* 2009, 10, 16-23.

73. Hoeman, K. W.; Lange, J. J.; Roman, G. T.; Higgins, D. A.; Culbertson, C. T., Electrokinetic trapping using titania nanoporous membranes fabricated using sol-gel chemistry on microfluidic devices. *Electrophoresis* 2009, 30, 3160-3167.

74. Zaltzman, B.; Rubinstein, I., Electro-osmotic slip and electroconvective instability. *Journal of Fluid Mechanics* 2007, 579, 173-226.

75. Rubinstein, S.; Manukyan, G.; Staicu, A.; Rubinstein, I.; Zaltzman, B.; Lammertink, R.; Mugele, F.; Wessling, M., Direct observation of a nonequilibrium electro-osmotic instability. *Physical Review Letters* 2008, 101, 236101.

76. Jin, X.; Joseph, S.; Gatimu, E. N.; Bohn, P. W.; Aluru, N. R., Induced Electrokinetic Transport in Micro-nanofluidic Interconnect Devices. *Langmuir* 2007, 23, 13209-13222.

77. Huang, K.; Yang, R., Formation of ionic depletion/enrichment zones in a hybrid micro-/nano-channel. *Microfluid. Nanofluid.* 2008, 5, 631-638.

78. Plecis, A.; Nanteuil, C.; Haghiri-Gosnet, A.; Chen, Y., Electropreconcentration with charge-selective nanochannels. *Analytical Chemistry* 2008, 80, 9542-9550.

79. Wang, Y.; Pant, K.; Chen, Z.; Wang, G.; Diffey, W.; Ashley, P.; Sundaram, S., Numerical analysis of electrokinetic transport in micro-nanofluidic interconnect preconcentrator in hydrodynamic flow. *Microfluid. Nanofluid.* 2009, 7, 683-696.

80. Hlushkou, D.; Perdue, R.; Dhopeswarkar, R.; Crooks, R.; Tallarek, U., Electric field gradient focusing in microchannels with embedded bipolar electrode. *Lab on a Chip* 2009, 9, 1903-1913.

81. Wang, Y.-C.; Han, J., Pre-binding dynamic range and sensitivity enhancement for immuno-sensors using nanofluidic preconcentrator. *Lab on a Chip* 2008, 8, 392-394.

82. Lee, J. H.; Song, Y.-A.; Tannenbaum, S. R.; Han, J., Increase of Reaction Rate and Sensitivity of Low-Abundance Enzyme Assay Using Micro/Nanofluidic Preconcentration Chip. *Analytical Chemistry* 2008, 80, 3198-3204.

83. Song, Y.; Chan, M.; Celio, C.; Tannenbaum, S.; Wishnok, J.; Han, J., Free-Flow Zone Electrophoresis of Peptides and Proteins in PDMS Microchip for Narrow pI Range Sample Prefractionation Coupled with Mass Spectrometry. *Analytical Chemistry*, 242-247.

84. Kim, S. J.; Ko, S. H.; Kang, K. H.; Han, J., Direct seawater desalination by ion concentration polarization. *Nature Nanotechnology* 2010, 5, 297-301.

85. Becker, H.; Gärtner, C., Polymer microfabrication technologies for microfluidic systems. *Analytical and Bioanalytical Chemistry* 2008, 390, 89-111.

86. <http://www.chem.queensu.ca/people/faculty/oleschuk/research.html>

87. Olsson, A.; Larsson, O.; Holm, J.; Lundblad, L.; Ohman, O.; Stemme, G., Valve-less diffuser micropumps fabricated using thermoplastic replication. *Sensors and Actuators A: Physical* 1998, 64, 63-68.

88. Paust, N.; Litterst, C.; Metz, T.; Zengerle, R.; Koltay, P., Fully passive degassing and fuel supply in direct methanol fuel cells. *Proc. of the 21<sup>st</sup> IEEE MEMS, Tucson, USA* 2008, 34-37.

89. Abgrall, P.; Low, L.; Nguyen, N., Fabrication of planar nanofluidic channels in a thermoplastic by hot-embossing and thermal bonding. *Lab on a Chip* 2007, 7, 520-522.



90. Fiorini, G.; Chiu, D., Disposable microfluidic devices: fabrication, function, and application. *Biotechniques* 2005, *38*, 429-446.
91. [www.thinxxs.com](http://www.thinxxs.com).
92. Giselbrecht, S.; Gietzelt, T.; Gottwald, E.; Trautmann, C.; Truckenmüller, R.; Weibezahn, K.; Welle, A., 3D tissue culture substrates produced by microthermoforming of pre-processed polymer films. *Biomedical Microdevices* 2006, *8*, 191-199.
93. Weibel, D. B.; DiLuzio, W. R.; Whitesides, G. M., Microfabrication meets microbiology. *Nature Reviews Microbiology* 2007, *5*, 209-218.
94. Go, J.; Shoji, S., A disposable, dead volume-free and leak-free in-plane PDMS microvalve. *Sensors and Actuators A: Physical* 2004, *114*, 438-444.
95. Yin, H.; Huang, Y.; Fang, W.; Hsieh, J., A novel electromagnetic elastomer membrane actuator with a semi-embedded coil. *Sensors and Actuators A: Physical* 2007, *139*, 194-202.
96. Lee, J.; Park, C.; Whitesides, G., Solvent compatibility of poly (dimethylsiloxane)-based microfluidic devices. *Analytical chemistry* 2003, *75*, 6544-6554.
97. Shah, K.; Shin, W.; Besser, R., A PDMS micro proton exchange membrane fuel cell by conventional and non-conventional microfabrication techniques. *Sensors and Actuators B: Chemical* 2004, *97*, 157-167.
98. Lange, S.; Benes, V.; Kern, D.; Hörer, J.; Bernard, A., Microcontact printing of DNA molecules. *Analytical Chemistry* 2004, *76*, 1641-1647.
99. Barbulovic-Nad, I.; Lucente, M.; Sun, Y.; Zhang, M.; Wheeler, A.; Bussmann, M., Bio-microarray fabrication techniques-a review. *Critical reviews in biotechnology* 2006, *26*, 237-259.
100. Fujii, S.; Tokuyama, T.; Abo, M.; Okubo, A., Simple microfabrication method of glass plate using high-viscosity photoresist for micro analytical systems. *The Analyst* 2004, *129*, 305-308.
101. Coltro, W.; Piccin, E.; Silva, J.; Lago, C.; Carrilho, E., A toner-mediated lithographic technology for rapid prototyping of glass microchannels. *Lab on a Chip* 2007, *7*, 931-934.
102. Karnakis, D.; Knowles, M.; Alt, K.; Schlaf, M.; Snelling, H. Comparison of glass processing using high-repetition femtosecond (800 nm) and UV (255 nm) nanosecond pulsed lasers, *Proceeding of SPIE* 2005, *5718*; pp 216-227.
103. Sayah, A.; Parashar, V.; Pawłowski, A.; Gijs, M., Elastomer mask for powder blasting microfabrication. *Sensors and Actuators A: Physical* 2005, *125*, 84-90.
104. Sayah, A.; Thivolle, P.; Parashar, V.; Gijs, M., Fabrication of microfluidic mixers with varying topography in glass using the powder-blasting process. *Journal of Micromechanics and Microengineering* 2009, *19*, 085024 (8pp).
105. Yamahata, C.; Lacharme, F.; Burri, Y.; Gijs, M., A ball valve micropump in glass fabricated by powder blasting. *Sensors and Actuators B: Chemical* 2005, *110*, 1-7.
106. Kim, S.; Han, J., Self-sealed vertical polymeric nanoporous-junctions for high-throughput nanofluidic applications. *Analytical Chemistry* 2008, *80*, 3507-3511.
107. Rajan Kumar, R. L. S. a. M. G. P., Chips & Tips: A method for rapid fabrication of microfluidic devices. *Lab on a*

*Chip* Jun 30, 2009.

108. Bartholomeusz, D.; RW, B.; Andrade, J., Xurography: rapid prototyping of microstructures using a cutting plotter. *Journal of Microelectromechanical Systems* 2005, *14*, 1364-1374.

109. Kim, J.; Surapaneni, R.; Gale, B., Rapid prototyping of microfluidic systems using a PDMS/polymer tape composite. *Lab on a Chip* 2009, *9*, 1290-1293.

110. Tsao, C.; DeVoe, D., Bonding of thermoplastic polymer microfluidics. *Microfluid. Nanofluid.* 2009, *6*, 1-16.

111. Wu, H.; Huang, B.; Zare, R., Construction of microfluidic chips using polydimethylsiloxane for adhesive bonding. *Lab on a Chip* 2005, *5*, 1393-1398.

112. Chow, W.; Lei, K.; Shi, G.; Li, W.; Huang, Q., Microfluidic channel fabrication by PDMS-interface bonding. *Smart materials and structures* 2006, *15*, S112-S116.

113. Solognac, D., Glass microchips for bio-chemical analysis: technologies and applications. *PhD Thesis, Ecole Polytechnique Federale de Lausanne* 2003.

114. Yamahata, C.; Lacharme, F.; Gijs, M., Glass valveless micropump using electromagnetic actuation. *Microelectronic engineering* 2005, *78*, 132-137.

115. Ng, S.; Tjeung, R.; Wang, Z.; Lu, A.; Rodriguez, I.; de Rooij, N., Thermally activated solvent bonding of polymers. *Microsystem Technologies* 2008, *14*, 753-759.

116. Berdat, D.; Rodriguez, A.; Herrera, F.; Gijs, M., Label-free detection of DNA with interdigitated micro-electrodes in a fluidic cell. *Lab on a Chip* 2008, *8*, 302-308.

117. Min, K.; Tanaka, S.; Esashi, M., Fabrication of novel MEMS-based polymer electrolyte fuel cell architectures with catalytic electrodes supported on porous SiO<sub>2</sub>. *Journal of Micromechanics and Microengineering* 2006, *16*, 505-511.

118. Song, B.; Sivagnanam, V.; Vandevyver, C.; Hemmliä, I.; Lehr, H.; Gijs, M.; Bünzli, J., Time-resolved lanthanide luminescence for lab-on-a-chip detection of biomarkers on cancerous tissues. *Analyst* 2009, *134*, 1991-1993.

# *Chapter 4*

## **Microfabrication Technologies for Rapid Prototyping**

**Abstract:** In this chapter, we analyze three rapid prototyping methods used throughout the thesis work. First, we describe the details used in the powder blasting process for PMMA and glass chips for realization of ball-valve micropumps and active-valve micropumps, respectively. Another rapid prototyping technique for disposable devices is PDMS molding which can be utilized either for magnet-integrated membrane fabrication for realization of micropumps or for the applications of fuel cells and protein preconcentrators in the microfluidic format. In the third part, in order to realize the microfluidic direct methanol fuel cells and the biomolecule preconcentrators, we combine elastomeric material molding and rigid Nafion strip cutting, leading to a cost-effective and high-efficiency microfabrication and integration strategy. Last but not the least, different bonding methods including glass fusion bonding, PDMS-glass adhesive bonding and irreversible mechanical clamping employed in the thesis work are listed as essential steps for backend processing of the final devices.

## 4.1 Rapid prototyping I: powder blasting micro-erosion process

Powder blasting technology is a mechanical erosion of a mask-protected substrate by using a high-speed powder beam. As introduced in Chapter 3, it is extensively studied and well developed in our laboratory for diverse applications like MEMS and microfluidic devices<sup>1-5</sup>.

### 4.1.1 Experimental setup

A typical powder blasting machine consisting of several components is illustrated in Fig. 4-1a. First, the powder blaster is used to regulate the flow of abrasive powders which are accelerated by nozzle. The machine used in our laboratory is an abrasive jet machine type HP-2 from Texas Airsonics (<http://www.texasairsonics.com>). The impact of abrasive powders can be easily tuned by varying the applied pressure with the range from 1-6 bars. A dust collector is connected to the equipment in order to remove the used powders. To obtain a homogeneous exposure of the substrate, an X-Y linear translator is employed.

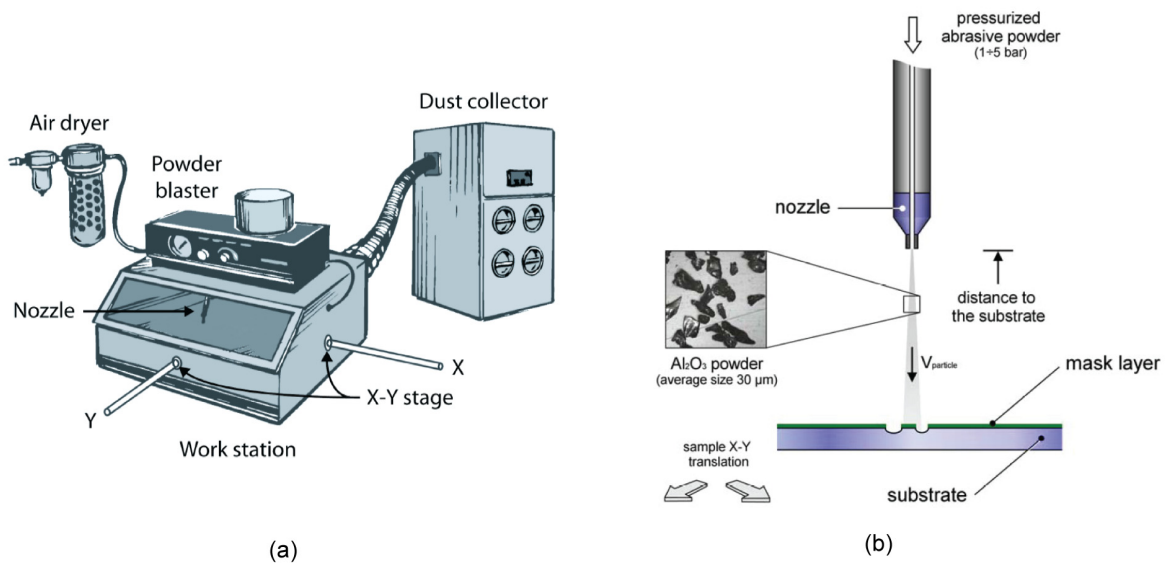


Figure 4-1: (a) A typical powder blasting system. (b) Schematic diagram of the microerosion process by powder blasting<sup>6</sup>.

Fig. 4-1b presents the powder blasting microerosion process with different components which will be analyzed below.

- **Nozzle:** It is connected to the powder blaster by a plastic tube and itself made of tungsten carbide providing good resistance to wear. According to different applications, one can vary the distance between nozzle and substrate (2 cm-6 cm) and its approaching angle (25°-90°).

- **Mask:** The protective mask should have extraordinary resistance to erosion by powder blasting. For all the applications in the thesis, metallic masks are always used which are conveniently fabricated by laser cutting. Other types of masks can be soft PDMS or Ordyll, the latter bearing suitable for mass production in industry.
- **Substrate:** PMMA and glass are chosen as base substrate in the thesis for magnetic micropumps. However, powder blasting is not limited to these two materials, and it can erode most of the hard materials like silicon, ferrite<sup>2</sup> etc.
- **Powder:** The abrasive powders used in the process are alumina (Al<sub>2</sub>O<sub>3</sub>) with an average particle size of 30 μm. It is the most commonly used type of particles, since it has sharp edges and excellent hardness (Mohs' hardness=9). However, due its micrometer size, safety rules should always be followed. For example, wearing a lab coat and a protective mask are necessary to prevent powder inhalation.

#### 4.1.2 Mechanism of powder blasting

The rate of material removal is a significant parameter for the powder blasting process. The evaluation of erosion rate is defined as:

$$E_{rate} = \frac{\text{weight of removed material}}{\text{weight of impacting particles}} \quad (4-1)$$

The detailed study was carried out by P.J. Slikkerveer *et al.*<sup>7,8</sup>, where he introduced the erosion efficiency  $E_{eff}$ :

$$E_{eff} = \frac{\text{weight of removed material}}{U_k} \quad (4-2)$$

where  $U_k$  is the kinetic energy of an incoming particle.

Combining Eqs. 4-1 and 4-2, one can easily deduce the relation between erosion rate and efficiency:

$$E_{rate} = \frac{1}{2} E_{eff} \cdot v_{particle}^2 \quad (4-3)$$

Consider a given substrate,  $E_{eff}$  is found to be an important parameters to evaluate the powder blasting process, because the erosion behavior of a single particle impact on the substrate is affected by the kinetic energy of the particle. Based on the model proposed by P.J. Slikkerveer *et al.*<sup>9</sup>, we are able to find that the erosion efficiency will be determined by several characteristics of materials:

1. Density of the abrasive particles  $\rho$
2. Young's modulus of the substrate  $E$

3. Fracture toughness of the substrate (material's resistance to the crack growth)  $K_{IC}$
4. Indentation hardness (material's resistance to permanent deformation)  $H$

To further understand the properties of materials used in the thesis for powder blasting, it is worthwhile to list them in a table (see [Table 4-1](#)).

*Table 4-1: Typical densities, toughness, hardness of some materials*

Material	Density (g/cm <sup>3</sup> )	Young's modulus $E$ (GPa)	Fracture toughness $K_{IC}$ (MPa m <sup>0.5</sup> )	Hardness $H_k$ (kg/mm <sup>2</sup> )	Mohs' hardness
$Al_2O_3$	3.9	390	3.5	2100	9
<i>Plexiglas (PMMA)</i> <sup>6</sup>	1.19	3.3	1.1	250	-
<i>Borosilicate D263</i> <sup>10</sup>	2.51	72.9	0.89	590	-

#### 4.1.3 PMMA microchip fabricated by powder blasting

Powder blasting has been demonstrated to be a simple and rapid technique to prototype three dimensional (3D) structures in PMMA. Combining with standard milling tools, it allowed us to fabricate complex microstructure with inexpensive strategy. Subsequently, the patterned PMMA layers can be assembled into 3D microfluidic structure by using thermal chemical bonding.

##### *PMMA for microfluidic devices*

PMMA, as an economical alternative to polycarbonate (PC) when extreme strength is not necessary, is a widely used polymer in industry. From aspect of microfluidics, this material is extensively used due to its good chemical resistance to many products and excellent optical properties. For particular interest of disposable microfluidic devices in the thesis, PMMA appears as good plastic material, thanks to its low cost.

##### *Fabrication process of PMMA sheets by powder blasting*

Planar structures like microchannels, and chambers are realized by powder blasting technology. First, the steel masks are simply patterned by a Nd:YAG laser. Due to its low eroded rate compared to the substrate material, in principle, the mask can be used for many cycles. However, the minimum feature size on the mask will be obviously enlarged after several time uses, which imposes a limitation on the lifetime of the masks. The mask is tightly attached to the substrate using adhesive tape or wax.

The PMMA sheets (250  $\mu\text{m}$ , 375  $\mu\text{m}$  thick *Plexiglas*® in our chip) are used for realizing microchips. The erosion parameters for microchannels, chambers as well as inlet/outlet holes should be distinguished. Since the etched depth for all the structures in the PMMA microchip equals the thickness of the sheet, controlling the velocity of the X-Y linear translation is less

important, while an air pressure of 0.16 MPa and a distance nozzle-substrate of 6 cm are kept constant. For microchannel, ball valve stopping structure and chamber erosion, the dynamic mode is adopted, where the scanned area is equal to the sheet area ( $36 \times 22 \text{ mm}^2$ ). In the case of drilling holes for inlet and outlet, the static mode is always employed. Fig. 4-2 shows the powder blasted ball-stop structure.

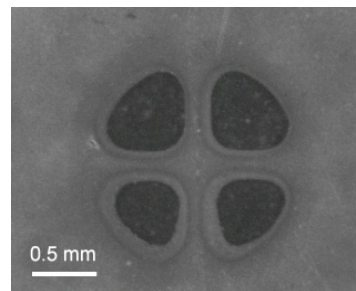


Figure 4-2: The microscopic photograph of ball-stop structure after powder blasting.

The complex parts, like the ball valve seat are micromachined through standard milling tools in the workshop at EPFL (photograph shown in Chapter 5).

#### *PMMA Layer assembly*

Different from the adhesive or solution bonding methods introduced in Chapter 3, chemical thermal bonding is used for assembly of the PMMA layers. A solution of triethylene glycol dimethacrylate (Fluka Chemie, No. 90412) is spread on the surface of patterned PMMA layer. Hereafter, several well-aligned layers are stacked and bonding is realized by a hot press at  $70^\circ\text{C}$  under a little external pressure for 5 min.

#### **4.1.4 Glass microchip fabricated by powder blasting**

Encouraged by the simplicity of the fabrication process for PMMA microfluidic chips, it is interesting to extend powder blasting to glass microchips composed of several layers, which are subsequently assembled in a bonding step. The active-valve glass micropump (in Chapter 6) is obtained using this method, as described hereafter. Several steps should be well followed to realize the active-valve micropump. They include: depth controlled erosion by powder blasting for two glass layers; glass fusion bonding; PDMS-glass adhesive bonding for pumping membrane integration.

#### *Advantage of glass microfluidic devices*

Glass as optically transparent material has an excellent chemicals resistance to most chemicals and its remarkably biocompatibility enables its easy integration into many types of bio-chips in the

microfluidic format. Since the glass slides used in our micropump are simply cover slips, they are cheap and have the potential to be produced in batch for realization of disposable chips.

*Processing of glass slide*

An active-valve micropump comprises two individual glass layer (0.4 mm thickness, tolerance  $\pm 20 \mu\text{m}$ , Menzel, Braunschweig, Germany) and a magnetic PDMS membrane (fabrication details in Section 4.2). As seen from Fig. 4-3, with a tightly attached metallic mask to the glass slide, the 1<sup>st</sup> glass slide first undergoes depth-controlled erosion by powder blasting with the parameters indicated in Table 4-2.

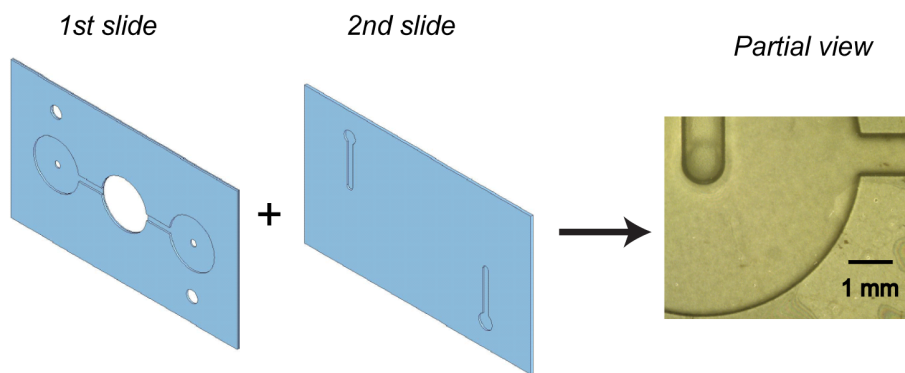


Figure 4-3: 3D microfluidic structure formed by two individual glass slides eroded by powder blasting.

Table 4-2: The list of parameters used for powder blasting erosion of the 1<sup>st</sup> glass slide.

<b>Powder material</b>	Al <sub>2</sub> O <sub>3</sub> , 30 $\mu\text{m}$
<b>Impact angle</b>	90°
<b>Scanning speed X</b>	2.2 mm/s
<b>Scanning speed Y</b>	78 mm/s
<b>Abrasive mass flow rate</b>	12 g/min
<b>Blasting pressure</b>	0.15 MPa
<b>Scanning area</b>	40×10 mm <sup>2</sup>

The erosion time is the only variable in the process to vary the desired depth, and the time-dependent erosion depth is shown in Fig. 4-4. The erosion depth is measured by optical profilometer (*GFM-MikroCAD*, Teltow/Berlin, Germany). One should note that the equivalent depth of microchannel and chamber is attributed to the large mask feature size (1 mm width for the channel and 8 mm for the chamber), and its quantitative analysis have been already studied by E. Belloy *et al.*<sup>11</sup> and A. Pawlowski *et al.*<sup>12</sup>. To complete the erosion process of the 1<sup>st</sup> slide, a second mask defining the middle chamber and four holes (two for inlet/outlet, the other two for valving



chamber fluid connections) is required to be placed on the backside of the etched glass slide. Then, the 1<sup>st</sup> glass slide is eroded from its backside without depth controlling. Alignment is an important parameter during these two processes.

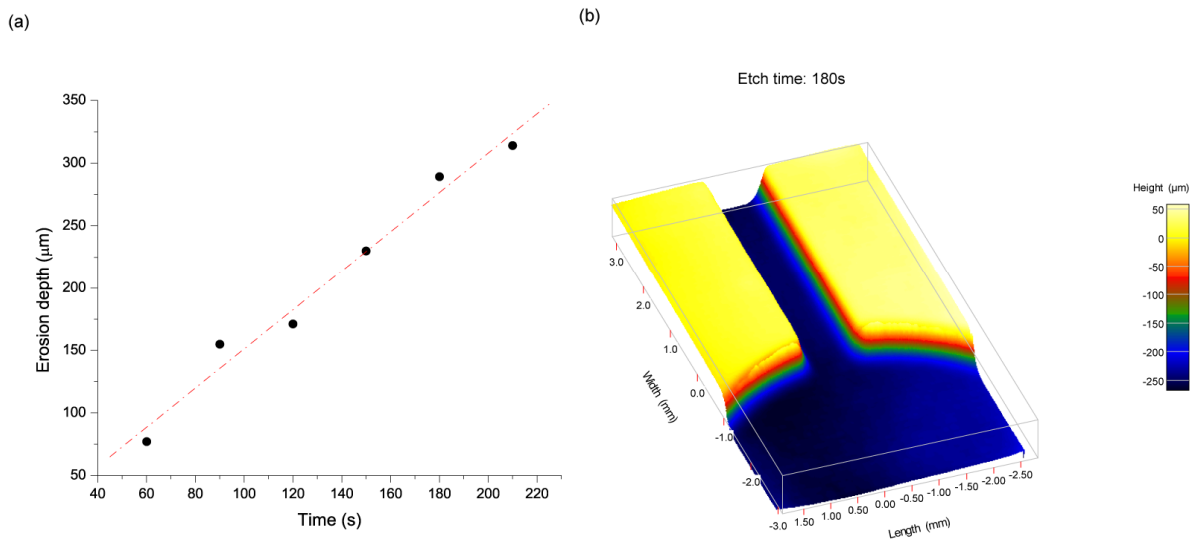


Figure 4-4: (a) Erosion depth of the microchannel/chamber as a function of powder blasting time. (b) The profile of the etched microchannel and chamber after an etching time of 180 s.

The 2<sup>nd</sup> glass slide is etched using the same method but with a different scanned area corresponding to its specific geometry and details will not be repeated here.

### Glass slides fusion bonding

#### ➤ Mechanism

The chemical mechanism of the glass fusion bonding process is governed by the condensation of two Si-OH groups on the pre-bonded substrates into a strong Si-O-Si siloxane bond under release of H<sub>2</sub>O<sup>13</sup>.

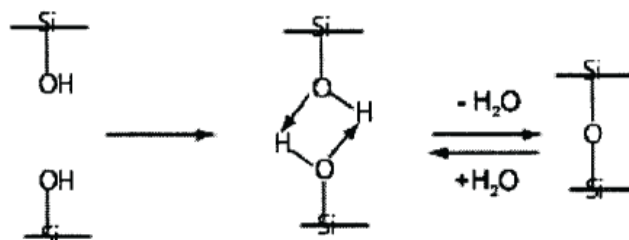


Figure 4-5: Chemical reaction at bonding interface leading to glass-glass bonding<sup>13</sup>.

Fig. 4-5 depicts the molecule mechanism of glass-glass bonding on a molecule level. First, the hydrophilic surfaces are brought into intimate contact, thus, the hydrogen bonds link the two

layers of glass together. Siloxane bonds will be formed when the silanols groups at the contact interface react under removal of water molecules.

### ➤ Experimental realization

Fusion bonding for different types of glass substrates is a mature technology in our laboratory. Our fusion bonding process is based on the bonding experiment done by D. Solignac <sup>14</sup>. First, the glass substrates should be thoroughly cleaned after erosion by powder blasting and in our experiment, isopropanol and Piranha solution are used. Then, two layers of glass slides are stacked and aligned before starting the bonding. The thermal treatment curve is depicted in Fig. 4-6 and it reveals three different plateaus A, B and C during the process. Glass substrates are first heated at 120°C to eliminate the remaining water, as indicated in plateau A. In plateau B, we have chosen to heat the sample at a temperature compromised between the strain point (529°C) and the glass transition temperature ( $T_g = 557^\circ\text{C}$ ) for one hour. The last plateau C stands for the bonding temperature for the glass chip and it is selected between  $T_g$  and the softening temperature (736°C). Thus, it is reasonable to choose a temperature of 655°C in our experiment for borosilicate glass fusion bonding. Finally, the bonded glass chip should be brought back to room temperature at a low cooling rate 1.3°C/min, since fast cooling results in apparition of stresses. A view on a detailed view of the bonded microstructured glass slides are shown in the right part of Fig. 4-3.

The glass slides for our active-valve micropump have been successfully bonded by using this simple method. It also provides the possibility of bonding multiple layers of substrates which have close values of thermal expansion coefficients.

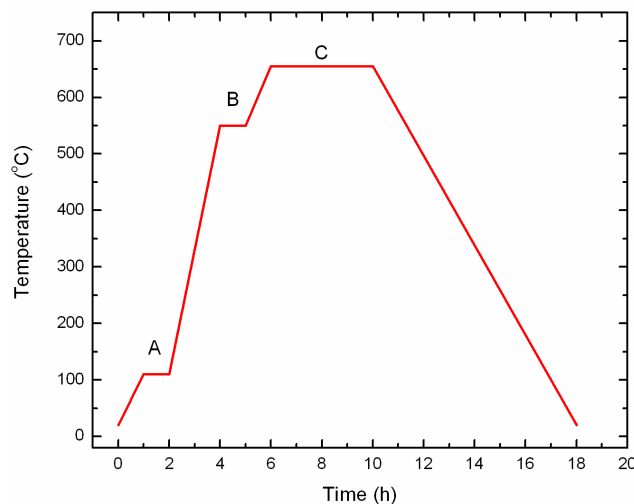


Figure 4-6: Temperature treatment for glass bonding. The glass substrates are first heated to 120°C for one hour to get rid of the remaining water (A). Subsequently, in order to have homogeneous temperature at sample, the substrates are heated at 550°C for one hour (B). Afterwards, the chips are heated at 655°C for 4 hours (C) before cooling down to room temperature.

## 4.2 Rapid prototyping II: PDMS molding technology

PDMS is a very popular elastomeric material for fabricating flexible membranes for micropumps as well as microfluidic channels. In the thesis, we not only take advantages of its large elasticity but also use its moldable properties to embed some rigid components like permanent magnets. In the applications of microfluidic DMFCs and preconcentration chips, the molded PDMS channel networks are capable of integrating a rigid Nafion strip without any leakage. Commercially available *Sylgard 184* silicone was used for all devices. It is chosen due to its high flexibility and compatibility with a hot sterilization treatment (130°C). The mixing ratio of PDMS prepolymer and curing agent was always kept as 10:1 in the work of this thesis.

### 4.2.1 Molding of the magnetic PDMS membrane for PMMA micropumps

#### *PDMS membrane with embedded permanent magnet*

First, for the PMMA ball-valve micropump, in order to realize the membrane with embedded permanent magnet, we have chosen a cylindrical NdFeB magnet ( $\phi = 3$  mm, height= 3mm). In Fig. 4-7a, as already developed by C. Yamahata <sup>6</sup>, we used this molding technology to integrate the magnet into the membrane using a two-step molding process. The final membrane (see Fig. 4-7b) has an external diameter of 10 mm. The membrane rigidity was measured to be  $K=800$  N/m, and the membrane weight was  $M_m=0.25$  g <sup>6</sup>.

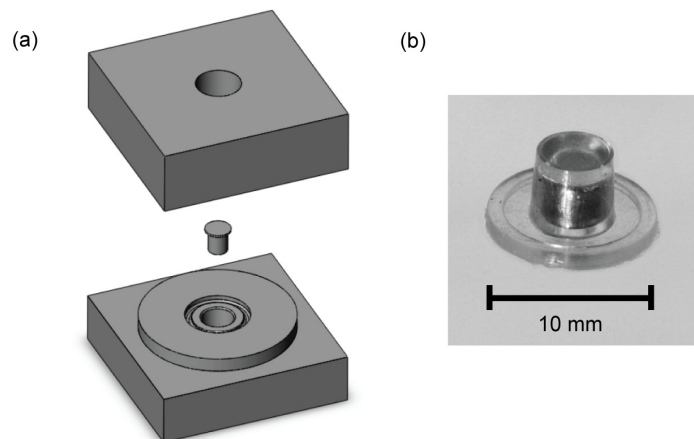


Figure 4-7: (a) Schematic 3D view of the mould with the central part used for easy removal of the membrane indicated. (b) Photograph of a PDMS membrane with embedded NdFeB permanent magnet <sup>6</sup>.

#### *PDMS membrane integration into a PMMA microchip*

Since there are a few available bonding methods for PDMS and PMMA, we adopt a micromachined thick PMMA plate with optimized geometry to hold the molded membrane. The

final assembly is completed by chemical adhesive bonding of all the PMMA layers. A schematic illustration will be shown in [Chapter 5](#).

#### 4.2.2 Molding of the magnetic PDMS sheet for active-valve micropumps

Inspired by the molding method used above for a single magnetic PDMS membrane, it is interesting to extend this technology to mold a PDMS sheet with series of permanent magnets for our active-valve micropump (see details in [Chapter 6](#)).

##### *PDMS sheet with series of embedded permanent magnets*

Encouraged by the two-step molding described by C. Yamahata<sup>6</sup> for a single membrane with embedded magnet, one can easily mold a PDMS sheet with a series of permanent magnets embedded. However, some differences should be noted. As seen from [Fig. 4-8a](#), the mold is simply made from aluminum and partial polymerization for centering the magnets using small quantity of liquid PDMS is demanded as the first step. The tricky thing for positioning the magnet at center can be solved by using a plate comprising three magnets at exact places underneath the mold. After partial polymerization of the PDMS, the magnets remain entrapped, and the molding process can be completed by adding liquid PDMS and removing the extra PDMS by a plastic blade (PMMA 0.25 mm thick) or pressing a thick PMMA plate (2 mm) on top with a certain load. Subsequently, the sheet is heated at 75°C for 2 hours for polymerization. These two methods allow excellent thickness control of the PDMS sheet which is determined by the inner height of the mold.

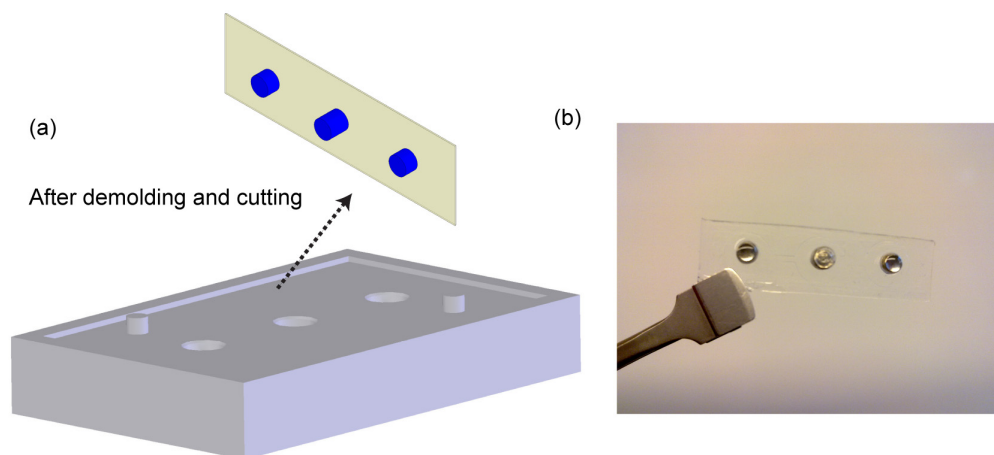


Figure 4-8: (a) Illustration of the mold for PDMS sheet with multiple embedded permanent magnets. (b) Photograph of the permanent magnets embedded in the PDMS sheet.

Combination of spin-coat technology and the molding method for magnetic PDMS membranes enables easy variation of the membrane thickness. Before demolding and cutting to the desired

size (11 mm× 40 mm) from the mold, one can spin coat additional liquid PDMS onto the polymerized membrane. For example, a layer of 100  $\mu\text{m}$  thick PDMS can be realized by setting the spin-coat speed at 1000 rpm for 20 s (spin-coater: Delta 20-BLE, Laboratory Equipment GmbH, Singen, Germany). A set of parameters for spin-coating PDMS can be found in E. Dahan's PhD thesis<sup>15</sup>. Thus, one can obtain permanent magnets embedded in a membrane of various thicknesses, which provides flexibility to optimize the membrane thickness for the micropump. In Chapter 6, two different sheet thicknesses of 450  $\mu\text{m}$  and 600  $\mu\text{m}$  are used for evaluating the performance of active-valve micropumps. Fig. 4-8b is a photograph of a PDMS sheet with embedded permanent magnets.

#### *Adhesive bonding of the PDMS sheet to the glass stack*

Different from the PDMS membrane clamped in the PMMA micropump, adhesive bonding is proposed for assembly of the PDMS sheet with the fusion-bonded glass stack.

As illustrated in Fig. 4-9 (I), a liquid PDMS layer (the mixing ratio of PDMS prepolymer and curing agent is 10:1) with thickness of 20  $\mu\text{m}$  is spun onto a glass slide by a spin-coater. The liquid PDMS is then transferred to a thick PDMS stamp (Fig. 4-9 (II)), which is subsequently transferred to the etched glass substrate (Fig. 4-9 (III)). After removal of the thick PDMS stamp (Fig. 4-9 (IV)), only 5  $\mu\text{m}$  thick liquid PDMS is left on the top of the etched glass stack. Liquid PDMS leakage into the microchannels and chambers can be avoided due to this negligible thickness, compared to the depth of the microfluidic structures. After curing at 75°C for 2 hours, the PDMS sheet and glass stack are adhesively bonded together (Fig. 4-9 (V)).

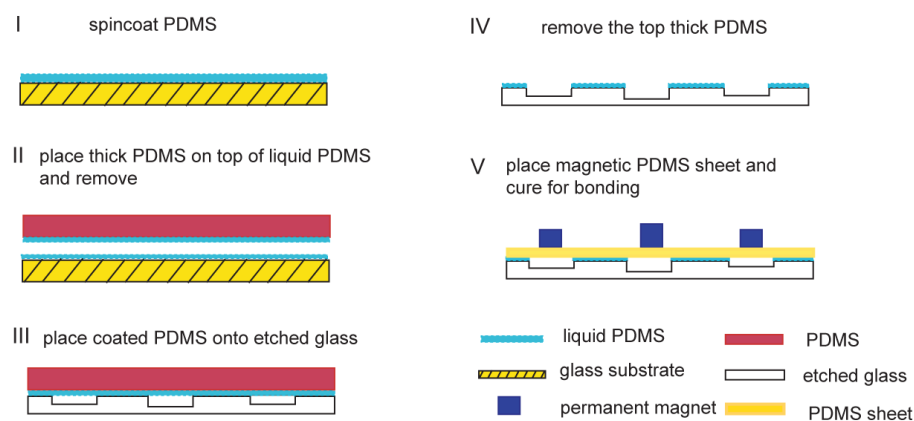


Figure 4-9: Adhesive bonding process for the PDMS sheet with the glass stack.

The photograph of the adhesively bonded PDMS-glass stack in micropump format is shown in Chapter 6.

### *Gluing fluidic connections*

Finally, PMMA cylindrical tubes are glued to the micropump with an Epo-Tek epoxy solution (Epo-Tek 301-2, Epoxy Technology Inc., Billerica, Massachusetts, USA) at 80°C for 2 hours, forming the fluidic connectors.

### **4.2.3 PDMS microchannels replicated from a SU8 mold**

Before moving to [Chapter 7](#) and [Chapter 8](#), it is worthwhile to introduce the molding technology for microfluidic channels for both fuel cell and preconcentration devices. An aluminum mold offers an easy solution for molding a PDMS membrane; however, it fails when the feature size is less than 300  $\mu\text{m}$ . SU8 as epoxy based negative photoresist with its high aspect ratio and straight vertical walls becomes an attractive material for MEMS applications. The most popular application of SU8 microstructures is their use as a mold for different types of elastomeric materials including PDMS. SU8 mold microfabrication flow is adapted from PhD thesis of E. Dahan<sup>15</sup>.

### *Microstructuring of SU8*

The different steps of a typical process for SU-8 photolithography are described here, as shown in [Fig. 4-10](#)<sup>15</sup>:

#### ➤ Substrate preparation

Glass or silicon substrates can be used, the latter having better adhesion properties with respect to SU-8. In this thesis, silicon substrates were used. To ensure good adhesion, the substrate must be exposed to oxygen plasma before use.

#### ➤ Spin-coating

The resist is spread on the wafer by spin-coating at a controlled speed to obtain the desired thickness ([Fig. 4-10a](#)). GM 1075 is used, since it is suitable for layers between 100 and 400  $\mu\text{m}$ .

#### ➤ Soft bake

The resist is then prebaked in order to evaporate the solvent. Ramping and stepping of the soft bake temperature is recommended for a well-controlled evaporation rate.

#### ➤ Exposure

The SU-8 contains acid-labile groups and a photoacid generator. Exposure to UV light ([Fig. 4-10b](#)) generates a low concentration of acid which will act as a catalyst of the cross-linking process. However, cross-linking does not take place at room temperature. The exposure dose is proportional to the film thickness.

#### ➤ Post-exposure bake

The SU-8 is heated on a hotplate up to a temperature of 95°C to cross-link the exposed parts ([Fig. 4-10c](#)). Slow ramps of temperature ( $\pm 2^\circ\text{C}$ ) for heating and cooling are essential to minimize internal stress which could lead to adhesion problems of the cross-linked structures.

### ➤ Development

The exposed SU-8 layers are developed in a solution of propylene glycol methyl ether acetate (PGMEA) (Fig. 4-10d) to get the desired microstructures. Finally, the structures are rinsed with isopropyl alcohol and dried.

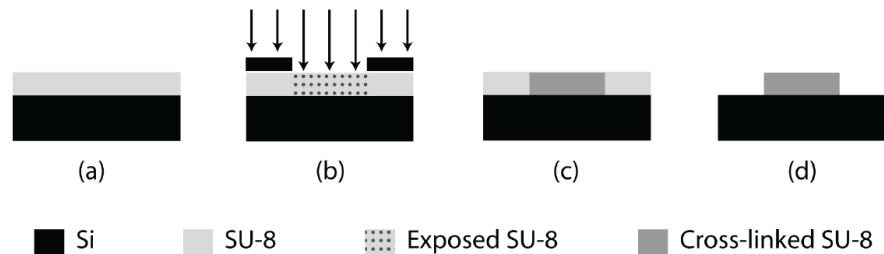


Figure 4-10: Steps for the photolithographic patterning of SU-8 resist. a) Spin-coating of SU-8 on a Si wafer and soft bake. b) Exposure under UV light through a photomask. c) Post exposure bake for cross-linking of the exposed parts. d) Removing unexposed resist in the developer bath for the desired structure <sup>15</sup>.

### Molding PDMS chips from the SU8 molds

The SU-8 molds used in this project are divided into two types according to the requirement. As seen from Fig. 4-11a, the long structures for replica of microchannels are designed for the microfluidic DMFC which offers a large area for loading catalysts to enhance the fuel cell's performance. However, this does not provide a satisfactory solution for the preconcentration device, since it demands V-shaped microchannels for getting fluorescence signal amplified in a small concentrated area. Thus, the design in Fig. 4-11b is chosen for the preconcentrator.

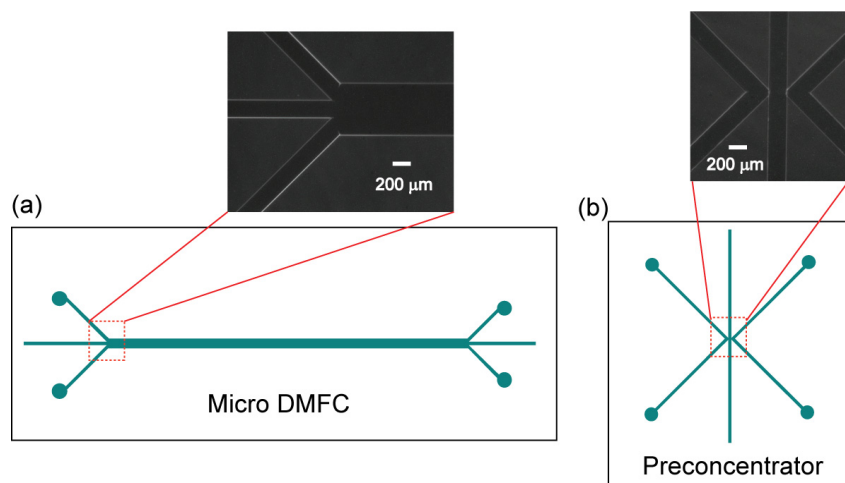


Figure 4-11: SU8 mold design for (a) micro-DMFC and (b) a protein preconcentrator device.

Once the SU-8 mold (approximately 170 μm height for two cases) is ready, we can easily pour PDMS onto the mold and cure it at 75°C for at least 2 hours. After peeling off the polymerized

PDMS from the mold, holes are punched by a blunt needle to form inlet and outlet. Before integration of the Nafion strip into the PDMS chip, the latter should be rinsed by liquid soap to eliminate any debris on the surface.

### 4.3 Rapid prototyping III: Cutting and integration of the Nafion strip

Nafion, as notable material for ion-permselective applications, is less affordable. Thus, maintaining the device performance at a high level while reducing the amount of Nafion used is highly demanded for many applications. Cutting, as an unusual technology that evolved rapidly in recent years, is chosen in the thesis for realization of two types of microfluidic devices: the micro-DMFC and the preconcentrator device.

#### 4.3.1 Preparing the Nafion strip

##### *Cutting the Nafion strip*

A Nafion membrane 117 is obtained from DuPont™. The nominal thickness of the as-prepared H<sup>+</sup> form in its dry state is approximately 175-183 μm. Using adhesive tape as spacer, I conveniently bind two razor blades together, which forms the cutting adjustment in our experiment. By applying different types of adhesive tapes, one can easily tune the spacer in cutting; however, in our two applications, the cut width of the strip is fixed around 200 μm.

##### *Pretreatment of the Nafion strip*

Before placing into the guiding microchannel, the cut Nafion strip is conditioned by a series of steps: subsequently, we used 10% H<sub>2</sub>O<sub>2</sub>, deionized (DI) water H<sub>2</sub>O, 1 M H<sub>2</sub>SO<sub>4</sub> and DI H<sub>2</sub>O baths during 2 hours each at 80°C. The diagram is illustrated in Fig. 4-12. The preconditioned Nafion strip will be kept in DI water for storage.

However, for biocompatibility in our preconcentration device, Nafion strips need extra pretreatment steps to convert their H<sup>+</sup> form into a Na<sup>+</sup> form. After previous procedures, Nafion strips will be repeatedly rinsed in DI water until pH=7. Subsequently, the strips are soaked into 1M NaOH for 24 hours and then rinsed again with DI water until pH=7. Finally, the Nafion strips are immersed in a 0.1M NaCl solution.

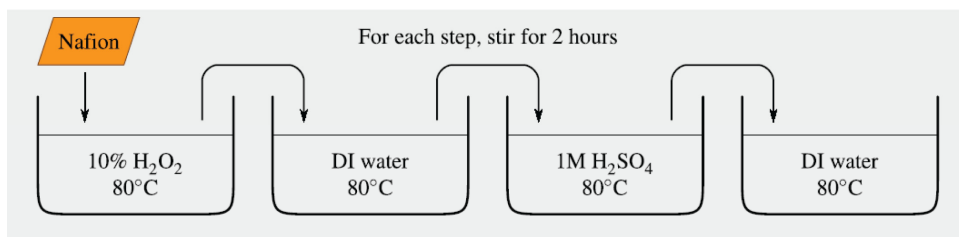


Figure 4-12: Illustration of Nafion pretreatment for the fuel cell application.



### 4.3.2 Integration of the Nafion strip

#### *Placing Nafion strip within guiding channel*

As seen from Fig. 4-11, both types of chips are designed with a guiding channel in the middle to accommodate the Nafion strip. Placing the Nafion strip into the guiding channel can be simply done by utilizing a cleaned sharp needle under microscopic observation. Fig. 4-13a is a photograph of the microfluidic fuel cell with inserted Nafion strip. We used two color solutions to verify the absence of leakage for the Nafion strip-embedded chip, as shown in Fig. 4-13b.

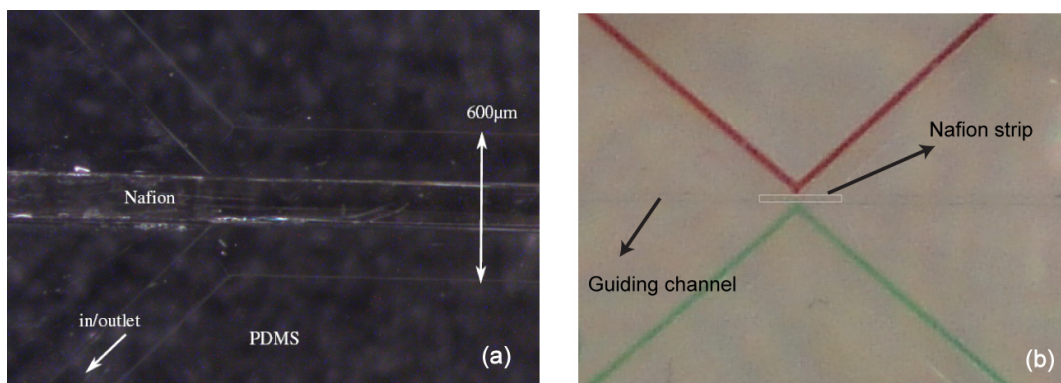


Figure 4-13: (a) Photograph of a Nafion strip separating two microfluidic channels by using a middle guiding channel in the fuel cell chip. (b) Photograph of the preconcentration device, which has two microfluidic channels with filled red and green color dye solutions, indicating no leakage across the Nafion strip.

Using a guiding channel is suitable for integrating any rigid strip into the elastomeric microchannels, making it an interesting principle for various microfluidic applications where microscale membranes are demanded.

#### *Mechanical clamping the chip*

As already clarified in Chapter 3, when the microfluidic substrates are bio-functionalized, or when versatile materials with different physical or chemical properties need to be combined, reversible bonding offers appropriate solution for assembly.

In the cases of the fuel cell and preconcentrator, where Nafion strips are accommodated in a PDMS chip, the requirement for mechanical clamping is that it should be leakage-free. PMMA plates are chosen as upper and lower parts for the clamping system due to its optically transparency. Attention should be paid during the screwing, since too tight pressing will lead to the cracks on the glass slide and obvious deformation of the PDMS chip.

## 4.4 Conclusion

In this chapter, we have presented three categories of rapid prototyping methods involved in the thesis. Powder blasting as a low-cost microfabrication technique for PMMA and glass chips will be employed for ball-valve micropumps (Chapter 5) and active-valve micropumps (Chapter 6), respectively. PDMS molding technology could be used for magnet-integrated membrane fabrication for the two types of micropumps. Moreover, to realize the microfluidic DMFC (Chapter 7) and biomolecule preconcentrator (Chapter 8), the combination of elastomeric material molding and rigid Nafion strip cutting lead to extremely efficient microfabrication. Various bonding methods including glass fusion bonding, PDMS-glass adhesive bonding and irreversible mechanical clamping are also introduced as complementary part for each type of rapid prototyping process.

## References

1. Lacharme, F.; Gijs, M., Pressure injection in continuous sample flow electrophoresis microchips. *Sensors and Actuators B: Chemical* 2006, *117*, 384-390.
2. Saidani, M.; Gijs, M., Three-dimensional miniaturized power inductors realized in a batch-type hybrid technology. *Journal of Micromechanics and Microengineering* 2002, *12*, 470-474.
3. Sayah, A.; Thivolle, P.; Parashar, V.; Gijs, M., Fabrication of microfluidic mixers with varying topography in glass using the powder-blasting process. *Journal of Micromechanics and Microengineering* 2009, *19*, 085024 (8pp).
4. Solignac, D.; Sayah, A.; Constantin, S.; Freitag, R.; Gijs, M., Powder blasting for the realisation of microchips for bio-analytic applications. *Sensors and Actuators A: Physical* 2001, *92*, 388-393.
5. Yamahata, C.; Lacharme, F.; Burri, Y.; Gijs, M., A ball valve micropump in glass fabricated by powder blasting. *Sensors and Actuators B: Chemical* 2005, *110*, 1-7.
6. Yamahata, C., Magnetically actuated micropumps. *PhD thesis, Ecole Polytechnique Federale de Lausanne* 2005.
7. Slikkerveer, P., Mechanical etching of glass by powder blasting. *PhD thesis, Eindhoven* 1999.
8. Slikkerveer, P.; Bouten, P.; De Haas, F., High quality mechanical etching of brittle materials by powder blasting. *Sensors and Actuators A: Physical* 2000, *85*, 296-303.
9. Slikkerveer, P.; Bouten, P., Erosion and damage by sharp particles. *Wear* 1998, *217*, 237-250.
10. <http://www.naugatuckglass.com/downloads/D263T.pdf>
11. Belloy, E.; Thurre, S.; Walckiers, E.; Sayah, A.; Gijs, M., The introduction of powder blasting for sensor and microsystem applications. *Sensors and Actuators A: Physical* 2000, *84*, 330-337.
12. Pawlowski, A.; Sayah, A.; Gijs, M., Accurate masking technology for high-resolution powder blasting. *Journal of Micromechanics and Microengineering* 2005, *15*, S60-S64.
13. Tong, Q.; Lee, T.; Gösele, U.; Reiche, M.; Ramm, J.; Beck, E., The role of surface chemistry in bonding of standard silicon wafers. *Journal of the Electrochemical Society* 1997, *144*, 384-389.

14. Solignac, D., Glass Microchips for Bio-chemical Analysis: Technologies and Applications, *PhD Thesis, Ecole Polytechnique Federale de Lausanne* 2003.
15. Dahan, E., Integrated microfluidic system for non-invasive electrophysiological measurement on xenopus oocytes. *PhD Thesis, Ecole Polytechnique Federale de Lausanne* 2008.



# Chapter 5

## Ball-Valve Micropumps Actuated By Planar Electromagnetic Actuators

(adapted versions of:

<sup>1</sup> **M. Shen**, C. Yamahata, M.A.M. Gijs, A high-performance compact electromagnetic actuator for a PMMA ball-valve micropump, *Journal of Micromechanics and Microengineering*, 2008, 18 , 025031 (9pp).

<sup>2</sup> **M. Shen**, C. Yamahata, M.A.M. Gijs, Miniaturized PMMA ball-valve micropump with cylindrical electromagnetic actuator, *Microelectronic Engineering*, 2008, 85, 1104-1107)

**Abstract:** In this chapter, we report the design, fabrication and testing of a low-cost hybrid PMMA ball-valve micropump with two types of planar actuator, firstly a compact rectangular electromagnetic actuator and secondly a cylindrical electromagnetic actuator. The finite element method is used to calculate the optimum geometry of the electromagnetic circuits. The microfluidic structure is built out of seven PMMA sheets or plates that are microstructured by simple powder blasting and conventional machining. A high-temperature resistant PDMS membrane with embedded permanent magnet is clamped into the PMMA structure, giving rise to a large actuation stroke, making the micropump bubble-tolerant and self-priming. For example, the water flow rate for the ball-valve micropump actuated by the first type of electromagnetic actuator is as high as 3.6 mL/min and 6.8 mL/min at 500 mW and 2 W actuation power, respectively. The backpressure amounts nearly to 40 kPa at 2 W. A similar performance can be attained when the second type of actuator for the micropump is employed. Thanks to the improved electromagnetic actuator, our micropump system has been considerably improved in terms of miniaturization and efficiency, compared with previous work. The frequency-dependent flow rate can be well interpreted by a *RLC* equivalent model, as already discussed in [Chapter 2](#).

## 5.1 Introduction

Commonly used in laboratory experiments for the precise dispensing of fluids, miniaturized pumps have also attracted more and more attention for Lab-On-a-Chip (LOC) applications<sup>3,4</sup>. A large number of different types of micropumps, especially piezoelectrically actuated reciprocating micropumps, have been fabricated in silicon<sup>5,6</sup>. Multiple techniques for microfabrication, and various principles of valving<sup>7,8</sup> and actuation have been proposed. T. Pan *et al.*<sup>9</sup> and C. Yamahata *et al.*<sup>10-12</sup> have realized several electromagnetically actuated micropumps with excellent performances. When low-cost and easy-to-make pumping solutions are envisaged, PMMA is a very interesting material for the microfluidic pumping circuit. Ball-valves, which have nearly perfect opening/closure behavior and are capable of withstanding high backpressures, are highly preferred in reciprocating micropumps. A first type of ball-valve micropump was made by stereolithography in polymer material<sup>13</sup> and an active electromagnetically actuated ball-valve was realized in silicon/glass<sup>14</sup>.

### 5.1.1 Advantages of planar compact electromagnets

Recently, different PMMA ball-valve micropumps with either pneumatically<sup>15</sup> or electromagnetically actuated<sup>10-12,16-18</sup> membranes were reported. In the case of electromagnetic actuation, commercial electromagnets are commonly reported. Their drawbacks are that they are not optimally designed for combination with a microfluidic structure and that they have a relatively large size. Moreover, compact volumes for both the microfluidic structure and actuation system are always required when portability is an issue to be addressed. Some criteria should be satisfied for a good planar compact electromagnet:

- Compact volume
- Low power consumption
- Efficient heat dissipation
- Large stroke of the pumping membrane

### 5.1.2 Design and working principle

#### *Working principle of micropump*

Fig. 5-1 shows the working principle of our reciprocating micropump: the oscillation of a flexible diaphragm gives rise to the periodic increase and decrease of the pumping chamber volume. Two passive ball-valves are placed at the entrance and exit of the pumping chamber to rectify the pulsed flow<sup>16</sup>. In the diagram shown in Fig. 2-3 of Chapter 2, our hydraulic system was represented in terms of a simple *RLC* electrical circuit. The specific values for our micropump will be presented later.

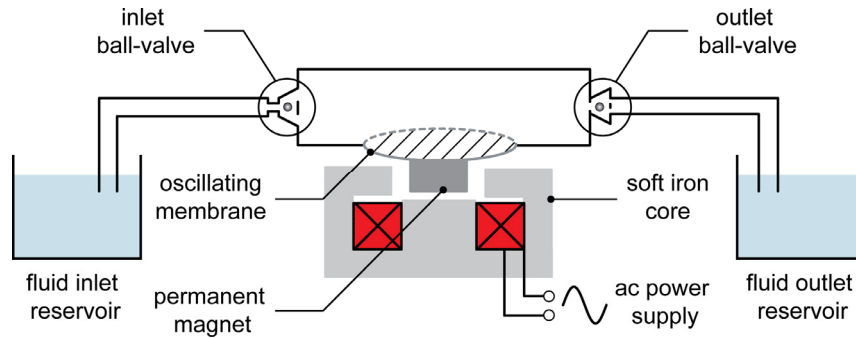


Figure 5-1: Schematic diagram of the electromagnetically actuated reciprocating ball-valve micropump.

### Minimum compression ratio for self-priming and bubble-tolerant pumping

For the basic operation condition, the pressure amplitude  $|\Delta p|$  generated from the movement of the membrane should exceed the critical pressure  $\Delta p_{crit}$  in order to open the valve.

The pressure peak  $\Delta p$  that occurs in the pump chamber can be calculated using the following expression:

$$V_0 + \Delta V = V_0(1 - k\Delta p) \quad (5-1)$$

with  $k$  the compressibility of the liquid.

Thus, for designing of a liquid micropump, the criterion for the minimum compression ratio  $\varepsilon_{lq}$  should be  $\varepsilon_{lq} > k|\Delta p_{crit}|$ . However, this condition is valid only if the chamber is completely filled with liquid. If a bubble is somehow entrapped in the chamber, the minimum compression ratio becomes  $\varepsilon_{lq} > \frac{1}{\gamma} \frac{|\Delta p_{crit}|}{p_0}$  for the low-frequency micropump ( $\gamma=1$ ,  $p_0$  the atmospheric pressure), as suggested by M. Richter *et al.*<sup>19</sup> for a gas pump.

The critical pressure  $\Delta p_{crit}$  to open the valve can be calculated using an energy argumentation. First, we assume the pumping chamber is filled with the gas and the valve is wet, which is the worst assumption for a self-priming and bubble-tolerant liquid pump.

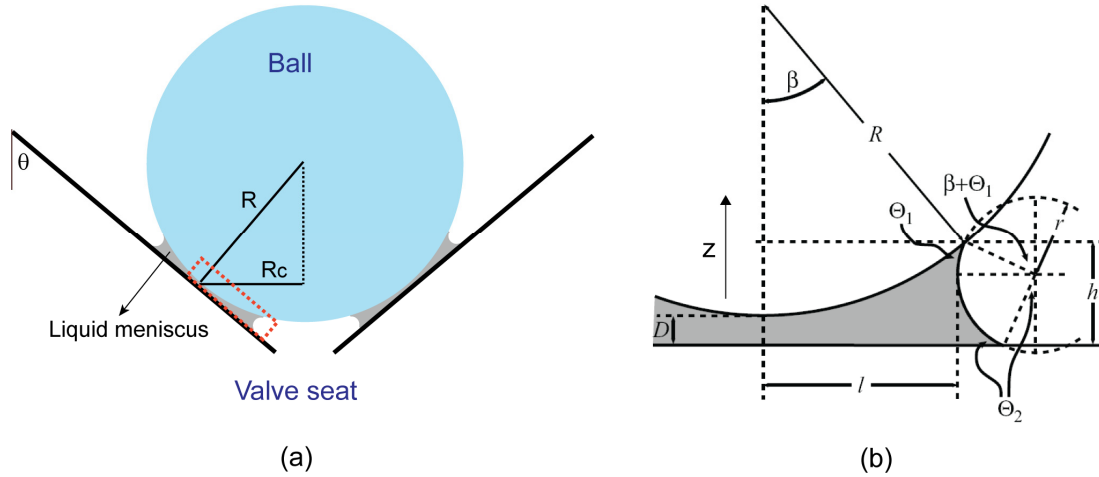


Figure 5-2: (a) Geometry of ball situated on a valve seat. (b) A liquid meniscus is trapped between ball and plane of valve seat <sup>20</sup>.

Considering the geometry of the valve seat (see Fig. 5-2a), the pressure  $p$  on the meniscus is expressed as:

$$p = p_{crit} \cdot \sin \theta \quad (5-2)$$

For simplicity, we assume the water remaining focus a flat thin ring (radius  $R_c$ , width  $2l$  and height  $D$ , specific geometry is indicated in Fig. 5-2b). The energy change when moving by the ball is expressed as:

$$\begin{aligned} dE &= dE_1 + dE_2 = 2 \cdot 2\pi R_c \sigma_{LV} \cdot dz - 2 \cdot 2\pi R_c (\sigma_{SL} - \sigma_{SV}) \cdot (2dl) \\ &= 4\pi R_c \sigma_{LV} \cdot dz - 8\pi R_c (\sigma_{SL} - \sigma_{SV}) \cdot dl \end{aligned} \quad (5-3)$$

$\sigma_{LV}$ ,  $\sigma_{SL}$ ,  $\sigma_{SV}$  are the surface tension of the liquid-vapor, liquid-solid, solid-vapor interface, respectively.

By deriving the energy and assuming a constant liquid volume, the pressure can be written as:

$$\Delta p = \frac{dE}{\pi R_c^2 dz} = \frac{4\sigma_{LV}}{R_c} - \frac{8(\sigma_{SL} - \sigma_{SV})}{R_c} \frac{dl}{dz} \approx \frac{4\sigma_{LV}}{R_c} - \frac{8(\sigma_{SL} - \sigma_{SV})}{R_c} \frac{l}{D} \quad (5-4)$$

Thus, the critical pressure  $\Delta p_{crit}$ , for the particular case of the ball valve seat with parameters indicated, is written as:

$$\Delta p_{crit} = \frac{4\sigma_{LV}}{R \cos \theta \sin \theta} - \frac{8(\sigma_{SL} - \sigma_{SV})}{R \cos \theta \sin \theta} \cdot \frac{l}{D} \quad (5-5)$$

In the thesis, we have designed the ball with a radius 0.5 mm and the angle  $\theta$  of the valve seat as  $60^\circ$ .  $\sigma_{LV}$  has the well-known value of 0.0725 N/m for the water-air interface and



$\sigma_{SL} - \sigma_{SV} = -\sigma_{LV} \cos \Theta_1$  is  $-0.025 \text{ N/m}^{21}$ . The contact angle is the  $\Theta_1 \approx \Theta_2 \approx 70^\circ$  for stainless steel and PMMA<sup>21, 22</sup>. Here, we assume the stainless steel ball and PMMA have the same surface properties.

$l/D$  is a parameter related to the contact angles of the liquid on the substrate interface  $\Theta_1, \Theta_2$  and relative humidity (see Fig. 5-2b). Assuming a very small liquid meniscus, the angle  $\beta$  is very small

and  $R \gg l$ , from which we obtain the analytical expression  $r = \frac{R(1 - \cos \beta) + D}{(\cos \Theta_1 + \cos \Theta_2)}$

and  $l = R \sin \beta - r[1 - \cos(\Theta_1 + \beta)]$ <sup>20</sup>. Let's say, for example,  $\beta = 0.5^\circ$  and  $D = 0.5 \text{ } \mu\text{m}$  (approximately the interface roughness). Thus,  $l/D \approx 7.7$ . Finally, we obtain that the critical pressure to open the valve is approximately 8.4 kPa. In addition, if the pressure caused by the mass of ball is taken into account, the critical pressure will be increased to around 8.6 kPa. This points out that, for a self-priming and bubble-tolerant micropump using a ball valve with dimensions indicated above, the compression ratio should be  $\varepsilon > 0.086$ . The higher the value  $\varepsilon$ , the more gas-tolerant the pump will be, thus, it is advantageous to achieve a large volume stroke to have a self-priming pump.

## 5.2 Electromagnetic actuator realization

### 5.2.1 Realization of a first type of compact electromagnetic actuator

#### *Experimental realization of actuator I*

Electromagnetic actuation has the potential to generate large deflections and large forces, depending on the design, materials used and the dimension of the system<sup>23</sup>. Fig. 5-3a is a schematic three-dimensional (3D) diagram of the electromagnetic actuator; this magnetic circuit is composed of a soft iron structure (outer size: 20 mm  $\times$  15 mm  $\times$  9 mm), a coil and an integrated permanent magnet – with magnetization along the cylinder axis – that will be embedded in the PDMS pumping membrane. We call the structure in Fig. 5-3a 'A-type' and the related structure without cover soft iron structure 'B-type'. Figs. 5-3b and 5-3c are photographs of an 'A-type' compact electromagnetic circuit having a coil with  $N = 1500$  turns of copper wire (wire diameter  $\phi_{Cu} = 0.1 \text{ mm}$ , Magnebond® CAB-200 from Lacroix & Kress GmbH, coil resistance  $R_{Cu} = 101.5 \text{ } \Omega$ ). We have chosen this wire as a compromise between mechanical strength and electrical power consumption. The insert of Fig. 5-3c is an optical photograph showing the cross-section of the hexagonal coil winding pattern. The copper filling factor of the coil is 80 %. We used a NdFeB permanent magnet with a diameter of  $\phi_{mag} = 3 \text{ mm}$  and a height of  $h_{mag} = 3 \text{ mm}$  (Maurer Magnetic

AG, Gr uningen, Switzerland). By applying an external sinusoidal current to the coil, alternating attractive and repulsive magnetic forces between the permanent magnet and the electromagnetic circuit are induced. An important parameter in the magnetic actuation circuit is the air gap  $\delta$  between the lower side of the permanent magnet and the top of the electromagnet core (see further). The reason for designing and choosing such soft iron structure will be analyzed below.

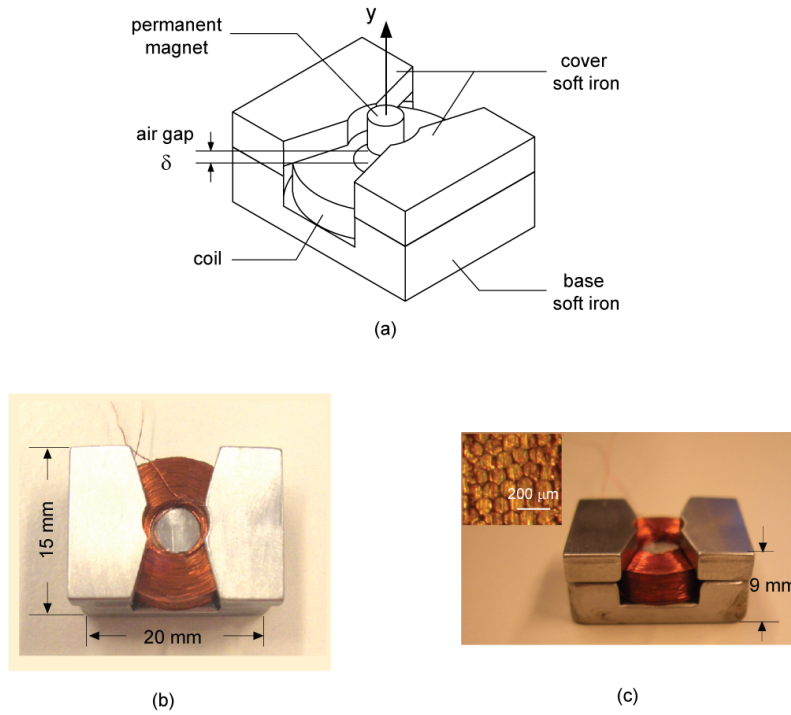


Figure 5-3: Electromagnetic actuator: (a) 3D diagram of an ‘A-type’ electromagnetic actuator with permanent magnet; (b) top view and (c) side view of the compact electromagnetic circuit with as insert the hexagonal winding pattern of the coil cross-section.

**Finite element simulation for actuator I**

The electromagnetic ‘A-type’ circuit described above is chosen based on numerical simulations, due to its improved magnetic induction and flux distribution. First, two dimensional (2D) FEM (Comsol Multiphysics™ 3.2) simulation is used to improve the soft iron structure(a nonlinear B-H curve for permeability is employed.). We have studied the 2D soft iron structures of Fig. 5-4. The structures differ by the absence of the cover soft iron for the ‘B-type’ structure, as we have shown above in Fig. 5-3a.

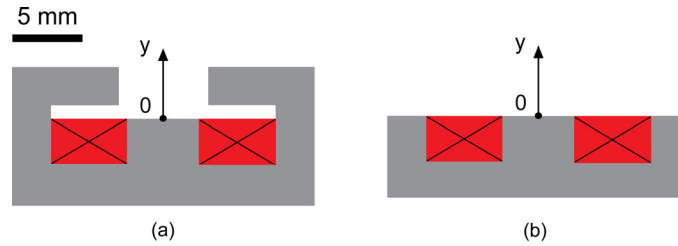


Figure 5-4: Schematic diagram of (a) 'A-type' and (b) 'B-type' electromagnetic cores used in the 2D FEM simulation.

Since the magnetic force is proportional to the gradient of the magnetic induction<sup>6, 7, 14</sup>, it is significant to study the vertical gradient  $dB_y/dy$  generated by the electromagnetic circuit. Indeed, the force  $F_y$  in the  $y$ -direction for a point-like permanent magnet can be written as:

$$F_y = M_y \int_V \frac{dB_y}{dy} dV \quad (5-6)$$

where  $M_y$  is the magnetization of the permanent magnet,  $V$  its volume, and  $B_y$  the vertical component of the magnetic flux density produced by the coil/soft iron circuit. Fig. 5-5a shows the simulated gradient  $dB_y/dy$ , using a DC coil actuation current of 100 and 200 mA for the 'A-type' structure, and 200 mA for the 'B-type' structure. It shows that the 'A-type' magnetic circuit can provide the highest magnetic force. To verify the simulation prediction, a miniaturized Hall sensor (Teslameter model 6010, F.W. Orlando, USA) is employed to measure the magnetic induction  $B_y$  along the central  $y$  line of the 'A-type' electromagnetic circuit. In Fig. 5-5b, we plot the experimentally determined magnetic induction gradients  $dB_y/dy$ . Though a deviation exists between simulation and experiment, the tendency and optimized position fit well, proving that the simplified 2D FEM simulation can predict the real experiments appropriately. Probable reasons for the deviations are, first, that the thermal effect on the magnetic induction distribution is not negligible, especially for larger coil currents. Second, the exact structure of the soft iron core is neither axisymmetric nor planar. Third, the material properties used in the simulation are standard values for soft iron, which may not perfectly represent the actual parameters.

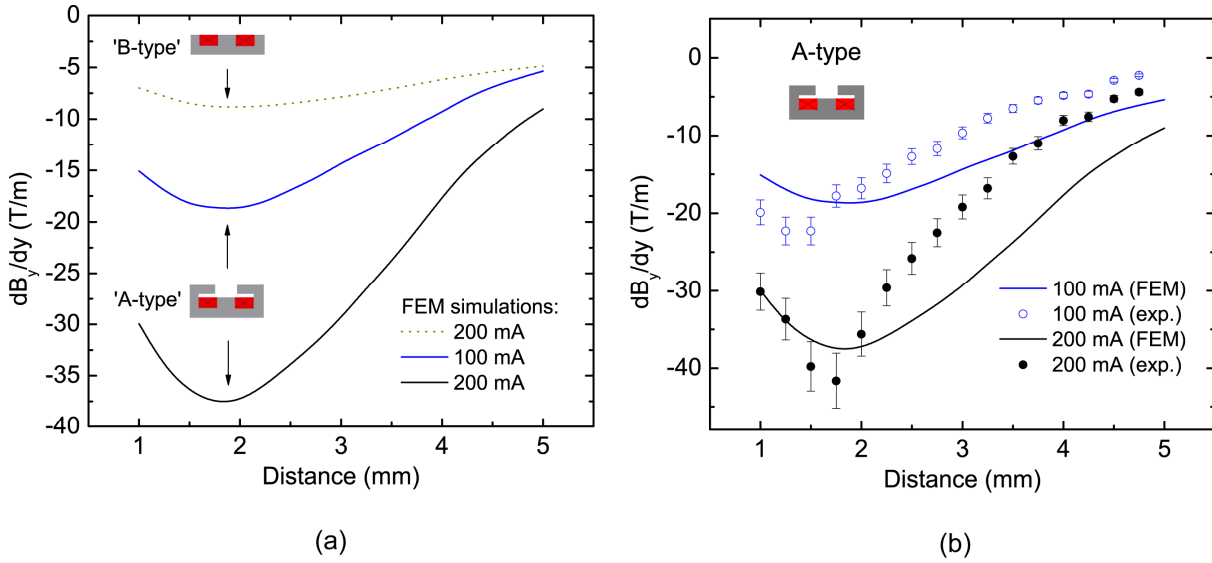


Figure 5-5: (a) FEM simulation results for  $dB_y/dy$  along the y-axis for 'A-type' (DC current of 100 mA and 200 mA) and 'B-type' (200 mA) cores. (b) Comparison between simulation and experiment for  $dB_y/dy$  along the y-axis for 100 mA and 200 mA DC coil current in the case of the 'A-type' structure.

To optimize the magnetic induction distribution  $\vec{B}$  within the electromagnetic circuit / permanent magnet system, 2D FEM is also employed to analyze the magnetic induction for different values of the vertical air gap  $\delta$  between the soft iron structure and the permanent magnet. We have measured the magnetic induction of the NdFeB permanent magnet using a Hall probe and obtained a value of 320 mT at the surface of the magnet. From this value, we derive a y-component of the magnetization  $M_y = 506$  kA/m, taking into account the demagnetization factor of the permanent magnet ( $\sim 0.5$ )<sup>10, 24</sup>. Parameters in the FEM simulation therefore are: a 2D permanent magnet of 3 mm in width and 3 mm in height having a magnetization of  $M_y = 506$  kA/m, and a DC coil current of 200 mA. Due to the presence of the soft iron structure, we expect forces to be smaller in the repulsive mode (positive coil current) than in the attractive mode (negative coil current). Fig. 5-6 shows the magnetic induction in the repulsive mode for different cases: Figs. 5-6a and 5-6b are for the 'A-type' soft iron structure with an air gap  $\delta = 1.5$  mm and 1 mm, respectively, while Fig. 5-6c is for the 'B-type' soft iron structure with an air gap  $\delta = 1.5$  mm.

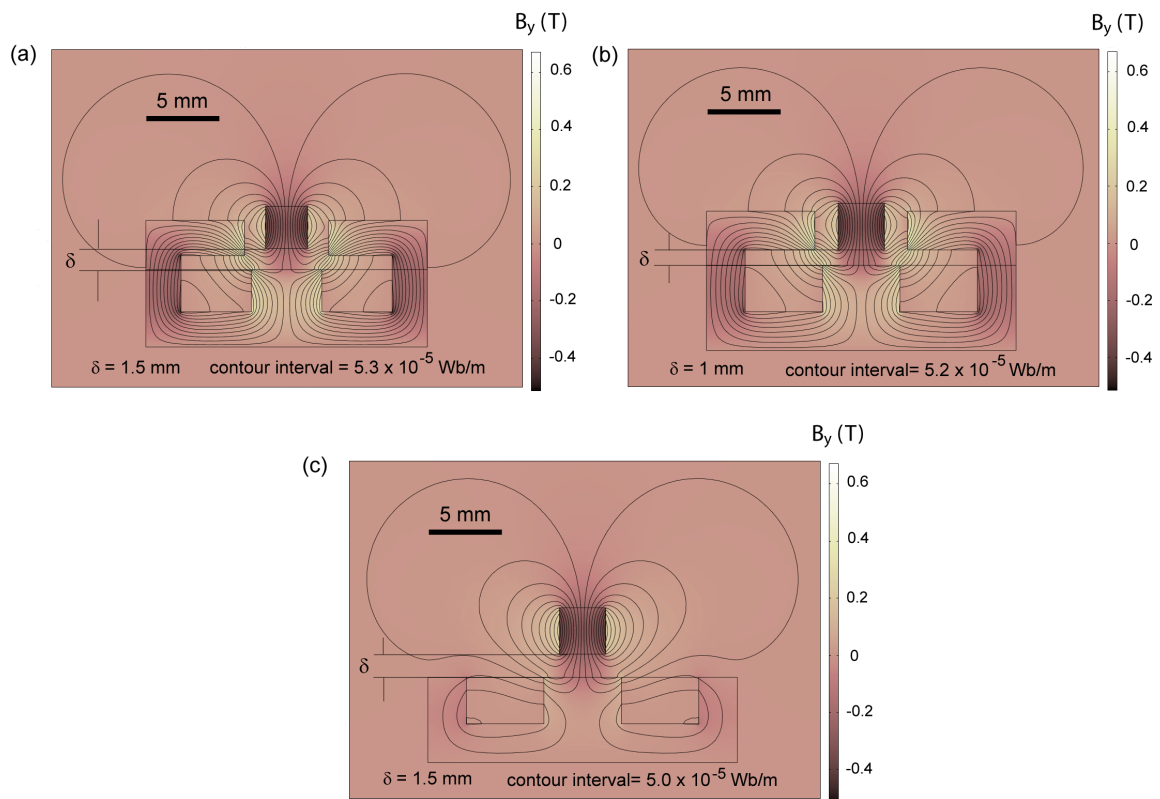


Figure 5-6: FEM calculation of the magnetic induction in the electromagnetic actuator circuit for an air gap of (a)  $\delta = 1.5$  mm and (b)  $\delta = 1$  mm for the 'A-type' core, (c)  $\delta = 1.5$  mm for the 'B-type' core. The simulations were performed for a DC current of 200 mA, in the repulsive mode with the contour intervals of magnetic potential indicated.

From the density of magnetic flux lines in the soft iron structure, it is easy to find out that the strongest interaction between magnet and soft iron structure appears in Fig. 5-6a for an air gap  $\delta = 1.5$  mm. The 'B-type' structure without soft iron cover is characterized by a highly reduced magnetic induction.

#### Measurement of actuation force for actuator I

We also directly measure the electromagnetic forces of the electromagnetic circuit of Fig. 5-3b and Fig. 5-3c by mounting the pump on a digital balance (Mettler Toledo AG104) and varying the distance with the electromagnet. The latter is operated with DC coil currents in both repulsive and attractive mode. The measured weight difference is proportional to the electromagnetic force and is directly related to the pressure exerted in the pumping chamber. As shown in Fig. 5-7, for the same amplitude of the coil current, the attractive electromagnetic forces are much larger than the repulsive forces. This is because in our electromagnetic system consisting of a moving magnet and a soft magnetic circuit, the resulting force on the magnet is generally composed of an

attractive contribution due to the induced magnetization of the soft material by the permanent magnet and a contribution due to the presence of the electromagnet <sup>17</sup>. Furthermore, the results indicate that the maximum repulsive electromagnetic force can be achieved at an optimized air gap of  $\delta = 1.5$  mm, which provides valuable data for the pump assembly. Based on our FEM calculations and force measurements, we employ an improved ‘A-type’ actuator with an air gap  $\delta = 1.5$  mm from permanent magnet in our pumping experiments (see Fig. 5-3b and Fig. 5-3c).

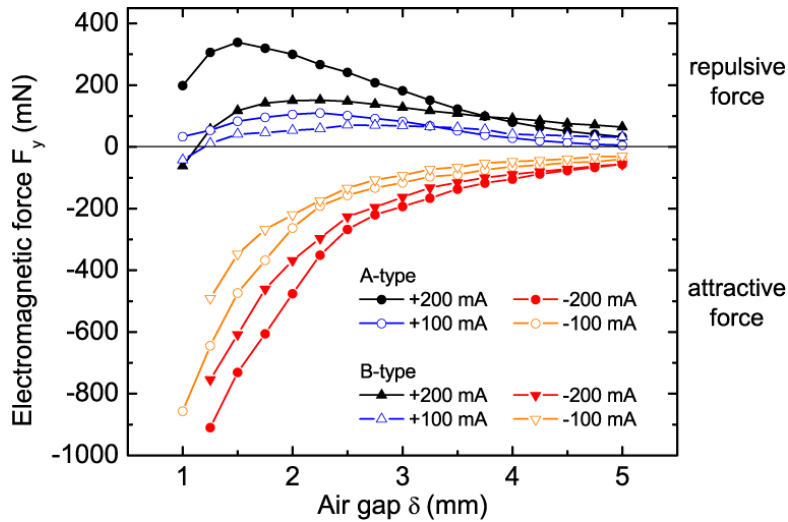


Figure 5-7: Electromagnetic force exerted on the membrane embedded magnet as a function of the air gap  $\delta$  for both ‘A-type’ and ‘B-type’ cores (DC coil current of 100 mA and 200 mA).

#### Measurement of thermal response for actuator I

Using a thermometer, we have also measured the temperature rise for the actuator during half an hour of operation using an AC rms current of 70 mA and 140 mA at 15 Hz, respectively (see Fig. 5-8). We find that the actuator reaches a temperature of 27 °C and 38 °C at 30 min, respectively.

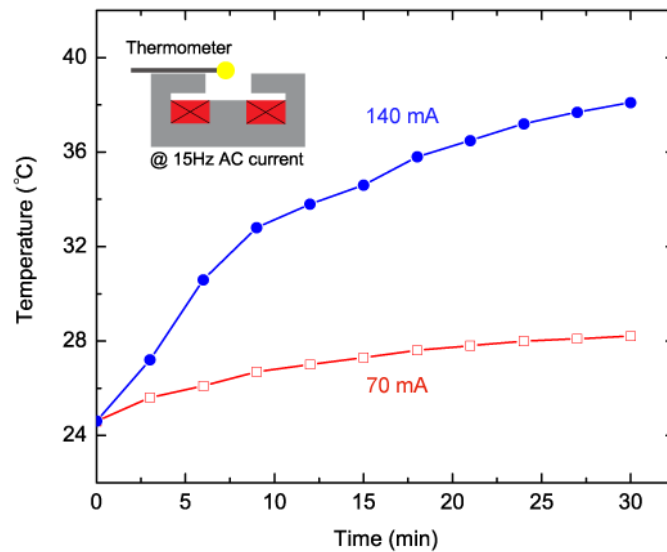


Figure 5-8: The measured temperature rise for the actuator during half an hour of operation using an AC rms current of 70 mA and 140 mA at 15 Hz, respectively.

## 5.2.2 Realization of a second type of planar cylindrical electromagnetic actuator

### *2D-axialsymmetrical simulation for actuator II*

In our previous work<sup>10, 11, 16, 18</sup>, a cylindrical non-optimized commercial coil (4800 turns, Agrate Brianza, Italy) with soft iron as magnetic core, was employed as the electromagnetic actuator. Here, two dimensional (2D) axisymmetrical FEM (Comsol Multiphysics™ 3.2) simulation is used to optimize the soft iron structure for the cylindrically structured actuator. The parameters are: a 2D permanent magnet of 3 mm in width and 3 mm in height with a y-component magnetization of  $M_y = 506$  kA/m, and a 200 mA DC coil current.

As shown in Fig. 5-9, the commercial actuator is named as ‘C-type’; the miniaturized ones are ‘D-type’ (E-core) and ‘E-type’ (E-core with cover structure). The cover soft iron in the ‘E-type’ core gives rise to an enhanced magnetic flux and more closed magnetic loop.

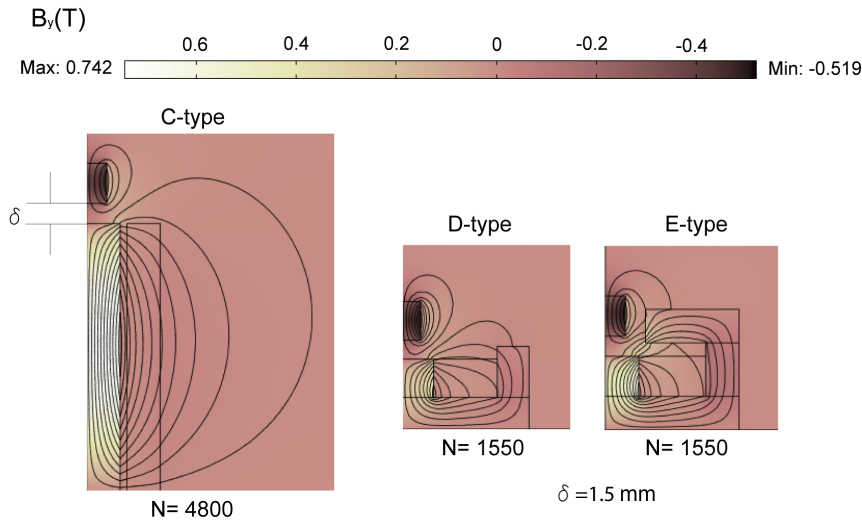


Figure 5-9: Magnetic flux density distribution representing the interaction between permanent magnet and ‘C-type’, ‘D-type’ and ‘E-type’ structures, respectively, for an air gap  $\delta = 1.5$  mm. The actuation is operated in repulsive mode with DC coil current of 200 mA.

In Table 5-1, by using a 200 mA DC actuation current, the ‘E-type’ core improves the magnetic force by a factor of 1.7 and 1.4 in attractive and repulsive mode, respectively. Furthermore, the height of the ‘E-type’ actuator has been dramatically miniaturized to only  $\frac{1}{4}$ .

Table 5-1: Comparison of the three types of magnetic circuits.

Items	C-type	D-type	E-type
Repulsive force ratio ( $F_{re}/F_{re,C}$ )	1	0.80	1.40
Attractive force ratio ( $F_{at}/F_{at,C}$ )	1	0.87	1.71
Length	20 mm	5.5 mm	5.5 mm
Coil turns	4800	1550	1550
Electric power ( $I_{rms}=140$ mA)	7.5 W	2 W	2 W

Fig. 5-10 is a schematic diagram of the actuator II (‘E-type’ actuator) which is our preferred choice: cylindrical soft iron structures, a copper coil and a permanent magnet (magnetization along the cylinder axis). The coil contains 1550 turns of copper wire (coil resistance  $R_{Cu} = 104.5 \Omega$ ). A NdFeB magnet (Maurer Magnetic AG) with a diameter of  $\phi_{mag} = 3$  mm and a height of  $h_{mag} = 3$  mm is chosen.



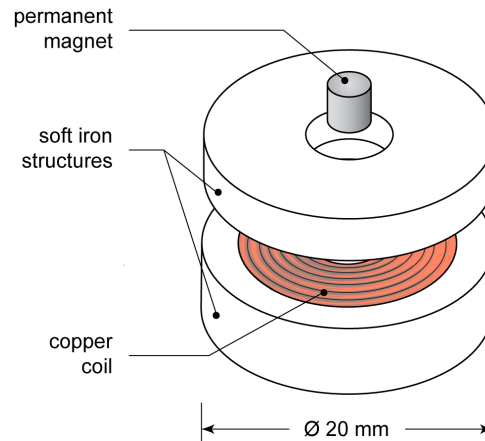


Figure 5-10: Electromagnetic actuator: 3D assembly of the soft iron parts with permanent magnet (E-type actuator-actuator II).

#### Measurement of actuation force for actuator II

We measured the electromagnetic forces of the electromagnetic circuit of Fig. 5-10 with DC coil currents  $I_{dc}$  in both the repulsive and attractive mode. The measured electromagnetic force determines the pressure of the pumping chamber. As shown in Fig. 5-11, with the same amplitude of the coil current, the attractive electromagnetic forces are much larger than the repulsive forces.

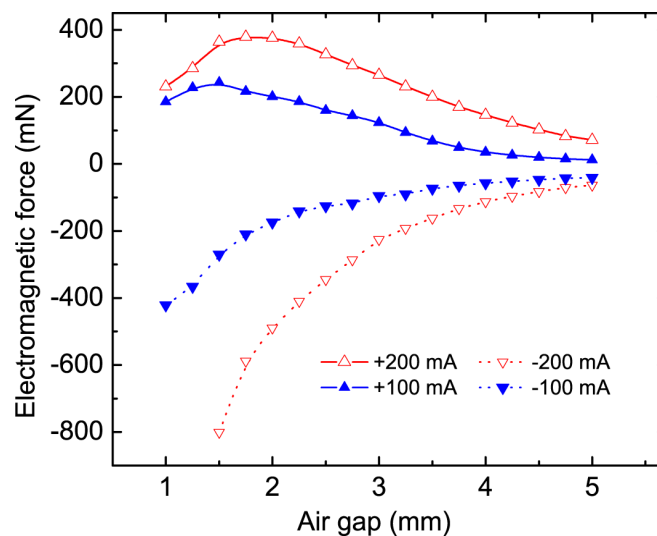


Figure 5-11: Electromagnetic force on the membrane embedded permanent magnet as a function of the air gap  $\delta$  for the 'E-type' cores (DC coil current of 100 mA and 200 mA).

The reason for the unsymmetrical forces has been explained before in Section 5.2.1. The maximum repulsive electromagnetic force is obtained at an air gap of around 1.75 mm at 200 mA and 1.5 mm at 100 mA, which we use in the following for the characterization of the micropump system.

### 5.2.3 Comparison with commercial electromagnets

Electromagnetic actuators, including voice coil actuators<sup>25-27</sup>, solenoid actuators<sup>28</sup> etc., have been widely used in industry. Since our design is similar to these commercial actuators and some of them have been already incorporated into a micropump<sup>29</sup>, it is worthwhile to compare their performances with that of our actuator (see Table 5-2). Our improved actuators have the lowest height and the ratio between force and power consumption is competitive with the commercial products. Due to the embedded permanent magnet in the PDMS membrane as moving part, the total stroke of our actuator is limited by the compliance of the membrane in the microfluidic cavity and the soft iron structure (1.3 mm).

Table 5-2: Comparison of the performances between our actuators and different commercial electromagnets

Items	Moving part	Size	Peak force	Power
OES LVCM 013-013-01 <sup>25</sup>	Coil	19.8 mm × $\phi$ 12.7 mm	0.6 N	1.25 W
H2W NCC 01-04-001-1X <sup>26</sup>	Coil	12.7 mm × $\phi$ 11.1 mm	0.8 N	1 W
Beikimco LA 05-05-000A <sup>27</sup>	Coil	12.7 mm × $\phi$ 12.7 mm	0.7 N	1.5 W
Bicron SD0420N <sup>28</sup>	Iron plunger	20 mm × (10 mm × 11 mm)	0.2 N	1.1 W
Planar actuator I	Permanent magnet	9 mm × (20mm × 15mm)	0.7 N	2 W
Planar actuator II	Permanent magnet	9 mm × $\phi$ 20 mm	0.8 N	2 W

## 5.3 Micropumps fabrication

### 5.3.1 Magnetic membrane fabrication

The microfabrication of the microfluidic chip is similar to that reported in reference<sup>16</sup>. In order to have stable pumping, self-priming and bubble tolerance of the pump, a flexible membrane with large deflection amplitude is mandatory<sup>19</sup>. The PDMS membrane with the integrated permanent magnet is obtained using a two-step molding process<sup>10, 11</sup>, as already shown in Fig. 4-7a in Section 4.2.1 from Chapter 4. Though PDMS is gas- and water vapor-permeable, this phenomenon has no impact on the pumping of liquids. The final membrane has an external diameter of 10 mm and height of 5 mm (see Fig. 4-7b)<sup>16</sup>.

### 5.3.2 Microfluidic layers design and fabrication

The complete micropump is composed of seven PMMA sheets or plates of thicknesses 0.25, 0.375 and 2 mm (see Fig. 5-12a). Layers 1, 2 and 5 serve as microfluidic channel structures for both inlet and outlet. Layers 3 and 4 are specially designed as ball-stop and ball-valve seat layers. The design principle and its microscopic structure will be presented in Section 5.4.2. Layers 5

and 6 provide the active pumping volume. Layer 7 is a support for the PDMS membrane with integrated magnet. PMMA layers were fabricated either with precision milling tools for the thick plates (ball-valve seat layer 4 and lowest layer 7), or using the powder blasting technique (other layers). We have recently demonstrated the potential of powder blasting for the realization of microfluidic three-dimensional structures in PMMA, using an erosion-resistant metal mask mechanically fixed on the PMMA sheet<sup>17, 30</sup>.

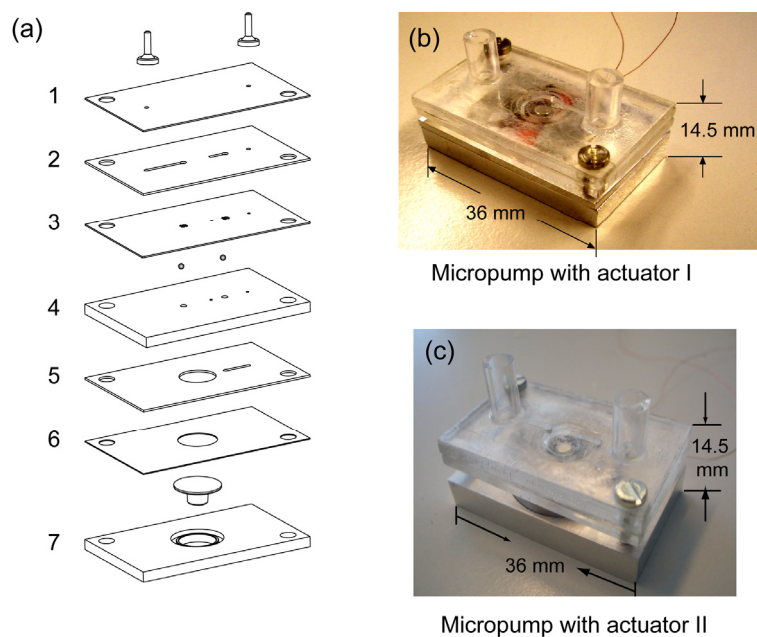


Figure 5-12: (a) Burst view of the fluidic structure of the micropump consisting of seven PMMA layers, two stainless steel balls, and a PDMS magnetic membrane. (b) Photograph of the complete micropump system consisting of the compact electromagnetic actuator I with its support and the fluidic PMMA structure. (c) Photograph of the complete micropump system consisting of the cylindrical electromagnetic actuator II with its support and the fluidic PMMA structure.

During the layers assembly process, a solution of triethylene glycol dimethacrylate (Fluka Chemie, No. 90412) is spread on the surface of a PMMA sheet before bonding. Stainless steel balls (1 mm in diameter, Kellenberg Roll- Technik AG, Oetwil am See, Switzerland) are used as the check valves. Afterwards, the bonding is realized in a hot press at 70°C for 5 minutes for each layer bonding step. For the fluidic connections to the chip surface, cylindrical PMMA connectors are polished and glued with epoxy solution at 80°C for 2 h (Epo-Tek 301-2, Epoxy Technology Inc., Illerica, Massachusetts, USA). Fig. 5-12b and Fig. 5-12c shows a photograph of the complete micropump system consisting of the fluidic PMMA structure with two types of compact electromagnetic actuators I and II with its support, respectively. The external dimension of the assembled micropump system is 36 mm × 18 mm × 14.5 mm.

## 5.4 Micropumps characterization

### 5.4.1 Experimental setup

The microfluidic circuit of the pump is clamped to the electromagnet by two screws leaving an optimized air gap between the coil plane and the bottom of the permanent magnet. Sinusoidal excitation (HP 6827A Bipolar Power supply/Amplifier) is employed to supply power to the electromagnetic actuator and the frequency is triggered by a waveform generator (Agilent 33120A). De-ionized (DI) water is chosen as base liquid to test the micropump. By taking the experimental value of the repulsive magnetic force approximately 400 mN at the optimized air gap and the membrane stiffness  $K=800$  N/m, the average deflection of the membrane is approximated as 0.32 mm. Considering the dead volume of the pumping chamber of 24  $\mu$ L, the compression ratio is calculated as 0.5, a value much higher than the minimum compression ratio for our ball-valve micropump (see the calculation in Section 5.1.2). Therefore, there is no need for priming the micropump in advance<sup>19</sup>.

The flow rate-backpressure dependence is usually measured with a water-filled tube, providing a hydrostatic backpressure  $\rho gH$  ( $H$  the height of the column of liquid) and a digital balance is used to record the flow rate as illustrated in Fig. 5-13. The frequency dependent flow rate at zero backpressure could be easily measured just by removing the external hydrostatic back-pressure and monitoring the mass difference at certain time period. The maximum hydrostatic backpressure at certain actuation frequency can be obtained when the flow rate through the micropump becomes zero. However, if the backpressure is too high to be monitored by measuring the column of liquid, pressure sensor mounted at the outlet will provide accurate results.

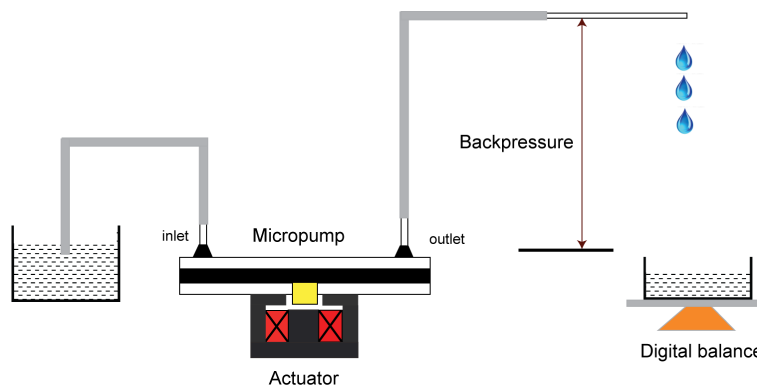


Figure 5-13: Measurement setup for backpressure and flow rate of the micropump.

For simplicity, to evaluate the ball-valve efficiency of the micropump, the external actuation sources are eliminated. The flow rectification ability can be obtained in both forward and reverse

direction by imposing certain hydrostatic pressure at inlet or outlet, as seen further.

### 5.4.2 Ball-valve design and characterization

The design of the ball-valve is shown in the inset of Fig. 5-14: the resulting seat angle of  $120^\circ$  has been chosen for optimization of flow sealing and easy fabrication by conventional tools. The inset of Fig. 5-14 also shows an optical photograph of the cross-section of the micropump showing the integrated ball-valve. The flow rectification ability of the ball valves is evaluated on the pump without any external actuation<sup>31</sup>. The flow rate is measured under a static pressure difference between the inlet and the outlet of the micropump and is shown in Fig. 5-14. The forward flow rate of the ball-valves is approximately proportional to the pressure difference and is 12 mL/min at 22.5 kPa (2.25 m H<sub>2</sub>O). In contrast, the backward flow rate is 0.15 mL/min at 25 kPa (2.5 m H<sub>2</sub>O). The backward leakage flow rate of the ball-valves is much smaller in comparison with the forward flow rate, leaving little effect on the net flow rate.

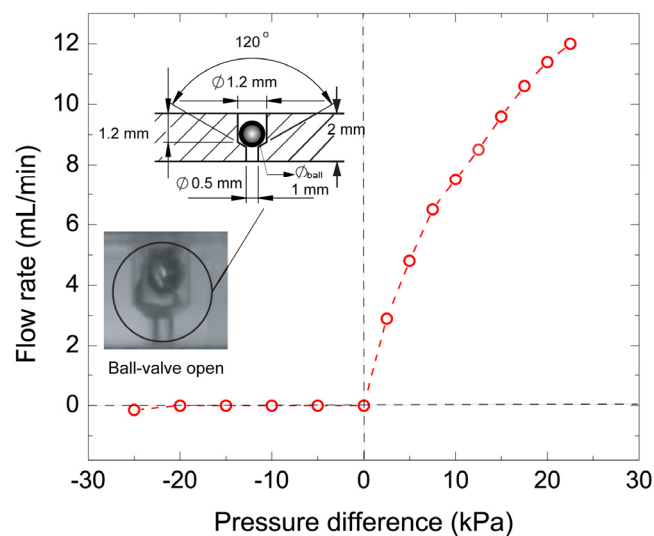


Figure 5-14: Characterization of the two ball-valves for both forward and reverse directions at different hydrostatic pressures. This measurement was performed directly on the micropump. The inset is a photograph of an integrated ball-valve in the micropump with the geometry of the ball-valve seat depicted as well.

### 5.4.3 Frequency-dependent flow rate and backpressure for the pumping of water

#### Flow rate measurement

The flow rate / frequency dependence of the micropump without any backpressure is shown in Fig. 5-15a with a rms coil actuation current of 70 mA ( $100 \text{ mA}/\sqrt{2}$ ) and 140 mA ( $200 \text{ mA}/\sqrt{2}$ ) for three different actuation structures (A, B, E). The graph indicates for structure A, *i.e.* actuator I, a maximum water flow rate of 6.8 mL/min for a 140 mA rms actuation current at a frequency

around 15-20 Hz, which is the resonant frequency of the pump. It also shows that the maximum flow rate is 3.6 mL/min at the same frequency, when actuated at 70 mA rms. For the structure E, *i.e.* actuator II, the similar behavior of frequency-dependent flow rate at 70 mA rms is shown. However, structure B, due to its lack of the cover soft iron structure, can only provide a maximum flow rate of 4 mL/min by applying the current of 140 mA rms.

### Backpressure measurement

The maximum backpressure (at zero flow rate) of our ball-valve micropump system is measured with a pressure sensor (XFPMC-100, Pewatron AG) mounted in a closed chamber or by observation of the hydrostatic pressure of a water column at the pump outlet. Fig. 5-15b shows the maximum backpressure at rms actuation currents of 70 mA and 140 mA for actuators I and II. For both actuators, at these currents, a highest value of the maximum backpressure  $\Delta P_{max}$  of 20 kPa ( $\Leftrightarrow$  2 m H<sub>2</sub>O) and 35 kPa ( $\Leftrightarrow$  3.5 m H<sub>2</sub>O) is obtained at the resonant frequency, respectively. The results reveal that the two compact planar electromagnetic actuators are able to achieve a similar excellent pumping performance at the same actuation currents, confirming the essential role of optimized soft iron structures for concentrating the magnetic flux. However, small differences regarding the pumping performance for the two types of actuators are attributed to the uncertainties arising from the measurements.

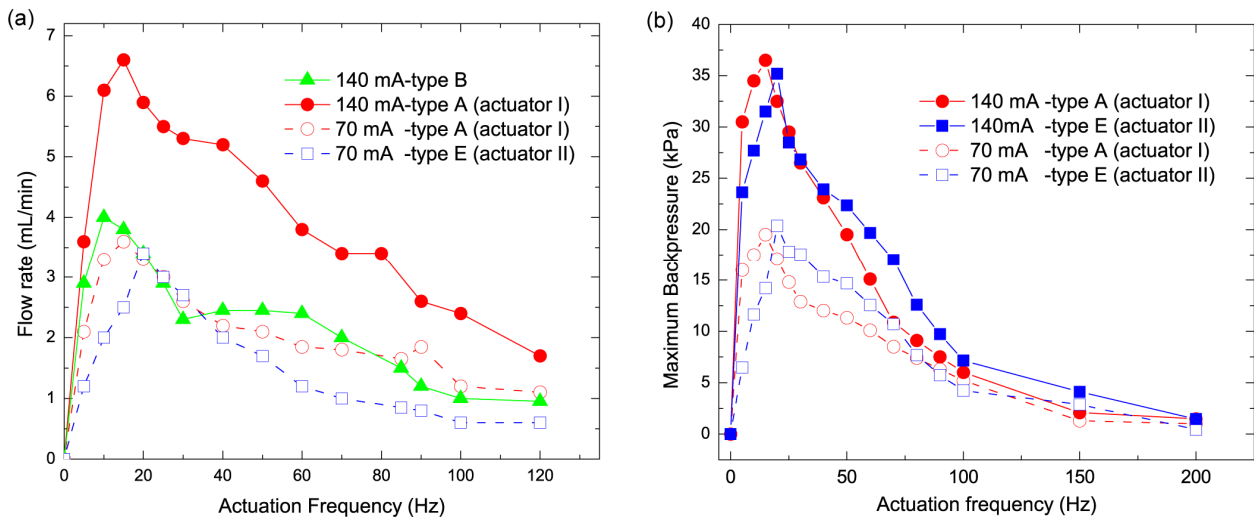


Figure 5-15: (a) Water flow rate of the ball-valve micropump as a function of the actuation frequency for two values of the rms coil current. (b) Measurement of the frequency-dependent backpressure of the ball-valve micropump. The results are obtained for different type of electromagnetic circuits, including actuator I and II.

### Measurement of backpressure-dependent flow rate

Fig. 5-16 shows the nearly linear decrease of the flow rate with backpressure for the micropump driven by actuator II. Indeed, the flow rate  $Q$  is simply proportional to the pressure

difference between pumping chamber and pump outlet.

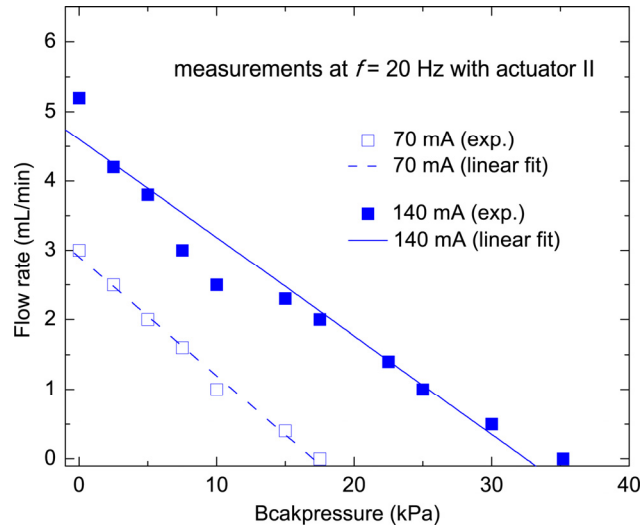


Figure 5-16: Flow rate–backpressure characteristic of the micropump actuated at 20 Hz with actuator II. The full lines are linear regression curves.

## 5.5 Simplified lumped circuit model

To explain the experimental flow rate–frequency characteristics of Fig. 5-15a, we introduce the *RLC* equivalent circuit, as already shown in Fig. 2-3. The *RLC* equivalent model<sup>10, 16, 32, 33</sup> for the volumetric flow rate  $Q$  as a function of the pulsation  $\omega$  is given by Eq. 2-29 and describes well the experimental curves of Fig. 5-15a. We use the following parameters:  $Q_0$  is the maximum flow rate, which is the average flow rate measured at resonant frequency. Table 5-3 summarizes all the fluidic parameters that we use to calculate  $R$ ,  $L$  and  $C$  from Table 2-1.

Table 5-3: Fluidic parameters used for calculating  $R$ ,  $L$ ,  $C$  and  $Q(\omega)$

DI water	$\rho = 1000 \text{ kg/m}^3$ $\mu = 1.0 \times 10^{-3} \text{ N s/m}^2$
Microfluidic circuit	$w = 0.8 \text{ mm}$ ; $h = 0.375 \text{ mm}$ ; $l = 8 \text{ mm}$ ; $D_H = 0.51 \times 10^{-3} \text{ m}$
PDMS membrane	$K = 800 \text{ N/m}$ $A_m = 3.85 \times 10^{-5} \text{ m}^2$
$R = 4.75 \times 10^9 \text{ N s/m}^5$ ; $L = 2.66 \times 10^7 \text{ kg/m}^4$ ; $C = 1.85 \times 10^{-12} \text{ m}^5/\text{N}$ ; $f_0 = 22 \text{ Hz}$	

The deduced fluidic properties are:  $R = 4.75 \times 10^9 \text{ N s/m}^5$ ,  $L = 2.66 \times 10^7 \text{ kg/m}^4$  and  $C = 1.85 \times 10^{-12} \text{ m}^5/\text{N}$ . Note that we do not use any fitting parameters in our theoretical analysis. The

calculated resonant frequency is  $f_0 = 22$  Hz.

The normalized dash-dot curve showing the frequency dependent flow rate in Fig. 5-17 has been directly calculated from Table 2-1. Although only the damping effect of the fluidic channel is taken into account, the calculated position and width of the resonant peak are in excellent agreement with the experimental data <sup>10, 16</sup>.

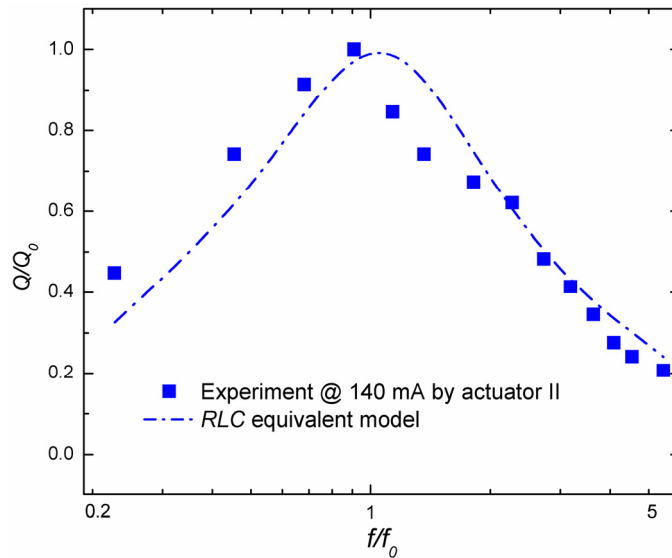


Figure 5-17: Measurement and calculated flow rates of a ball-valve micropump.

## 5.6 Performance compared with other micropumps

Beside the frequency-dependent flow rate and backpressure, the pumping power  $P_{pump} = \Delta P_{max} \cdot Q_{max} / 4$  is also an estimated parameter characterizing the performance.

The efficiency of the micropump is expressed as  $\eta = P_{pump} / P_{actuator}$  accordingly, with  $P_{actuator}$  the power consumption of the actuator. As described in the review by D.J. Laser *et al.*<sup>6</sup>, it is instructive to compare our micropump system with some previously reported reciprocating micropumps (see Table 5-4). The thermopneumatic<sup>34</sup> and shape-memory alloy driven<sup>35</sup> micropump bear a relatively low efficiency of only a few  $10^{-5}$ %. Electrostatic and electrowetting actuation used by R. Zengerle *et al.*<sup>36</sup> and K. Yun *et al.*<sup>37</sup> were proven to be really promising to offer a high pumping efficiency 0.1–0.4%. The PDMS ball-valve micropump made by T. Pan *et al.*<sup>9</sup> which was actuated by a printed circuit board (PCB) microcoil has much lower efficiency than when operated using a micromotor. For our improved micropump system, we obtain an efficiency of 0.06%, a factor 2 better compared to the previous work by C. Yamahata *et al.*<sup>16, 18</sup> at the same power consumption of 500 mW for the actuator.



Table 5-4: Comparison of the performances between our work and other reciprocating micropumps

Author	Actuator	Valves	Materials	$Q_{max}$ (mL/min)	$\Delta P_{max}$ (kPa)	$\eta$	Package size $V_{pump}$ (mm <sup>3</sup> )
Pan 2005 <sup>9</sup>	Electromagnetic (micromotor)	Ball	PDMS	0.8	7.5	0.76%	2500
Pan 2005 <sup>9</sup>	Electromagnetic (microcoil)	Ball	PDMS	1.0	3.6	0.012%	600
Van de Pol 1990 <sup>34</sup>	Thermopneuma -tic	Check	Si- Glass	0.034	5	$3.6 \times 10^{-5}$ %	3000
Bernard 1998 <sup>35</sup>	Shape-memory alloy	Flap	Si-NiTi	0.05	0.5	1.7 $\times 10^{-5}$ %	560
Zengerle 1995 <sup>36</sup>	Electrostatic	Flap	Si	0.85	29	0.39%	98
Yun2002 <sup>37</sup>	Electrowetting	Flap	Glass-SU8-Si-s ilicon rubber	0.07	0.7	0.12%	NA
This work	Electromagnetic	Ball	PMMA-PDMS	6.8	37	0.052%	11484

In order to further figure out the universal characteristics of micropumps, independent of their actuators or valving principles, as proposed by D.J. Laser *et al.*<sup>6</sup> and A. Doll<sup>38</sup>, we calculate the self-pumping frequency  $SPF \equiv Q_{max} / V_{pump}$  and the power density  $p = P_{pump} / V_{pump}$  for micropumps in Table 5-4 and the commercial ThinXXS micropump<sup>39</sup>. The self-pumping frequency and power density are significant parameters referring to the influence of pump performance on size. As shown in Fig. 5-18, due to the relatively small packaging size, the electrostatically actuated micropump<sup>36</sup> scores particularly well on aspects of both self-pumping frequency and power density, making it suitable for implantable biomedical devices. The electromagnetic actuated micropump<sup>9</sup> limited by its actuator size is less promising for an implantable application, however, such pumps can be used as integrated components for low-cost portable LOC devices when the total size is the secondary consideration. Our ball-valve micropump belongs to this category. The commercially available piezoelectrically actuated micropump ThinXXS2000 exhibits moderate power density, indicating a sound balance between the requirement for fluid dispensing and mass fabrication<sup>39</sup>. Thermopneumatic micropump as reported by F. Van De Pol *et al.*<sup>34</sup> tends to produce low flow rates and low pressures relative to its size. This must be judged against low cost manufacturing associated with this type of micropumps.

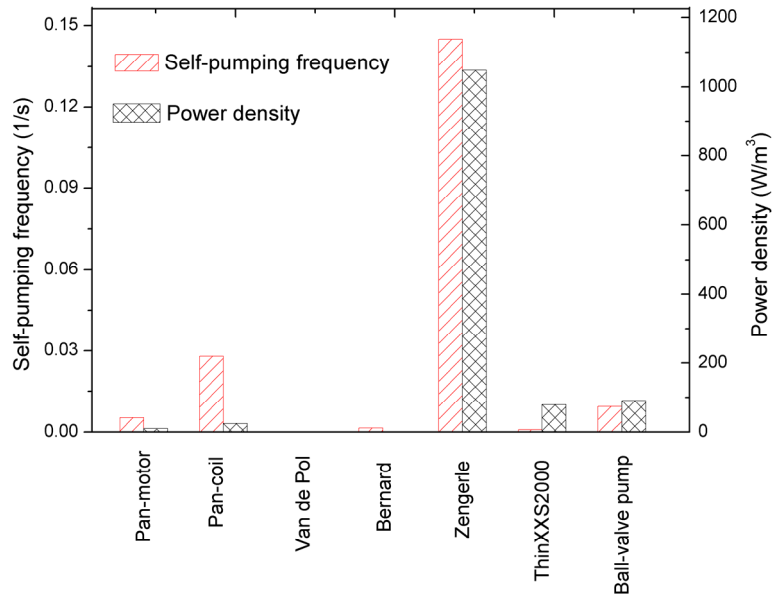


Figure 5-18: The comparison of self-pumping frequency and power density for some reciprocating micropumps.

We can easily point out the advantages of our micropump system with respect to the literature: (i) use of a low-cost material: PMMA, PDMS; (ii) easy fabrication method and modular assembly of the microfluidic and magnetic actuation circuit, meeting the requirement of industry; (iii) flat pumping geometry suitable for miniaturization; (iv) self-priming micropump, thanks to the use of magnetically actuated membrane with large deflection. The following actuation power losses play a role in our micropump system, besides the fluidic losses in the microchannels: resistive losses due to the coil windings and magnetic hysteresis losses in the magnetic core material<sup>40</sup>.

## 5.7 Conclusion

In this chapter, we have reported a PMMA ball-valve micropump actuated by two types of a miniaturized electromagnet. The design and fabrication of the microfluidic device included seven structured PMMA layers and a PDMS actuation membrane with embedded rare-earth magnet. The two types of electromagnetic actuation systems consisted of soft iron parts and a copper coil arranged in a very compact volume and they were proven to be good actuators by FEM analysis. For example, when the first type of actuator was utilized for the micropump, the corresponding pumping rate can reach 3.6 mL/min for an electromagnetic power consumption of 500 mW, and 6.8 mL/min for 2 W. A maximum backpressure of 20 kPa and 37 kPa can be achieved for an actuation power of 500 mW and 2 W, respectively. A similar performance can be attained when the the second type of actuator for the micropump was employed. We can finally note from our

data that the micropump shows optimal behavior at the resonant frequency of the microfluidic circuit, as already discussed in [Chapter 2](#).

## References

1. Shen, M.; Yamahata, C.; Gijs, M., A high-performance compact electromagnetic actuator for a PMMA ball-valve micropump. *Journal of Micromechanics and Microengineering* 2008, *18*, 025031 (9pp).
2. Shen, M.; Yamahata, C.; Gijs, M., Miniaturized PMMA ball-valve micropump with cylindrical electromagnetic actuator. *Microelectronic engineering* 2008, *85*, 1104-1107.
3. Olsson, A.; Stemme, G.; Stemme, E., A valve-less planar fluid pump with two pump chambers. *Sensors & Actuators: A. Physical* 1995, *47*, 549-556.
4. Tay, F., *Microfluidics and BioMEMS applications*. Springer Netherlands: 2002.
5. Doll, A.; Heinrichs, M.; Goldschmidtboeing, F.; Schrag, H.; Hopt, U.; Woias, P., A high performance bidirectional micropump for a novel artificial sphincter system. *Sensors and Actuators A: Physical* 2006, *130*, 445-453.
6. Laser, D.; Santiago, J., A review of micropumps. *Journal of Micromechanics and Microengineering* 2004, *14*, R35-R64.
7. Messner, S.; Schaible, J.; Sandmaier, H.; Zengerle, R., Three-way silicon microvalve for pneumatic applications with electrostatic actuation principle. *Microfluidics and Nanofluidics* 2006, *2*, 89-96.
8. Oh, K.; Ahn, C., A review of microvalves. *Journal of Micromechanics and Microengineering* 2006, *16*, R13.
9. Pan, T.; McDonald, S.; Kai, E.; Ziaie, B., A magnetically driven PDMS micropump with ball check-valves. *Journal of Micromechanics and Microengineering* 2005, *15*, 1021-1026.
10. Yamahata, C. Magnetically actuated micropumps. *PhD thesis, Ecole Polytechnique Federale de Lausanne*, 2005.
11. Yamahata, C.; Lacharme, F.; Gijs, M., Glass valveless micropump using electromagnetic actuation. *Microelectronic engineering* 2005, *78*, 132-137.
12. Yamahata, C.; Gijs, M. Plastic micropumps using ferrofluid and magnetic membrane actuation, *17<sup>th</sup> EEE International Conference on MEMS*, Maastricht, Netherland, 2004; pp 458-461.
13. Carrozza, M.; Croce, N.; Magnani, B.; Dario, P., A piezoelectric-driven stereolithography-fabricated micropump. *Journal of Micromechanics and Microengineering* 1995, *5*, 177-179.
14. Krusemark, O.; Feustel, A.; Müller, J. In *Micro ball valve for fluidic micropumps and gases*, Kluwer Academic Publishers: 1998; p 399.
15. Sin, A.; Reardon, C.; Shuler, M., A self-priming microfluidic diaphragm pump capable of recirculation fabricated by combining soft lithography and traditional machining. *Biotechnology and bioengineering* 2004, *85*, 359-363.
16. Yamahata, C.; Lacharme, F.; Burri, Y.; Gijs, M., A ball valve micropump in glass fabricated by powder blasting. *Sensors and Actuators B: Chemical* 2005, *110*, 1-7.
17. Yamahata, C.; Lotto, C.; Al-Assaf, E.; Gijs, M., A PMMA valveless micropump using electromagnetic actuation.

*Microfluidics and Nanofluidics* 2005, 1, 197-207.

18. Yamahata, C.; Lacharme, F.; Matter, J.; Schnydrig, S.; Burri, Y.; Gijs, M. Electromagnetically actuated ball valve micropumps, *Proceedings of 13<sup>th</sup> International Conference on Solid-State Sensors, Actuators and Microsystems (Transducers 2005)*, Seoul, South Korea 2005, pp 192-196.
19. Richter, M.; Linnemann, R.; Woias, P., Robust design of gas and liquid micropumps. *Sensors and Actuators A: Physical* 1998, 68, 480-486.
20. Butt, H.; Kappl, M., *Surface and interfacial forces*. 2010, Wiley-VCH Verlag GmbH&Co.
21. Chaudhury, M. K., Interfacial interaction between low-energy surfaces. *Materials Science and Engineering: R: Reports* 1996, 16, 97-159.
22. Roero, C., Contact angle measurements of sessile drops deformed by a DC electric field. *Proc. of 4<sup>th</sup> International Symposium on Contact Angle, Wettability and Adhesion, Philadelphia, USA, 2004*.
23. Fu, Y.; Ghantasala, M.; Harvey, E.; Qin, L., Design and fabrication of a hybrid actuator. *Smart Materials and Structures* 2005, 14, 488-495.
24. Lee, J.; Co, E.; Rochester, N., Measurement of magnetic fields in axial field motors. *IEEE Transactions on Magnetics* 1992, 28, 3021-3023.
25. <http://www.oesincorp.com/VCM/LVCM-013-013-01.htm>.
26. <http://www.h2wtech.com/noncommmdactu.htm>.
27. <http://beikimco.com/products/linearvoicecoil.php>.
28. <http://www.bicronusa.com/dframesolenoids.html>.
29. Kim, J.; Xu, X., Laser-based fabrication of polymer micropump. *Journal of Microlithography, Microfabrication, and Microsystems* 2004, 3, 152-158.
30. Yamahata, C.; Chastellain, M.; Parashar, V.; Petri, A.; Hofmann, H.; Gijs, M., Plastic micropump with ferrofluidic actuation. *Journal of Microelectromechanical Systems*, 2005, 14, 96-102.
31. Sim, W.; Yoon, H.; Jeong, O.; Yang, S., A phase-change type micropump with aluminum flap valves. *Journal of Micromechanics and Microengineering* 2003, 13, 286-294.
32. Bourouina, T.; Grandchamp, J., Modeling micropumps with electrical equivalent networks. *Journal of Micromechanics and Microengineering* 1996, 6, 398-404.
33. Francais, O.; Bendib, S., Electrical analogies applied on a volumetric micropump "highlighting of its fluidic resonant frequency" *Proceedings-SPIE the International Society for Optical*, United State 2001.
34. Van de Pol, F.; Van Lintel, H.; Elwenspoek, M.; Fluitman, J., A thermopneumatic micropump based on micro-engineering techniques. *Sensors and Actuators A: Physical* 1990, 21, 198-202.
35. Benard, W.; Kahn, H.; Heuer, A.; Huff, M., Thin-film shape-memory alloy actuated micropumps. *Journal of Microelectromechanical Systems*, 1998, 7, 245-251.
36. Zengerle, R.; Kluge, S.; Richter, M.; Richter, A., A bidirectional silicon micropump. *17<sup>th</sup> IEEE International Conference on MEMS, Amsterdam, Netherlands* 1995, pp.19-24.
37. Yun, K.; Cho, I.; Bu, J.; Kim, C.; Yoon, E., A surface-tension driven micropump for low-voltage and low-power operations. *Journal of Microelectromechanical Systems* 2002, 11, 454-461.

38. Doll, A., Development of a high performance micropump for an artificial sphincter system, *PhD thesis, Technische Fakultät* 2008.
39. IMM *thinXXS XXS2000 Data Sheet*. [www.thinxxs.com](http://www.thinxxs.com).
40. Ko, C.; Yang, J.; Chiou, J., Efficient magnetic microactuator with an enclosed magnetic core. *Journal of Microlithography, Microfabrication, and Microsystems* 2002, 1, 144-149.



# Chapter 6

## Active-Valve Micropump Actuated By A Rotating Magnetic Assembly

(adapted version of:

<sup>1</sup> **M. Shen**, L. Dovat, M.A.M. Gijs, Magnetic active-valve micropump actuated by a rotating magnetic assembly. *Sensors and Actuators B: Chemical*, in press, 2010, (DOI:10.1016/j.snb.2009.10.033))

**Abstract:** We report on a high-efficiency and self-priming active-valve micropump consisting of a microfluidic chamber structure in glass that is assembled with a PDMS elastic sheet. The latter comprises two valving membranes and a central pumping chamber actuation membrane, having each an integrated permanent magnet that is magnetically actuated by arc-shaped NdFeB permanent magnets mounted on the rotation axis of a DC minimotor. The choice of this actuation principle allows very low-voltage (0.7 V) and low power (a few 10 mW) operation of the micropump. For the realization, we use affordable powder blasting glass micropatterning and PDMS molding technologies. A flow rate of 2.4 mL/min and up to 7 kPa backpressure are obtained at the micropump resonance frequency of around 12 Hz, values that are much higher than reported so far for such type of micropump.

## 6.1 Introduction

### 6.1.1 Necessity for low power micropump

Microfluidics has provided attractive solutions for many problems in chemical and biological analysis, especially for in-field use or point-of-care testing, for pharmaceutical applications (drug discovery) and food quality analysis<sup>2</sup>. Irrespective of the field, precise dosing and transport of small volumes of fluid are frequently needed. Various types of micropumps have been developed for this purpose. A number of actuation methods, based on electrodynamic, electro-osmotic, electromagnetic, magnetic or thermopneumatic principles, or actuation using bubbles, shape memory alloys or hydrogels, have been investigated<sup>3-10</sup>. When considering a micropump from the viewpoint of self-priming ability and easy manufacturability, a magnetic actuation principle using an elastomeric membrane with embedded permanent magnet was proposed as very interesting option<sup>11, 12</sup>. However, one should notice that such external electromagnetic actuator with coil presents an issue of heating, which requires a higher input power; thus, external magnets with controllable movement, such as rotation, are highly demanded since it can also provide alternating magnetic forces while consume less power<sup>13</sup>. Reducing the complexity of micropump fabrication is also essential, when disposability and mass-fabrication are issues to be addressed. A planar peristaltic pump without complex mechanical moving parts has emerged as a good candidate for simple fabrication, thereby increasing the reliability of microfluidic application<sup>13, 14</sup>. A peristaltic pump consists of at least three equivalent pumping chambers that are sequentially operated to generate a pulsed flow. Such type of pump offers an interesting solution for manipulation of biological samples with no risk of channel blocking, which can be an issue for many integrated LOC applications.

### 6.1.2 Design and working principle

#### *Micropump working principle*

As shown in Fig. 6-1a, the magnetic active-valve micropump consists of three chambers (8 mm in diameter) in series formed by assembly of two glass slides. The central actuation chamber, acts as a pumping chamber like in a displacement micropump<sup>11, 12</sup>, while the left and right chambers act as valves. Here we exploit the peristaltic actuation principle, but we dimension the two valving chambers with a smaller depth than that of the central pumping chamber, resulting in an increased backpressure of the pump<sup>15</sup>. A PDMS sheet, in which three cylindrical permanent magnets are embedded is adhesively bonded on the top of these chambers. The central magnet has a height of 3 mm and its diameter is 3 mm, while the magnets situated on top of the two valving chambers are 2 mm in height and 3 mm in diameter. The working principle of the magnetic active-valve micropump is illustrated in Fig. 6-1b. A magnetic actuator is formed by mounting three pairs of arc-shaped magnets with  $2\pi/3$  phase difference on the axis of a minimotor. For easy



assembly and robust operation, this actuator is placed underneath the micropump (separation distance between the micropump and arc-shaped magnets  $d = 1.8 \text{ mm}$ ) and the rotating magnetic field of the actuator assembly induces a six-phase actuation sequence of the PDMS membranes.

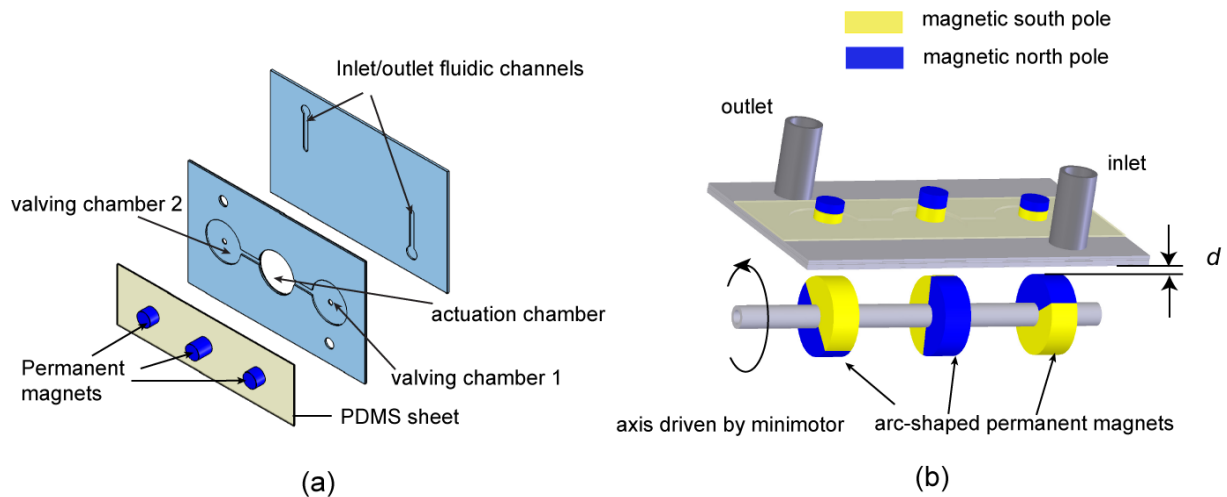


Figure 6-1: (a) Explosion view of the active-valve micropump and (b) the principle of magnetic actuation.

#### Minimum compression ratio for self-priming and bubble-tolerant pumping

Inspired by the calculation of the minimum compression ratio for active-valve micropumps done by A. Geipel *et al.*<sup>16</sup> and the for micropumps with check valves done by M. Richter *et al.*<sup>17</sup>, we have applied the latter method to our own active-valve micropump. A worst case during the pumping is corresponding to the situation where a bubble or air cavity is trapped in the liquid flow path; in this case the displacement of the air-liquid interface and related surface wetting phenomena play a significant role.

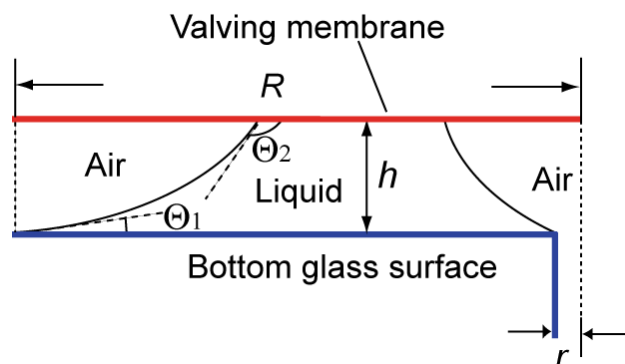


Figure 6-2: Axial-symmetrical schematic diagram of trapped water between two pockets of air (not to scale).

Fig. 6-2 is an axial-symmetrical diagram of the active valve, indicating the contact

angles  $\theta_1$  and  $\theta_2$ , surface tension  $\sigma_{LV}$  (water-air interface) and assuming that our valving chamber is filled with a residue of water with air bubbles trapped around. Here, we perform the similar calculation as what we have done in [Section 5.1.2](#) for the ball valve micropump without going to detail. The final critical pressure is expressed as follows:

$$\Delta p_{crit} = \frac{2(R+r)\sigma_{LV}}{r^2} + \frac{(\sigma_{LV} \cos\theta_1 + \sigma_{LV} \cos\theta_2)(R^2 - r^2)}{r^2 h} \quad (6-1)$$

For our active-valve micropump, we have the initial height  $h=250 \mu\text{m}$ ,  $R= 4 \text{ mm}$ ,  $r= 0.5 \text{ mm}$ , the  $\sigma_{LV} = 0.0725 \text{ N/m}$ , the contact angle  $\theta_1 = 30^\circ$  of water on glass<sup>18</sup>, and the contact angle  $\theta_2 = 105^\circ$  on untreated bare PDMS<sup>19</sup>. With these parameters, the minimum compression ratio for self-priming and bubble-tolerant characteristics becomes  $\varepsilon > 0.14$ . However, perhaps it is the worst case for the pumping. If we assume that the air bubble is only situated at the inlet (radius  $r$ ) and the rest of the chamber is filled with water, the calculated minimum compression ratio becomes only  $\varepsilon > 0.01$ .

## 6.2 Rotating magnetic assembly as actuator

### 6.2.1 Actuation sequence analysis

#### *Comparing actuation sequences*

As described above, in order to realize the peristaltic pumping, it is essential to employ a periodic external actuation sequence on these three membranes. N.J. Graf *et al.*<sup>20</sup> compared different actuation sequences, as shown in [Fig. 6-3a](#). The backpressure measurements indicate that operation in a six-phase mode allows the highest attainable maximum backpressure ([see Fig. 6-3b](#)), which is a significant parameter for pumping performance evaluation.

For the  $120^\circ$  signal, there is no point throughout the actuation cycle where at least one valve is not completely closed. For the  $90^\circ$  signal, as pressure builds at the outlet, backflow can occur between steps 2 and 3 when the outer valves change from open to closed, and closed to open, respectively. The situation is even more extreme in the  $60^\circ$  pattern, where in step 3 all three valves are open, allowing for complete backflow from outlet to inlet as pressure builds on the outlet side of the pump<sup>20</sup>. Thus, it is instructive to choose a six-phase actuation sequence with a phase variation of  $120^\circ$  as our preferred magnetic actuation sequence.

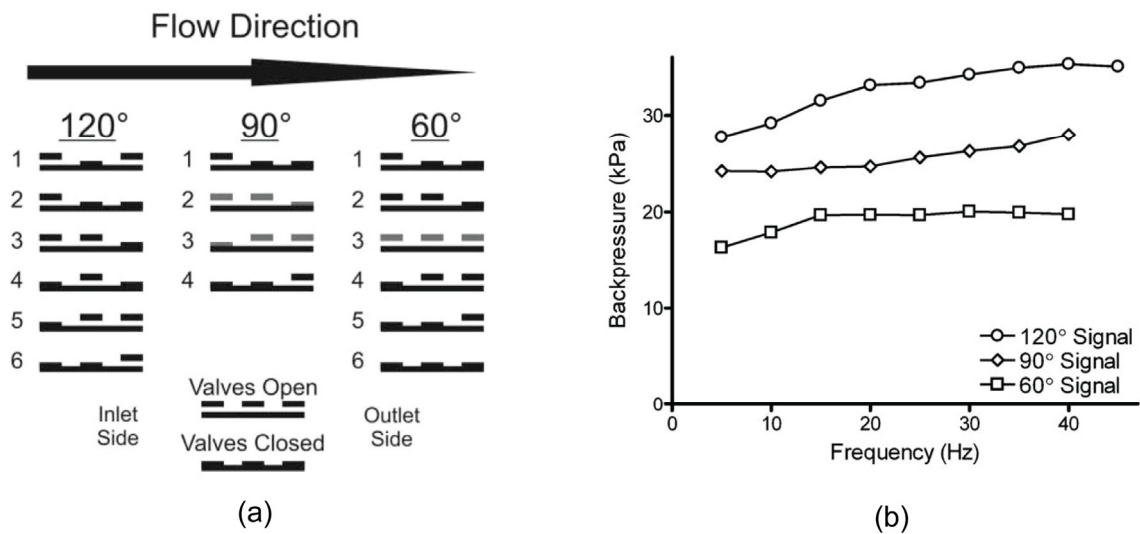


Figure 6-3: (a) Actuation sequence for these peristaltic micropump valves. Three unique square wave signal sequences are achieved by varying the phase of the signal sent to each of the actuators. These sequences can be referred to with phase difference of 120°, 90°, and 60°. (b) Effect of actuation frequency on maximum attainable backpressure. Actuation patterns with phase differences of 120°, 90° and 60° were compared<sup>20</sup>.

#### Choice of the actuation sequence

As illustrated in Fig. 6-4, the six-phase actuation enables the fluid transport from the inlet to the outlet port through the pumping and valving chambers. The flow rates can be varied by simply changing the rotation speed of the minimotor.

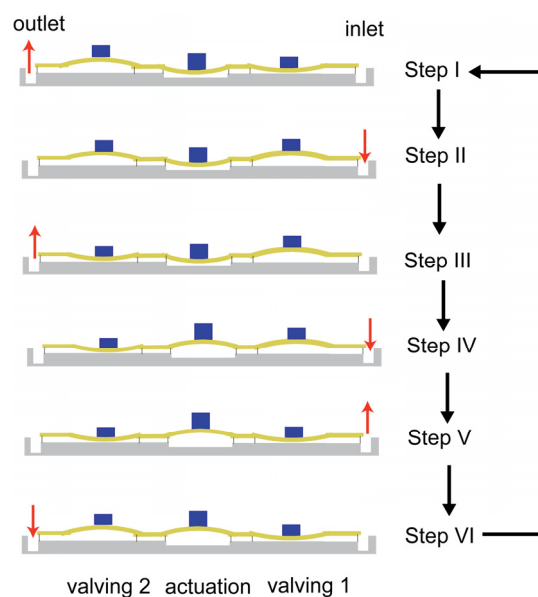


Figure 6-4: Six-phase actuation sequence of the active-valve micropump.

### 6.2.2 Magnetic force measurement

Fig. 6-5 illustrates the dipole-like magnetic force exerted by the arc-shaped magnets on the embedded permanent magnets of the central actuation chamber and the in- and outlet valving chambers during one rotation cycle of the minimotor. This force was measured using a digital balance (PT 310, Sartorius AG, Goettingen, Germany). The gap between the arc-shaped magnets and embedded permanent magnets, defined by the total thickness of the glass-PDMS structure and the separation distance  $d$ , is 3 mm. The results confirm that the phase difference between these three magnetic forces is  $2\pi/3$  forming a six-phase actuation sequence.

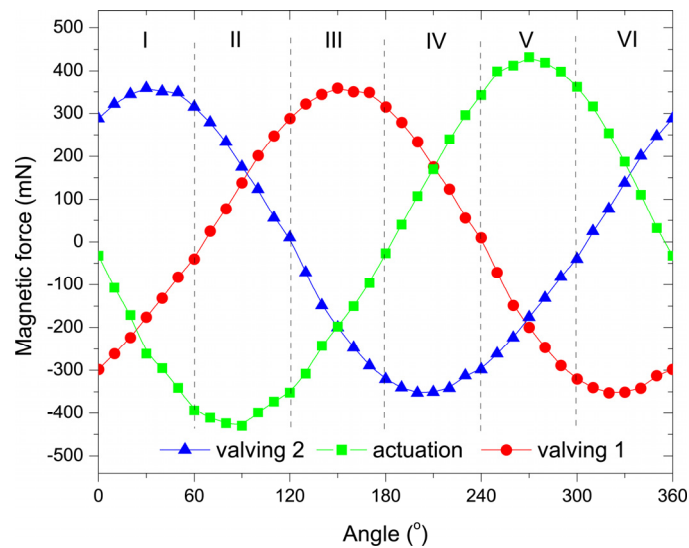


Figure 6-5: Magnetic force exerted on the two valving membranes and the central pumping membrane, as measured by a digital balance. The gap between the membrane-embedded and arc-shaped magnets is 3 mm.

### 6.3 Micropump fabrication

Two rapid prototyping techniques are used for microfabrication of the micropump: powder blasting technology for the glass substrates and a molding method for realisation of the magnetic PDMS membrane. Affordable glass slides (24 mm × 40 mm × 0.4 mm, Manzel, Braunschweig, Germany) are used for the micropump construction. Powder blasting, as an attractive microfabrication tool for rapid prototyping, is used with the operation parameters listed in Table 4-2<sup>21</sup>. The depth of the valving chamber as a function of the powder blasting time is shown in Fig. 4-4 in Chapter 4. For our micropump, the selected depth for the microchannels and the valving chambers is approximately 250 μm (deeper than our previous work of 180 μm<sup>22</sup>), while the central actuation chamber has a depth of 400 μm. After cleaning the etched glass substrates, the two layers are stacked and a high-temperature fusion bonding process at 655 °C is used to bond the glass substrates subjected to a force of 20-50 mN<sup>11</sup>, and the time-dependent temperature

control is plotted in Fig. 4-6 in Chapter 4.

The PDMS sheet with embedded permanent magnets (Grade N48, Maure Magnetic SA, Grüningen, Switzerland) is realized using a molding technology<sup>11,12</sup>, as described in Section 4.2.2 in Chapter 4. Hereafter the PDMS sheet (two thicknesses  $\sim 450\ \mu\text{m}$  and  $\sim 600\ \mu\text{m}$  are studied) is adhesively bonded to the glass using liquid PDMS as adhesive layer, a method enabling easy replacement and experimental variation<sup>23</sup>. The detailed process flow can be found in Fig. 4-9 in Chapter 4. Finally, PMMA cylindrical tubes are glued to the micropump with an Epo-Tek epoxy solution (Epo-Tek 301-2, Epoxy Technology Inc., Billerica, Massachusetts, USA) at  $80\ ^\circ\text{C}$  for 2 hours, forming the fluidic connectors.

The finalized active-valve micropump is shown in Fig. 6-6a. Fig. 6-6b is an optical microscopy image of one valving chamber. The magnetic actuator assembly with the arc-shaped NdFeB permanent magnets (N48, diametrically (parallel) magnetized, Xinchang Magnet Industry Co.,Ltd, Xiamen, China) mounted on the axis of a minimotor (Type: 1724T006SR, Minimotor SA, Croglio, Switzerland) and the complete micropump system in its experimental setup are shown in Fig. 6-6c and 6-6d, respectively.

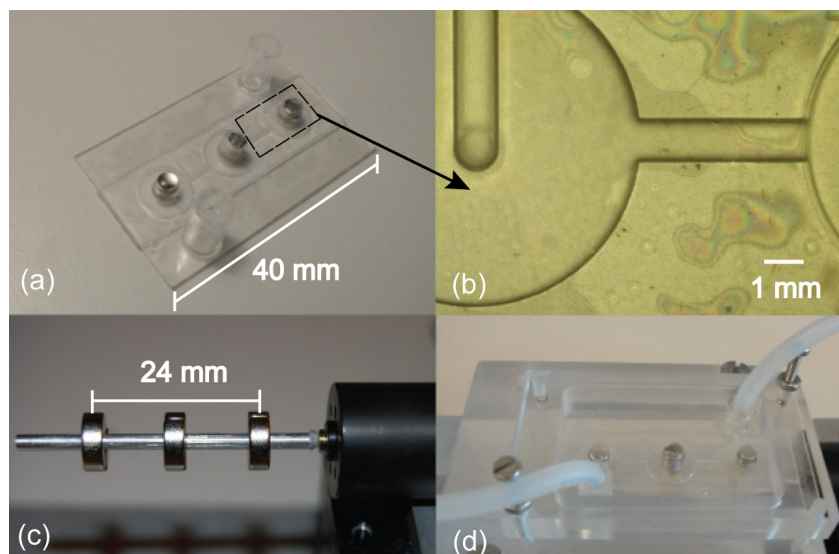


Figure 6-6: Photographs of (a) the assembled micropump, (b) a valving chamber with connecting channel, (c) the magnetic actuator assembly mounted on the axis of a minimotor and (d) the micropump system with connecting tubes.

## 6.4 Micropump characterization

### 6.4.1 Micropump characterization

#### *Frequency-dependent flow rate and backpressure measurement*

Fig. 6-7a shows the frequency-dependent water flow rate at zero backpressure for a thickness of

the PDMS sheet of 450  $\mu\text{m}$  and 600  $\mu\text{m}$ , respectively. A separation distance  $d = 1.8$  mm is used for robust micropump operation. Decreasing the distance in principle allows higher actuation forces, but can also lead to rupture and mechanical failure of the permanent magnet-PDMS integrated sheet assembly.

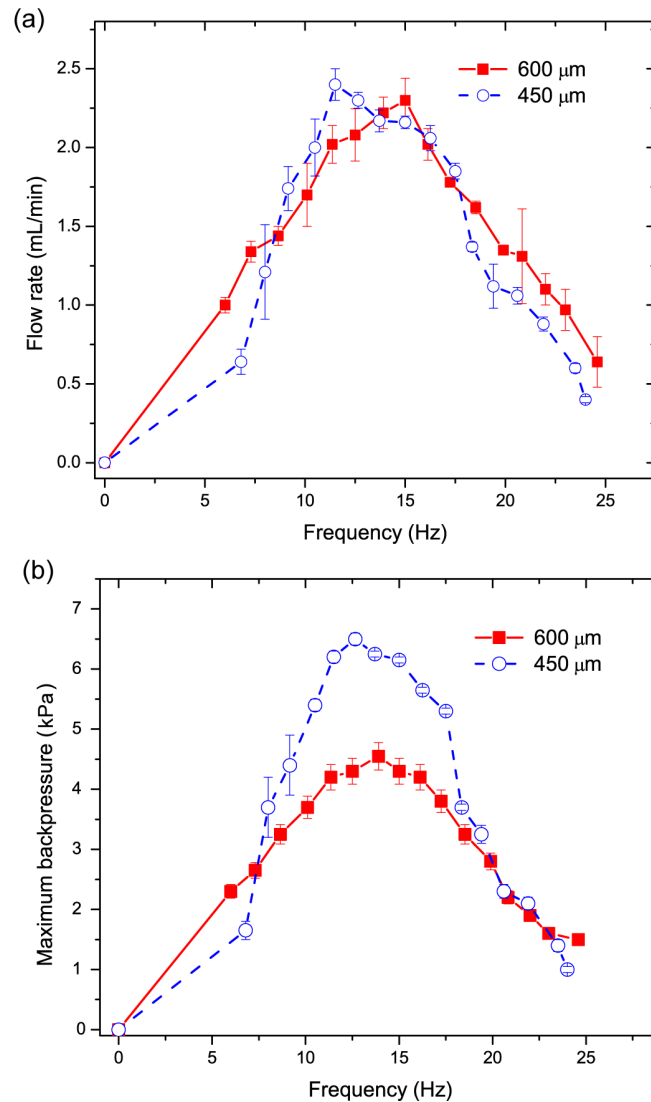


Figure 6-7: (a) Experimental frequency-dependent flow rate for two thicknesses of the PDMS sheet (450  $\mu\text{m}$  and 600  $\mu\text{m}$ ). The separation distance  $d$  is 1.8 mm. (b) Measured backpressure at various actuation frequencies.

A maximum flow rate of 2.4 mL/min is achieved at the resonance frequency of  $\sim 12$  Hz for a sheet thickness of 450  $\mu\text{m}$ , while the flow rate obtained with the 600  $\mu\text{m}$  membrane is 2.3 mL/min and the resonance frequency has shifted to  $\sim 15$  Hz. The thicker membrane leads to a smaller deflection, when subjected to the rotating magnetic field. Thus, the membrane capacitance is smaller, leading to the higher resonance frequency. Furthermore, we observe that the active-valve

micropump is self-priming and it works well, even if there are air bubbles remaining in the chambers, thanks to the high compression ratio due to large deformation of the membrane.

As shown in Fig. 6-7b, the micropump system is capable of pumping water up to a backpressure of 7 kPa at resonance, and this while the minimotor only consumes 50 mW. For the membrane thickness of 600  $\mu\text{m}$ , due to the larger operational separation distance between the membrane-integrated magnets and rotating magnetic assembly, the magnetic interaction is reduced, and, hence, the power consumption at resonance is only 30 mW. By changing the separation distance  $d$  between the actuator and micropump to 1.6 mm, the flow rate and backpressure at resonance obtained are only increased by  $10 \pm 2\%$  for the two membrane thicknesses.

#### *Backpressure dependent flow rate measurement*

As expected for a reciprocating micropump, the relation between flow rate and backpressure follows the linear regression depicted in Fig. 6-8, obtained using application of 0.7 V to the minimotor.

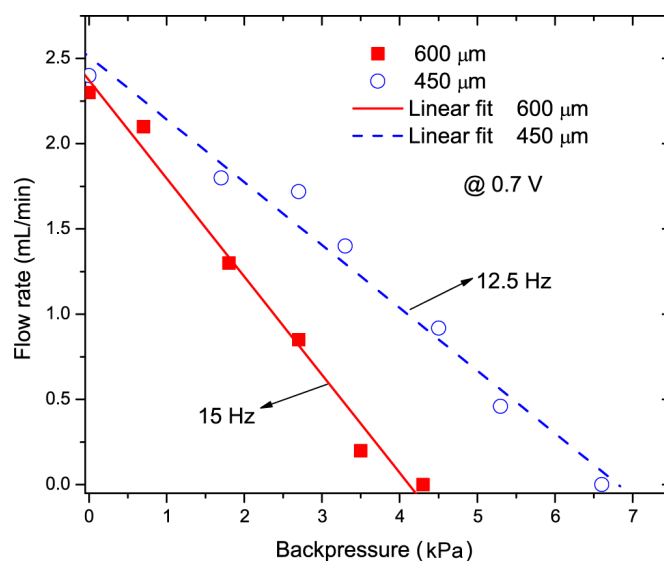


Figure 6-8: The water flow rate-backpressure characteristics at resonance for the two PDMS sheet thicknesses. The lines are linear regression curves. The experiment is conducted at 0.7 V voltage applied to the minimotor.

#### 6.4.2 Backflow effect study

Due to the working principle of the six-sequence actuation method for a peristaltic-like micropump, the backflow effect arising from the operation will affect its performance. Therefore, it is instructive to study the backflow by capturing the video (Pixelink PL-B742F) at certain time lapses, as shown in Fig. 6-9. The sequence of images points out that despite of the backflow, the amount of the forward flow exceeds that of the back flow, providing an apparent net flow rate from



the inlet to the outlet during one cycle.

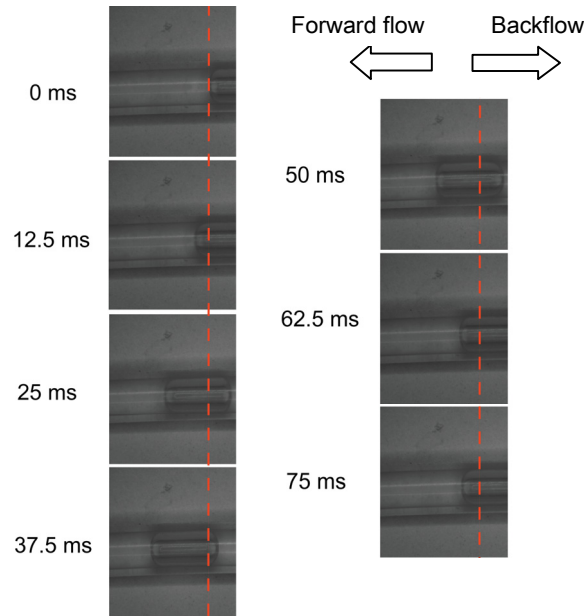


Figure 6-9: Flow video images of the active-valve micropump with a PDMS sheet thickness of  $450\ \mu\text{m}$ , when actuated by  $0.7\ \text{V}$  at  $14.5\ \text{Hz}$ . The air column was trapped in the liquid at the outlet tube for monitoring the movement.

## 6.5 Lumped circuit model

### 6.5.1 RLC equivalent circuit

A numerical simulation of our active-valve micropump, based on a lumped  $RLC$  circuit model, has been implemented using Simulink in MATLAB<sup>10</sup>. Since the active-valve micropump has one central actuation chamber and two valving chambers, each with oscillating PDMS membrane, the equivalent circuit becomes rather complex (see the diagram of Fig. 6-10).

The six-phase actuation forces are considered as power sources for the three individual PDMS membranes. For simplicity, the actuation signals  $U_{valve}$  and  $U_{actuation}$  are modeled as sinusoidal waves with phase difference of  $2\pi/3$  and amplitude proportional to the magnitude of the magnetic forces shown before. The capacitance of the membranes  $C_m$ , the chambers  $C_{actuation}$ ,  $C_{valve}$  and the inductances of the central actuation chamber  $L_{actuation}$  and the two valving chambers  $L_{valve}$  are taken into account; these inductances include the contributions from both the membrane and chamber liquid volume. The rectifying effect of the flow is modeled by a diode in combination with a fluidic resistance that is different whether the membrane deflects in the upward or downward direction. Constant resistances  $R_{actuation}$  or  $R_{valve}$  are set as adjustable parameters for the membrane downward position. Zero resistance is selected when the PDMS membrane deflects upwards,



because the increased volume of the chamber leads to a strongly decreased flow resistance. The connecting channels between the central actuation and valving chambers, the in-and outlet channels, as well as the connection tubes are represented by resistances and inductances arranged in series, connected in parallel to capacitances.

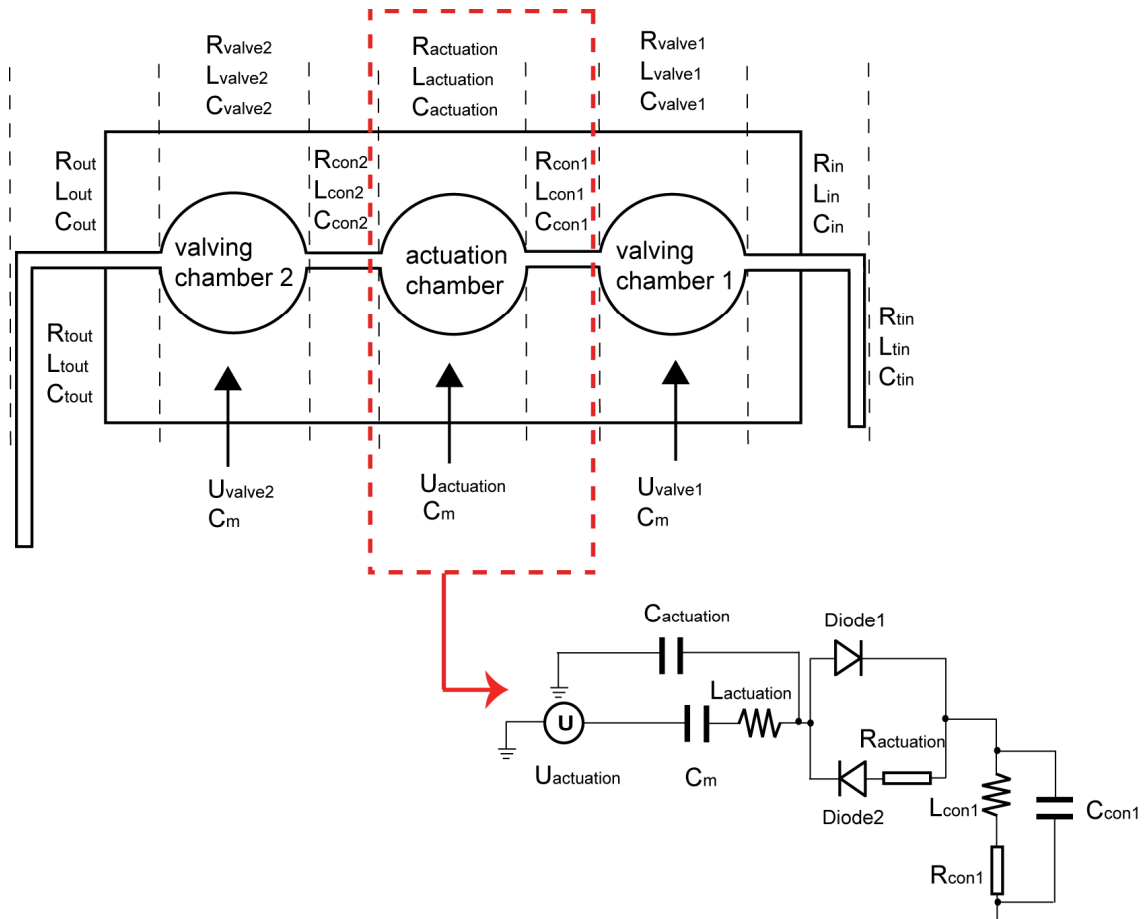


Figure 6-10: Equivalent circuit diagram of the active-valve micropump. The RLC-circuit for the indicated block, corresponding to the central actuation chamber, its corresponding membrane and connecting channel, is represented on the lower right.

The various physical and geometrical values of the micropump components are listed in [Table 6-1](#). The PDMS membrane properties are obtained from the work of D. Shaw *et al.*<sup>24</sup> where they prepare the sample in the same way as we do; and its shape factor can be simply estimated from the formula in the literature<sup>25</sup>.

Table 6-1: Geometrical and physical parameters of the active-valve micropump used for the lumped circuit model simulation.

Elements	Value
Membrane/ chamber diameter $d_m$	8 mm
Membrane thickness $h_m$	600 $\mu\text{m}$
Young's modulus of PDMS $E$	1.5 MPa
Poisson's ratio of PDMS $\nu$	0.49
PDMS density $\rho_{PDMS}$	965 $\text{kg}/\text{m}^3$
Magnet diameter $d_{mag}$	3 mm
Actuation magnet mass $m_a$	157 mg
Valving magnet mass $m_v$	107 mg
Actuation chamber depth $h_a$	400 $\mu\text{m}$
Valving chamber depth $h_v$	250 $\mu\text{m}$
Connecting/ inlet/ outlet channel width $w_{con}/w_{in}/w_{out}$	1 mm
Connecting/ inlet/ outlet channel depth $h_{con}/h_{in}/h_{out}$	250 $\mu\text{m}$
Connecting channel length $l_{con}$	4 mm
Inlet/ outlet channel length $l_{in}/l_{out}$	8 mm
Inlet/ outlet tube diameter $d_{tin}/d_{tout}$	1.6 mm
Inlet tube length $l_{tin}$	300 mm
Outlet tube length $l_{tout}$	700 mm
Water density $\rho$	10 <sup>3</sup> $\text{kg}/\text{m}^3$
Water compress-permissibility $k$	2.2 $\times 10^9$ Pa
Water viscosity $\mu$	10 <sup>-3</sup> N s/m <sup>2</sup>

Table 6-2 summarizes all the calculated values assigned to the parameters in this lumped circuit model. All resistances, except  $R_{actuation}$  and  $R_{valve1}/R_{valve2}$ , inductances, as well as the capacitance of the membranes, chambers and channels are calculated based on the formulas mentioned in the work of Y. Hsu *et al.*<sup>10</sup>, E. Morganti *et al.*<sup>26</sup> and our previous work<sup>12</sup>.

Table 6-2: Calculated parameters for the components of the lumped circuit model

Components	Calculated value
Membrane capacitance $C_m$	$1.68 \times 10^{-12} \text{ m}^5 / \text{N}$
Actuation chamber inductance $L_{actuation}$	$1.3 \times 10^5 \text{ kg/m}^4$
Valving chamber inductance $L_{valve1}/L_{valve2}$	$2.9 \times 10^5 \text{ kg/m}^4$
Actuation chamber capacitance $C_{actuation}$	$9.1 \times 10^{-18} \text{ m}^5 / \text{N}$
Valving chamber capacitance $C_{valve1}/C_{valve2}$	$5.7 \times 10^{-18} \text{ m}^5 / \text{N}$
Connecting channel resistance $R_{con1}/R_{con2}$	$6.35 \times 10^9 \text{ N s/ m}^5$
Connecting channel inductance $L_{con1}/L_{con2}$	$1.6 \times 10^7 \text{ kg/m}^4$
Connecting channel capacitance $C_{con1}/C_{con2}$	$4.55 \times 10^{-19} \text{ m}^5 / \text{N}$
Inlet/ outlet channel resistance $R_{in}/R_{out}$	$1.28 \times 10^{10} \text{ N s/ m}^5$
Inlet/ outlet channel inductance $L_{in}/L_{out}$	$3.2 \times 10^7 \text{ kg/m}^4$
Inlet/ outlet channel capacitance $C_{in}/C_{out}$	$9.1 \times 10^{-19} \text{ m}^5 / \text{N}$
Inlet tube resistance $R_{tin}$	$1.86 \times 10^9 \text{ N s/ m}^5$
Inlet tube inductance $L_{tin}$	$1.5 \times 10^8 \text{ kg/m}^4$
Inlet tube capacitance $C_{tin}$	$2.74 \times 10^{-16} \text{ m}^5 / \text{N}$
Outlet tube resistance $R_{tout}$	$4.34 \times 10^9 \text{ N s/ m}^5$
Outlet tube inductance $L_{tout}$	$3.47 \times 10^8 \text{ kg/m}^4$
Outlet tube capacitance $C_{tout}$	$6.38 \times 10^{-16} \text{ m}^5 / \text{N}$

### 6.5.2 Comparison with experimental results

The numerical result at different actuation frequencies is plotted by the dashed curve in Fig. 6-11, whereby the maximum flow rate is set to the experimental value at resonance. The only fitting parameters are  $R_{actuation} = 4.5 \times 10^9 \text{ N s/ m}^5$  and  $R_{valve1}/R_{valve2} = 6.9 \times 10^{10} \text{ N s/ m}^5$ , which together determine the width of resonance of Fig. 6-11. At high frequencies, the experimental results are well below the numerical simulation, which can be attributed to a non-perfect closure of the valving membranes and associated backflow effects.

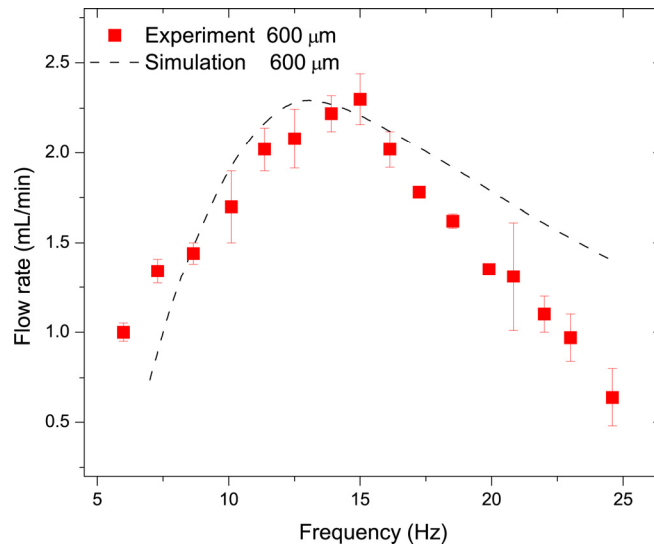


Figure 6-11: Comparison between the experimental results and numerical lumped circuit simulations for the active-valve micropump with 600  $\mu\text{m}$  thick PDMS sheet.

## 6.6 Comparison with the state-of-the-art

The criteria for choosing a micropump for laboratory use are: low-cost, easy-to-make, tunable flow rate, high backpressure, low power consumption as well as self-pumping frequency. Table 6-3 summarizes the performance of our magnetic active-valve micropump with peristaltic micropumps previously reported in literature. Jeong *et al* proposed a thermopneumatic peristaltic micropump in glass by using a deformable PDMS layer and demonstrated a flow rate of 0.022 mL/min<sup>9</sup>. Piezoelectric and light-weight piezo-composite actuators (LIPCAs) were used in peristaltic micropumps made, either by cleanroom processing involving silicon, or by molding PDMS microstructures<sup>15, 27</sup>. Due to the smaller size of the valving chambers in the work of F. Goldschmidtboing *et al*<sup>15</sup>, the micropump backpressure can be as high as 40 kPa, which is the highest value reported so far. Owing to the very small design and packing size of the F. Goldschmidtboing's micropump (400 mm<sup>3</sup>), its self-pumping frequency ( $Q_{max}/V_{pump}$ ) amounts to 0.06 1/s, a value 30 times higher than factor for our micropump. Though the PDMS micropump driven by LIPCAs enables fast prototyping and low power consumption (45 mW), its low backpressure limits its application<sup>27</sup>. The work by T. Pan *et al*<sup>13</sup> is similar to our active-valve micropump, since it also used permanent magnets for actuation, which result in relatively large packaging size (2000 mm<sup>3</sup>). However, due to its three-phase actuator design, backflow effects result in a low flow rate and backpressure and its self-pumping frequency is much lower than our system, only 1/10.

As we have already mentioned in Chapter 5, the self-pumping frequency is a significant parameter to judge the pumps' appropriate application. From the comparison, we could easily say

the micropumps using piezoelectric actuators own particular advantages for implantable devices due to their extremely compact size, while the micropumps with magnetic actuations could be integrated merely in certain applications where low operation voltage is a priority.

Therefore, from this table, it is easy to point out that our magnetic active-valve micropump benefits from a low-cost and rapid prototyping manufacturability, a suitable flow rate and backpressure range compatible with a microfluidic application, as well as low energy consumption. It has a high potential to be integrated in portable applications where a battery is used. However, its large packaging size could be an obstacle for its integration in implantable surgery system.

*Table 6-3: Characteristics of peristaltic micropumps reported in literature.*

<b>Author</b>	<b>Actuation</b>	<b>Material</b>	<b>Maximum flow rate</b>	<b>Backpressure</b>	<b>Power</b>
O.C. Jeong <sup>9</sup>	Three-phase thermopneumatic	Glass /PDMS	0.022 mL/min	NA	NA
F. Goldschmidtböing <sup>15</sup>	Six-phase piezoelectric	Silicon	1.4 mL/min	40 kPa	NA
M. Pham <sup>27</sup>	Four-phase mini LIPCA's	PDMS	0.9 mL/min	1.8 kPa	45 mW
T. Pan <sup>13</sup>	Three-phase magnets on minimotor axis	PDMS	0.024 mL/min	0.33 kPa	11 mW
This work	Six-phase arc-shaped magnets on minimotor axis	Glass /PDMS	2.4 mL/min	6.6 kPa	50 mW

## 6.7 Conclusion

In this chapter, the simple and affordable powder blasting and molding technologies have been used for microfabrication of a magnetic active-valve micropump in glass/PDMS. It exhibited a high backpressure up to 7 kPa and a flow rate of 2.4 mL/min, making it a promising component for microfluidic integration. Our magnetic active-valve micropump used arc-shaped permanent magnets mounted on the rotation axis of DC minimotor in a six-phase configuration and can be very easily operated without requiring any external driving circuit. The choice of this actuation

principle allowed very low-voltage (0.7 V) and low power (a few 10 mW) operation of the micropump. We also have developed a simplified *RLC* equivalent model that predicts the correct resonance frequency of our micropump. We can anticipate that the excellent characteristics of our micropump, thanks to the use of the low power magnetic actuation principle and a high deflection magnetic membrane, led to an advantageous use of such type of pump in future portable LOC applications.

## References

1. Shen, M.; Dovat, L.; Gijs, M., Magnetic active-valve micropump actuated by a rotating magnetic assembly. *Sensors and Actuators B: Chemical* 2009.
2. Reyes, D.; Iossifidis, D.; Auroux, P.; Manz, A., Micro total analysis systems. 1. Introduction, theory, and technology. *Analytical Chemistry* 2002, 74, 2623-2636.
3. Laser, D.; Santiago, J., A review of micropumps. *Journal of micromechanics and microengineering* 2004, 14, R35-R64.
4. Zeng, S.; Chen, C.; Mikkelsen, J., Fabrication and characterization of electroosmotic micropumps. *Sensors and Actuators B: Chemical* 2001, 79, 107-114.
5. Tsai, J.; Lin, L., A thermal-bubble-actuated micronozzle-diffuser pump. *Journal of microelectromechanical systems* 2002, 11, 665-671.
6. Benard, W.; Kahn, H.; Heuer, A.; Huff, M., Thin-film shape-memory alloy actuated micropumps. *Journal of Microelectromechanical Systems*, 1998, 7, 245-251.
7. Richter, A.; Klatt, S.; Paschew, G.; Klenke, C., Micropumps operated by swelling and shrinking of temperature-sensitive hydrogels. *Lab on a Chip* 2009, 9, 613-618.
8. Khoo, M.; Liu, C. A novel micromachined magnetic membrane microfluid pump, *Proceedings of the International Conference of the IEEE Engineering in Medicine and Biology Society*, Chicago, IL, USA 2000, pp. 1-4.
9. Jeong, O.; Park, S.; Yang, S.; Pak, J., Fabrication of a peristaltic PDMS micropump. *Sensors and Actuators A: Physical* 2005, 123, 453-458.
10. Hsu, Y.; Li, J.; Le, N., An experimental and numerical investigation into the effects of diffuser valves in polymethylmethacrylate (PMMA) peristaltic micropumps. *Sensors and Actuators A: Physical* 2008, 148, 149-157.
11. Yamahata, C.; Lacharme, F.; Gijs, M., Glass valveless micropump using electromagnetic actuation. *Microelectronic Engineering* 2005, 78, 132-137.
12. Shen, M.; Yamahata, C.; Gijs, M., A high-performance compact electromagnetic actuator for a PMMA ball-valve micropump. *Journal of Micromechanics and Microengineering* 2008, 18, 025031(9pp).
13. Pan, T.; Kai, E.; Stay, M.; Barocas, V.; Ziaie, B. A magnetically driven PDMS peristaltic micropump, *Proceedings of the 26<sup>th</sup> Annual International Conference of the IEEE EMBS*, San Francisco, CA, USA 2004, pp. 2639-2642.
14. Yobas, L.; Tang, K.; Yong, S.; Ong, E., A disposable planar peristaltic pump for lab-on-a-chip. *Lab on a Chip*

2008, 8, 660-662.

15. Goldschmidtböing, F.; Doll, A.; Heinrichs, M.; Woias, P.; Schrag, H.; Hopt, U., A generic analytical model for micro-diaphragm pumps with active valves. *Journal of Micromechanics and Microengineering* 2005, 15, 673.
16. Geipel, A.; Goldschmidtböing, F.; Doll, A.; Jantscheff, P.; Esser, N.; Massing, U.; Woias, P., An implantable active microport based on a self-priming high-performance two-stage micropump. *Sensors and Actuators A: Physical* 2008, 145-146, 414-422.
17. Richter, M.; Linnemann, R.; Woias, P., Robust design of gas and liquid micropumps. *Sensors and Actuators A: Physical* 1998, 68, 480-486.
18. Sumner, A. L.; Menke, E. J.; Dubowski, Y.; Newberg, J. T.; Penner, R. M.; Hemminger, J. C.; Wingen, L. M.; Brauers, T.; Finlayson-Pitts, B. J., The nature of water on surfaces of laboratory systems and implications for heterogeneous chemistry in the troposphere. *Physical Chemistry Chemical Physics* 2004, 6, 604-613.
19. Mata, A.; Fleischman, A.; Roy, S., Characterization of Polydimethylsiloxane (PDMS) Properties for Biomedical Micro/Nanosystems. *Biomedical Microdevices* 2005, 7, 281-293.
20. Graf, N.; Bowser, M., A soft-polymer piezoelectric bimorph cantilever-actuated peristaltic micropump. *Lab on a Chip* 2008, 8, 1664.
21. Pawlowski, A.; Sayah, A.; Gijs, M., Accurate masking technology for high-resolution powder blasting. *Journal of Micromechanics and Microengineering* 2005, 15, S60-S64.
22. Shen, M.; Gijs, M., High-performance magnetic active-valve micropump, *Proceedings of 15<sup>th</sup> International Conference on Solid-State Sensors, Actuators and Microsystems (Transducers 2009)*, Denver, USA 2009, pp. 1234-1237.
23. Wu, H.; Huang, B.; Zare, R., Construction of microfluidic chips using polydimethylsiloxane for adhesive bonding. *Lab on a Chip* 2005, 5, 1393-1398.
24. Shaw, D.; Sun, T., Optical properties of variable-focus liquid-filled optical lenses with different membrane shapes. *Optical Engineering* 2007, 46, 024002 (6pp).
25. Bardell, R.; Sharma, N.; Forster, F.; Afromowitz, M.; Penney, R., Designing high-performance micro-pumps based on no-moving-parts valves. *Microelectromechanical systems (MEMS), ASME* 1997, 354, pp. 47-53.
26. Morganti, E.; Fuduli, I.; Montefusco, A.; Petasecca, M.; Pignatelli, G., SPICE modelling and design optimization of micropumps. *International Journal of Environmental Analytical Chemistry* 2005, 85, 687-698.
27. Pham, M.; Nguyen, T.; Goo, N., Development of a peristaltic micropump for bio-medical applications based on mini LIPCA, *ICIUS 2007*, Bali, Indonesia, 2007, pp. 126-131.





# Chapter 7

## Monolithic Micro-Direct Methanol Fuel Cell With Microfluidic Channel-Integrated Nafion Strip

(adapted version of:

<sup>1</sup> M. Shen, S. Walter, M.A.M. Gijs, Monolithic micro-direct methanol fuel cell in polydimethylsiloxane with microfluidic channel-integrated Nafion strip. *Journal of Power Sources*, 2009, 193, 761-765)

**Abstract:** We demonstrate a monolithic polymer electrolyte membrane fuel cell by integrating a narrow (200  $\mu\text{m}$ ) Nafion strip in a molded PDMS structure. We propose two designs, based on two 200  $\mu\text{m}$ -wide and two 80  $\mu\text{m}$ -wide parallel microfluidic channels, sandwiching the Nafion strip, respectively. Clamping the PDMS/ Nafion assembly with a glass chip that has catalyst-covered Au electrodes, results in a leak-tight fuel cell with stable electrical output. Using 1 M  $\text{CH}_3\text{OH}$  in 0.5 M  $\text{H}_2\text{SO}_4$  solution as fuel in the anodic channel, we compare the performance of (I)  $\text{O}_2$ -saturated 0.5 M  $\text{H}_2\text{SO}_4$  and (II) 0.01 M  $\text{H}_2\text{O}_2$  in 0.5 M  $\text{H}_2\text{SO}_4$  oxidant solutions in the cathodic channel. For the 200  $\mu\text{m}$  channel width, the fuel cell has a maximum power density of 0.5  $\text{mW}/\text{cm}^2$  and 1.5  $\text{mW}/\text{cm}^2$  at room temperature, for oxidant I and II, respectively, with fuel and oxidant flow rates in the 50-160  $\mu\text{L}/\text{min}$  range. A maximum power density of 3.0  $\text{mW}/\text{cm}^2$  is obtained, using oxidant II for the chip with 80  $\mu\text{m}$ -wide channel, due to an improved design that reduces oxidant and fuel depletion effects near the electrodes.

## 7.1 Introduction

### 7.1.1 Advantages of planar microfluidic fuel cells

Microfabricated liquid fuel cells are of increasing interest for high-energy density portable applications<sup>2-4</sup>. Fuel cells operating on liquid fuel, like methanol, allow a simple system design and low temperature operation. The overall performance of a fuel cell is a very sensitive function of parameters, like the choice of electrodes and catalysts, fuel and oxidant solutions, the use of a proton exchange membrane (PEM) or not, and the microfluidic design. Moreover, easy assembly and the use of affordable materials and system components are important issues. A high electrical output power density can be obtained in rather complex bipolar micro-direct methanol fuel cells (micro-DMFC), in which the PEM or membrane electrode assembly (MEA) is sandwiched between fuel and oxidant flow chambers<sup>3-7</sup>. In a monolithic fuel cell design, the anodic and cathodic channels are realized in the same substrate, which allows easy prototyping. Monolithic designs can include a proton exchange membrane<sup>8, 9</sup>, or can be membraneless<sup>10-13</sup>. In the former case, membrane integration and leakage can present an issue, while a membraneless strategy requires high-precision fuel and oxidant flows (a few hundreds of  $\mu\text{L}/\text{min}$ ) to maintain the liquid junction. Using PDMS elastomeric fluidic channels can avoid leakage problems during hybrid integration of the PEM<sup>8</sup> or of electrodes<sup>14</sup>. The latter approach was shown particularly interesting for high electrical power output, when porous electrodes with high catalytic surface area are used<sup>14</sup>.

### 7.1.2 Design and working principle

PDMS is chosen as material for our micro-DMFC, because of its easy application and its good chemical resistance<sup>15</sup>. [Figs. 7-1a](#) and [7-1b](#) are schematic oblique and side views of the planar micro-DMFC, respectively. The device is based on three components: a PDMS chip with patterned microchannels, a narrow Nafion strip and a float glass substrate with catalytic electrodes. This planar structure allows the protons generated at the anode to be transferred to the cathode, without requiring a complex MEA. As illustrated in [Fig. 7-1c](#), the individual microfluidic channels of fuel and oxidant are simply formed by placing the rigid 200  $\mu\text{m}$ -wide Nafion strip using a dedicated guiding channel in the PDMS chip.

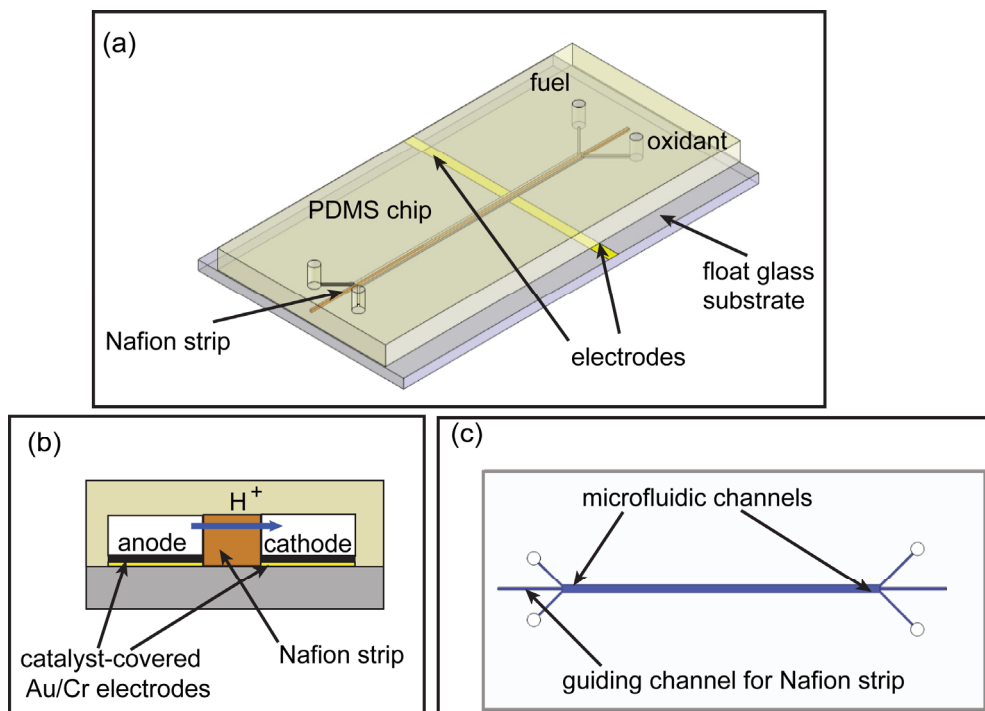


Figure 7-1: (a) Oblique schematic view of the micro-DMFC. (b) Cross-section of the micro-DMFC with integrated Nafion strip (not to scale). (c) Top view of the PDMS chip design (chip size: 15 mm×36 mm).

## 7.2 Experimental

### 7.2.1 Microfabrication process

The fabrication of the planar micro-DMFC includes the following steps, shown in Fig. 7-2: (1) a 170  $\mu\text{m}$  thick SU8 structure for definition of the microchannel is patterned on a Si wafer, (2) PDMS (Sylgard 184, Dow Corning Inc. Midland, MI) is poured onto this master structure and it is cured at 75  $^{\circ}\text{C}$  for 2 h, after which the PDMS chip with integrated guiding channel is peeled off from the mold. (3) Using a metallic shadow mask, we deposit a 100 nm thick Au electrode using a 5 nm chromium adhesion layer (Auto 306 Resistance evaporation system, Edwards, Crawley, UK) on a piranha-cleaned glass slide (Menzel GmbH, Braunschweig, Germany). Annealing at 150  $^{\circ}\text{C}$  for 2 hours is required to enhance the adhesion between the metal and glass slide. (4) Pt/Ru (Pt: Ru=1:1) catalyst, supported on carbon black with metal content 60 % (BASF fuel cell Inc., Somerset, US), is mixed with Nafion solution (5 wt% Nafion 5112, DuPont) and isopropanol, giving a final Pt/Ru concentration of 5 mg/mL and a catalyst/ Nafion ratio of 7: 3<sup>10</sup>; this mixture is wet-sprayed using an airbrush (Evolution Two in One, Harder & Steenbeck, Norderstedt, Germany) onto the Au electrode, forming the anode of the  $\mu$ -DMFC. A similar procedure is applied for depositing Pt/C catalyst on the cathode. The catalyst loading on the electrode is  $\sim 2 \text{ mg/cm}^2$ . (5) A Nafion strip is cut from a larger Nafion 117 membrane (thickness 175  $\mu\text{m}$ , DuPont) by in house-made adjustable razor blades and is conditioned by a series of steps: subsequently, we use 10%  $\text{H}_2\text{O}_2$ , deionized

water (DI) H<sub>2</sub>O, 1 M H<sub>2</sub>SO<sub>4</sub> and DI H<sub>2</sub>O baths during 2 hours each at 80 °C, as described in Section 4.3.1 of Chapter 4. (6) The Nafion strip is placed precisely in between the fuel and oxidant microfluidic channels by means of a guiding channel. (7) The assembly of the planar micro-DMFC is completed by placing the Nafion strip-integrated PDMS chip on top of the catalyst-covered glass chip.

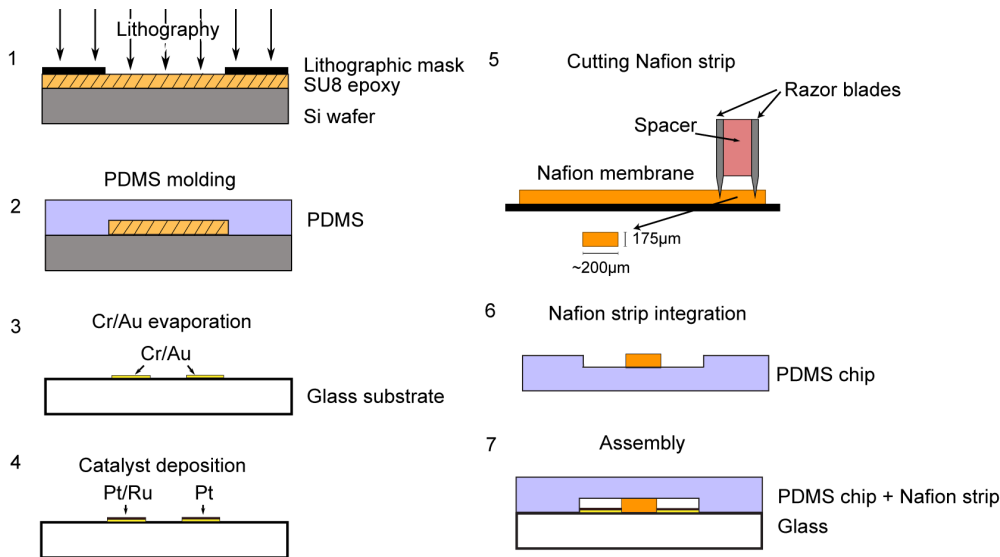
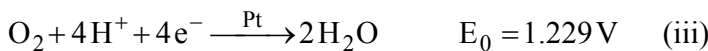
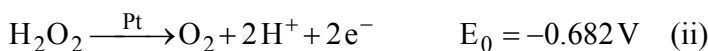
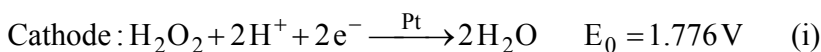
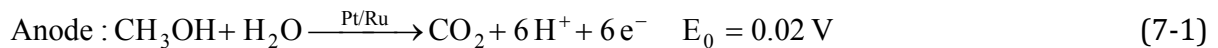


Figure 7-2: Schematic of the micro-DMFC fabrication process.

## 7.2.2 Chemicals and reactions

The performance of the planar micro-DMFC is assessed at room temperature and ambient pressure. The fuel (1 M CH<sub>3</sub>OH/ 0.5 M H<sub>2</sub>SO<sub>4</sub>) is fed to the anodic microfluidic channel and the oxidant (type I: 0.5 M H<sub>2</sub>SO<sub>4</sub>/ O<sub>2</sub> saturated, type II: 0.5 M H<sub>2</sub>SO<sub>4</sub>/ 0.01 M H<sub>2</sub>O<sub>2</sub>) to the cathodic microfluidic channel, respectively. Peristaltic pumps (ISM 831, ISMATEC, Glattbrugg, Switzerland) are connected to the chip for fuel and oxidant refreshment.

For the oxidant of type I, the reactions at anode and cathode are described in Eqs. 3-5 and 3-6, respectively and will not be repeated here. However, one should note that the chemical reactions at cathode, when using the oxidant of type II, becomes more complex, as it comprises the decomposition of H<sub>2</sub>O<sub>2</sub><sup>16</sup>. The reactions are expressed as follows:



(7-2)

The standard potential for direct hydrogen peroxide reduction, reaction Eq. 7-2-i, is more positive than found for most other oxidizers (e.g. oxygen or permanganate), therefore potentially establishing a higher electromotive force for fuel cell operation. However, the oxidation of peroxide to oxygen, reaction Eq. 7-2-ii, is facile on Pt, and occurs together with reaction Eq. 7-2-i. The oxygen generated from the  $\text{H}_2\text{O}_2$  decomposition will also be reduced in to water on the catalytic surface, as expressed in Eq. 7-2-iii. Thus, the open circuit potential is a mixed potential<sup>16</sup>.

### 7.2.3 Backend process and measurement setup

Finally, we mechanically clamp the device using two thick PMMA sheets with fluidic access holes and aluminium foil as current collectors. The top and cross-sectional views of the Nafion strip-integrated PDMS chip are depicted in Figs. 7-3a and 7-3b, respectively. The guiding channel (200  $\mu\text{m}$ ) in the PDMS results in accurate positioning of the Nafion strip. The PDMS chip with integrated Nafion strip and the glass chip with catalyst-covered electrodes are shown in Fig. 7-3c. A single planar micro-DMFC mounted in its experimental setup is shown in Fig. 7-3d.

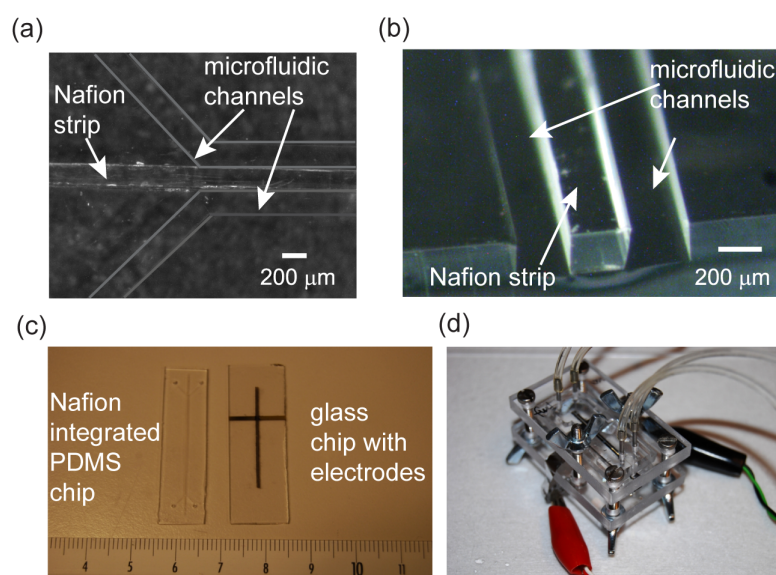


Figure 7-3: Photographs of (a) top view and (b) cross-sectional view of the PDMS microfluidic channels with 200  $\mu\text{m}$  Nafion strip integrated in the guiding channel. (c) Finalized PDMS and glass chips, and (d) the micro-DMFC mounted in its experimental setup.

Two types of chips with different microfluidic channel width and length are studied: chip A has a channel width of 200  $\mu\text{m}$  and a length of 24 mm, while chip B has a width of 80  $\mu\text{m}$  and a length of 11 mm.

A potentiostat/ galvanostat (AMETEK Princeton Applied Research 263A, Oak Ridge, TN, US) is used to evaluate the performance of the micro-DMFCs. We use 30-80  $\mu\text{L}/\text{min}$  flow rates for the fuel and 80-160  $\mu\text{L}/\text{min}$  flow rates for the oxidant. For Chip B, the smaller microfluidic channel

leads to a higher average flow velocity. A higher velocity is in favor of reduced fuel and oxidant depletion effects near the catalytic electrodes (see further)<sup>12</sup>.

## 7.3 Micro-DMFC characterization

### 7.3.1 Current density dependent cell potential and power density

#### *I-V and I-P curves*

As Fig. 7-4a indicates, when using oxidant I into Chip A, a limiting current density of 2.6 mA/cm<sup>2</sup> is obtained with fuel and oxidant flow rate of 50  $\mu$ L/min and 160  $\mu$ L/min, respectively. A higher flow rate of oxidant results in a better refreshment of the oxidant solution and, thus, a higher limiting current and power density. This is related to the low dissolubility of oxygen in the oxidant solution (1.2 mmol/kg at ambient pressure and temperature)<sup>17</sup>. Using oxidant II considerably enhances the maximum power density to 1.5 mW/cm<sup>2</sup>, which is nearly 3 times higher than when using oxidant I at identical fuel and oxidant flow rates. The open circuit potential (OCP) of 0.5 V using oxidant II is lower than the 0.55 V obtained using oxidant I, a small difference that can be explained by oxygen bubbles evolving from the H<sub>2</sub>O<sub>2</sub> reaction on the catalyst at the cathode<sup>10</sup>. Fig. 7-4a allows to conclude that oxidant II is the most promising for achieving a high power density.

Fig. 7-4b shows the performance of Chip B by feeding fuel and oxidant II at different flow rates. A higher limiting current and power density is obtained for a higher oxidant flow rate, while the fuel flow rate is not critical for the performance. This points to the oxidant reaction being performance-limiting for the micro-DMFC<sup>18</sup>. Crossover of methanol through the Nafion strip from the anodic microfluidic channel can reduce the oxidant concentration near the cathode<sup>19</sup>, an effect which can be reduced by having a better refreshment of oxidant using a higher flow rate. Compared to the highest power density of 1.5 mW/cm<sup>2</sup> using oxidant II in Chip A (see Fig. 7-4a), Chip B generates a power density up to 3 mW/cm<sup>2</sup> when operated under identical experimental conditions.

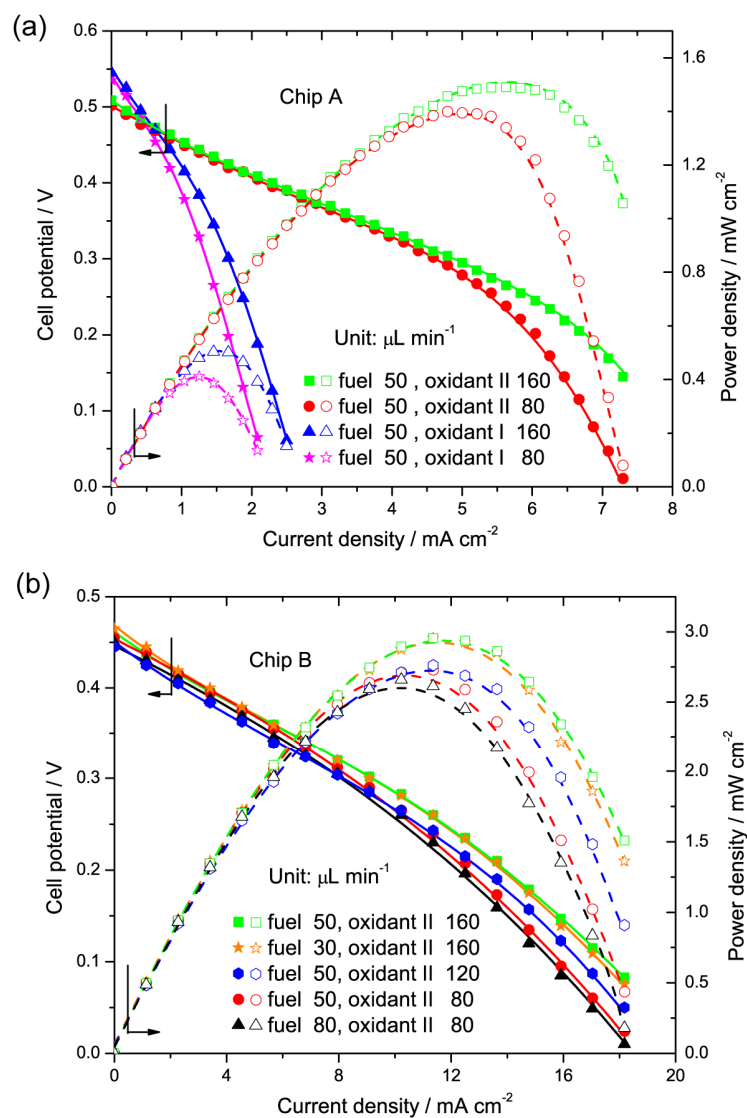


Figure 7-4: (a) Polarization and power density curves of a micro-DMFC using oxidant I and II for Chip A. Each electrode area in contact with fuel or oxidant is  $0.048 \text{ cm}^2$ . (b) Polarization and power density curves of a micro-DMFC using oxidant II in Chip B for different fuel/oxidant flow rates. Each electrode area in contact with fuel or oxidant is  $0.0088 \text{ cm}^2$ .

### Theoretical analysis

The main physico-chemical difference between Chip A and B is the cross-sectional velocity of oxidant and fuel (in case of  $80 \mu\text{L}/\text{min}$ , the average flow velocity for Chip A is  $39 \text{ mm}/\text{s}$ , while it is  $98 \text{ mm}/\text{s}$  for Chip B). A higher velocity clearly reduces oxidant depletion effects near the electrodes and is in favor of a higher reaction rate. We note that the ratio of the concentration boundary layer thickness  $4\sqrt{(DI)/U}$ <sup>12, 20</sup>, calculated at  $l=11 \text{ mm}$  downstream the fluidic channel for both chips, to the channel depth  $d$  is equal to 0.55 and 0.35 for Chip A and B, respectively, with  $D = 1.98 \times 10^{-9} \text{ m}^2/\text{s}$

the oxygen diffusion coefficient in the water-based oxidant solution<sup>21</sup>, and  $U$  the average velocity of the oxidant solution. This means that for chip B, oxidant depletion effects near the electrode surface are less important. Furthermore, as indicated in the numerical work of F. Chen *et al.*<sup>22</sup>, since the depletion zone along the electrode surface gradually grows downstreamwards, a longer microchannel should result in a lower average current density. This could also be an explanation for the better performance of Chip B, which has a shorter length of the microfluidic channel.

### 7.3.2 Durability study

Fig. 7-5 shows the cell potential as a function of time for Chip A and Chip B for a fuel flow rate of  $50 \mu\text{L}/\text{min}$  and an oxidant II flow rate of  $160 \mu\text{L}/\text{min}$ , first without current load and second with a current load. In all the cases, the potential nearly stays constant indicating the high stability of our micro-DMFC.

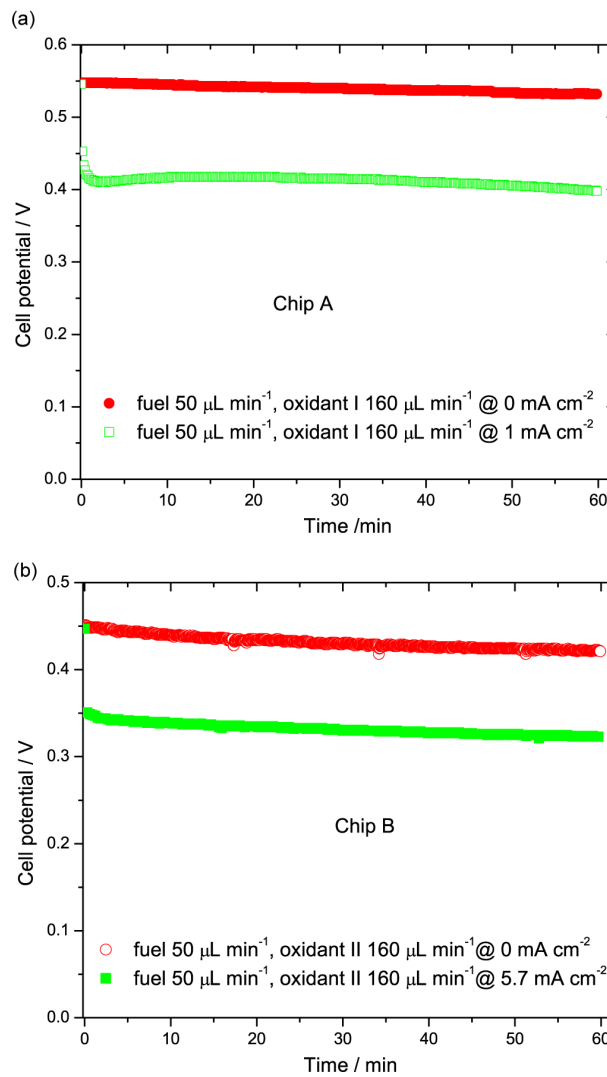


Figure 7-5: Time dependence of cell potential of (a) Chip A using oxidant I and under a  $0 \text{ mA}/\text{cm}^2$  and  $1 \text{ mA}/\text{cm}^2$  current load, respectively, (b) Chip B using oxidant II and under a  $0 \text{ mA}/\text{cm}^2$  and  $5.7 \text{ mA}/\text{cm}^2$  current load,



respectively.

### 7.3.3 The effect of oxidant composition

The effect of reactant concentration on the fuel cell's output is also experimentally studied, by varying the  $H_2O_2$  concentration in 0.5 M  $H_2SO_4$  as oxidant. Fig. 7-6a shows the polarization curves of Chip B when 0.1M  $H_2O_2$  in 0.5 M  $H_2SO_4$  (Oxidant III) is utilized. The impact of various  $H_2O_2$  concentrations in 0.5 M  $H_2SO_4$  on the overall fuel cell's performance in terms of maximum power density and limiting current density is shown in Fig. 7-6b.

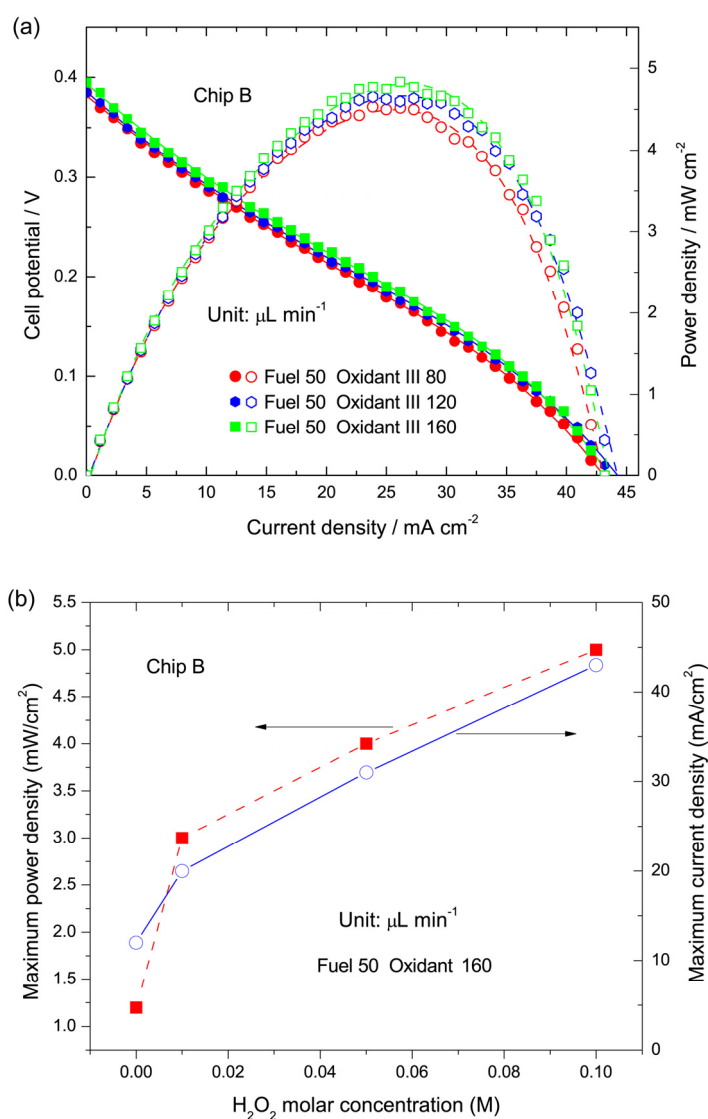


Figure 7-6: (a) Polarization and power density curves of a micro-DMFC using oxidant III in Chip B for different fuel/oxidant flow rates. Each electrode area in contact with fuel or oxidant is 0.0088 cm<sup>2</sup>. (b) Maximum power density and current density for Chip B obtained from various  $H_2O_2$  concentrations in 0.5M  $H_2SO_4$  as oxidant. 0 M  $H_2O_2$  in 0.5 M  $H_2SO_4$  is referred to case of the oxygen saturated in 0.5 M  $H_2SO_4$ .

One can easily notice that, by increasing the concentration of  $\text{H}_2\text{O}_2$  in the oxidant, both the maximum power density and limiting current density are significantly improved, indicating the more  $\text{H}_2\text{O}_2$  and its decomposed  $\text{O}_2$  involved in the cathodic reactions. Thus, it favors the cell's performance by reducing the depletion effect near the electrode. However, as shown in Fig. 7-6a, the open circuit voltage for the cell is only 0.4 V when the higher  $\text{H}_2\text{O}_2$  concentration of 0.1 M in 0.5 M  $\text{H}_2\text{SO}_4$  is fed to the cathodic microfluidic channel, which is attributed to the side effect of the concentrated  $\text{H}_2\text{O}_2$  involved in the reaction that dramatically aggravates the mixing potential effect, as revealed by Eq. 7-2.

#### 7.3.4 Study of external pumping

Figs. 7-7a and 7-7b show the performance of the fuel cell subjected to periodic pumping. It is worthwhile to note that the continuous pumping for both fuel and oxidant is the key to sustain the stable OCP, as a continuous flow helps reducing fuel and oxidant depletion effects near the electrodes.

Fig. 7-7a indicates that depletion effects can be annihilated and the performance of the OCP of the fuel cell can be recovered within 50 s when the pumping is switched on, in the case of using the oxidant I. However, by feeding oxidant II into the cathodic microchannel using periodic pumping, the recovery will be achieved within only 10 s. The most interesting phenomenon is the increase of OCP when using oxidant II, just after switching-off the pumping, and this is caused by the slow process of formation, and growth of gas bubbles over the cathodic electrode associated with  $\text{O}_2$  evolution from  $\text{H}_2\text{O}_2$ . Moreover, since the potential at the cathode is merely created by  $\text{O}_2$  reduction, the higher value of OCP can be expected. Thanks to the reduced depletion effect favored by the narrower microchannel in Chip B, the cell potential drops slower than in Chip A, as indicated in Fig. 7-7b.

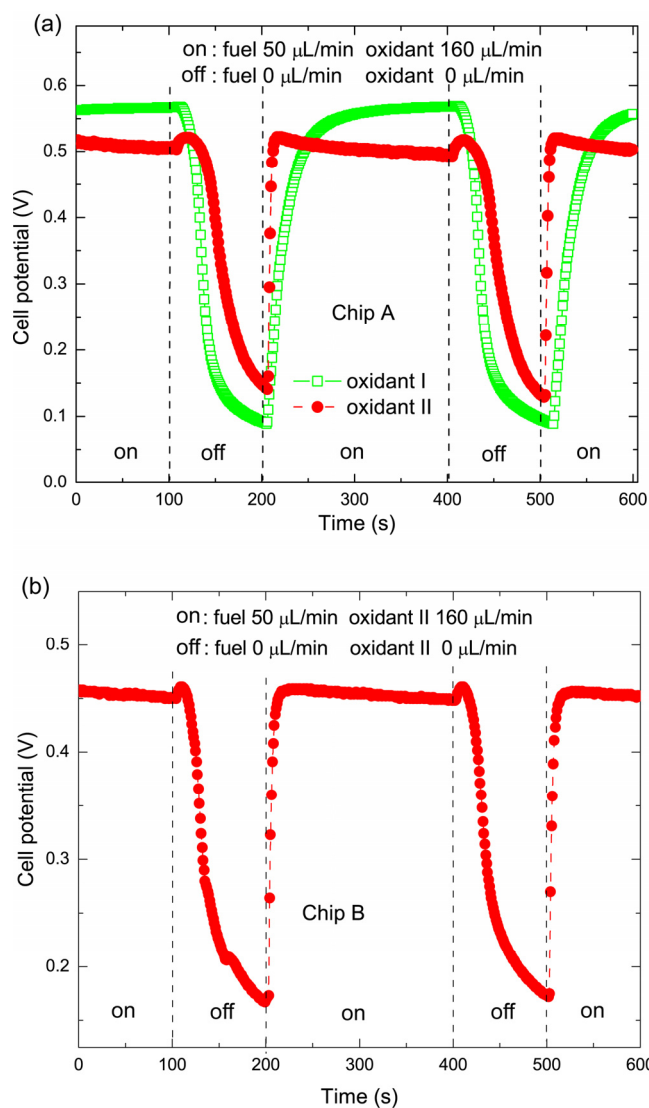


Figure 7-7: (a) Cell potential of Chip A recovery by periodic pumping of the fuel/oxidant solution. Both oxidants I and II are used. (b) Cell potential of Chip B recovery by periodic pumping of the fuel/oxidant II solution.

### 7.3.5 Comparison with the state-of-the-art

When comparing with literature, the power density of a PDMS-based planar micro-DMFC with patterned Nafion resin<sup>8</sup> is, despite the use of different fuel and oxidant, two magnitudes smaller than our device. The reported power density of 0.8 mW/cm<sup>2</sup> generated from a silicon-based micro-DMFC<sup>9</sup> is a factor 1.5 smaller than our Chip B (results not shown), when operating with the same oxidant I, but for higher fuel concentration (2 M CH<sub>3</sub>OH/ 0.5 M H<sub>2</sub>SO<sub>4</sub>). We checked that, by increasing the concentration of H<sub>2</sub>O<sub>2</sub> in 0.5 M sulfuric acid to 0.1 mol/L, an even higher output power density of 5 mW/cm<sup>2</sup> and a limiting current density of 43 mA/cm<sup>2</sup> is achieved for our Chip B. In this experiment, fuel (1 M CH<sub>3</sub>OH/0.5 M H<sub>2</sub>SO<sub>4</sub>) and oxidant (0.5 M H<sub>2</sub>SO<sub>4</sub>/0.1 M H<sub>2</sub>O<sub>2</sub>) are fed at 50  $\mu\text{L}/\text{min}$  and 160  $\mu\text{L}/\text{min}$ , respectively. This performance again indicates the important

role of the oxidant concentration in the cathodic microfluidic channel.

## 7.4 Conclusion

We have compared two micro-DMFC designs, in which two 200  $\mu\text{m}$ -wide and two 80  $\mu\text{m}$ -wide parallel microfluidic channels, are sandwiching a Nafion PEM strip, respectively. Using 1M  $\text{CH}_3\text{OH}$  in 0.5M  $\text{H}_2\text{SO}_4$  solution as fuel in the anodic channel, we compared the performance of (I)  $\text{O}_2$ -saturated 0.5 M  $\text{H}_2\text{SO}_4$  and (II) 0.01 M  $\text{H}_2\text{O}_2$  in 0.5 M  $\text{H}_2\text{SO}_4$  oxidant solutions in the cathodic channel. For the chip of 200  $\mu\text{m}$  channel width, the fuel cell reached a maximum power density of 0.5  $\text{mW}/\text{cm}^2$  and 1.5  $\text{mW}/\text{cm}^2$  at room temperature, for oxidant I and II, respectively, for fuel and oxidant flow rates in the 50-160  $\mu\text{L}/\text{min}$  range. A maximum power density of 3.0  $\text{mW}/\text{cm}^2$  was obtained for the chip of 80  $\mu\text{m}$ -wide channel, using oxidant II with higher oxidizing power. Our results indicated the important role of the oxidant concentration in the cathodic microfluidic channel, and the advantage a higher velocity has in reducing oxidant depletion effects near the electrodes. In future, we intend to explore an alternative PDMS stamping technology to bond the Nafion-integrated PDMS chip to the glass chip using a liquid PDMS bonding layer<sup>23</sup>, leading to a more compact micro-DMFC. Also the influence of channel geometry and fuel and oxidant flow effects will be further studied.

## References

1. Shen, M.; Walter, S.; Gijs, M., Monolithic micro-direct methanol fuel cell in polydimethylsiloxane with microfluidic channel-integrated Nafion strip. *Journal of Power Sources* 2009, *193*, 761-765.
2. Dyer, C., Fuel cells for portable applications. *Fuel Cells Bulletin* 2002, *2002*, 8-9.
3. Nguyen, N.; Chan, S., Micromachined polymer electrolyte membrane and direct methanol fuel cells-a review. *Journal of Micromechanics and Microengineering* 2006, *16*, R1-R12.
4. Kamarudin, S.; Daud, W.; Ho, S.; Hasran, U., Overview on the challenges and developments of micro-direct methanol fuel cells (DMFC). *Journal of Power Sources* 2007, *163*, 743-754.
5. Yen, T.; Fang, N.; Zhang, X.; Lu, G.; Wang, C., A micro methanol fuel cell operating at near room temperature. *Applied Physics Letters* 2003, *83*, 4056-4058.
6. Blum, A.; Duvdevani, T.; Philsoph, M.; Rudoy, N.; Peled, E., Water-neutral micro direct-methanol fuel cell (DMFC) for portable applications. *Journal of Power Sources* 2003, *117*, 22-25.
7. Lu, G.; Wang, C.; Yen, T.; Zhang, X., Development and characterization of a silicon-based micro direct methanol fuel cell. *Electrochimica Acta* 2004, *49*, 821-828.
8. Song, Y.; Batista, C.; Sarpeshkar, R.; Han, J., Rapid fabrication of microfluidic polymer electrolyte membrane fuel cell in PDMS by surface patterning of perfluorinated ion-exchange resin. *Journal of Power Sources* 2008, *183*, 674-677.

9. Motokawa, S.; Mohamedi, M.; Momma, T.; Shoji, S.; Osaka, T., MEMS-based design and fabrication of a new concept micro direct methanol fuel cell ( $\mu$ -DMFC). *Electrochemistry communications* 2004, 6, 562-565.
10. Li, A.; Chan, S.; Nguyen, N., A laser-micromachined polymeric membraneless fuel cell. *Journal of Micromechanics and Microengineering* 2007, 17, 1107-1113.
11. Jayashree, R.; Gancs, L.; Choban, E.; Primak, A.; Natarajan, D.; Markoski, L.; Kenis, P., Air-breathing laminar flow-based microfluidic fuel cell. *Journal of the American Chemical Society* 2005, 127, 16758-16759.
12. Choban, E.; Markoski, L.; Wieckowski, A.; Kenis, P., Microfluidic fuel cell based on laminar flow. *Journal of Power Sources* 2004, 128, 54-60.
13. Tominaka, S.; Ohta, S.; Obata, H.; Momma, T.; Osaka, T., On-chip fuel cell: Micro direct methanol fuel cell of an air-breathing, membraneless, and monolithic design. *Journal of the American Chemical Society* 2008, 130, 10456-10457.
14. Kjeang, E.; Michel, R.; Harrington, D.; Djilali, N.; Sinton, D., A microfluidic fuel cell with flow-through porous electrodes. *Journal of the American Chemical Society* 2008, 130, 4000-4006.
15. Lee, J.; Park, C.; Whitesides, G., Solvent compatibility of poly (dimethylsiloxane)-based microfluidic devices. *Analytical Chemistry* 2003, 75, 6544-6554.
16. Kjeang, E.; Brolo, A. G.; Harrington, D. A.; Djilali, N.; Sinton, D., Hydrogen Peroxide as an Oxidant for Microfluidic Fuel Cells. *Journal of The Electrochemical Society* 2007, 154, B1220-B1226.
17. Kaskiala, T.; Salminen, J., Oxygen solubility in industrial process development. *Industry & Engineering Chemistry Research* 2003, 42, 1827-1831.
18. Chen, F.; Chang, M.; Lin, H., Analysis of a novel MEMS-based design of micro-direct methanol fuel cell. *Journal of Power Sources* 2008, 178, 125-131.
19. Valdez, T.I.; Narayanan, S.R.; Lewis, C., Chun, W., In: S.R. Narayanan, S. Gottesfeld and T. Zawodzinski, Editors, *Direct Methanol Fuel Cells PV 2001-4*, The Electrochemical Society Inc. 2001, pp. 265.
20. Crank, J., The mathematics of diffusion. Clarendon Press, Oxford, 1956.
21. Han, P.; Bartels, D., Temperature Dependence of Oxygen Diffusion in H<sub>2</sub>O and D<sub>2</sub>O. *The Journal of Physical Chemistry* 1996, 100, 5597-5602.
22. Chen, F.; Chang, M.; Lin, M., Analysis of membraneless formic acid microfuel cell using a planar microchannel. *Electrochimica Acta* 2007, 52, 2506-2514.
23. Wu, H.; Huang, B.; Zare, R., Construction of microfluidic chips using polydimethylsiloxane for adhesive bonding. *Lab on a Chip* 2005, 5, 1393-1398.



# Chapter 8

## Microfluidic Protein Preconcentrators Using Microchannel-Integrated Nafion Strip: Experiment and Modeling

(adapted version of:

<sup>1</sup>M. Shen\*, H. Yang\*, V. Sivagnanam, M.A.M. Gijs, Microfluidic protein preconcentrator using microchannel-integrated Nafion strip: experiment and modeling, *Analytical Chemistry*, in press, 2010 (DOI: 10.1021/ac102149f)

*\*The authors contribute equally to this work, M. Shen is mainly responsible for chip design, fabrication and simulation; H. Yang is mainly responsible for preconcentration experiment and simulation. )*

**Abstract:** In this chapter, we propose a simple microfluidic device for protein preconcentration based on the electrokinetic trapping principle. It comprises a narrow Nafion strip that is simply cut from a commercial membrane and is integrated in a molded PDMS microfluidic structure using a guiding channel. Mechanically clamping the PDMS/Nafion assembly with a glass substrate results in a rapid prototypable, leak-tight and easily disposable device. Our device preconcentrates negatively-charged fluorescent proteins located at the anodic microfluidic compartment side of the Nafion strip within a few minutes and up to a concentration factor of  $10^4$ . Moreover, we present a numerical study of the preconcentration effect by solving the coupled Poisson, Nernst-Planck and Navier-Stokes equations for our type of device, which provides insight into the mechanism of preconcentration. The electrical field across the ion-permselective Nafion generates concentration polarization, i.e. ion-depletion at the anodic side and ion-enrichment at the cathodic side for both types of ions, with local excess of mobile positive ions in the depleted concentration polarization zone, inducing a non-equilibrium electrical double layer in close proximity of the membrane. A voltage difference applied over the anodic compartment is used to generate the electrophoretic flow velocity of the negatively charged biomolecules. This, in combination with the electroosmotic flow in the opposite direction, which originates from the fixed charges on the channel walls and the induced space charge near the membrane, provides the basis for the preconcentration of the negative biomolecules.

## 8.1 Introduction

### 8.1.1 Necessity of using preconcentrators for biomolecule analysis

Microfluidic devices have many potential advantages over larger size biomedical analysis systems, for example, they enable integration of multiple biochemical processing steps onto a single monolithic device<sup>2,3</sup>. Applications, like biomolecule purification, accumulation, separation, reaction, as well as amplification have already been demonstrated on a miniaturized scale<sup>4-7</sup>. Micro-scale separation devices often can only analyze a small fraction of the available sample, which can pose a limit to the overall detection sensitivity, especially for the detection of low-concentration species. In proteomics, this problem is aggravated by the fact that targeted tracer molecules, for example, cytokines and biomarkers, are present only in very low concentrations (nM-pM range). Furthermore, no amplification technique exists for proteins and peptides, such as the polymerase chain reaction (PCR) for nucleic acids. Thus, a high-efficiency protein preconcentrator able to purify low concentration biomarkers from microliter sample volumes is extremely useful for implementation of high-sensitivity diagnosis in the microfluidic chip format<sup>8</sup>.

There are many techniques available for sample preconcentration in microfluidic devices. These include field-amplified sample stacking<sup>9</sup>, isotachopheresis<sup>10</sup>, isoelectric focusing<sup>11, 12</sup>, chromatographic trapping<sup>13, 14</sup>, electrokinetic trapping<sup>15-27</sup>, temperature-gradient focusing<sup>28</sup>, etc.. Electrokinetic trapping is particularly interesting, as it can be used for any charged biomolecule, and allows the use of simple fluid handling protocols. However, it generally calls for specially fabricated nanoporous membranes<sup>15-17, 21, 24, 29, 30</sup> or nanofluidic channels<sup>7, 18, 19, 22, 23, 31</sup>. Using advanced microfabrication techniques, the group of J. Han<sup>19, 23</sup> proposed a high-efficiency nanofluidic channel-based preconcentrator demonstrating a million-fold concentration of charged proteins. Kim *et al.*<sup>20</sup> successfully concentrated FITC-bovine serum albumin (BSA) by utilizing spontaneously formed nanochannels at a bonded PDMS-glass interface. Though cumbersome fabrication steps were avoided in this device, an extreme control of the PDMS-glass bonding operation was required. Alternatively, nanoporous polymer membranes were *in situ* formed inside microchannels, thereby avoiding complex clean room nanofabrication processes<sup>15, 17, 29, 30</sup>. *In situ* polymerization on-chip allows easy variation of chemical composition and surface charge of the nanoporous material, but may require the application of dedicated washing procedures and can result in a lack of control of the nanoporosity, when compared to optimized commercial ion-exchange membrane fabrication processes. Recent work using commercially available ion-exchange membranes (Nafion 115) for the electrokinetic capture of micron-size beads in a microfluidic channel was reported by U. Lindberg *et al.*<sup>32</sup>. Nafion is a highly ion-permselective membrane normally used in proton exchange membrane fuel cells<sup>33-35</sup>. Recently, we demonstrated a monolithic microfluidic fuel cell by integrating a narrow Nafion



strip in a molded PDMS structure<sup>36</sup>. Our design overcame many of the complex fabrication and assembly problems related to the membrane integration in a microfluidic structure and formed the technological basis for the present study.

### 8.1.2 Design and working principles

The preconcentrator is based on a glass substrate that is mechanically clamped with a PDMS chip, which has two microfluidic channels and a particular guiding channel for inserting the Nafion strip. The latter, having fixed negative charges and a pore mean size of the order of the electrical double layer (EDL) thickness, behaves as a cation-permselective membrane<sup>35</sup>. Fig. 8-1 shows the Nafion strip-separated microfluidic sample and buffer channels, forming the anodic and cathodic side of the device, respectively. The fluidic reservoirs of the cathodic compartment (buffer channel) are connected to  $V_B = 0$  V, while the remaining two reservoirs of the anodic compartment (sample channel) have positive voltage  $V_H$  and  $V_L$ , respectively.

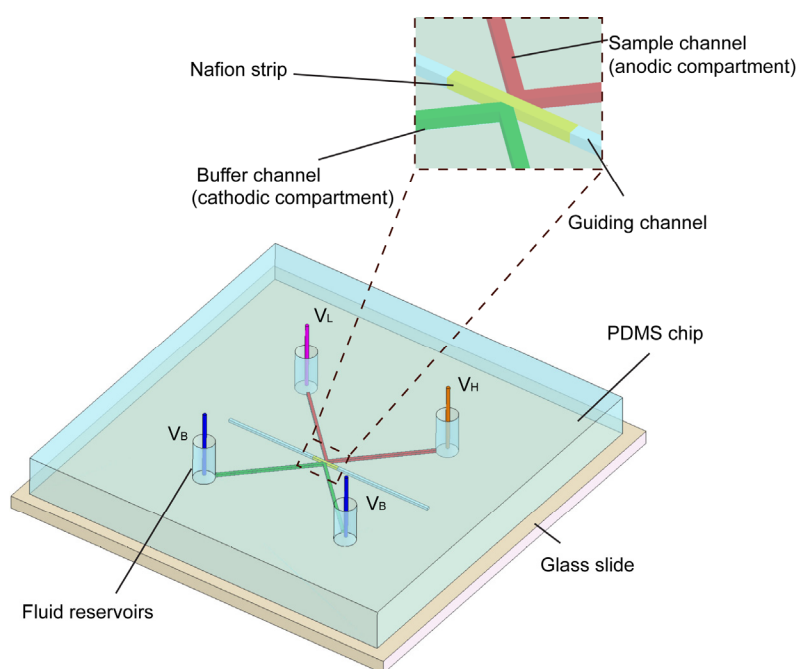


Figure 8-1: Schematic illustration of the protein preconcentration chip in PDMS with integrated Nafion strip, with definition of voltages applied to the reservoirs during operation. The zoom shows in more details the guiding channel for embedding the Nafion strip that separates the sample from buffer channels.

The electrical field across the ion-permselective Nafion generates concentration polarization (CP), i.e. ion-depletion at the anodic side and ion-enrichment at the cathodic side, with a local excess of mobile positive ions in the depleted CP zone, very close to the membrane, inducing a non-equilibrium EDL. The voltage difference ( $V_H - V_L$ ) imposed over the anodic compartment is

used to generate the electrophoretic flow velocity of the negative tracer biomolecules. This, in combination with the electroosmotic flow (EOF) induced by the fixed charges on the anodic channel walls (EOF of the first kind) and the EOF induced by the space charge of the non-equilibrium EDL (EOF of the second kind), provides the basis for the enrichment of the tracer biomolecules (see further).

## 8.2 Experimental

### 8.2.1 Materials and chemicals

The PDMS pre-polymer set (Sylgard 184) was purchased from Dow Corning Inc. (Midland, MI, USA). The float glass slide was purchased from Menzel GmbH (Braunschweig, Germany). Bovine serum albumin conjugated with Alexa Fluor® 647 (AF-BSA) was obtained from Invitrogen (Basel, Switzerland) and this was used as tracer proteins in the following experiment. The Nafion strip was cut from a larger Nafion 117 membrane (thickness 175  $\mu\text{m}$ , DuPont, USA). The mean pore size is 1-3 nm according to different literature reports<sup>35,37,38</sup>. The fixed volume charge concentration of the Nafion membrane is around  $-1200 \text{ mol/m}^3$ <sup>38</sup>. 1 $\times$ Phosphate Buffered Saline (PBS) (10 mM, pH=7.4) solution was prepared by diluting 10 $\times$ PBS concentrate solution purchased from Sigma-Aldrich Chemie GmbH (Buchs, Switzerland). The PBS-Tween (PBST) solution (pH=7.4) was prepared by mixing 0.5% v/v Tween-20 (Sigma-Aldrich) with 1 $\times$ PBS. A PBS-BSA 1% solution was obtained by diluting 1% (w/v) BSA (Sigma-Aldrich) in 1 $\times$ PBS. DI water of resistivity 18.2 M $\Omega\text{cm}$  was obtained from EPFL's Center of Micro- and Nanotechnology. Pt wires of diameter 0.25 mm were obtained from Goodfellow Cambridge Ltd. (Huntingdon, UK).

### 8.2.2 Microfluidic device fabrication

The master structure for replication of the PDMS chip was made from a  $\sim 170 \mu\text{m}$  thick negative SU-8 photoresist on a silicon substrate using standard processing, as reported before<sup>36</sup>. By utilizing two razor blades, we are able to cut a Nafion strip of  $\sim 200 \mu\text{m}$  width. The Na-form Nafion was prepared as follows<sup>39</sup>: after standard pretreatment steps<sup>36</sup>, the strip was stirred in 1 M NaOH at room temperature for 24 hours; then, it was several times rinsed with DI water until pH = 7. The strip was finally kept in 0.1 M NaCl solution for at least one day. The Na<sup>+</sup> form Nafion is less swollen and has a higher mechanical strength than the usual H<sup>+</sup> form Nafion<sup>40</sup>. After demolding the PDMS structure, the latter was flipped and the integration of the Nafion strip was realized thanks to the guiding channel. Using a diamond tip, a glass slide with a dimension of 28 mm  $\times$  28 mm was cut and mechanically assembled with the PDMS microstructure, using PMMA support sheets (3 mm thickness), enabling leakage-free functioning. The preconcentrator chip was finalized by placing four Pt wires as electrodes into the four fluidic reservoirs. The PDMS/glass preconcentrator chip with its mechanical clamping system is shown [Fig. 8-2a](#). The

overall dimension of the PMMA support is 45 mm × 50 mm. Fig. 8-2b shows in more detail a top view of the Nafion strip flanked by the two symmetric microfluidic channels.

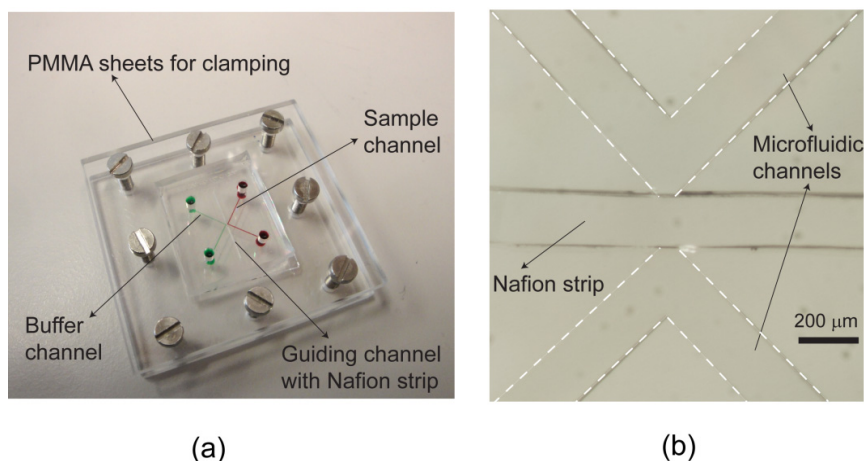


Figure 8-2: (a) Photograph of the PDMS preconcentration chip with its mechanical clamping setup. (b) Optical micrograph of the microfluidic circuit with integrated Nafion strip.

### 8.2.3 Protocols and measurement setup

For preconditioning, any impurities in both the sample and buffer channels were first removed by introducing PBST solution into the channels using syringes. Then, 1×PBS buffer solution was loaded into the buffer channel, while the sample channel was filled with PBS-BSA 1% solution for blocking the non-specific binding of the AF-BSA molecules on the channel walls. After 5 min, the latter solution was replaced by 1×PBS solution. Finally, the AF-BSA in 1×PBS solution was loaded into the sample channel with various concentrations (60 pM- 60 nM).

To activate the electrokinetic migration of the protein, first, the Pt electrodes in the two reservoirs of the buffer channel were connected to zero potential; at the same time, a bias voltage  $V_L$  and  $V_H$  was applied across the sample channel through the other two Pt electrodes. Fluorescence micrographs of the microchannel region juxtaposing the Nafion strip were captured using an Axiovert S100 (Zeiss) inverted microscope equipped with a CCD camera ORCA-C4742-95ER (Hamamatsu, Shizuoka Pref., Japan). The microscopy is equipped with a mercury short arc lamp HBO (Osram) and the appropriate filter set for Alexa Fluor® 647 (red). The exposure time used for capture the fluorescence signal was 2 s and the software AquaCosmos (Hamamatsu) was used for fluorescence image analysis.

## 8.3 Characterizations

### 8.3.1 Time dependent preconcentration

The most significant experimental parameters involved in the preconcentration are the

applied voltage across the membrane and the voltage difference ( $V_H - V_L$ ) in the anodic microfluidic compartment, as well as the tracer protein concentrations. Fig. 8-3 shows the fluorescence images obtained at time frames of 1 min, 5 min, 9 min and 11 min, respectively, for a 6 nM sample when exposed to a voltage difference of 10 V over the anodic compartment ( $V_H = 15$  V,  $V_L = 5$  V). A fluorescence spot becomes visible in the lower right part of the sample channel, the intensity of which increases with increasing time. This preconcentrated plug does not span the complete width of the channel.

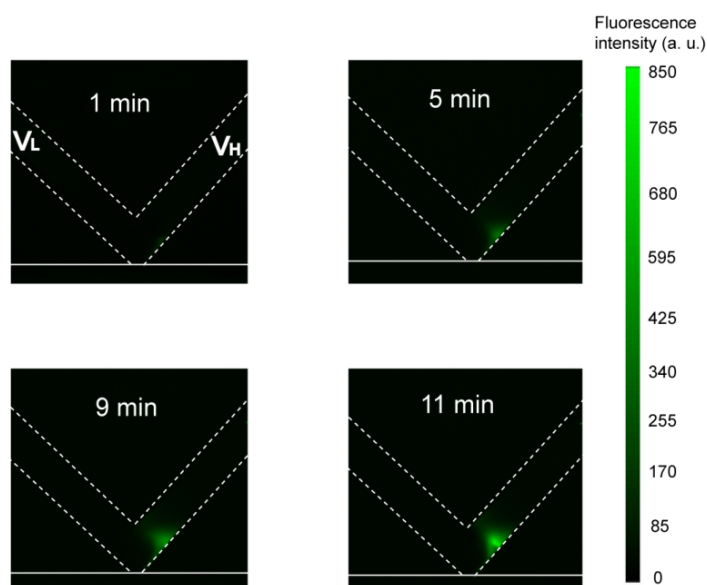


Figure 8-3: Fluorescence micrographs captured during preconcentration of a 6 nM AF-BSA sample after applying a voltage difference of 10 V ( $V_H = 15$  V,  $V_L = 5$  V) during 1 min, 5 min, 9 min and 11 min, respectively. Both buffer channel reservoirs (not shown) were kept at 0 V.

To quantify the preconcentration factor, we measured the fluorescence intensity of the preconcentrated plug as a function of time for three different AF-BSA initial concentrations (60 pM, 6 nM, and 60 nM). Each experimental data point and error bar shown in Fig. 8-4 corresponds to the average fluorescence intensity and variance, respectively, corresponding to a sampling area of 16 pixels around the maximum. In the case of the 6 nM AF-BSA concentration, the fluorescence intensity reaches after 10 min the intensity level of a 6  $\mu$ M AF-BSA reference solution filling the channel, implying a preconcentration factor of  $\sim 10^3$ . Similarly, the chip is able to effectively preconcentrate a low AF-BSA concentration of 60 pM by a factor  $\sim 2 \times 10^4$  within 7 min, indicating the high potential of our preconcentrator device.

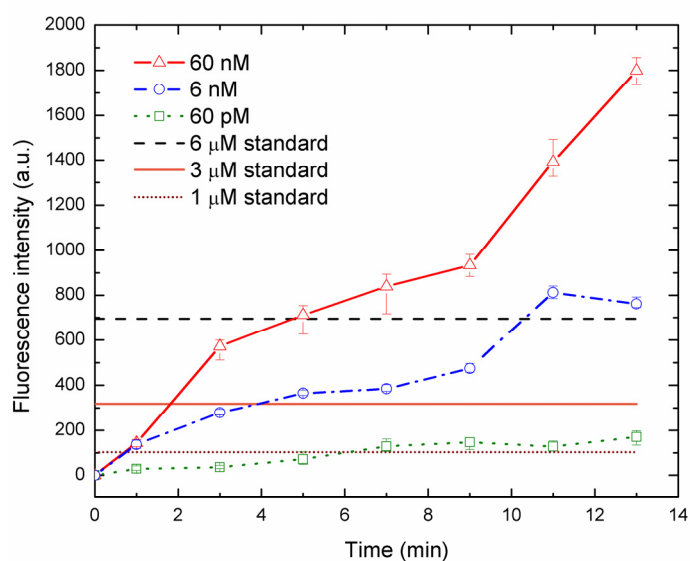


Figure 8-4: Time-dependence of the maximum fluorescence intensity of the preconcentrated plug for AF-BSA concentrations of 60 nM, 6 nM, 60 pM, respectively, with the applied electrical potential difference of 10 V ( $V_H=15$  V,  $V_L=5$  V). Also the fluorescence intensity from standard concentration samples (1  $\mu$ M, 3  $\mu$ M, 6  $\mu$ M) is shown.

### 8.3.2 Study the effect of voltage difference across anodic microchannel

We also measured the fluorescence intensity of the AF-BSA preconcentrated plug as a function of the voltage difference  $V_H-V_L$  for a specific time of 7 min (see Fig. 8-5). The fluorescent intensity of the preconcentrated plug increases with the voltage difference for both the 60 nM and 600 pM AF-BSA concentrations. One should note that our preconcentration voltages are of the lowest values reported yet due to the chosen geometrical parameters of the Nafion strip, holding promise for portable applications. In principle, the preconcentration effect could be considerably enhanced when the potential difference  $V_H-V_L$  would be further increased. However, we found a Nafion membrane deformation and rapid failure (after a few minutes) when applying voltages  $V_H, V_L > 20$  V. The reason for this phenomenon could be a low tolerance of the Nafion membrane to Joule heating<sup>32</sup>. Also, changes in the Nafion membrane during the experiment could be a factor affecting the time-dependent slope of the fluorescent intensity profiles of Fig. 8-4.

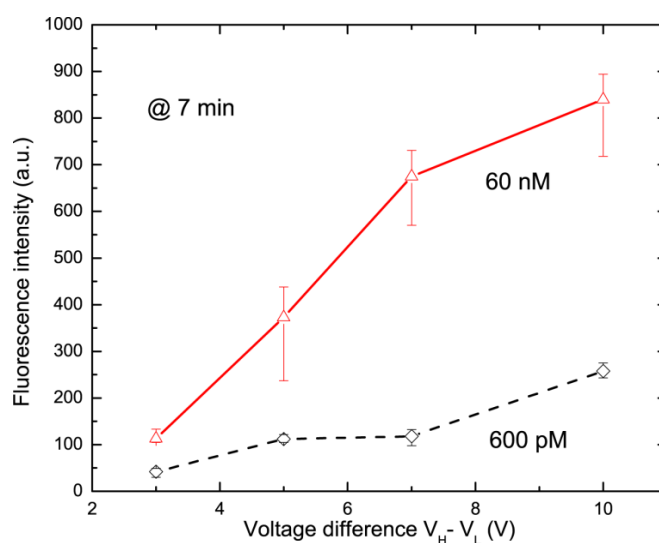


Figure 8-5: Maximum fluorescence intensity of the preconcentrated AF-BSA plug at a control time of 7 min, for initial concentrations of 60 nM and 600 pM, respectively, as a function of the voltage difference applied over the anodic compartment (keeping  $V_L = 5$  V).

## 8.4 Simulations and discussions

### 8.4.1 Model based on coupled equations

#### *Theoretical considerations*

In general, the electrokinetic motion of charged molecules in a microfluidic channel is at the basis of transport, separation, and enrichment of ionic species via the complex interplay of i) electrophoresis of the positive and negative ions of the background electrolyte, ii) electrophoresis of the tracer biomolecules, and iii) electro-osmosis of the background electrolyte driven by the charge imbalance in the EDL close to a solid-liquid interface<sup>15, 22, 29, 41</sup>. In this section, we start by introducing the essential features of the EDL, EOF and the ion permselectivity of the porous membrane, and then explain their influence on the numerical analysis.

When a nanoporous ion-permselective membrane is placed between two fluidic compartments and an external electrical field applied over it, CP develops, which is a complex of effects related to the formation of concentration gradients of ionic species in the electrolyte solution adjacent to the ion-permselective membrane interface<sup>41, 42</sup>. As the field is switched on, the co-ions (here, anions) move away from the anodic interface towards the anode, but their local withdrawal cannot be compensated by the few co-ions which actually remain inside the membrane due to its cation-selectivity (co-ion exclusion). Thus, the co-ion concentration decreases locally in the solution adjacent to the anodic interface and so does the counterion concentration to maintain local electroneutrality. At the opposite, that is, cathodic interface where counterions leave the membrane the electrolyte concentration correspondingly increases. This cathodic diffusion

boundary layer results in an enriched CP zone. For a negatively charged membrane (i.e. Nafion 117), the positive ions enter the membrane towards the cathode and get depleted in the anodic compartment in the vicinity of the membrane. To maintain charge neutrality, also the negative ion concentration increases/decreases in the cathodic/anodic compartment close to the membrane. However, the polarized ion current through the membrane creates a positive charge imbalance very close to the membrane interface, where diffusive transport is limited. The detailed theory and formula can be found at [Section 2.3.4](#) in [Chapter 2](#).

In our work, we combined the transient Nernst-Planck equations for both types of buffer ions with a proper description of the momentum transfer of the fluid, as expressed by the Navier-Stokes equation, and linked it with the electrical potential by applying the Poisson equation<sup>43-45</sup>. The Nernst-Planck equation describes the conservation of mass for ionic species in fluid medium in the presence of an applied electric field. In principle, the transport of positive ( $i=1$ ), negative ( $i=2$ ) buffer ions and the tracer molecules ( $i=3$ ) can be described by this equation:

$$\frac{\partial c_i(t)}{\partial t} = \nabla(D_i \nabla c_i(t) + z_i c_i(t) D_i \frac{F}{RT} \nabla \phi(t)) - \nabla c_i(t) \cdot \mathbf{u}(t) \quad (8-1)$$

where  $c_i$ ,  $D_i$  and  $z_i$  are the molar concentration of ionic species  $i$ , its corresponding diffusion coefficient and its corresponding valence, respectively.  $F$  is the Faraday constant,  $R$  and  $T$  represent the molar gas constant and temperature, respectively.  $\phi$  is the electric potential, and  $\mathbf{u}$  is the fluid velocity. This equation describes the flux of ions under the influence of both an ionic concentration gradient  $\nabla c_i(t)$  and an electrical field  $\mathbf{E} = -\nabla \phi$ .

Poisson's equation is used to describe the relation of the electrical potential and the local concentration distribution of buffer ions and charged tracer molecules:

$$\nabla^2 \phi = -\frac{\rho_{fix}}{\varepsilon_0 \varepsilon_r} - \frac{F}{\varepsilon_0 \varepsilon_r} \sum_i z_i c_i(t) \quad (8-2)$$

where  $\rho_{fix}$  is the volumetric fixed charge density of the membrane and  $\varepsilon_0$ ,  $\varepsilon_r$  the vacuum permittivity and the relative dielectric constant, respectively.

Moreover, the Navier-Stokes equation and the continuity equation for an incompressible fluid are incorporated into the model, which describes the motion of fluid:

$$\rho \frac{\partial \mathbf{u}(t)}{\partial t} + \rho(\mathbf{u} \cdot \nabla) \mathbf{u} = -\nabla p + \mu \nabla^2 \mathbf{u} - F \sum_i z_i c_i(t) \nabla \phi \quad (8-3)$$

$$\nabla \cdot \mathbf{u} = 0$$

where  $\nabla p=0$  indicates the absence of external hydrostatic pressure,  $\rho$  and  $\mu$  are the density and viscosity of the water-based fluid. The Navier-Stokes equation should be employed with the electrical body force term to incorporate the interaction between the local electrical field and ion



concentration gradients, as indicated in the third term on the right in Eq. 8-3.

The coupled equations above suggest that solving the mathematical model of a preconcentration system is highly complex, and that a numerical method is essential to provide a physical explanation of the phenomena that are at the basis of the preconcentration effect. Numerical modeling of preconcentration systems has been done before, leading to a theoretical understanding of the interplay of CP and electro-osmotic flow effects. However, the full numerical solution of Eqs. 8-1, 8-2, 8-3 requires an extremely fine mesh (a few nanometers) to correctly describe EDL-based effects, which is the reason why mostly micron-scale fluidic systems were simulated, in order to stay within computational resource limitations. We have used the software COMSOL Multiphysics™ (Version 3.5a) to solve the differential equations set for a two-dimensional microfluidic system of centimeter size, taking a fine mesh close to the membrane to describe CP-related charge imbalance effects, and taking a slip velocity boundary condition at the microfluidic channel walls to mimic the EOF of the first kind and thereby gain in computing power, as shown in the next section.

### Numerical simulation

Because of the model complexity, several specific assumptions and conditions were taken into account:

- i. The Brinkman equation for the porous medium (for example, the Nafion membrane) in absence of external hydrostatic pressure was adopted for describing the flow inside the membrane, taking into account the electrical body force from the mobile ions<sup>46</sup>:

$$\frac{\rho}{\varepsilon_p} \frac{\partial \mathbf{u}(t)}{\partial t} + \frac{\mu}{\kappa} \mathbf{u} = \frac{\mu}{\varepsilon_p} \nabla^2 \mathbf{u} - nF \sum_i z_i c_i(t) \nabla \phi$$

$$\nabla \cdot \mathbf{u} = 0 \quad (8-4)$$

where  $0 < \varepsilon_p < 1$  is the porosity and  $\kappa$  the permeability of the membrane, respectively. The correction factor  $n$  originates from the reduced velocity due to the electric double layer overlap effect within the pores; we used a value  $n = 0.1$  in our simulations<sup>15, 47, 48</sup>.

- ii. Because of the existence of the EDL due to the fixed charge on the interface between the microchannel and electrolyte solution, EOF of the first kind is generated by applying an electrical field over the microchannel. However, in the small region close to the membrane-microchannel interface, because of the CP phenomena, a secondary EDL due to the induced space charge develops, which generates locally a EOF of second kind. To be more precise, near the membrane, the effective EDL, which generates locally an EOF of the second kind, is resulting from the secondary EDL, complemented by the primary (quasi-equilibrium) EDL. In order to take into account these two kinds of EOF simultaneously and to reduce the complexity of the calculation process, EOF of the first kind was modeled as originating from an



effective velocity slip of the liquid at the microchannel walls based on the thin EDL assumption. The slip velocity is given by the Helmholtz-Smoluchowski formula<sup>41, 49, 50</sup>,

$$u_{1^{st} EOF} = -\frac{\varepsilon\zeta}{\mu} E_t \quad (8-5)$$

where  $E_t$  is the tangential electrical field just outside the double layer,  $\varepsilon$  and  $\mu$  are the permittivity and viscosity of the liquid (both assumed constant), and  $\zeta$  is the zeta potential. This approach permits avoiding the use of a very fine mesh to resolve EDL based effects in the anodic microchannel. Since the EOF of the first kind is implemented into the model in form of the boundary slip, the fixed surface charge on the microchannel walls are no longer considered<sup>51</sup>.

- iii. Another assumption is that we did not consider separate concentrations of the negative tracer biomolecules, as, due to the concentrations used, the former have little impact on the CP phenomena and flow velocity, even in the preconcentrated state.

Eqs. 8-1, 8-2, 8-3 and 8-4 were solved using the following boundary conditions: for the Nernst-Planck equation, the ion flux normal to the microchannel walls is zero and the ion concentrations at the four edges are kept constant; for the Poisson equation, fixed electrical potentials are assumed at the four edges of the microchannel: 5 V and 15 V are applied on the left and right edges of the anodic compartment, respectively, while the two edges of the cathodic compartment are connected to the ground. Slip boundary conditions are assumed on the channel walls for the fluid velocities in the Navier-Stokes equation, these values being obtained from Eq. 8-5. External pressure is assumed to be zero at all edges. The other parameters used in the calculation are listed in Table 8-1. We performed the simulation by assuming that the current is mainly carried by the ions of the electrolyte, the concentration of the tracer biomolecules being negligible with respect to the electrolyte ionic concentrations. An electrolyte ionic concentration of 1 mM was used (for both + and - ions), corresponding to a Debye length of 10 nm<sup>48, 52</sup>; moreover, an extremely fine mesh of 12 nm was employed at the microchannel / porous membrane interface to resolve the induced space charge effect. During the operation of the device, as a depletion zone locally forms in the anodic compartment close to the membrane, the Debye length dramatically increases there, in favor of even better numerical solution accuracy. Solving the coupled equations proved to be a highly non-trivial task and a convergent solution was reached if  $\rho_{fix}/F < (5-10)mM$ . We stress that the aim of our model is not to present a quantitative one-to-one correspondence between experiment and theory, but instead to provide us with basic insight into the complex physical mechanisms that are at the basis of the preconcentration effect.

Table 8-1: Parameters used in the COMSOL simulation

Diffusion coefficient of a positive/negative ion in the electrolyte *	$1.5 \times 10^{-9} \text{ m}^2/\text{s}$
Diffusion coefficient of a positive/negative ion in the membrane *	$2 \times 10^{-10} \text{ m}^2/\text{s}$
Membrane porosity $\epsilon_p$ *	0.28
Membrane permeability $\kappa^*$	$10^{-18} \text{ m}^2$
Assumed ion concentration (+ and -) in the electrolyte solution $C_0$	1 mM
Assumed fixed volumetric charge concentration of the membrane	1 mM

\* the values are taken and estimated from references <sup>38, 53, 54</sup>, which represents physical properties of porous membrane.

### 8.4.2 Results and discussions

Fig. 8-6a shows the simulated concentration of the positive and negative ions of the electrolyte both within the ion-selective membrane and at the anodic and cathodic compartment side. The calculation was done along the solid line of the insert shown in the lower-left corner of the figure, after application of the external voltage ( $V_L = 5 \text{ V}$ ,  $V_H = 15 \text{ V}$ ) during 1 min, 7 min and 15 min, respectively. The concentration of cations in the membrane is higher than that of the anions for the three cases, which is a direct consequence of the permselectivity of the membrane. Moreover, the ionic concentrations in the anodic compartment strongly decrease in time for both types of ions, while this is the opposite in the cathodic compartment (CP effect).

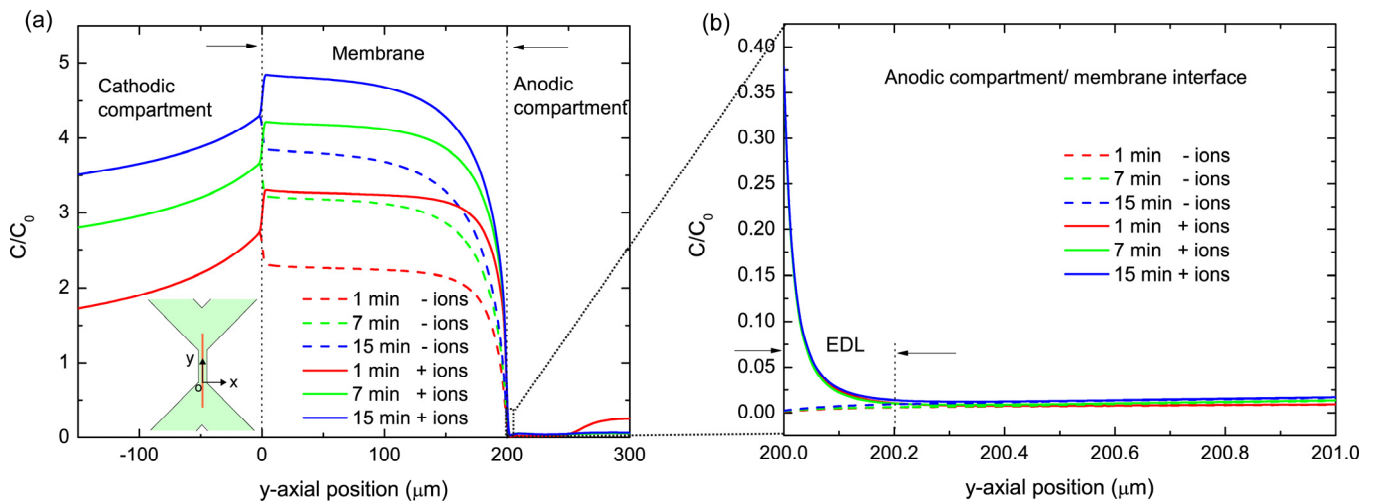


Figure 8-6: (a) Distributions for monovalent positive (full lines) and negative (dashed curves) ions of the background electrolyte after application of the external voltage ( $V_L=5 \text{ V}$ ,  $V_H=15 \text{ V}$ ) during 1 min, 7 min and 15 min, respectively. The calculation is done along the solid line shown in the insert at the lower-left. (b) Zoom on the ion distributions of the background electrolyte in a region close to the membrane, showing charge imbalance and formation of EDL.

As shown in Fig. 8-6b, very close to the membrane interface there is a local surplus of mobile positive ions. This result essentially points to the presence of an induced space charge region over a distance within the channel of about 200 nm. Such secondary EDL, as already suggested in<sup>41</sup>, is the origin of the EOF of the second kind in the anodic compartment, when a potential difference is applied over the latter. The dynamic change in the local ion concentration, hence in the resistivity, also results in a redistribution of local electrical potential and field. This type of behavior is in agreement with the experimental measurement of the local potential distribution in the anodic compartment of a nanochannel-based preconcentration device<sup>18</sup>.

Fig. 8-7a shows the simulated streamlines of the fluid in the anodic compartment and membrane area, after application of the external voltage ( $V_L=5$  V,  $V_H=15$  V) during 15 min. The normalized arrows indicate the flow direction. The tangential component of the electrical field originating from the potential difference ( $V_L-V_H$ ) across the anodic compartment provides the local driving force on the space charge of the EDL near the membrane, inducing the EOF of the second kind. As the latter is only created on the membrane-side of the microchannel, a vortex-like flow pattern is induced. The arrows shown in Fig. 8-7b represent the electrical field strength in an area defined by the dashed rectangle in Fig. 8-7a. Due to the ion depletion effect close to the membrane, the highest field strength is obtained in the region of the main vortex, creating locally an electrical field maximum, inducing an enhanced electrophoretic velocity on the negatively charged tracer biomolecules<sup>18</sup>. This leads to repulsion of the latter from this region. Thanks to the delicate balance between the electrophoretic and electro-osmotic driving forces, the negatively charged tracer molecules will be stacked just right of the field maximum in the anodic compartment, as experimentally observed in Fig. 8-3. Moreover, the topology of the experimental zone of concentration is indicating the presence of vortex-like structures indeed. Fig. 8-7c is a plot of the simulated flow profile in the anodic microchannel along the dotted line in Fig. 8-7a, after application of the external voltage ( $V_L=5$  V,  $V_H=15$  V) during 1, 7 and 15 min, respectively.

After 1 min, a predominantly flat velocity profile is observed across the channel, mainly caused by the EOF of the first kind, taken as  $3 \mu\text{m/s}$  in the model. Based on our experimental parameters, the BSA-coated microchannel under the applied electrical field can provide an EOF in the range of  $5\text{-}10 \mu\text{m/s}$ . However, in order to reach convergence in the simulation, we applied this smaller EOF in the microchannel via the Helmholtz–Smoluchowski slip condition (thin EDL assumption). For increasing times, the ionic depletion zone gets created and the secondary EDL and the vortex form, inducing locally a translational motion of the fluid (EOF of the second kind), as evidenced by the parabolic flow profiles. Our simulation results indicate that both kinds of EOFs are responsible for generation of the fluid velocity in the preconcentration device, while the EOF induced by the nanopores of the membrane is found to be two orders of magnitude smaller than the fluid velocity in the microchannel, and hence does not significantly contribute.

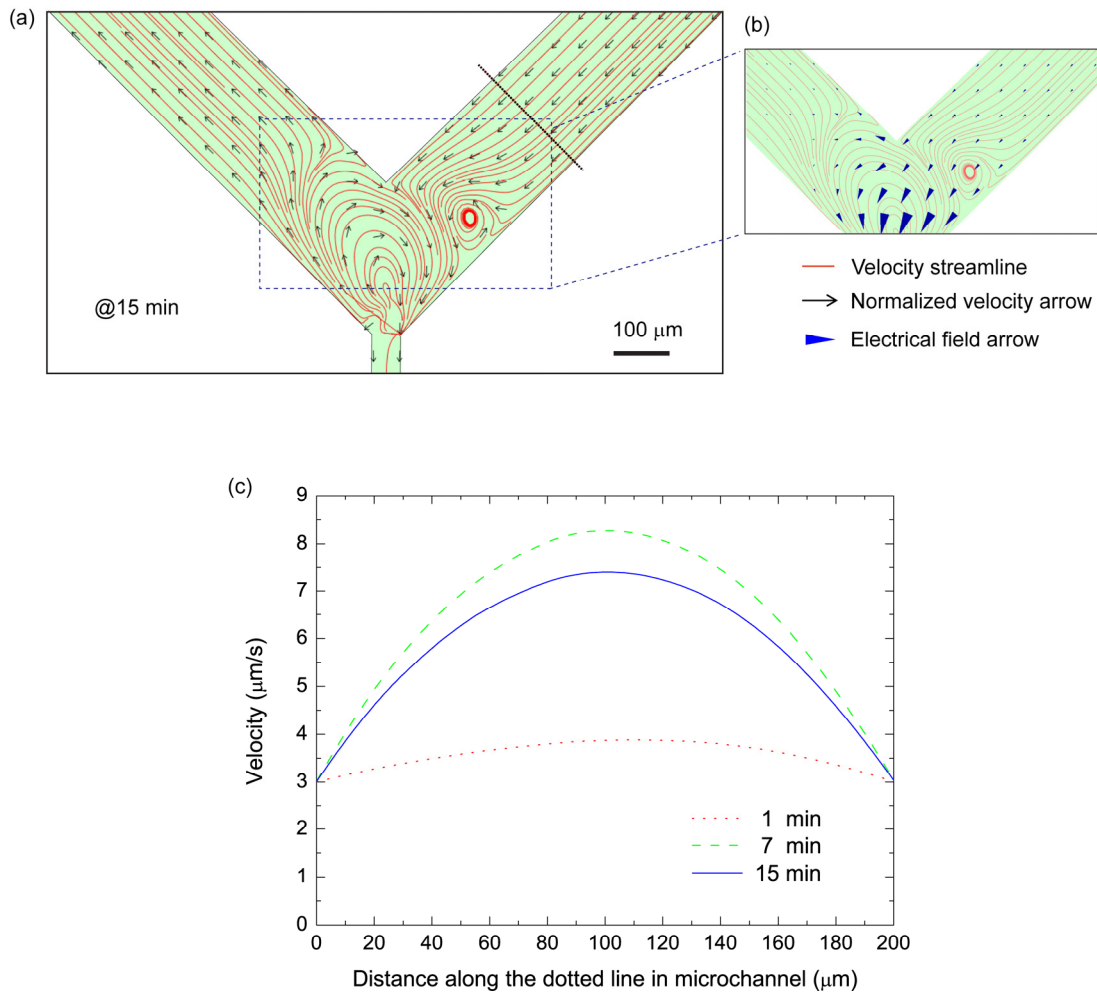


Figure 8-7: (a) Simulated fluid velocity streamlines (uniform density plot) with normalized arrows indicating the flow direction after application of the external voltage ( $V_L=5\text{ V}$ ,  $V_H=15\text{ V}$ ) during 15 min. A vortex-like flow behavior is observed as a consequence of the development of the EDL close to the membrane/anodic compartment interface. (b) Arrows representing the electrical field strength, superimposed on the velocity streamlines, in an area indicated by the dashed rectangle in (a). (c) Plot of the flow profile in the anodic compartment along the dotted line in (a), after application of the external voltage ( $V_L=5\text{ V}$ ,  $V_H=15\text{ V}$ ) during 1, 7 and 15 min.

### 8.5 Comparison with the state-of-the-art

It is also interesting to compare our preconcentration device with published preconcentration devices (see Table 8-2), where our device scores particularly well when considering affordability and portable aspects of lab-on-a-chip applications.

Table 8-2: Comparison with other work

Ref.	Filter material	Detection level	Enrichment factor (Time)	Voltage ( $V_L$ $V_H$ )
15	AA-co-HEMA hydrogel	Fluorescein (5 $\mu$ M)	100 (2 min)	100 V
17	Porous titania membrane (sol-gel)	2,7-dichlorofluorescein (31 nM)	$4 \times 10^3$ (7 min)	150 V 300 V
21	Surface-patterned Nafion	$\beta$ -Phycoerythrin (40 pM)	$5 \times 10^4$ (5 min)	25 V 50 V
23	Nanochannel	rGFP (33 fM)	$10^7$ (40 min)	5 V 10 V
24	Nanofissures	FITC-DSA (100 pM)	$10^3$ - $10^5$ (<10 min)	80 V 80 V
This work	Nafion 117 strip	AF-BSA (60 pM)	$2 \times 10^4$ (7 min)	5 V 15 V

First of all, our novel device is attractive thanks to the straightforward use of the commercial membrane, which avoids complex or *in situ* micro- and nano-fabrication. Second, our limit of detection is as low as tens of pM, competitive with other work. Third, the fast preconcentration ( $10^3$ - $10^4$  fold within several minutes) using only a low operation voltage (< 15 V) hold potential for future portable applications. It is worthwhile to notice that, in our device, as well as those of others, preconcentration occurred on the anodic side of the ion-selective membrane/nanochannel and is benefiting from the co-effect of the first kind and space charge-induced EOF (EOF of the second kind). Preconcentration was also reported on the cathodic side of an ion-permselective membrane, but primary EOF distorted here the phenomenon, and optimized preconcentration was found in this case for a non-charged membrane.

## 8.6 Conclusion

We have developed a simple protein preconcentrator using PDMS rapid prototyping technology and an original ion-permselective membrane assembly technique. Using low voltages (< 15 V), we are able to achieve a preconcentration factor of  $10^3$ - $10^4$  for various concentrations of AF-BSA within 10 min. Our device is capable to reach a sensitivity as low as 60 pM for AF-BSA detection, which is among the best performing preconcentration devices. It has the potential to be conveniently integrated into a (portable) microfluidic analytical system thanks to the low-voltage operation. The use of a microfluidic preconcentrator device has already shown to be at the basis of the enhancement of the analytical sensitivity of an Enzyme-Linked Immunosorbent Assay (ELISA): the limit of detection of prostate specific antigen was decreased to a few pg/mL, two orders of

magnitude lower than the result obtained when no preconcentration device was used. In future, this type of microfluidic preconcentration devices may be essential to providing miniaturization, automatized handling and may offer new analytical possibilities for proteomic applications on single cells.

We also have numerically solved the electrokinetic model consisting of four coupled equations, i.e. the Poisson, Nernst-Planck (two equations for the two buffer ions), and the Navier-Stokes equation (incorporated with continuity equation), which provided key insight into the mechanism of preconcentration. Our study has revealed that the permselective membrane-induced ion depletion at the anodic compartment side of the device gives rise to a secondary EDL and EOF of the second kind, and simultaneously contributes to a local electrical field maximum. This balance between the locally strong electrophoretic force on the negatively charged tracer biomolecules and the combined EOF of the first and the second kind of the bulk fluid is responsible for the biomolecule concentration in a part of the microfluidic channel, which is close to a vortex-like microfluidic pattern and where the electrical field is maximum, consistent with the experimental observations.

## References

1. Shen, M.; Yang, H.; Sivagnanam, V.; Gijs, M. A. M., Microfluidic Protein Preconcentrator Using a Microchannel-Integrated Nafion Strip: Experiment and Modeling. *Analytical Chemistry*, in press, 2010.
2. Ziaie, B.; Baldi, A.; Lei, M.; Gu, Y.; Siegel, R. A., Hard and soft micromachining for BioMEMS: review of techniques and examples of applications in microfluidics and drug delivery. *Advanced Drug Delivery Reviews* 2004, 56, 145-172.
3. Wereley, S.; Meinhart, C., Biomedical Microfluidics and Electrokinetics. *Complex Systems Science in Biomedicine* 2006, 657-677.
4. Broyles, B. S.; Jacobson, S. C.; Ramsey, J. M., Sample filtration, concentration, and separation integrated on microfluidic devices. *Analytical Chemistry* 2003, 75, 2761-2767.
5. Roper, M. G.; Shackman, J. G.; Dahlgren, G. M.; Kennedy, R. T., Microfluidic chip for continuous monitoring of hormone secretion from live cells using an electrophoresis-based immunoassay. *Analytical Chemistry* 2003, 75, 4711-4717.
6. Vilkner, T.; Janasek, D.; Manz, A., Micro total analysis systems. Recent developments. *Analytical Chemistry* 2004, 76, 3373-3386.
7. Schoch, R. B.; Han, J.; Renaud, P., Transport phenomena in nanofluidics. *Reviews of Modern Physics* 2008, 80, 839-883.
8. Li, J.; LeRiche, T.; Tremblay, T. L.; Wang, C.; Bonneil, E.; Harrison, D. J.; Thibault, P., Application of microfluidic devices to proteomics research. *Molecular & Cellular Proteomics* 2002, 1, 157.
9. Mourzina, Y.; Kalyagin, D.; Steffen, A.; Offenhäusser, A., Electrophoretic separations of neuromediators on

microfluidic devices. *Talanta* 2006, 70, 489-498.

10. Graß, B.; Hergenröder, R.; Neyer, A.; Siepe, D., Determination of selenoamino acids by coupling of isotachopheresis/capillary zone electrophoresis on a PMMA microchip. *Journal of Separation Science* 2002, 25, 135-140.

11. Cui, H.; Horiuchi, K.; Dutta, P.; Ivory, C. F., Isoelectric focusing in a poly (dimethylsiloxane) microfluidic chip. *Analytical Chemistry* 2005, 77, 1303-1309.

12. O'Neill, R. A.; Bhamidipati, A.; Bi, X.; Deb-Basu, D.; Cahill, L.; Ferrante, J.; Gentalen, E.; Glazer, M.; Gossett, J.; Hacker, K., Isoelectric focusing technology quantifies protein signaling in 25 cells. *Proceedings of the National Academy of Sciences* 2006, 103, 16153-16158.

13. Yang, W.; Sun, X.; Pan, T.; Woolley, A. T., Affinity monolith preconcentrators for polymer microchip capillary electrophoresis. *Electrophoresis* 2008, 29, 3429-3435.

14. Yu, C.; Davey, M. H.; Svec, F.; Frechet, J. M. J., Monolithic porous polymer for on-chip solid-phase extraction and preconcentration prepared by photoinitiated in situ polymerization within a microfluidic device. *Analytical Chemistry* 2001, 73, 5088-5096.

15. Dhopeswarkar, R.; Crooks, R. M.; Hlushkou, D.; Tallarek, U., Transient effects on microchannel electrokinetic filtering with an ion-permselective membrane. *Analytical Chemistry* 2008, 80, 1039-1048.

16. Hatch, A. V.; Herr, A. E.; Throckmorton, D. J.; Brennan, J. S.; Singh, A. K., Integrated Preconcentration SDS-PAGE of Proteins in Microchips Using Photopatterned Cross-Linked Polyacrylamide Gels. *Analytical Chemistry* 2006, 78, 4976-4984.

17. Hoeman, K. W.; Lange, J. J.; Roman, G. T.; Higgins, D. A.; Culbertson, C. T., Electrokinetic trapping using titania nanoporous membranes fabricated using sol-gel chemistry on microfluidic devices. *Electrophoresis* 2009, 30, 3160-3167.

18. Kim, S. J.; Li, L. D.; Han, J., Amplified Electrokinetic Response by Concentration Polarization near Nanofluidic Channel. *Langmuir* 2009, 25, 7759-7765.

19. Kim, S. J.; Wang, Y. C.; Lee, J. H.; Jang, H.; Han, J., Concentration polarization and nonlinear electrokinetic flow near a nanofluidic channel. *Physical Review Letters* 2007, 99, 44501(4pp).

20. Kim, S. M.; Burns, M. A.; Hasselbrink, E. F., Electrokinetic protein preconcentration using a simple glass/poly (dimethylsiloxane) microfluidic chip. *Analytical Chemistry* 2006, 78, 4779-4785.

21. Lee, J. H.; Song, Y. A.; Han, J., Multiplexed proteomic sample preconcentration device using surface-patterned ion-selective membrane. *Lab on a Chip* 2008, 8, 596-601.

22. Wang, Y.; Pant, K.; Chen, Z.; Wang, G.; Diffey, W. F.; Ashley, P.; Sundaram, S., Numerical analysis of electrokinetic transport in micro-nanofluidic interconnect preconcentrator in hydrodynamic flow. *Microfluidics and Nanofluidics* 2009, 7, 683-696.

23. Wang, Y. C.; Stevens, A. L.; Han, J., Million-fold preconcentration of proteins and peptides by nanofluidic filter. *Analytical Chemistry* 2005, 77, 4293-4299.

24. Yu, H.; Lu, Y.; Zhou, Y.; Wang, F.; He, F.; Xia, X., A simple, disposable microfluidic device for rapid protein concentration and purification via direct-printing. *Lab on a Chip* 2008, 8, 1496-1501.

25. Kim, S. J.; Song, Y. A.; Han, J., Nanofluidic concentration devices for biomolecules utilizing ion concentration polarization: theory, fabrication, and applications. *Chemical Society Reviews* 2010, *39*, 912-922.
26. Song, S.; Singh, A. K.; Kirby, B. J., Electrophoretic Concentration of Proteins at Laser-Patterned Nanoporous Membranes in Microchips. *Analytical Chemistry* 2004, *76*, 4589-4592.
27. Foote, R. S.; Khandurina, J.; Jacobson, S. C.; Ramsey, J. M., Preconcentration of Proteins on Microfluidic Devices Using Porous Silica Membranes. *Analytical Chemistry* 2004, *77*, 57-63.
28. Ross, D.; Locascio, L. E., Microfluidic temperature gradient focusing. *Analytical Chemistry* 2002, *74*, 2556-2564.
29. Hlushkou, D.; Dhopeswarkar, R.; Crooks, R.; Tallarek, U., The influence of membrane ion-permselectivity on electrokinetic concentration enrichment in membrane-based preconcentration units. *Lab on a Chip* 2008, *8*, 1153-1162.
30. Kim, P.; Kim, S. J.; Han, J.; Suh, K. Y., Stabilization of ion concentration polarization using a heterogeneous nanoporous junction. *Nano Letter* 2010, *10*, 16-23.
31. Wang, Y. C.; Han, J., Pre-binding dynamic range and sensitivity enhancement for immuno-sensors using nanofluidic preconcentrator. *Lab on a Chip* 2008, *8*, 392-394.
32. Jönsson, M.; Lindberg, U., A planar polymer microfluidic electrocapture device for bead immobilization. *Journal of Micromechanics and Microengineering* 2006, *16*, 2116-2120.
33. Neburchilov, V.; Martin, J.; Wang, H.; Zhang, J., A review of polymer electrolyte membranes for direct methanol fuel cells. *Journal of Power Sources* 2007, *169*, 221-238.
34. Nguyen, N. T.; Chan, S. H., Micromachined polymer electrolyte membrane and direct methanol fuel cells—a review. *Journal of Micromechanics and Microengineering* 2006, *16*, R1-R12.
35. Mauritz, K. A.; Moore, R. B., State of understanding of Nafion. *Chemical Reviews* 2004, *104*, 4535-4586.
36. Shen, M.; Walter, S.; Gijs, M. A. M., Monolithic micro-direct methanol fuel cell in polydimethylsiloxane with microfluidic channel-integrated Nafion strip. *Journal of Power Sources* 2009, *193*, 761-765.
37. <http://en.wikipedia.org/wiki/Nafion>.
38. Colinart, T.; Didierjean, S.; Lottin, O.; Maranzana, G.; Moyne, C., Transport in PFSA Membranes. *Journal of The Electrochemical Society* 2008, *155*, B244-B257.
39. Guan, J. Q.; Dai, Z. F.; Tung, C. H.; Peng, B. X., Fluorescence Enhancement and Photostability of Novel Pentamethine Cyanines in Nafion-Na<sup>+</sup> Membranes. *Journal of Fluorescence* 2000, *10*, 21-26.
40. Kawano, Y.; Wang, Y.; Palmer, R. A.; Aubuchon, S. R., Stress-strain curves of nafion membranes in acid and salt forms. *Polímeros* 2002, *12*, 96-101.
41. Hölzel, A.; Tallarek, U., Ionic conductance of nanopores in microscale analysis systems: Where microfluidics meets nanofluidics. *Journal of Separation Science* 2007, *30*, 1398-1419.
42. Leinweber, F. C.; Tallarek, U., Nonequilibrium electrokinetic effects in beds of ion-permselective particles. *Langmuir* 2004, *20*, 11637-11648.
43. Gregersen, M. M.; Okkels, F.; Bazant, M. Z.; Bruus, H., Topology and shape optimization of induced-charge electro-osmotic micropumps. *New Journal of Physics* 2009, *11*, 075019 (21pp).



44. Gregersen, M. M.; Bazant, M. Z.; Bruus, H., Numerical studies of nonlinear kinetics in induced-charge electro-osmosis, *XXII ICTAM*, Adelaide, Australia, Aug. 25-29, 2008.
45. Patankar, N. A.; Hu, H. H., Numerical simulation of electroosmotic flow. *Analytical Chemistry* 1998, *70*, 1870-1881.
46. Kuehl, S. A.; Sanderson, R. D., Electrokinetic salt rejection by a hypothetical one-dimensional inhomogeneous charged membrane. *The Journal of Physical Chemistry* 1988, *92*, 517-525.
47. Kang, K. H.; Xuan, X.; Kang, Y.; Li, D., Effects of dc-dielectrophoretic force on particle trajectories in microchannels. *Journal of Applied Physics* 2006, *99*, 064702.
48. Zeng, S.; Chen, C. H.; Mikkelsen, J. C., Fabrication and characterization of electroosmotic micropumps. *Sensors and Actuators B: Chemical* 2001, *79*, 107-114.
49. Dutta, P.; Beskok, A., Analytical solution of combined electroosmotic/pressure driven flows in two-dimensional straight channels: finite Debye layer effects. *Analytical Chemistry* 2001, *73*, 1979-1986.
50. Dukhin, S., Electrokinetic phenomena of the second kind and their applications. *Advances in Colloid and Interface Science* 1991, *35*, 173-196.
51. Wu, Z.; Li, D., Micromixing using induced-charge electrokinetic flow. *Electrochimica Acta* 2008, *53*, 5827-5835.
52. Hlushkou, D.; Perdue, R. K.; Dhopeswarkar, R.; Crooks, R. M.; Tallarek, U., Electric field gradient focusing in microchannels with embedded bipolar electrode. *Lab on a Chip* 2009, *9*, 1903-1913.
53. Lindheimer, A.; Molenat, J.; Gavach, C., A study of the superselectivity of Nafion perfluorosulfonic membranes. *Journal of Electroanalytical Chemistry* 1987, *216*, 71-88.
54. Lide, D. R., *CRC handbook of chemistry and physics*. CRC press: Boca Raton, FL1993.



# Chapter 9

## Conclusion and Outlook

### 9.1 Conclusion

The microfluidic devices realized using rapid prototyping processes presented in this thesis are of particular interest for LOC applications. Micropumps, owing to their significance for biomedical analysis related to their controlled dispensing rate, have been extensively studied in the thesis. The second type of microfluidic device that is designed and fabricated in this thesis is a micro-direct methanol fuel cell, in which a specially designed guiding channel allows us to integrate a Nafion proton exchange strip with the microfluidic channels. Utilizing the technological basis from the fuel cell, the protein preconcentration device presented in this thesis provides the high sensitivity detection of low-concentration biomolecules.

First, we have reported the realization of a low-cost hybrid PMMA ball-valve micropump with two types of planar actuator: (I) a compact electromagnetic actuator and (II) a cylindrical electromagnetic actuator, whose geometries were optimized by the finite element method. The microfluidic structure is composed of seven PMMA sheets or plates as well as an elastomeric membrane that are microfabricated by simple powder blasting and molding technologies, respectively. For example, the water flow rate for the ball-valve micropump actuated by the first electromagnet is as high as 3.6 mL/min and 6.8 mL/min at 500 mW and 2 W actuation power, respectively. The backpressure amounts nearly to 40 kPa at 2 W. Thanks to the improved electromagnetic actuators, our micropump system has been considerably improved in terms of miniaturization and efficiency compared with previous work.

Operating micropump at low power consumption is highly demanded, and thus we have developed the magnetic actuator which only consumes a few 10 mW for our active-valve micropump. The latter consists of a microfluidic chamber structure in glass that is assembled with a PDMS elastic sheet, which comprises two valving membranes and a central pumping chamber actuation membrane, having each an integrated permanent magnet that is magnetically actuated by arc-shaped NdFeB permanent magnets mounted on the rotation axis of a DC minimotor. The affordable powder blasting glass micropatterning and PDMS molding technologies have been used for the microfabrication. A flow rate of 2.4 mL/min and up to 7 kPa backpressure are obtained at the micropump resonance frequency of around 12 Hz, making it very promising for LOC integration.

As miniaturized power source, a microfluidic direct methanol fuel cell with embedded Nafion

strip has been demonstrated by integrating a narrow Nafion strip in a molded PDMS structure. Clamping the PDMS/ Nafion assembly with the catalysts functionalized glass chip results in a leak-tight fuel cell with stable electrical output. Furthermore, not only the channel geometry but also different types of oxidants, important parameters for the fuel cell's performance, have been studied. A maximum power density of  $3.0 \text{ mW/cm}^2$  has been obtained, using  $\text{H}_2\text{O}_2$  based oxidant for a chip with a  $80 \text{ }\mu\text{m}$ -wide channel, due to an improved design that reduces oxidant and fuel depletion effects near the electrodes.

Finally, a simple microfluidic device for protein preconcentration based on the electrokinetic trapping principle has been proposed. It comprises a narrow Nafion strip that was simply cut from a commercial membrane and is integrated in a molded PDMS microfluidic structure using a guiding channel. By using a similar assembly method as for the fuel cell, we are able to obtain a leak-tight and easily disposable device. It enables preconcentration of negatively-charged fluorescent proteins located at the anodic microfluidic compartment side of the Nafion strip within a few minutes and up to a concentration factor of  $10^4$ . Moreover, a numerical study of the preconcentration effect by solving the coupled Poisson, Nernst-Planck and Navier-Stokes equations for our type of device has been put forward, which provides insight into the mechanism of preconcentration.

## 9.2 Outlook

*Rapid prototyping:* Though several categories of low-cost and easy-prototyping technologies have been investigated in the thesis, batch production and control of cost require adaption of the laboratory-based microfabrication tools to an industrial environment. This could be carried out in the following ways:

1. Build a powder blasting machine with multiple nozzle jets, which provide a large working area, enabling parallel micromachining of large substrates at the same time.
2. For our PDMS chips, we have controlled the geometrical parameters using a spin-coater or using a blade to remove the excess PDMS, which is less applicable for mass production. Instead, polymer injection molding of micropump parts is an interesting solution with industrial relevance.
3. In the thesis, we put forward a Nafion strip cutting method using two parallel razor blades, which will be a very tricky technology when employed in industry. Therefore, a novel cutting method, such as based on a sliding machine for cutting tissue slides could be investigated. Furthermore, assembling the Nafion strip into the microfluidic channel under microscopy control is less practical, which may recall an alternative solution, like molding PDMS onto the cut Nafion strips.

*Micropumps:* We have developed two different types of micropump based on magnetic actuation in the thesis. For future integration into LOC systems, further steps should be undertaken:

1. The assembly steps for the PMMA ball-valve micropump system should be simplified and standardized: first, the chemical glue may be replaced by acetone for easy alignment; second, alignment of the micropump with the actuator should be improved in order to considerably reduce the mechanical instabilities.
2. In the thesis, the adhesive bonding between the PDMS magnetic sheet and the glass stack is employed for studying the pump's performance. However, permanent PDMS-glass bonding is also feasible and helpful in reducing the process complexity.

*Fuel cell:* Despite the fact that the micro-DMFC developed in the thesis exhibits a competitive performance, when compared with literature results, it still needs further efforts towards commercialization.

1. The mechanical clamping system used for the fuel cell assembly is at the basis of the stable performance. However, for further miniaturization, it is worthwhile to explore the option of oxygen plasma pretreatment of PDMS sheet and the glass substrates to form an irreversible bonding. This enables easy assembly of the fuel cell without the need of mechanical fixture.
2. In miniaturized power sources for LOC applications, output power is always an issue to be considered. Though our micro-DMFC is able to deliver power of in a range of 100  $\mu\text{W}$ , this is still far from practical needs in power supply. In order to use such novel micro-DMFC, a series connection of multiple fuel cells is necessary.
3. Optimizing the catalysts loading as well as varying the width of Nafion strip should also be topics of further study.

*Protein preconcentrator:* A simple and high-efficiency protein preconcentrator has been developed in the thesis, with a detailed study of the physics of the preconcentration phenomena. But, one should notice there are still some open questions remaining before its integration in LOC system.

1. As the same issue, which we have already discussed for the future work on the micro-DMFC, the mechanical fixture could be eliminated and replaced by irreversible bonding.
2. Although we have carried out some characterization of the device, it is not enough to understand its overall performance. Thus, further experiments using this type of devices should be focused on varying the charge of the tracer biomolecules by adjusting pH values as well as varying the types of biomolecules.
3. Future work will also be required for further optimization of the device's geometry. Smaller microchannels and interfaces of Nafion strip/microchannels will result in a small

preconcentration area with strongly amplified fluorescence signal, which allows even better biomolecule purification.

# Acknowledgement

First, I would like to thank, from the depth of my heart, Prof. Martin Gijs, my thesis director, for giving me an opportunity to come to Lausanne and pursue my doctoral study at his laboratory of LMIS2. He gave me a lot of freedom to explore and try out new ideas for my thesis. He is always very kind and patient for answering all my questions, though sometimes I came to his office to reset his brain. His encouragement to write papers for publication based on the results is always gratefully appreciated.

I acknowledge Prof. Adrian Ionescu (NANOLAB, EPFL) for accepting to be the president of the thesis jury committee. I would like to extend my gratitude and thanks to Prof. Peter Woias (IMTEK, Germany), Prof. Paul Muralt (LC, EPFL) and Dr. Ludovic Dovat (Gotec SA) for accepting to be the jury members for reading and evaluating this thesis.

I would like to express my sincere thanks to Gotec SA for financial supporting during the four years. Not only we have excellent collaboration for developing the miniaturized disposable micropump, but also their technical support for initializing the new applications in aspect of microfluidic devices, like the fuel cell in the thesis, is gratefully appreciated. I would like to extend my gratitude to Dr. Ludovic Dovat who always gave me a lot of inspiring ideas for solving the technical problems that I had met during the experiments and also to his patience for characterizing my papers and presentations. Moreover, I am thankful to Mr. Luis-Miguel Ablanque, Mr. Bruno Gourdin, and Mr. Fabien Dierckx for fruitful discussions. I would like to dedicate this thesis to the late Mr. Bertrand Reuse from Gotec SA.

I am grateful to Dr. Christophe Yamahata from our group. His deep knowledge in micropump related field and his extraordinary skills in dealing with figures are always of great help during my thesis work. Many thanks to my roommate Dr. Abdel Jalil Sayah who helps me to solve many technical problems during my PhD study, especially for powder blasting, spin-coating. I would like to thank the other colleagues of our lab, Dr. Virendra Kumar Parashar, Dr. Qasem Alramadan and Dr. Thomas Lehnert for their scientific kind support during the course of my research. Special thanks to Hui, for her collaboration in fabricating and characterizing the protein preconcentration devices, and especially for her constructive suggestions for solving problems in numerical simulation. Here, I would like to thank Venkat for sharing his expertise in fluorescence microscopy, Fred, Cumhur and Yves for helping me to solve different practical problems related to microfluidics. I thank all my other colleagues for providing me help during my thesis: Josias, Elodie, Emile, Tuna, Rana, Ulrike, Daniel, Jagoda.

All through my thesis, I have precious opportunity to assist Prof. Gijs to train students who significantly contributed to this work during their master and semester projects. Stephan Walter

## Acknowledgement

has worked on the development of fuel cells during his master project and Sohrab Emami-Naini has worked on micropump platform for two semesters.

I sincerely give thanks to all the CMI staff members for their support and for sharing their microfabrication expertise timely. I also thank the ATPR Mechanical Workshop for their assistance in manufacturing numerous components related to my experimental set-ups. My special thanks to Marie Halm, Rose-Mary Apotheloz, Sylvie Clavel, Kathlyn Mayor and Melis Martin for all their help, always with a big smile, in all administrative issues.

I express my gratitude to all my Chinese friends in EPFL who offer me numerous assistances in the aspect of my daily life. Particular thanks to Dr. Hua Zhang, Jin Li, Yan Yan, Fengda Sun, Dr. Hongyan Bi, Liang Qiao, Zhaolu Diao, Cheng Yu, Yu Lu, Dr. Lina Huang, Dr. Tiankai Zhu, Dr. Yu Bai, Shenqi Xie, Ji Cao, Di Jiang.

The support and love of my family have been the endless fuel for my PhD study. Great thanks to my parents, parents in law, my aunt, uncle and my sister. Finally, I express my deep love and gratitude to my husband Dr. Peng Xu (Tony), with whom I shared all the happiness and tears during the four years in Lausanne.



# Publications

## Journal papers

- [1] **M. Shen**, H. Yang, V. Sivagnanam, M.A.M. Gijs, Microfluidic protein preconcentrator using microchannel-integrated Nafion strip: experiment and modeling, *Analytical Chemistry*, in press, 2010 (DOI: 10.1021/ac102149f).
- [2] **M. Shen**, S. Walter, L. Dovat, M.A.M. Gijs. Planar micro-direct methanol fuel cell prototyped by rapid powder blasting, *Microelectronic Engineering*, submitted.
- [3] **M. Shen**, S. Walter, M.A.M. Gijs, Monolithic micro-direct methanol fuel cell in polydimethylsiloxane with microfluidic channel-integrated Nafion strip, *Journal of Power Sources*, 2009, 193, 761-765.
- [4] **M. Shen**, L. Dovat, M.A.M. Gijs, Magnetic active-valve micropump actuated by a rotating magnetic assembly, *Sensors and Actuators B: Chemical*, in press, 2009. (DOI: 10.1016/j.snb.2009.10.033)
- [5] **M. Shen**, C. Yamahata, M.A.M. Gijs, A high-performance compact electromagnetic actuator for a PMMA ball-valve micropump, *Journal of Micromechanics and Microengineering* 2008, 18, 025031 (9pp).
- [6] **M. Shen**, C. Yamahata, M.A.M. Gijs, Miniaturized PMMA ball-valve micropump with cylindrical electromagnetic actuator, *Microelectronic Engineering*, 2008, 85(5-6) 1104-1107.

## International conferences

- [1] **M. Shen**, S. Walter, and M.A.M. Gijs. Planar micro-direct methanol fuel cell prototyped by rapid powder blasting. In *Digest 36<sup>th</sup> International Conference on Micro- and Nano-Engineering*, Genoa, Italy, 19-22 September 2010 (Oral presentation)
- [2] **M. Shen**, M.A.M. Gijs, High-performance magnetic active-valve micropump, *Proceeding of Solid-State Sensors, Actuators and Microsystems Conference*, Denver, USA, 2009, pp. 1234-1237 (Poster presentation)
- [3] **M. Shen**, S. Walter, M.A.M. Gijs, Rapid prototyping of micro-direct methanol fuel cell in PDMS with microchannel-integrated Nafion strip, *Proceeding of Solid-State Sensors, Actuators and Microsystems Conference*, Denver, USA, 2009, pp. 533-536 (Poster presentation)
- [4] **M. Shen**, C. Yamahata, and M.A.M. Gijs. Miniaturized PMMA ball-valve micropump with cylindrical electromagnetic actuator. In *Digest 33<sup>rd</sup> International Conference on Micro- and Nano-Engineering*, Copenhagen, Denmark, 23-26 September 2007 (Poster presentation)

## Publications



# Curriculum Vitae



**Name:** SHEN Meng    **Birthday:** May 6,1981    **Nationality:** P.R.China

**Email:** meng.shen@epfl.ch, amengmimi@gmail.com

## Education

- 2006-Now    PhD candidate, Laboratory of Microsystems,  
                  **Ecole Polytechnique Fédérale de Lausanne (EPFL)**, Switzerland
- 2003-2006    MSc    Condensed matter physics, **Fudan University**, Shanghai, China
- 1999-2003    BSc    Physics, **Nanjing University of Information Science and  
                  Technology** (originally Nanjing Institute of Meteorology), Nanjing, China

## Working and research experiences

**2006-2010**

**Research assistant, Laboratory of Microsystems, EPFL**

- ***Biomedical magnetic micropumps***
  - I. Optimize electromagnetic actuator's geometry and physical parameters by building an electrical-mechanical coupled model with Finite Element Analysis(FEA )method
  - II. Develop PMMA ball-valve micropump characterized by high precision, large range of adjusting dosage by rapid prototyping technology
  - III. Design and fabricate peristaltic-like (active-valve) PDMS/glass disposable and biocompatible micropump with its high-efficiency rotating magnetic actuator
- ***Miniaturized energy sources-fuel cell***
  - I. Realize planar micro methanol fuel cell with particular microfluidic guiding channel using molding technology
  - II. Study the dynamic ion transport of fuel cell by FEA method
  - III. Electrochemical analysis for fuel cell and electrodes
- ***Lab-on-a-chip biomedical analysis***
  - I. Realize membrane integrated protein preconcentration chip with low operation voltage for portable biomolecule analysis
  - II. Predict the experimental observation by modeling the dynamic behavior for preconcentration chip by solving strongly coupled equations using FEA method

**2003-2006    Research assistant, Laboratory of soft condensed matter, Fudan University**

- I. Prepare the colloidal electrorheological fluid: polymer coated TiO<sub>2</sub> nanoparticles
- II. Calculate particle interaction for electrorheological fluid by FEA
- III. Lab management: purchase instrument and consumables for lab, negotiate with big suppliers on the market,

arrange the affaires for foreign visitors

---

## **Other activity**

➤ **2005-2006 Leadership in branch project of Challenging Cup-Tang creative action-**

*synthesize counter-cut nanosized giant electrorheological fluid material*

1. Project management: organize meetings and coordinate activities for group members
  2. Write technical reports and give presentations
- 

## **Languages**

- Fluent in English
  - Basic knowledge of French
- 

## **Technical computational skills**

- Model: COMSOL Multiphysics(7 years), ANSYS(1years), MATLAB(10 years), Simulink(10 years)
  - Design: SolidWorks(4 years), Labview(2 years), C++(3 years), VB(2 years)
- 

## **Award and Scholarship**

- Chinese government award for outstanding self-financed student abroad (2009)
- Second-class and third-class graduates award at Fudan University (2004-2005)
- 3<sup>rd</sup> award in "Jiangsu undergraduates technique and innovation competition" (2002)
- First-class and second-class awards during undergraduate period (1999-2003)